Post-translational regulation of BiP by FICD-mediated AMPylation and deAMPylation

Luke Aleksander Perera

Jesus College

January 2021

This thesis is submitted to the University of Cambridge for the degree of Doctor of Philosophy

Preface

This thesis is the result of my own work and includes nothing which is the outcome of work done in collaboration except as declared below and specified in the text. It is not substantially the same as any work that has already been submitted before for any degree or other qualification except as declared below and specified in the text. It does not exceed the prescribed 60,000-word limit for the Clinical Medicine and Clinical Veterinary Medicine Degree Committee.

Parts of this work have been presented in the following publication:

Perera LA, Rato C, Yan Y, Neidhardt L, McLaughlin SH, Read RJ, Preissler S & Ron D (2019) An oligomeric state-dependent switch in the ER enzyme FICD regulates AMPylation and deAMPylation of BiP. *EMBO J.* **38:** e102177

Note, this publication is cited (largely in the introduction) in reference to work that forms part of this publication and was principally carried out by collaborators. My own contributions to this manuscript, which are distributed throughout the results section of this thesis, do not include explicit citation of this publication.

In the following work, protein partial deuteration (required for the SANS experiment presented in **Chapter 2.2**) was carried out by collaborators Juliette M. Devos and Michael Haertlein (Deuteration lab, Institut Laue-Langevin, Grenoble, France). Matchout deuterated cell pastes were then sent to me in the UK for further protein purification.

Collaborators Nathan Zaccai (Cambridge Institute for Medical Research) and Sylvain Prévost (Institut Laue-Langevin, Grenoble, France) assisted with the SANS experimental planning and data acquisition.

The in vitro FP-based deAMPylation experiments were carried out by Steffen Preissler (Cambridge Institute for Medical Research), following my plans for the assays. I then processed and analysed the data as presented.

Cláudia Rato da Silva (formerly Cambridge Institute for Medical Research) provided advice on the in vivo experiments.

Abstract

Post-translational regulation of BiP by FICD-mediated AMPylation and deAMPylation

Luke Aleksander Perera

Regulation of the amount and activity of Binding Immunoglobulin Protein (BiP) contributes to protein-folding homeostasis. BiP's abundance is modulated transcriptionally by the canonical unfolded protein response (UPR). Conversely, a metazoan-specific, endoplasmic reticulum (ER)-resident, Fic domain containing protein (FICD) is able to dynamically adjust BiP's activity through AMPylation and deAMPylation. These two mutually antagonistic reactions, catalysed by the single active site of FICD, are reciprocally regulated by an oligomeric state-dependent switch. Under conditions of low unfolded protein load this bifunctional (monomeric) Fic enzyme AMPylates and inactivates excess ATP-bound BiP. However, with increasing ER stress dimeric FICD rapidly deAMPylates the inactive BiP-AMP store — enabling extra BiP to re-enter the chaperone cycle and thereby increase the organelle's chaperone capacity (in a post-translational strand of the UPR). In this thesis, through structural, biochemical and biophysical techniques, I address the fundamental nature of FICD's post-translational regulation of BiP. By obtaining high-resolution crystal structures of trapped deAMPylation complexes (of FICD•BiP-AMP) I elucidate the basis of FICD substrate engagement, reveal the mechanism of Fic domain deAMPylation and clarify the essential role of the gatekeeper Glu234 residue (characteristic of the Fic domain inhibitory α-helix) in this hydrolytic reaction. These structures also explain FICD's exquisite selectivity for its AMPylation substrate — ATP-bound, domain-docked BiP — with FICD's tetratricopeptide repeat domain binding a tripartite assembly of BiP's nucleotide binding domain, docked linker and substrate binding domain, that is unique to the aforementioned Hsp70-state. My studies also shed light on the structural basis of the monomerisation-dependent switch between FICD's two mutually antagonistic activities — which centres on a monomerisation-induced increase in gatekeeper Glu234 flexibility. Upon monomerisation, increased Glu234 flexibility permits AMPylation competent binding of MgATP in FICD's active site whilst simultaneously impairing the ability for Glu234 to properly align an attacking water molecule for efficient deAMPylation of BiP-AMP.

Acknowledgments

It feels like quite a long time ago that I first started working in the Ron lab. Still fresh-faced from my undergraduate studies I joined the Ron lab full of optimism, on my second rotation project of my master's degree, at the beginning of January 2016. Unperturbed during this initial three-month encounter with the lab, I re-joined in October of the same year to embark upon my PhD. Many moons later, and over 5 years since initially setting foot in the lab, this is where I find myself.

Throughout my time in the lab, I have always felt very well supported by all of my colleagues, but I would like to thank a few in particular by name. Firstly, I would like to acknowledge Yahui Yan. Yahui is almost entirely responsible for training me in the dark art that is protein crystallography and for this I am very grateful. Secondly, my work builds on the pioneering studies conducted by Cláudia Rato da Silva and Steffen Preissler. Not only did both of these individuals lay the foundations of the lab's interest in the AMPylation of BiP and FICD, but they also continued to provide invaluable contributions in this field throughout my time in the lab. Working together as a very multidisciplinary team, and with their mentorship, I believe we achieved a lot. I am sure the thesis I am presenting here would be very different without their help. Last, and not least, I would like to thank David for his valuable, keen and astute supervision. David has always made time to discuss my project and to provide discerning feedback and suggestions.

One of the things I was keen to instigate after joining the lab, was a 3.30 pm 'lab' coffee break. I eventually managed to coerce a few colleagues to join me, and in the halcyon days pre-COVID 19 the daily event had become a fairly well-established tradition. I therefore thank the members of the Ron lab who regularly joined me to discuss science, news and life (over coffee). In particular, and in order of frequency of attendance, I would like to thank Cláudia, Yahui, Heather Harding and Luka Smalkinskaite.

I would also like to thank my college community and friends for their support throughout my (protracted) length of time as a member of the University of Cambridge, since starting my undergraduate studies way back in 2012.

Most importantly, I would like to thank my family. In particular my sisters, parents and grandparents who have been integral to the shaping of the person I am today.

Table of Contents

List of Figures and Tables

Abbreviations

α_{inh}	Inhibitory alpha helix
A[*M/T*]P(FAM)	N^6-(6-Amino)hexyl-A[*M/T*]P-6-FAM
BiP	Binding-immunoglobulin protein
BLI	Bio-layer interferometry
BtFic	*Bacteroides thetaiotaomicron* Fic protein
CdFic	*Clostridium difficile* Fic protein
CMP	Contrast match point
COM	Centre of mass
Δ^iG	Free energy change upon interface formation
$\Delta\rho$	Sample contrast (SLD difference between protein and buffer, $\rho_{protein} - \rho_{buffer}$)
DSF	Differential scanning fluorimetry
eIF2α	Eukaryotic initiation factor 2α
E. coli	*Escherichia coli*
ER	Endoplasmic reticulum
EfFICD	*Enterococcus faecalis* FIC Protein
FACS	Fluorescence-activated cell sorting
FAM	6-Carboxyfluorescein (6-FAM)
Fic	Filamentation induced by cAMP
dFICD	Dimeric FICD
FICD	Fic domain containing protein
FP	Fluorescence polarisation
FPLC	Fast protein liquid chromatography
GRP78	Glucose-regulated protein 78
GS-ATase	Glutamine Synthetase Adenylyltransferase
HPLC	High-performance liquid chromatography
Hsp70	Heat shock protein 70
HYPE	Huntingtin yeast interacting protein E
IB	Immunoblot
IEF	Isoelectric focusing
IP-RP-HPLC	Ion-pair reversed-phase HPLC
JDP	J-domain protein
K_D	Equilibrium dissociation constant

K_D^{eff}	Effective equilibrium dissociation constant
k_{off}	Dissociation/off-rate
k_{on}	Association/on-rate
K_M	Michaelis constant
λ	Wavelength
M_W	Molecular weight
mFICD	Monomeric FICD^{L258D}
MS	Mass spectrometry
NBD	Nucleotide binding domain
NEF	Nucleotide exchange factor
NmFic	*Neisseria meningitides* fic protein
OG	Oregon Green 488 dye
PAGE	Polyacrylamide gel electrophoresis
PISA	Protein interfaces, surfaces and assemblies' service
PPM	Metal-dependent protein phosphatase
PTM	Post translational modification
q	Magnitude of the scattering vector
R_g	Radius of gyration
R_m	R_g at infinite contrast
RER	Rough ER
RMSD	Root-mean-square deviation
SANS	Small angle neutron scattering
SAXS	Small angle X-ray scattering
SBD	Substrate binding domain
SD	Standard deviation
SE	Standard error
SEM	Standard error of the mean
SLD	Scattering length density
S_N2	Bimolecular nucleophilic substitution
SubA	Subtilisin A
TMR	Tetramethylrhodamine-5-maleimide
TPR	Tetratricopeptide repeat
UPR	Unfolded protein response

Chapter 1: Introduction

Chapter 1.1: The BiP chaperone cycle

Protein folding homeostasis in the endoplasmic reticulum (ER) is essential for cell viability and proper cellular function. A failure to maintain folding homeostasis in this cellular compartment can lead to an accumulation of misfolded proteins, cell death and a number of diseases (Balch *et al*, 2008; Walter & Ron, 2011). ER homeostasis is achieved through the ability of a cell to match the ER folding capacity to the burden of unfolded protein. As the major ER chaperone, binding-immunoglobulin protein (BiP) dominates the chaperoning capacity of the ER (Bakunts *et al*, 2017). BiP both acts as the sensor and principal responder to increased ER stress (Kozutsumi *et al*, 1988; Chang *et al*, 1989; Bakunts *et al*, 2017; Vitale *et al*, 2019; Amin-Wetzel *et al*, 2019). In response to an excess of unfolded proteins, well-defined transcriptional and translational programmes, which constitute the unfolded protein response (UPR), are initiated (Walter & Ron, 2011). These result in a considerable transcriptional upregulation of BiP, so as to increase the amount of ER chaperone to match the levels of unfolded client.

BiP (also known as glucose-regulated protein 78; GRP78) is a member of the ubiquitous and highly conserved heat shock protein of 70 kDa (Hsp70) chaperone family. There is a high degree of structural conservation across all Hsp70s. These proteins are made up of two domains, a nucleotide binding domain (NBD) and a substrate binding domain (SBD), separated by an interdomain linker. In turn, the SBD is composed of two distinct subdomains an α-helical lid subdomain (SBDα) and a β-sheet rich subdomain (SBDβ), which contains a groove responsible for binding extended/unfolded client peptides. BiP, as an ER chaperone carries out a number of essential functions, most notably the facilitation of de novo secretory-pathway protein folding, an inhibition of protein aggregation and a regulation of protein degradation and secretion (Otero *et al*, 2010). All of these functions, which are also shared by other Hsp70 members in varying cellular environments, are solicited through the binding of (partially) unfolded clients within BiP's SBD. In so doing, BiP either elicits an ATP-dependent holdase function (Sekhar *et al*, 2015) or unfoldase activity on the client protein. The latter mediated, at least in part, through a J-domain protein (JDP) stimulated mechanism of substrate ultra-affinity and an excluded volume-based effect dubbed entropic pulling (De Los Rios & Barducci, 2014; De Los Rios *et al*, 2006; Mayer & Gierasch, 2019).

The ability of BiP to act as an effective chaperone is predicated on its capacity to undergo large conformational changes: from a linker buried and lid open ATP-bound state (BiP:ATP) with fast substrate on and off rates; to a linker exposed and lid closed ADP state (BiP:ADP) with slow substrate binding kinetics and much longer substrate residency times (Kityk *et al*, 2015; Yang *et al*, 2015). Both ligands (nucleotide and substrate peptides) and protein co-chaperones (JDP and nucleotide exchange factors; NEFs) act as allosteric modulators of the Hsp70 conformational equilibrium (Zhuravleva *et al*, 2012). Biochemical insights into this chaperone cycle have gradually been complemented by solution structure and crystallographic snapshots of Hsp70 proteins in two principal conformations and bound to various cofactors (**Figure 1.1.1**).

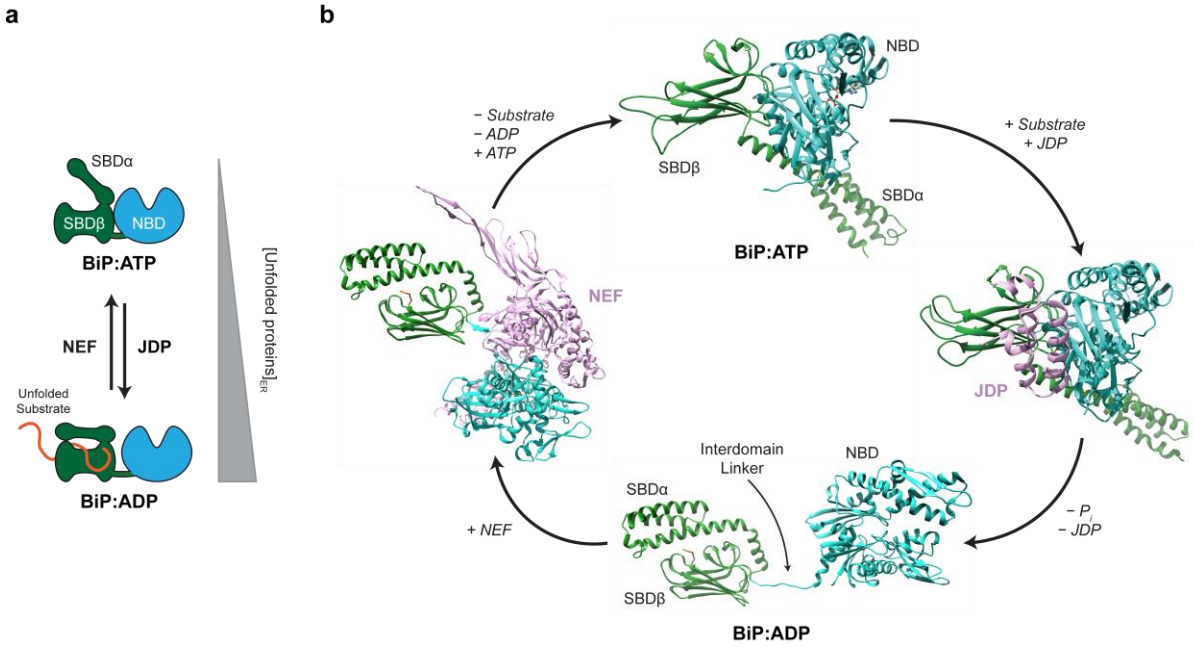

Figure 1.1.1: The allosteric BiP chaperone cycle. **a,** A cartoon representation of the chaperone cycle. BiP, like all Hsp70 proteins, can exist in two major conformations. In the presence of MgATP, BiP principally assumes a domain-docked conformation (BiP:ATP) with low substrate affinity. In the absence of nucleotide or presence of MgADP, BiP favours its domain-undocked, linker extended and lid-closed state (BiP:ADP), which possesses high substrate affinity. This equilibrium can be modulated by changing nucleotide content, levels of unfolded substrate (grey) and by co-chaperone proteins — nucleotide exchange factors (NEFs) and J-domain proteins (JDPs). Schematised (sub)domain architecture is annotated: substrate binding domain-α/β (SBDα/β); nucleotide binding domain (NBD). **b,** Structural view of the BiP chaperone cycle. Domains are colour-coded as in **a**. All structures are presented in the same view and are aligned to BiP in the ATP-state (PDB 5E84) via its SBDβ or, in the case of the Hsp70•JDP structure, via its NBD. The Hsp70•JDP structure is in fact derived from the *E. coli* homologues (DnaK•DnaJ; PDB 5NRO) and does not contain an SBD-bound substrate. BiP in the ADP-state is an overlay of an SBDα-truncated BiP structure (PDB 7A4U) with an intact BiP SBD (PDB 5E85, both structures are coloured in green) that is bound to an unfolded peptide substrate (orange). The latter (PDB 5E85) is also superposed on the

Hsp70•NEF complex (lid-truncated bovine Hsc70 with yeast (Hsp110) NEF protein Sse1; PDB 3C7N). Co-chaperones are coloured in pink.

The amount of active BiP, able to progress through the chaperone cycle, is tightly regulated by altering the amount of BiP in the ER and by modulating BiP's activity. The former is achieved through transcriptional regulation mediated by the canonical UPR. This results in a proteostasis system which contains inherent latencies associated with transcription, translation and chaperone protein turnover. Conversely, BiP activity can be modulated through post-translational modification (PTM), which offers a more dynamic means of regulating the functional ER chaperone capacity (Preissler & Ron, 2019). The best understood regulatory PTM is BiP adenylylation, more commonly known as AMPylation.

Chapter 1.2: Post-translational modification of BiP

BiP was identified as the principal target for incorporation of radioactive signal upon in vivo treatment of cells with [^{3}H]-adenosine (Carlsson & Lazarides, 1983). BiP was also radioactively labelled upon incubation of cells with [^{32}P]-orthophosphate and upon ex vivo (cell lysate) treatment with [^{32}P]-NAD^{+} (Chambers *et al*, 2012; Carlsson & Lazarides, 1983). On this basis the BiP modification was originally misidentified as ADP-ribosylation (Carlsson & Lazarides, 1983). Subsequent mass spectrometry (MS) analysis has definitively identified this PTM to represent AMPylation (Ham *et al*, 2014; Preissler *et al*, 2015b) — the covalent addition of an AMP moiety from an ATP co-substrate onto a hydroxyl group containing protein side chain. Both in vivo and in vitro, BiP AMPylation is specifically localised to the covalent modification of Thr518, a residue within the loop linking β7 and β8 ($\ell_{7,8}$) of BiP's SBDβ (Preissler *et al*, 2015b; Broncel *et al*, 2016; Casey *et al*, 2017). This finding was consistent with the previous assignment of ADP-ribosylation to BiP's SBD (Gaut, 1997; Chambers *et al*, 2012).

BiP AMPylation is an inactivating modification, heavily biasing BiP towards its ATP-state (independent of NBD nucleotide content), resulting in high rates of BiP-substrate dissociation and reduced ATPase activity (Wieteska *et al*, 2017; Preissler *et al*, 2015b). The bulky modification of $\ell_{7,8}$ is sufficient to trap BiP, crystallographically, in its domain-docked ATP-state despite being made nucleotide free (apo) during protein purification (**Figure 1.2.1**). It also renders BiP refractory to JDP-mediated ATPase stimulation (Preissler *et al*, 2017b). The mechanism of BiP inactivation afforded by AMPylation presumably reflects a decreased

propensity for the reorganisation of $\ell_{7,8}$ (and by extension the shift from a β8/β5 to a β8/β7 sheet) required for the transition the SBDβ from its ATP- to ADP-state (Preissler *et al*, 2017b; Zhuravleva & Gierasch, 2015). Conversely, the same lid (SBDα)-truncated BiP construct, when left unmodified and made apo, crystallises (as anticipated) in its domain-undocked ADP-state (**Figure 1.1.1b**; PDB 7A4U) (Preissler *et al*, 2020).

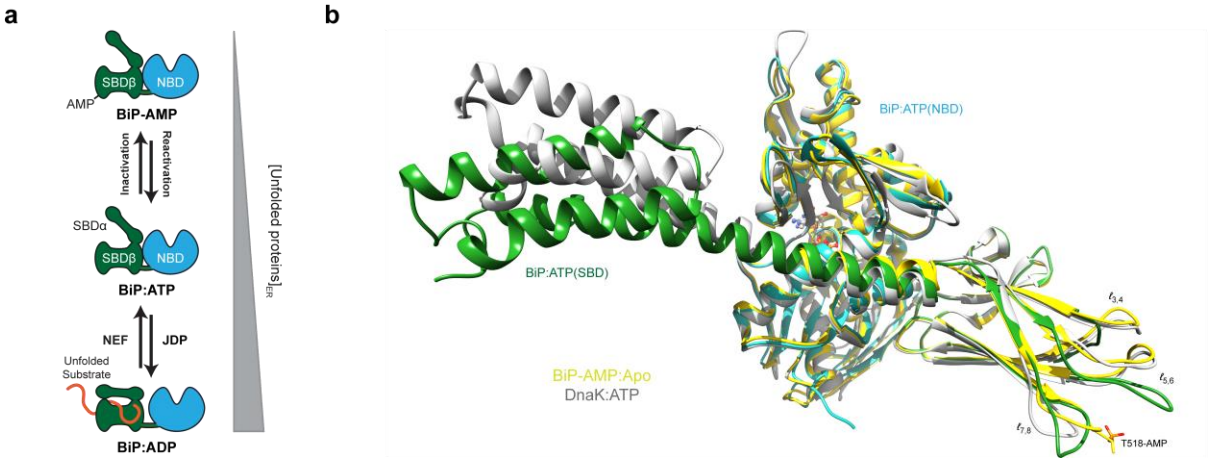

Figure 1.2.1: AMPylation inactivates BiP by locking it in an ATP like–state. a, A cartoon representation of the chaperone cycle extended to schematise the additional role of BiP AMPylation in providing a readily accessible buffer of inactive chaperone. **b,** Alignment (via the NBD) of BiP:ATP (PDB 5E84; coloured as in **a** and **Figure 1.1.1b**) with SBDα-truncated BiP-AMP:Apo (PDB 5O4P; yellow) and DnaK:ATP (PDB 4B9Q; grey). Despite being free of nucleotide BiP-AMP clearly adopts a domain-docked, lid-open, ATP-state conformation; with very little deviation from other ATP-bound Hsp70 structures in the NBD region. The modified Thr518 (shown), within the BiP-AMP structure, had limited obvious electron density corresponding to the AMP-moiety, as a result only the α-phosphate is modelled. The minor deviation in SBDβ conformation visible between BiP:ATP and BiP-AMP:Apo is largely localised to flexible loops (in particular $\ell_{5,6}$), attributable to the corrupting effects of a $\ell_{3,4}$ truncation introduced into the former and AMPylation of $\ell_{7,8}$ in the latter.

Consistent with the inactivating character of BiP AMPylation, this modification is temporally dynamic and the levels of BiP-AMP are modulated in vivo in order to meet the protein folding demand within the ER. For example, around 40–60% of the entire BiP pool becomes AMPylated within 2–3 h of cycloheximide induced inhibition of protein synthesis, both in cells (Laitusis *et al*, 1999; Preissler *et al*, 2015b) and in the pancreas of treated mice (Chambers *et al*, 2012). Likewise, mice subjected to overnight fasting (which results in a physiological depreciation in pancreatic protein synthesis) exhibited a similar induction of BiP AMPylation, which could be rapidly reversed (within 1 h) by refeeding, to a basal level of ~15% AMPylated BiP (Chambers *et al*, 2012). Significant, BiP AMPylation has also been observed in cells following the resolution of acute ER stress (Preissler *et al*, 2015b). That is to say, in the

aftermath of significant UPR-mediated transcriptional upregulation of BiP, in a regime following the removal of pharmacological stressors. Under such conditions levels of chaperone presumably far exceed the chaperoning requirements of unfolded client protein (Bakunts *et al*, 2017), triggering the observed post-translational inactivation of excess chaperone. It should be noted that in earlier studies, as mentioned above, the authors believed the BiP PTM in question was ADP-ribosylation (Carlsson & Lazarides, 1983; Laitusis *et al*, 1999; Chambers *et al*, 2012). Quantification of the degree of BiP modification was achieved by utilising a characteristic (PTM induced) shift in BiP protein migration on an isoelectric focusing (IEF) gel. It has since been demonstrated that the IEF shift is entirely AMPylation dependent, as knockout of the identified AMPylase abrogates this phenomenon (Preissler *et al*, 2015b).

Conversely, as exemplified by mouse refeeding experiments, it has been extensively demonstrated that (in a range of cell lines) as ER stress is increased the pool of BiP-AMP is swiftly deAMPylated, reactivating the reserve chaperone capacity to enable extra BiP to productively engage in the chaperone cycle (Laitusis *et al*, 1999; Chambers *et al*, 2012; Preissler *et al*, 2015b). Thus, BiP-AMPylation enables the ER to both reduce the effects of transient ER stresses (through deAMPylation) and ameliorate the possibility of over-chaperoning (through AMPylation). As BiP is reported to have a half-life in the order of days (Hendershot *et al*, 1988; Gulow *et al*, 2002; Lau *et al*, 2016; Wang *et al*, 2017), a BiP buffering system based on dynamic AMPylation/deAMPylation is able to operate on a time-scale that is inaccessible to a homeostatic feedback system mediated solely by transcriptional regulation and protein-turnover. Moreover, the former timescale is better matched to the transient short-term fluctuations in ER unfolded protein load associated with in vivo demands on secreted protein synthesis (Chambers *et al*, 2012). These properties of the BiP-AMPylation and deAMPylation system may contribute to the phenotype observed in the *Drosophila* visual system, whereby impairing the ability to AMPylate BiP results in light-induced blindness (Rahman *et al*, 2012; Moehlman *et al*, 2018)

Until relatively recently protein AMPylation was considered to be a PTM that was exclusively catalysed by bacterial proteins and often by bacterial effector proteins. Fortunately, on account of a horizontal gene transfer from bacteria into the last common metazoan ancestor, there exists a single AMPylation capable Fic protein exemplar within the mammalian proteome (Khater & Mohanty, 2015a). This protein, FICD, is ER localised and is solely responsible for BiP AMPylation (Ham *et al*, 2014; Sanyal *et al*, 2015; Preissler *et al*, 2015b).

Chapter 1.3: AMPylation

There are only a small number of identified protein families capable of AMPylating (also known as adenylylating) hydroxyl groups in order to covalently link an AMP moiety, via a phosphodiester bond, to a target protein. This contrasts with the more transient AMPylation catalysed by a number of enzyme families, including aminoacyl-tRNA synthetases and non-ribosomal peptide synthetases. These enzymes facilitate carboxyl group adenylation, resulting in the formation of a mixed anhydride linkage, the product of which often represents a short-lived reaction intermediate.

There are three major classes of protein hydroxyl group AMPylating enzymes. The first to be identified was characterised by *E. coli* glutamine synthetase adenylyl transferase (GS-ATase), which AMPylates glutamine synthetase (GS) (Kingdon *et al*, 1967; Hennig *et al*, 1970; Brown *et al*, 1971). The GS-ATase protein family is itself part of a larger nucleotidyl transferase protein superfamily. The second class of AMPylators, the DrrA-like protein family, represents a rare group of proteins with a taxonomical distribution limited to strains of *Legionella pneumophila* (Muller *et al*, 2010; Khater & Mohanty, 2015a). The N-terminal AMPylation relevant domain of DrrA (also known as SidM) is ATase-like, sharing considerable structural homology and the catalytic GS-ATase GxDxD motif. However, other than the conserved catalytic residues the sequence similarity between GS-ATase and DrrA is small and they possess divergent substrate specificities (Khater & Mohanty, 2015a) — the former AMPylates GS whereas DrrA AMPylates host organism small GTPases (Muller *et al*, 2010). The third canonical AMPylase protein family is characterised by a Fic (filamentation induced by cAMP) protein fold. AMPylation activity of a Fic protein was initially observed in a bacterial effector protein (VopS) of the human pathogen *Vibrio parahaemol* (Yarbrough *et al*, 2009), despite the domain being originally identified 20 years previously from an *E. coli* mutation resulting in the eponymous filamentation phenotype (Utsumi *et al*, 1982). Fic domain proteins are evolutionarily unrelated to either GS-ATase or DrrA like proteins. In addition, SelO (a selenocysteine containing pseudokinase that is evolutionarily conserved across bacteria and eukaryotes) has recently been described to possess AMPylation and uridine monophosphate transferase (UMPylation) activity (Sreelatha *et al*, 2018; Yang *et al*, 2020). However, the degree to which SelO is able to AMPylate endogenous targets, either in vitro or in vivo, remains to be determined.

Since the discovery of Fic domain mediated AMPylation by VopS, many other Fic domain containing proteins with AMPylation activity have been characterised. Moreover, a number of other chemistries catalysed by this domain have also been documented, including phosphorylation, phosphocholination and UMPylation (Castro-Roa *et al*, 2013; Campanacci *et al*, 2013; Feng *et al*, 2012); illustrating the potential versatility of the Fic domain fold. It is the largest of the three AMPylase families, and is found across the bacterial domain of life and scattered throughout the archaeal and eukaryotic phylogenetic branches, with a distribution indicative of a bacterial origin followed by multiple horizontal gene transfer events (Khater & Mohanty, 2015a). Fic domain containing proteins, along with the related Doc domain proteins, contain a conserved active site Fic motif: HPFx(D/E)GN(G/K)R_1xxR_2. Additionally, the bacterial effector protein *Pseudomonas* AvrB, despite lacking the Fic motif, shares considerable structural homology with the Fic domain. Together the Fic, Doc and AvrB family proteins have been grouped into one Fido superfamily, despite catalysing divergent chemical reactions (Kinch *et al*, 2009; Khater & Mohanty, 2015a, 2015b).

The mechanism of Fic domain protein catalysed AMPylation, based on a body of biochemical, structural and computation work, is fairly well understood (Luong *et al*, 2010; Xiao *et al*, 2010; Khater & Mohanty, 2015b). The AMPylation reaction requires Mg^{2+} coordination of ATP's α- and β-phosphates and the conserved histidine of the Fic motif is required for general base catalysis (**Figure 1.3.1**). Following nucleophilic attack of the target protein hydroxyl group into the ATP α-phosphate, an AMPylated protein and pyrophosphate (PP_i) are the resulting products (**Figure 1.3.1**).

Fic proteins are also characterised by the presence of glutamate containing alpha inhibitory helix (α_{inh}), which is responsible for autoinhibition of canonical Fic AMPylation activity (Engel *et al*, 2012; Goepfert *et al*, 2013). Depending on whether the α_{inh} is a separate protein (as a bacterial antitoxin) or is N- or C-terminally contiguous with the Fic domain; Fic domain proteins are classified as either class I, II or III, respectively (Engel *et al*, 2012). The inhibitory glutamate of Fic α_{inh} has been demonstrated to sterically and electrostatically occlude ATP γ-phosphate binding, and to compete with the γ-phosphate for interaction with a conserved arginine (R_2) of the Fic motif. The inhibitory glutamate forces a binding orientation of ATP (the co-substrate for AMPylation), within the Fic domain active site, such that its α-phosphate is incompatible with in-line nucleophilic attack of the target hydroxyl group (Engel *et al*, 2012; Goepfert *et al*, 2013).

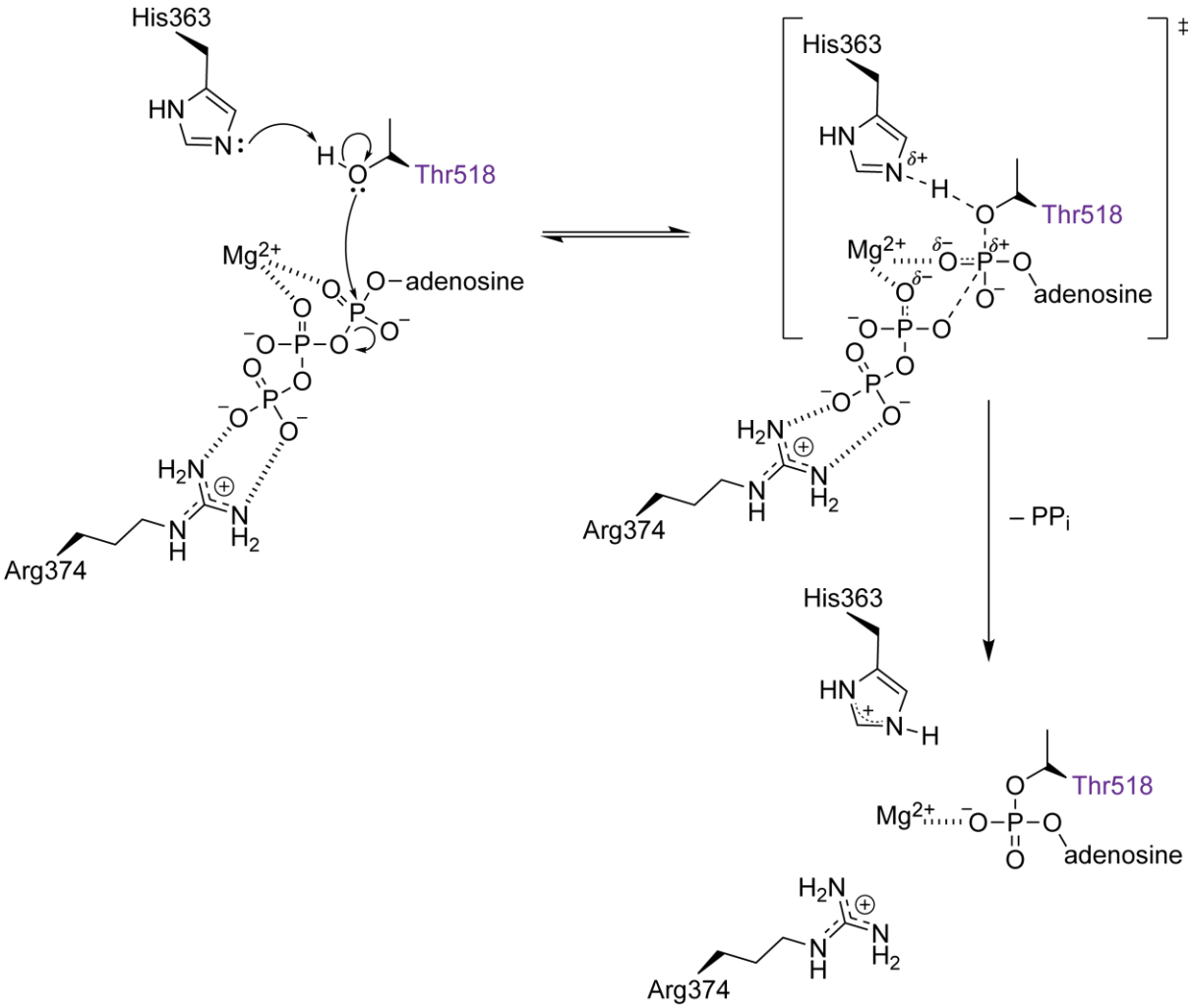

Figure 1.3.1: Reaction scheme for Fic domain catalysed protein AMPylation. Residues are labelled according to human FICD amino acid sequence. Additionally, the target residue is depicted as FICD's endogenous target — BiP's Thr518 (purple). Note, other Fic proteins are capable of modifying different hydroxyl group-containing amino acids. R_2 of the Fic motif (Arg374) forms a salt bridge to ATP's γ-phosphate, enabling the binding of ATP such that its α-phosphate is correctly positioned for in-line nucleophilic attack of the target hydroxyl group. The Fic motif histidine (His363) catalyses a concerted deprotonation of the hydroxyl group which attacks the backside of the α-phosphate's phosphoanhydride bond (in a general base catalysed S_N2-type reaction). Extra (partial; δ) negative charge, delocalised through the α- and β-phosphates, is stabilised by Mg^{2+} coordination and the Fic domain oxyanion hole (not shown). Following product (PP_i and BiP-AMP) dissociation proton exchange with the solvent can regenerate the original active site protonation state (not shown). Partial covalent bonds in the proposed transition state (‡) are depicted with dashed lines, and polar interactions with hashed lines.

Like the unrelated DrrA family, many Fic proteins act as bacterial effector proteins targeting host protein small GTPases. Conversely, the metazoan specific Fic domain containing protein (FICD) is responsible for the AMPylation of the ER Hsp70 protein, BiP (Sanyal *et al*, 2015; Ham *et al*, 2014; Preissler *et al*, 2015b). FICD is a class II Fic protein which is thought to have

evolved from the product of a horizontal gene transfer of a class II Fic domain, from a bacterial species, into the metazoan last common ancestor (Khater & Mohanty, 2015a). It has been demonstrated to be an ER localised, type II membrane protein (Bunney *et al*, 2014; Sanyal *et al*, 2015). Human FICD (also known as huntingtin yeast interacting protein E; HYPE) and its metazoan homologues exhibit a high degree of sequence and structural conservation. For instance, although the *C. elegans* Fic protein (FIC-1) is one of the most distant metazoan relatives of human FICD (sharing 38% amino acid identity) it possesses an almost identical tertiary and quaternary structure (Bunney *et al*, 2014; Truttmann *et al*, 2016). Both homologues reveal a compact, all α-helical, tripartite composition: a two TPR motif TPR domain (which follows the transmembrane domain and 62 predicted unstructured ER luminal residues), followed by a C-terminal capping helix which is continuous with an α-helical linker to the catalytic Fic domain (**Figure 1.3.2**). Human FICD forms a dimer both in crystallo and in solution, via a bipartite dimerisation interface, which possesses a nanomolar dissociation constant (Perera *et al*, 2019). Moreover, the dimer interface is also highly conserved amongst FICD homologues, being present (and facilitating dimerisation) in both worms and flies (Truttmann *et al*, 2016; Casey *et al*, 2017).

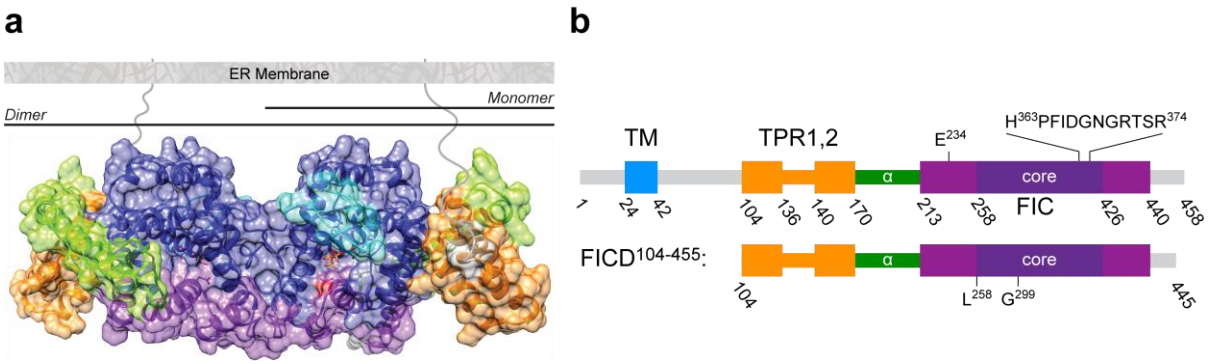

Figure 1.3.2: FICD domain structure. **a,** A human FICD dimer crystal structure (PDB 6I7G; residues 104–445) is displayed with ribbon and semi-opaque surface representation. The protein is coloured according to its domain organisation, as schematised in **b**. In addition, the Fic domain flap region which covers the hydrophobic adenosine binding pocket is also highlighted (residues 311–323; turquoise). The dimer is also modelled with its unstructured N-terminal region (grey) anchoring it to the ER membrane (and within the ER lumen). **b,** Schematic representation of FICD's domain organisation. The transmembrane domain (blue), the TPR domain (orange), the α-helical linker (green), the Fic domain (purple) and the core Fic domain (deep purple) are indicated. Selected residues are also annotated: inhibitory Glu234 (at the end of α_{inh}), Leu258 (within the principal dimer interface surface), Gly299 (within the secondary dimer interface surface) and the Fic motif. Bottom, schematic of the FICD residue range used for in vitro studies within this work.

FICD's ability to AMPylate and inactivate BiP is conserved across metazoa, having been observed in flies, mammals and worms (Ham *et al*, 2014; Preissler *et al*, 2015b; Truttmann *et al*, 2016). Moreover, it appears that endogenous FICD very selectively AMPylates BiP, with high throughput screening techniques only identifying BiP as an FICD modified target which colocalises with FICD in the ER lumen (Broncel *et al*, 2016; Truttmann *et al*, 2016). Furthermore, as mentioned above, FICD specifically modifies Thr518 of BiP. In addition, FICD selectively AMPylates the ATP-state of BiP; as evidenced by its substrate preference for BiP mutants which are more biased towards the domain-docked state and by FICD's inability to AMPylate BiP mutants which cannot domain-dock in response to ATP or the isolated BiP SBD (which also cannot assume an ATP-like state conformation) (Preissler *et al*, 2015b). The means by which FICD specifically engages BiP:ATP is unknown.

In general, Fic proteins are thought to engage their substrates via the formation of an intermolecular β-sheet — utilising the Fic domain flap to facilitate positioning of the target hydroxyl group within the Fic domain active site. This has been observed for the post-AMPylation cocrystal structure of the Fic protein IbpA (which lacks an α_{inh}) bound to its (in crystallo) AMPylated substrate Cdc42-AMP (PDB 4ITR) and in structures of Fic proteins in which crystal packing effects result in β-sheet flap engagement (Xiao *et al*, 2010; Goepfert *et al*, 2013). As also exemplified by the structure of IbpA•Cdc42-AMP (the only existing co-complex structure of a Fic protein bound to its cognate target protein), Fic proteins often contain very divergent target recognition modules which are separate from the catalytic Fic domain (reviewed in Harms *et al*, 2016). For example, in the case of IbpA and VopS, specific arm subdomains have evolved to recognise their target small GTPases (Xiao *et al*, 2010; Luong *et al*, 2010). It is therefore tempting to speculate that the TPR domains of FICD may also contribute towards its ability to specifically recognise and bind BiP:ATP. Moreover, as client binding within the SBD partitions Hsp70s away from their ATP-state (**Figure 1.1.1**), FICD's substrate preference for ATP-state BiP suggests a simple mechanism for coupling BiP AMPylation to low protein folding loads.

The ability for BiP to be reversibly and dynamically AMPylated is intrinsic to the utility of this modification as a means of buffering chaperone capacity within the ER. As protein AMPylation results in a stable, phosphodiester linked, covalent modification; removal of this moiety necessitates the action of a deAMPylase enzyme.

Chapter 1.4: DeAMPylation

Through work that was initiated during my Master of Research degree rotation project in the Ron lab, we found that FICD was able to catalyse deAMPylation of BiP both in vitro and in vivo and that endogenous FICD was responsible for the deAMPylation of BiP in cells (Preissler *et al*, 2017a). This deAMPylation activity, although functionally opposed to AMPylation, represented a chemically distinct reaction and not simple micro-reversibility of the former — generating BiP and AMP as deAMPylation products. Moreover, we found that the catalytic Fic motif His363 and the α_{inh}-located Glu234 (previously only associated with its role in autoinhibiting AMPylation) were entirely necessary for this deAMPylation activity (Preissler *et al*, 2017a). In so doing, we demonstrated FICD to be a bifunctional enzyme in which both mutually antagonistic activities were catalysed in its single active site; a feature which is only present in a small number of other bifunctional enzymes including RNA polymerase which catalyse both mRNA transcription and proofreading in a single active site (reviewed in Sydow & Cramer, 2009).

The finding that FICD is a deAMPylator of BiP-AMP has subsequently been reproduced in the *Drosophila* system (Casey *et al*, 2017) and also in a divergent class III Fic protein from the bacterium *Enterococcus faecalis* (EfFic) (Veyron *et al*, 2019). A previous bioinformatic analysis of prokaryotic Fic proteins indicated that class I and III Fic proteins are likely both of monophyletic origin and are both derived from a single branch of class II Fic proteins (Engel *et al*, 2012). Therefore, the observation that both FICD (a class II Fic protein) and a distantly related bacterial class III Fic protein possesses deAMPylation activity, that is dependent on a conserved glutamate residue which is structurally homologous to FICD's Glu234, suggests that Fic domain bifunctionality may be a widespread and largely overlooked feature across a large branch of the Fic protein family.

To date FICD is the only known eukaryotic protein to be identified with bona fide deAMPylation activity. Conversely, there are two known bacterial deAMPylating enzymes, the *Legionella pneumophila* effector protein SidD and the *E. coli* protein GS-ATase. The latter represents an interesting parallel to FICD, as GS-ATase (the first identified AMPylase) is also a bifunctional enzyme. However, unlike FICD, it uses separate homologous domains to catalyse AMPylation and deAMPylation. The latter is facilitated by GS-ATase's Adenylyl Removase domain via a phosphorolytic mechanism (Anderson & Stadtman, 1970). Structural analysis of *E. coli* GS-ATase has confirmed that both domains assume a nucleotidyl transferase

fold (Xu *et al*, 2004, 2010). Conversely, SidD, which catalyses deAMPylation of host protein GTPases, is structurally homologous to a metal-dependent protein phosphatase despite significant sequence divergence (Chen *et al*, 2013). Both proteins catalyse deAMPylation mechanisms which are depended on a binuclear metal centre (**Figure 1.4.1**), a common feature amongst proteins which catalyse phosphodiesterase or phosphomonoesterase reactions. Furthermore, SidD also has a strict requirement for Mg^{2+} ions (Chen *et al*, 2013).

Contrarily, FICD like other Fic proteins only has a single divalent ion binding site and is evolutionarily unrelated to either GS-ATase or SidD. It is, therefore, very likely that FICD (and other Fic proteins) exhibit a disparate deAMPylation mechanism. Based on AMP being a products of Fic-protein deAMPylation, the mode of nucleotide binding in the Fic domain active site and the requirement for a conserved glutamate and histidine, speculative inferences have been made that the Fic deAMPylation reaction is acido-basic and hydrolytic in nature (Preissler *et al*, 2017a; Perera *et al*, 2019; Veyron *et al*, 2019). However, the enzymology of FICD-mediated deAMPylation remains to be determined.

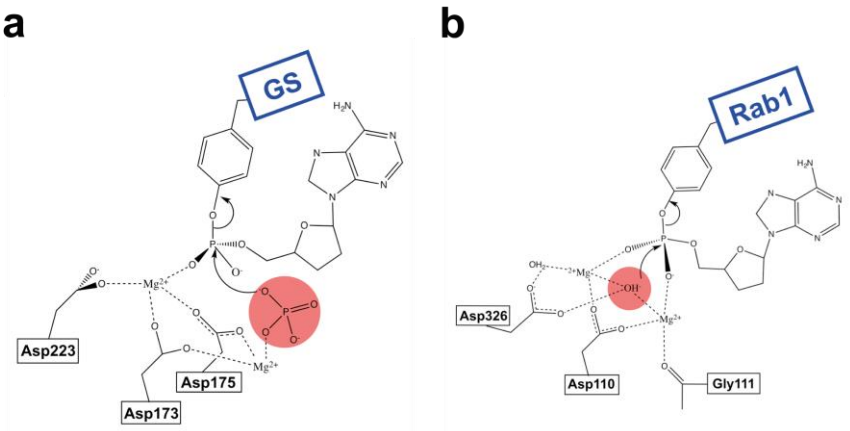

Figure 1.4.1: Proposed mechanisms of deAMPylation catalysed by GS-ATase and SidD. a, GS-ATase is known to catalyse a phosphorolytic deAMPylation reaction within its adenylyl removase domain, producing ADP and unmodified GS. The proposed catalytic mechanism is based on similarity with other nucleotidyl transferases and conservation of the aspartic acid triad which scaffolds the binuclear metal centre. **b,** Likewise, the mechanism of SidD hydrolysis is inferred from the phosphatase reaction pathway catalysed by related metalloenzyme. Figure adapted from (Chen *et al*, 2013).

It has already been noted that levels of BiP-AMP appear to be stably and dynamically adjusted in order to meet the protein folding demands within the ER (Preissler *et al*, 2015b). Such a system, catalysed by a single bifunctional enzyme, necessitates a means of regulating these two mutually antagonistic activities.

Chapter 1.5: Reciprocal regulation of FICD's bifunctionality

Like many other class II or class III Fic proteins, in which the autoinhibitory α_{inh} forms part of the extended Fic domain, FICD exhibits very little AMPylation activity in vitro (either with respect to autoAMPylation, which is often the sole readout for many Fic proteins without identified substrates, or substate-directed AMPylation). In fact, in a wild type context dimeric FICD activity was found to be heavily biased towards its deAMPylation activity (Preissler *et al*, 2017a). This in vitro observation was consistent with previous in vivo findings, in which rescuing the ability of *FICD*$^{-/-}$ Chinese hamster ovary (CHO) cells to accumulate AMPylated BiP could only be achieved by transient transfection with FICD^{E234G}, that is to say, FICD lacking its AMPylation-inhibiting glutamate (Preissler *et al*, 2015b).

Conversely, a much lower-level (stable) expression of wild type FICD in *FICD*$^{-/-}$ CHO cell, which was still expressed at a considerably higher level than endogenous FICD, was able to afford some level of BiP AMPylation rescue (Perera *et al*, 2019). This was suggestive of a protein dosage effect on the regulation of FICD activity. This hypothesis was further corroborated by the observation that overexpression of a monomeric variant of FICD (FICD^{L258D}) was able to induce conspicuous BiP-AMPylation in *FICD*$^{-/-}$ CHO cells. Unlike in wild type cells, this was the case under both basal and protein translation inhibited (cycloheximide treated) conditions, although the levels of AMPylated BiP were able to be further increased (from their elevated basal level) by cycloheximide treatment. This in turn, was consistent with a model in which monomerisation of FICD results in a switching of the enzyme from a poor to a proficient AMPylase.

A large body of in vitro work confirmed this finding. Indeed, by utilising the nature of a catalytically dead (His363Ala) and constitutively dimeric (disulphide-linked) FICD ($_{S\text{-}S}$FICD$^{A252C\text{-}H363A\text{-}C421S}$) to tightly bind and effectively trap BiP-AMP, the effects of monomerisation on FICD's mutually antagonistic activities was deconvoluted. It was found (using [α-^{32}P]-ATP as the AMPylation co-substrate) that monomeric FICD^{L258D} catalysed AMPylation of BiP at a rate around 19-fold greater than that of the dimeric wild type enzyme. Concomitantly, by analysing the fluorescence polarisation decrease associated with the deAMPylation-mediated release of fluorescent AMP(FAM) from covalently labelled BiP-AMP(FAM), the deAMPylation activity of FICD was also observed to be diminished by monomerisation. In this assay, in which substrate concentrations were limiting, monomerisation reduced the deAMPylation activity by around 50% (Perera *et al*, 2019).

Importantly, the apparent oligomeric state-dependent regulation of FICD's enzymatic activity was not restricted to the context of monomerising mutations introduced into FICD. When diluted into the nanomolar concentration range, which is in the order of the measured dimerisation K_D, wild type FICD conspicuously acquired the ability to catalyse an appreciable accumulation of BiP-AMP. Moreover, the biphasic relationship between wild type FICD concentration and BiP-AMP accumulation was entirely dependent on the ability of FICD to monomerise at low concentration. This was illustrated by the fact that accumulation of BiP-AMP upon dilution of wild type FICD^{A252C} occurred only under (reducing) conditions, in which its dimer interface was no longer covalently enforced by an intermolecular disulphide bond (Perera *et al*, 2019).

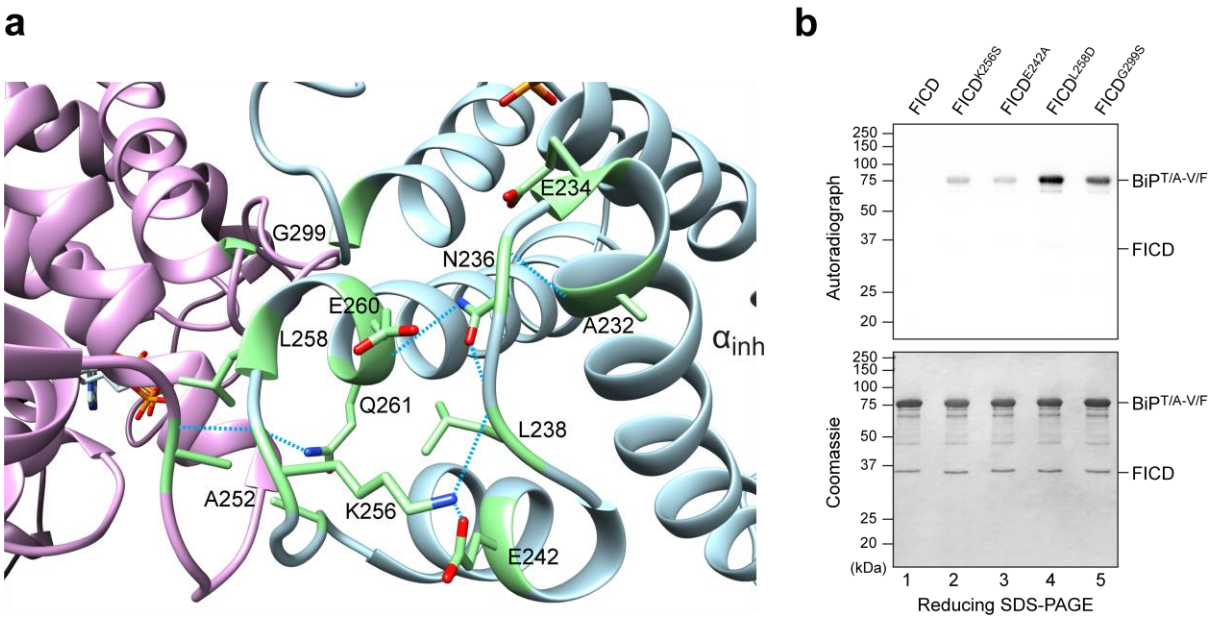

Figure 1.5.1: FICD's dimer interface and putative dimer-relay network. a, The conserved bipartite dimer interface of FICD is illustrated, based on a human FICD crystal structure (PDB 6I7G). One protomer is shown in pink and the other in blue. Residues involved in a putative hydrogen bond network from the major/larger dimerisation interface to the active site (in the region of Glu234, atop the α_{inh}) are labelled and highlighted in green, with H-bonds represented by dotted blue lines. Gly299 which resides in the smaller, secondary dimer interface is also highlighted. Note, FICD^{G299S} is partially dimeric in solution, which contrasts with the fully monomeric FICD^{L258D}. **b,** BiP$^{T229A-V461F}$ AMPylation measured by covalent incorporation of [α-^{32}P]-AMP. Dimer-relay FICD mutants (Lys256Ser and Glu242Ala), at concentrations at which they are principally dimeric, are significantly more prone to AMPylate BiP than wild type (dimeric) FICD. Gel produced by Steffen Preissler.

These in vivo and in vitro findings (experiments principally conducted by Cláudia Rato da Silva and Steffen Preissler, respectively) provide strong support for a model wherein FICD monomerisation results in reciprocal regulation of AMPylation and deAMPylation activity,

strongly favouring substrate AMPylation. However, the mechanistic basis of this enzymatic switch is undetermined. A small hint was afforded by structural observations from previous FICD dimer structures, in which a hydrogen bond (H-bond) network linking the dimer interface to the α_{inh} (and the active site) was apparent (**Figure 1.5.1a**). Moreover, mutations in this putative dimer-relay also caused an increase in the ability of FICD to mediate BiP-AMP accumulation, without significantly weakening the dimer interface (**Figure 1.5.1b**).

In a parallel to FICD, oligomerisation has been observed to affect autoAMPylation of the class III Fic protein from *Neisseria meningitidis* (NmFic), which in turn modulates its ability to autoinhibit AMPylation of its substrate (Stanger *et al*, 2016). Moreover, mutations in the dimer interface of *Clostridium difficile*'s class II Fic protein (CdFic) also increased its autoAMPylation activity (Dedic *et al*, 2016). Conversely, although monomeric FICD^{L258D} exhibits a slight increase in autoAMPylation activity relative to wild type FICD, the overall efficiency of this reaction is very low (much less than the efficiency of substrate modification) with only a tiny proportion of the total FICD^{L258D} being modified (Perera *et al*, 2019). Some degree of FICD autoAMPylation has been identified, by peptide MS/MS, of FICD's Ser79/Thr80 and Thr183 in both a wild type and FICD^{E234G} context (Sanyal *et al*, 2015). The latter, FICD^{E234G}, being AMPylation unrestrained and deAMPylation incapable exhibits much more pronounced substrate and autoAMPylation than FICD^{L258D} (Perera *et al*, 2019). However, crystallisation of the structured region of FICD^{E234G} (residues 104–445; as used in the in vitro studies in Perera *et al*, 2019), in the presence of high concentrations of MgATP, revealed no extra density corresponding autoAMPylation of Thr183 or across the rest of the protein (which was largely well resolved; PDB 4U07) (Bunney *et al*, 2014). This provides further support for their being a very low stoichiometry of FICD auto-modification, even under favourable mutational and environmental conditions. Furthermore, as previously observed, monomerisation of FICD^{E234G} via the introduction of Leu258Asp reduces autoAMPylation activity (Bunney *et al*, 2014; Perera *et al*, 2019). All of this data is consistent with a conclusion that FICD monomerisation does not result in an inherent increase in autoAMPylation proficiency or activity. Thus, the reciprocal regulation of FICD activity, afforded by monomerisation, cannot be a consequence of alterations in FICD's limited ability to autoAMPylate. The underlying mechanism behind FICD's oligomeric state-dependent switch remains unknown.

Chapter 1.6: Aims

FICD represents an extremely interesting enzyme with an ability to both inactivate and reactivate BiP, the major endoplasmic reticulum chaperone, and thereby modulate chaperoning capacity within the ER. To date, it is the only bona fide identified metazoan AMPylator and the only example of a eukaryotic deAMPylator. Understanding the basis of FICD's ability to modify BiP, and the mechanistic basis of how FICD is itself regulated, will enable a fundamental understanding of the metazoan post-translation unfolded protein response. Moreover, a detailed understanding of an endogenous bifunctional regulator of BiP activity, may eventually pave the way for rational drug design with the aim of enhancing FICD's ability to inactivate BiP. This is particularly topical, in the current environment of a global pandemic, with mounting evidence that small molecule inhibitors of Hsp70s, and BiP in particular, may provide pan-antiviral therapeutic benefit (Chan *et al*, 2006; Taguwa *et al*, 2015, 2019).

The catalytic mechanism of Fic domain mediated AMPylation, based on the analysis of a large number of bacterial Fic proteins, is fairly well understood. Conversely, very little is known about the nature of FICD-mediated deAMPylation, although it is likely that this mechanism is conserved across a number of other bacterial Fic domain proteins. Moreover, Fic proteins are evolutionarily and structurally very distinct from the two previous identified deAMPylase enzymes (both of which are of bacterial origin), and to my knowledge there exists no structures of a deAMPylase bound to its deAMPylation substrate.

In a similar vein, there only exists one structure of a Fic protein bound to its endogenous substrate. It is thought that the majority of Fic proteins have incorporated a wide variety of specific substrate targeting domains — which have presumably (co)evolved to suit each Fic protein's specific clientele. In the case of FICD, indications that it is able to specifically bind ATP-state BiP may provide an additional layer of substrate-level regulation of BiP AMPylation (with levels of low unfolded protein naturally resulting in more BiP:ATP as less BiP SBD is engaged by unfolded peptide). Support for the existence of substrate-level regulation of BiP AMPylation is provided in vivo by the observation that cells only expressing a constitutively monomeric FICD retain a measure of regulated BiP AMPylation (Perera *et al*, 2019). Whether or not FICD is able to specifically recognise the ATP-state of BiP remains unconfirmed and the means of any such recognition is completely undetermined.

Finally, monomerisation of FICD has been robustly demonstrated to concomitantly increase FICD's AMPylation activity and decrease its ability to deAMPylate BiP. Changes in

oligomeric state regulating enzyme activity is far from a rare occurrence. For example, a number of transmembrane ER proteins such as the UPR sensor Ire1 are regulated in such a fashion (Walter & Ron, 2011; Amin-Wetzel *et al*, 2019). Conversely, I am not aware of another example of oligomeric state-dependent reciprocal regulation of enzymatic activity within a single bifunctional active site, as exhibited by FICD (and potentially its homologues). Fully elucidating the cause of this enzymatic switch requires a fundamental understanding of both the means of deAMPylation and AMPylation at play.

In this thesis, I therefore aim to provide an in-depth exploration into the mechanistic functioning and regulation of FICD bifunctionality. Through a structure-led approach I address three fundamental themes pertaining to the nature of FICD's post-translational regulation of BiP. Firstly, I elucidate the mechanism by which FICD engages and deAMPylates BiP-AMP. Secondly, I explain FICD's exquisite selectivity for its AMPylation substrate — ATP-bound and domain-docked BiP. I then reveal the structural basis of FICD's monomerisation-dependent increase in AMPylation activity and concomitant decrease in deAMPylation activity. Finally, I touch on a potential in vivo route of transducing changing levels of ER unfolded protein load into an adjustment of FICD's monomer-dimer equilibrium.

Chapter 2: The mechanism of eukaryotic deAMPylation

Chapter 2.1: Capturing a deAMPylation complex

In order to elucidate the mechanism of BiP-AMP deAMPylation, a crystal structure of FICD engaged with AMPylated BiP was required. In order to facilitate the crystallisation of such a complex the FICD mutation His363Ala was leveraged. As noted previously, mutation of FICD's catalytic histidine not only renders the protein devoid of all enzymatic activity (**Chapter 1.4,** Preissler *et al*, 2017a), but also enables the formation of a stable complex of $FICD^{H363A}$•BiP-AMP (**Chapter 1.5,** Perera *et al*, 2019). This substrate-trapping facilitated copurification of FICD and BiP-AMP by size exclusion chromatography (SEC) (**Figure 2.1.1a**). As the dimer of FICD is a more active deAMPylase than monomeric FICD considerable efforts were made to obtain a cocrystal structure of the former with BiP-AMP. A complex of recombinantly expressed and, otherwise wildtype, dimeric human $FICD^{H363A}$ and in vitro AMPylated Chinese hamster BiP (in various forms and mutant varieties) readily copurified and crystallised in a wide range of polyethylene glycol (PEG) conditions. However, despite extensive attempts at crystal optimisation (for example, macro and microseeding, hanging and sitting drop, different temperature and microbatch-under-oil crystallisation, in situ diffraction, crystal dehydration and annealing) these crystals only yielded very weak diffraction data. The reason for these crystals being refractory to even mediocre X-ray diffraction remains unknown, although one could speculate that they possessed too much internal heterogeneity.

Fortunately, a combination of introducing the monomerising Leu258Asp mutation into the ER luminal and predicted structured portion of FICD (residues 104–445) and truncation of BiP's flexible α-helical lid (residues 27–549) produced a heterodimeric $FICD^{L258D\text{-}H363A}$•$BiP^{T229A\text{-}V461F}$-AMP complex that crystallised and yielded two very similar sub-2 Å datasets (**Figure 2.1.1b**; **Table 1**). Copurification was achieved by the injection of FICD:BiP-AMP in an approximate 3:2 molar ratio in the presence of 250 μM MgATP; the subsequent SEC yielded a complex elution peak corresponding in elution volume to that expected from a 97 kDa heterodimeric complex of $FICD^{L258D\text{-}H363A}$•$BiP^{T229A\text{-}V461F}$-AMP (**Figure 2.1.1a**).

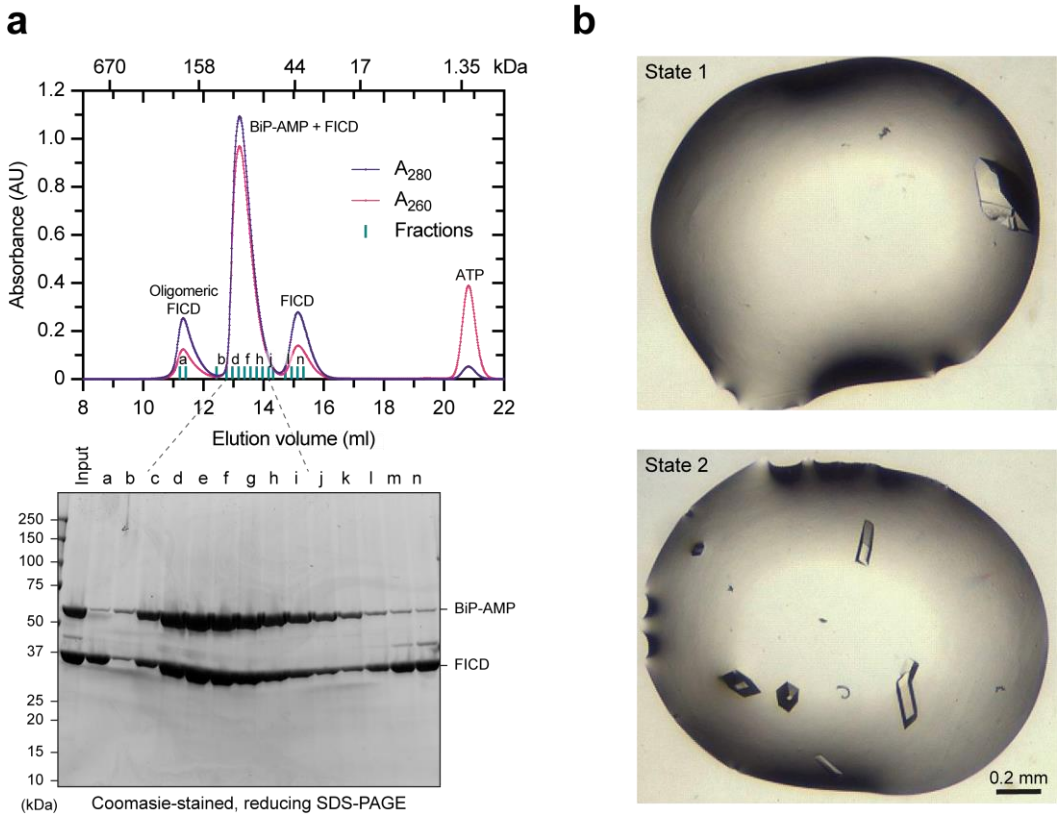

Figure 2.1.1: Copurification and crystallisation of FICD•BiP-AMP. a, FPLC gel filtration chromatogram and reducing SDS-PAGE analysis of the indicated fractions. FICD's His363Ala mutation facilitates trapping and SEC-based copurification, of a deAMPylation complex of monomeric FICD$^{L258D-H363A}$ and lid-truncated BiP$^{T229A-V461F}$-AMP. The elution volumes of molecular weight standards run on the same SEC column are indicated above. A protein peak containing excess (39 kDa) monomeric FICD (from the 3:2 injection ratio of FICD:BiP-AMP) is also labelled. An unidentified high molecular weight (non-aggregated and relatively stable) species principally containing FICD (see fraction *a*, labelled oligomeric FICD) is also evident. This species is not present when FICD$^{L258D-H363A}$ is gel filtered in isolation. **b,** The pooled protein fractions (*c-i* from **a**) enabled heterodimer crystallisation and sub-2 Å X-ray diffraction. The sitting drops, containing the crystals which gave rise to the state 1 and state 2 deAMPylation complex crystals, are pictured. State 1 crystals were obtained from sitting drop reservoir conditions of 0.1 M MES pH 6.5, 10% PEG 4000 and 0.2 M NaCl; state 2 crystals were obtained from conditions of 0.1 M Tris pH 8.0 and 25% PEG 400 (see **Materials and Methods**).

It should be noted, the use of residues 28–549 of BiP excludes the signal sequence and unstructured acidic N-terminal region and removes the majority of BiP's lid subdomain (SBDα helix B [SBDα-B] and the α-helical bundle). The latter potentially facilitated greater crystal homogeneity by removing the part of the lid (SBDα-B) which is documented in the *E. coli* Hsp70 homologue (DnaK) to, in the Hsp70 ATP-state, only interact transiently with the NBD and partially unfold in solution (Zhuravleva *et al*, 2012; Rist *et al*, 2006). Furthermore, removal of the distal part of the lid also accelerates substrate dissociation rates from the SBD and

thereby decreases the opportunity for BiP to bind FICD, or itself, as a substrate. Conversely, an intact BiP has a high propensity to bind its own interdomain linker and oligomerise, especially in the absence of ATP-replenishment (Preissler *et al*, 2015a, 2020).

	FICD•BiP-AMP DeAMPylation (State 1)[a]	FICD•BiP-AMP DeAMPylation (State 2)[a]
Data collection		
Synchrotron stations	DLS I04-1	DLS I04-1
Space group	$P2_12_12$	$P2_12_12$
Molecules in a.u.[b]	2 (2)	2 (2)
a,b,c; Å	95.37, 104.08, 105.63	95.00, 103.89, 104.79
α, β, γ; °	90.00, 90.00, 90.00	90.00, 90.00, 90.00
Resolution, Å	105.63–1.70 (1.73–1.70)	52.40–1.87 (1.92–1.87)
R_{merge}	0.085 (1.299)	0.087 (1.793)
$\langle I/\sigma(I)\rangle$	10.3 (1.2)	11.9 (1.0)
$CC_{1/2}$	0.992 (0.585)	0.999 (0.536)
Unique reflections	115633 (5639)	86247 (6270)
Completeness, %	99.8 (99.3)	100.0 (100.0)
Redundancy	6.6 (6.5)	6.6 (6.9)
Refinement		
R_{work}/R_{free}	0.195 / 0.221	0.177 / 0.231
Atoms (non-H)	7868	7575
Average B-factor, Å^2	29.0	37.4
RMS Bond length, Å	0.003	0.003
RMS Bond angle, °	1.171	1.199
Ramachandran favoured region, %	98.37	98.49
Ramachandran outliers, %	0	0
MolProbity score [c]	0.81 (100th)	1.04 (100th)
PDB code	7B7Z	7B80

Table 1: DeAMPylation complex data collection and refinement statistics. Both deAMPylation complexes contain [a]FICD$^{L258D-H363A}$ (residues 104–445) bound to BiP$^{T229A-V461F}$-AMP (residues 27–549). Values in parentheses correspond to the highest-resolution shell, with the following exception: [b]The number of molecules in the asymmetric unit cell (a.u.) is shown with the number of molecules in the biological unit in parentheses. [c]The MolProbity score as a percentile is shown in parentheses, higher is better.

The ability to maintain BiP as a monomeric species was further facilitated by introduction of the characterised BiP mutations Thr229Ala and Val461Phe, which render BiP ATPase and substrate-binding deficient but otherwise allosterically intact (Gaut & Hendershot, 1993; Petrova *et al*, 2008). The lack of ATP hydrolysis, enabled by the former, allows BiP to remain bound to MgATP and therefore in its domain-docked state for prolonged periods of time; a feature which favours AMPylation by FICD and also disfavours BiP substrate binding and oligomerisation (Preissler *et al*, 2015b, 2015a).

Furthermore, excluding the signal sequence regions (which are not present in the mature form of either protein) Chinese hamster and human BiP are essentially identical. From residues 20–654 there is only one residue that varies, a mutation of Ala650Ser from the human to hamster protein. This amino acid is in the unstructured C-terminus of the protein, two amino acids upstream of the terminal KDEL sequence and is not present in the crystallised BiP-AMP construct (residues 27–549). The use of human FICD and hamster BiP together, therefore, effectively represents a homologous human system.

State 1 and state 2 crystals yielded very similar deAMPylation complex diffraction datasets and overall structures with almost identical intermolecular contacts (**Table 1** and **Figure 2.1.2**). As the state 1 crystal diffracted to a higher resolution (1.70 rather than 1.87 Å) all future figures in this chapter will be derived from analysis of the state 1 deAMPylation complex structure. I will return to the relevance of the state 2 crystal in **Chapter 4**.

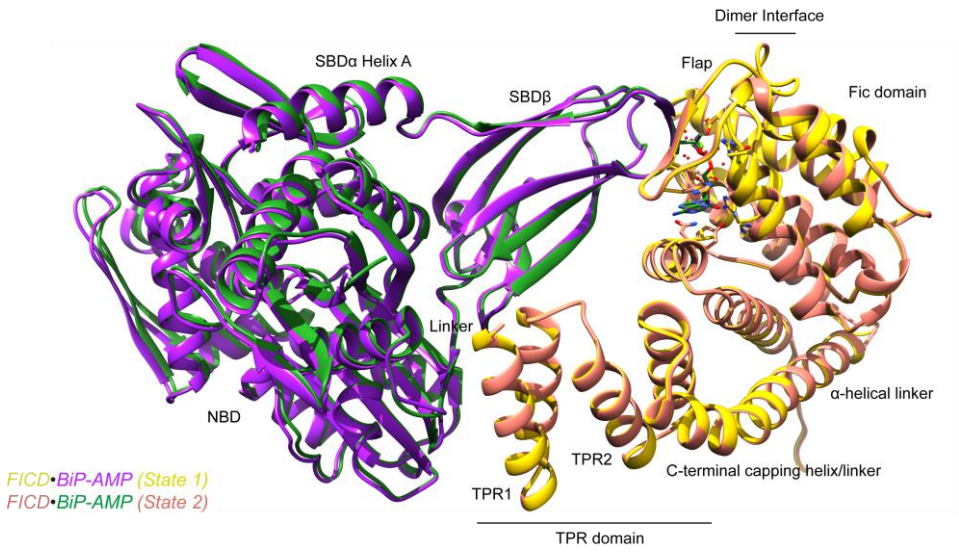

Figure 2.1.2: Comparison between state 1 and state 2 deAMPylation complex structures. The two structures are nearly identical in terms of overall conformation and intermolecular contacts. Features (including domains and subdomains) of FICD and BiP-AMP are labelled, and the bound AMP moiety (along with its interacting residues) are shown as sticks.

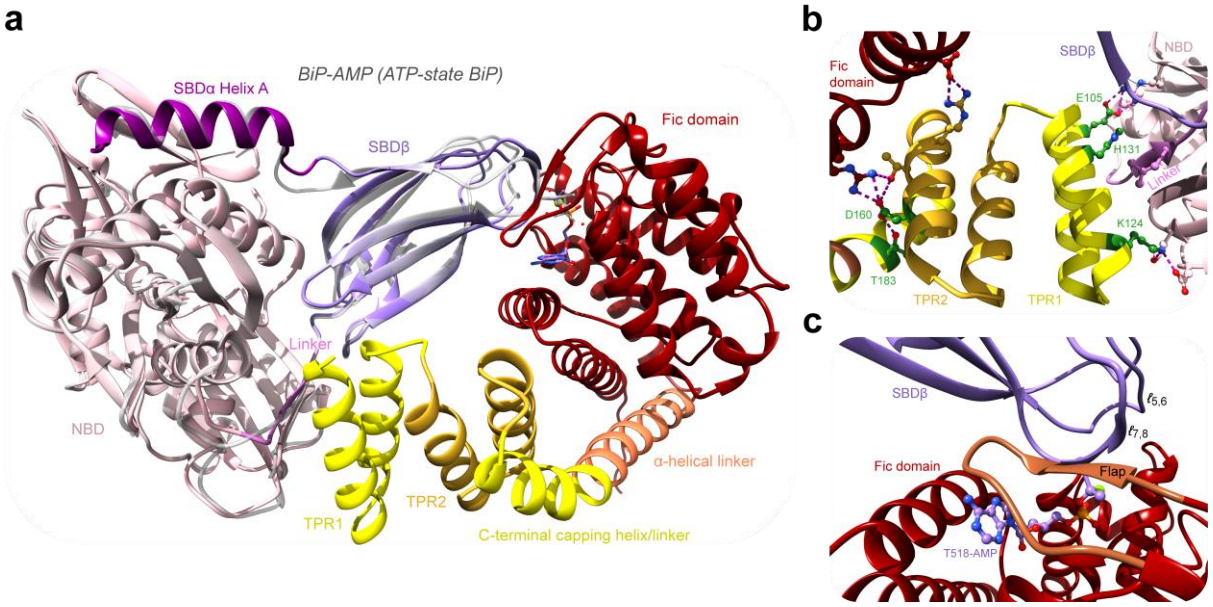

Figure 2.1.3: Protein-protein interaction surfaces within the deAMPylation complex. The deAMPylation complex crystal structure is colour-coded to illustrate its (sub)domain organisation. **a,** Structural superposition (based on alignment of the NBD) of the (state 1) deAMPylation complex with the ATP-state of isolated BiP-AMP (PDB 5O4P, light grey). **b,** The intermolecular interaction surface of FICD(TPR1) with BiP is highlighted (viewed from inside the complex, looking outwards towards the bulk solvent). The BiP surface is tripartite, composed of its NBD, interdomain linker and SBDβ. Selected interdomain contacting residues are shown (including the contacts formed between FICD's TPR2 motif and Fic domain). Polar interactions (hydrogen bonds and/or salt bridges) are depicted by pink dashed lines. Residues mutated in this study are shown in green and labelled. **c,** The second protein-protein intermolecular surface is made up of BiP $\ell_{7,8}$ and $\ell_{5,6}$ and the catalytic Fic domain. The Fic domain flap (which forms an intermolecular β-sheet with $\ell_{7,8}$) is highlighted in brown.

The BiP-AMP, crystallised in both structures, is clearly present in a domain-docked, ATP-like state — as evidenced by the close similarity to the isolated ATP-state BiP-AMP structure (the ATP-state Hsp70 prominently featured in **Figure 1.2.1b**). Across all 521 Cα pairs the ATP-state BiP-AMP structure only possesses a 1.02 Å root-mean-square deviation (RMSD) from the deAMPylation complex AMPylated BiP molecule (**Figure 2.1.3a**; state 1 structure is shown). The tertiary structure in the NBD region is particularly similar, with only 0.48 Å RMSD across the 384 Cα pairs.

The deAMPylation complex displays an extensive bipartite protein-protein interface totalling approximately 1366 Å^2. The marginally larger of the two interfaces is formed by engagement of BiP with FICD's tetratricopeptide repeat domain motif 1 (TPR1). FICD(TPR1) contacts a tripartite BiP surface (695 Å^2) comprised of BiP's NBD, linker and SBDβ (**Figure 2.1.3b** and **Figure 2.1.4**). The second surface is comprised of the Fic catalytic domain engaging BiP's

SBDβ, markedly in the region of the AMPylated target residue (Thr518 within $\ell_{7,8}$). This protein-protein interaction region (totalling 671 Å^2) prominently features the Fic flap which forms an antiparallel, intermolecular β-sheet with BiP $\ell_{7,8}$ (**Figure 2.1.3c** and **Figure 2.1.5a**).

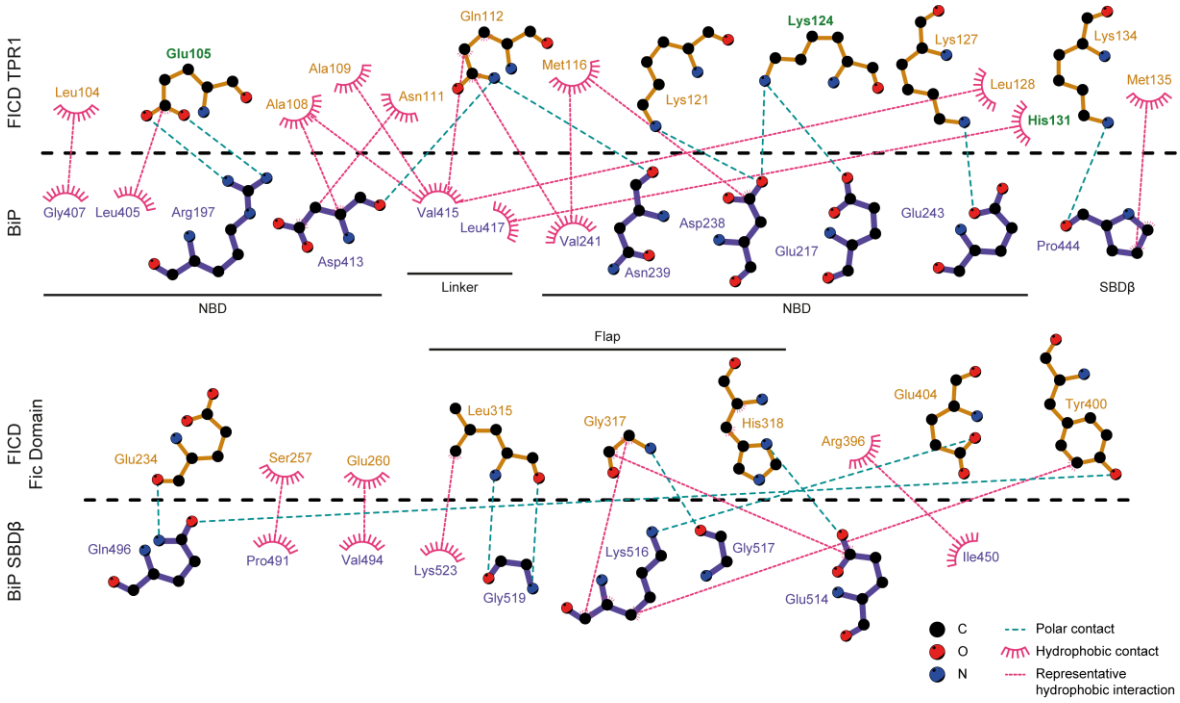

Figure 2.1.4: Schematised view of all FICD•BiP-AMP intermolecular contacts. All polar (hydrogen bonds and electrostatic interactions) and hydrophobic protein-protein contacts between FICD and BiP are illustrated. The (sub)domain origin of the interacting residue is also annotated. Residues mutated in the study are labelled in green.

Flap-mediated, sequence independent registration of target protein has been previously observed in other Fic proteins (Xiao *et al*, 2010; Goepfert *et al*, 2013). FICD's Fic flap does not hydrophobically clamp the target residue (BiP's Thr518-AMP) (**Figure 2.1.5a**). Instead, FICD's Val316 (at the end of the Fic flap β-strand) makes a number of hydrophobic interactions with the adenosine ring of the AMP moiety. This is unlike the Fic protein-substrate complex of IbpA•Cdc42-AMP (PDB 4ITR, **Figure 2.1.5b**) and the Fic proteins structures of VbhA/VbhT(Fic) (PDB 3SHG) and SoFic (PDB 3EQX), which display crystallographically induced Flap•peptide binding, in which a hydrophobic target residue clamp was observed (Xiao *et al*, 2010; Goepfert *et al*, 2013). The discrepancy between the FICD deAMPylation complex presented here and previous Fic•(pseudo)substrate structures suggests that the hydrophobic clamp is not a universal feature of Fic protein substrate engagement.

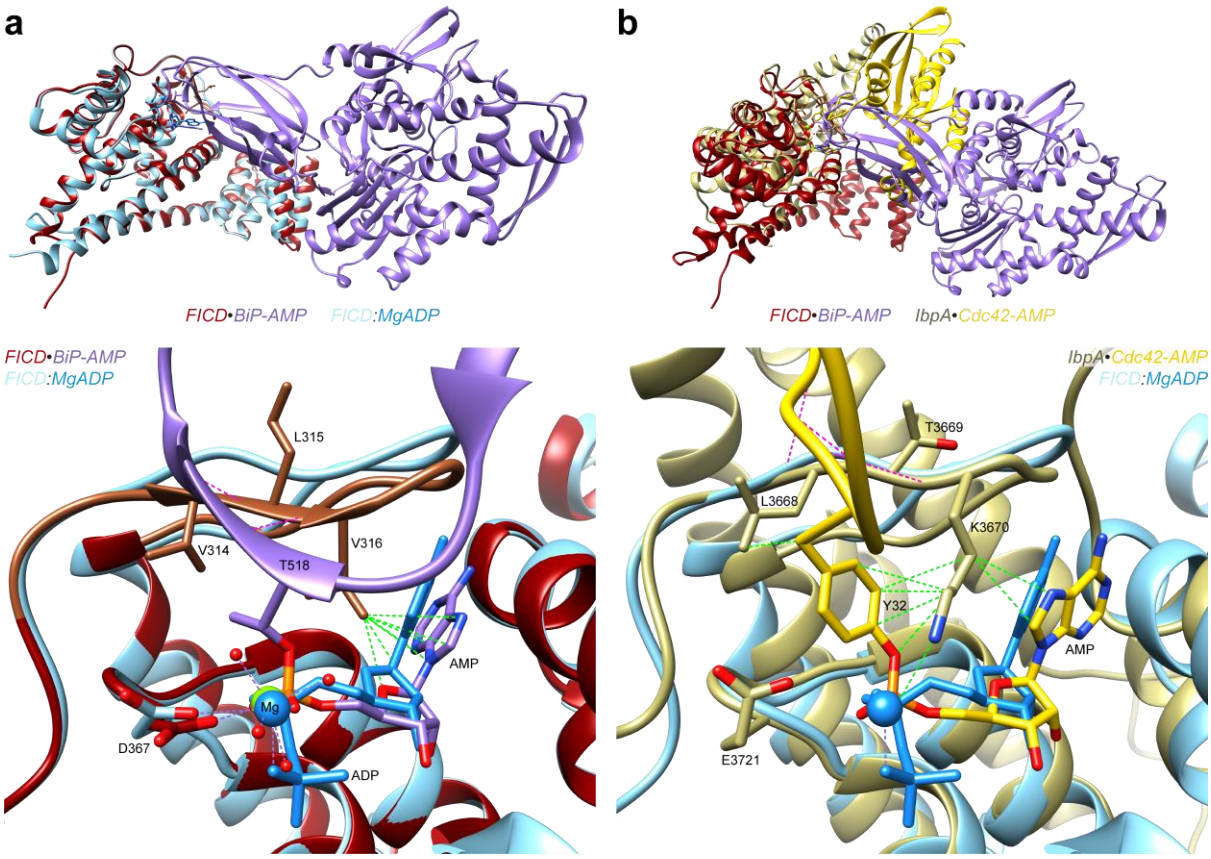

Figure 2.1.5: The Fic flap does not clamp BiP's Thr518. Structural superpositions of the state 1 deAMPylation complex (FICD•BiP-AMP) with a single protomer of the dimeric FICD:MgADP structure (PDB 4U0U) and the IbpA•Cdc42-AMP post-AMPylation structure (PDB 4ITR), as indicated. All structures are aligned by residues 348–384 of FICD (which encompasses the conserved Fic motif). The lower panels present more focussed views of the Fic domain flap-substrate interacting regions. Hydrogen bonds are indicated with pink dashed lines and hydrophobic interactions are annotated with green dashed lines. **a, below,** The side chains of residues Val314 and Val316, which are located within the Fic domain flap of FICD (residues 311–323, highlighted in brown) and sit either side of BiP(Thr518-AMP), are not within hydrophobic interaction distance of the Thr518 side chain. **b, below,** In contrast, the Fic flap of IbpA (via Leu3668 and Lys3670) clamps the Tyr32 target residue of Cdc42 (as annotated). Note, both FICD's Val316 and, to a lesser extent, IbpA's Lys3670 form hydrophobic contacts with the adenosine ring. The FICD:MgADP structure is shown for reference in both lower panels.

As expected, the AMP moiety (covalently attached to BiP's Thr518) was inserted into the Fic domain active site, contributing an additional 306 Å^2 interaction surface to the deAMPylation complex. The adenosine bound in FICD's Fic domain hydrophobic pocket occupies approximately the same position as in previous (poorer resolved) FICD:nucleotide complexes (Bunney *et al*, 2014) (**Figure 2.1.3c**, **Figure 2.1.5a**).

Although monomeric FICD retains the ability to deAMPylate BiP, its deAMPylation activity is reduced relative to the wild type dimeric form of the Fic protein (Perera *et al*, 2019). In an

effort to understand how applicable the contacts observed between BiP-AMP and FICD^{L258D} may be to a heterotetrameric complex (formed by saturation of both active sites of a dimeric FICD with BiP-AMP), two monomeric FICD-containing deAMPylation complexes (state 1) were superposed with a dimeric FICD structure (PDB 4U0U; 2.58 Å RMSD over 334 Cα pairs across each FICD protomer). In addition, the complete BiP lid was built into the deAMPylation complex via alignment of the full-length BiP:ATP structure (**Figure 2.1.6**). Note, the full-length BiP:ATP structure (PDB 5E84) is largely similar to the isolated (lid-truncated) BiP-AMP structure (PDB 5O4P) (**Figure 1.2.1**) and should provide a good indication of the position of the intact ATP-state BiP lid (which includes SBDα's helix B and α-helical bundle).

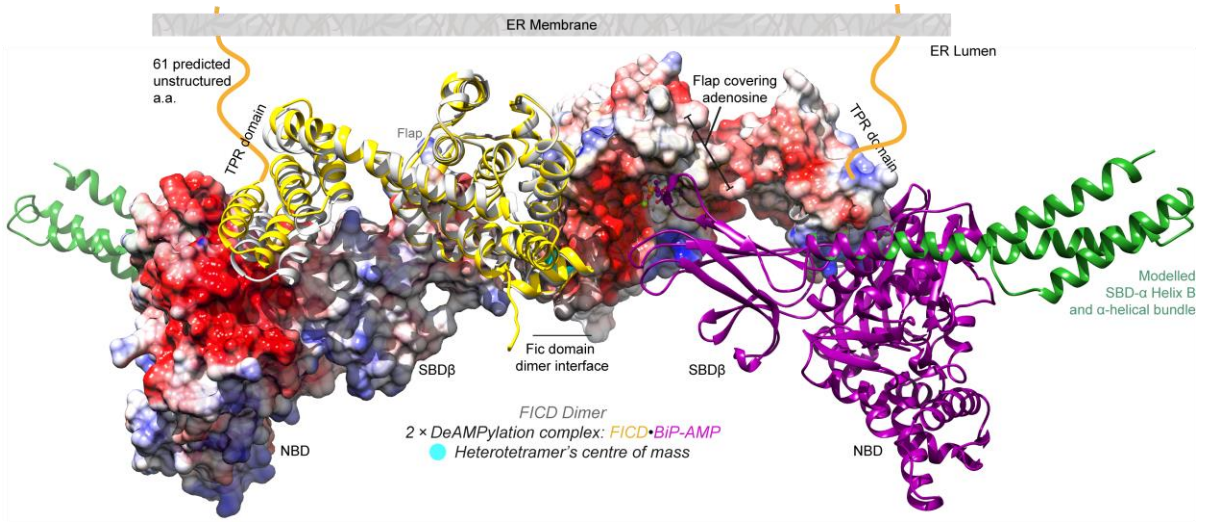

Figure 2.1.6: The heterodimeric crystal structure is compatible with FICD dimerisation. Superposition of two heterodimeric crystal structures (purple BiPs and yellow FICDs) with an FICD dimer structure (PDB 4U0U, grey). In addition, the full-length BiP lid is modelled (green) based on alignment with the BiP:ATP structure (PDB 5E84). This alignment suggests that the heterodimer crystal structure is fully compatible with a transformation into a full length heterotetramer deAMPylation complex, and with the proposed ER membrane orientation of FICD. The unstructured linker joining the ER membrane to the resolved portion of FICD (starting at expression-tag Ser103 followed by FICD residues 104–445) is cartooned in orange. Semi-transparent (alternate) surfaces are shown, coloured according to coulombic electrostatic potential. Note the charge complementarity between the BiP(NBD), negative/red visible on the left, and FICD(TPR1), positive/blue visible on the right. The neutral/hydrophobic surface of FICD's adenosine binding pocket, partially covered by its flap, is also visible on the right, bound to BiP's Thr518-AMP residue. For illustrative purposes the N-terminal unstructured region of FICD is shown in the context of an ER membrane (grey rectangle).

The resulting structural alignment demonstrates that that the heterodimeric deAMPylation crystal structure is compatible with a deAMPylation complex of dimeric FICD engaging two full-length BiP-AMP molecules and with the type II transmembrane orientation of FICD

(Bunney *et al*, 2014; Sanyal *et al*, 2015). Moreover, the alignment with dimeric FICD (**Figure 2.1.6**) also reveals intra-TPR domain movement (of the deAMPylation complex FICD) away from the catalytic core, especially in the TPR1 motif region. This is likely a corollary of the TPR1 motif's interaction with the tripartite BiP surface in the context of the deAMPylation complex.

Chapter 2.2: Heterotetramer solution structure validation

The process of crystal packing during macromolecular protein crystallography inherently results in the formation of non-physiological protein-protein interactions. Very weak affinity surface contacts or low probability protein states can also be stabilised by the high protein concentrations required for crystallisation or the particular crystal packing environment. There are a number of ways to assess the potential physiological significance of protein-protein interfaces observed crystallographically. For instance, the majority of non-natural crystal contacts are small in surface area and form relatively non-specific protein-protein interfaces. This contrasts with the deAMPylation complex crystal structures in which the bipartite protein-protein interface (totalling 1370 $Å^2$), noted above, is very large and much greater in surface area than any other contacts observed in the crystal structure. Moreover, the PISA estimated solvation free energy gain (Δ^iG) upon formation of this interface (excluding the AMP contribution) is –7.3 kcal/mol. The probability of achieving a lower Δ^iG for the given interface area, if residues were selected at random from the protein surface, was estimated to be 0.35 (*P*-value). The PISA calculated Δ^iG *P*-value being < 0.5 suggests that the hydrophobicity of the observed protein-protein interface is higher than would be expect from a crystallisation artifact (Krissinel & Henrick, 2007). Importantly, the observation that the covalently attached AMP residue sits within the active site of FICD (which is known to be responsible for additional and removal of the AMP moiety to/from BiP) is the strongest indication that the observed protein interface is physiological.

Nevertheless, it is important to further assess the significance of the protein-protein interface observed in the deAMPylation complex and in particular the importance of the FICD(TPR)-BiP interface. As mentioned above, the heterodimeric deAMPylation crystal structure appears compatible with dimerisation of FICD and with a full-length BiP lid subdomain (**Figure 2.1.6**). However, it is known that monomeric FICD although capable of deAMPylation is a poorer deAMPylase than dimeric FICD (Perera *et al*, 2019). Therefore, it does not necessarily follow

that dimeric FICD will interact with BiP-AMP in the same fashion. Moreover, irrespective of concentration or crystal packing artifacts, crystals provide a single structural snapshot, presumably of a local energy minimum. This may deviate from the average structure of a protein (complex) in solution.

Therefore, in order to assess the validity of the structural insights gained from the heterodimeric deAMPylation complex crystal (obtained with monomeric FICD$^{L258D\text{-}H336A}$ and a lid-truncated BiP-AMP), and its applicability to the complex formed between dimeric FICD (a stronger deAMPylase than FICD^{L258D}) and BiP-AMP, a solution-based structural method was employed using intact proteins (dimeric FICD^{H363A} and 'full-length' BiP$^{T299A\text{-}V461F}$). It should be noted, that the full-length BiP commonly used for in vitro experiments, and throughout this study, is in fact composed of BiP residues 27–635. As mentioned above this excludes the N-terminal signal sequence and short unstructured acidic patch. In addition, truncation to residue 635 removes the C-terminal 19 amino acids which are unstructured and include the KDEL region. These regions are not required for the vitro functionality of BiP (Preissler *et al*, 2015a, 2015b).

Low-resolution structures of biomacromolecules can be resolved in solution by small angle X-ray and neutron scattering (SAXS/SANS). SAXS is sensitive to electron density, while SANS is sensitive to atomic nuclei. For mixed complexes with two components, contrast variation SANS is able to distinguish between proteins that are differentially isotopically labelled. To enable this analysis, matchout (partially) deuterated proteins were expressed by collaborators working in the Institut Laue–Langevin Deuteration laboratory (Grenoble, France). *E. coli* cell pellets were shipped to the UK to enable further protein purification. Partially deuterated (d*Protein)* and non-deuterated (h*Protein*) complexes of dimeric FICD^{H363A} and full-length BiP$^{T299A\text{-}V461F}$-AMP were copurified by SEC into buffers with varying D_2O content. Contrast variation solution scattering data were subsequently collected (**Figure 2.2.1**).

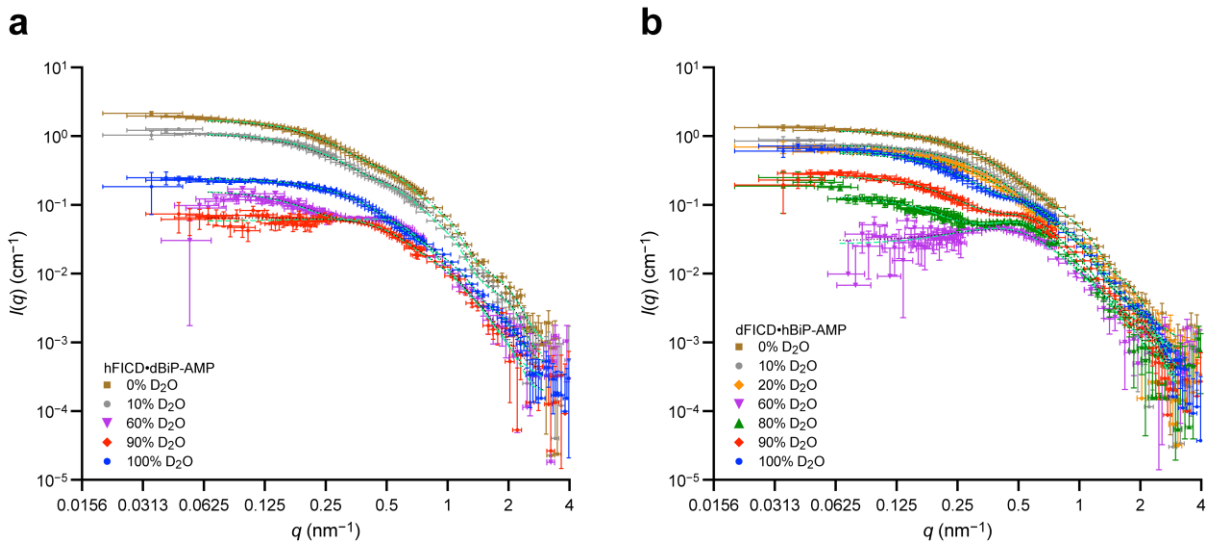

Figure 2.2.1: Small angle neutron scattering curves. Buffer subtracted contrast variation SANS data from complexes of a, non-deuterated FICD^{H363A} (hFICD) with partially deuterated BiP$^{T229A-V461F}$-AMP (dBiP-AMP) and b, partially deuterated FICD^{H363A} (dFICD) with non-deuterated BiP$^{T229A-V461F}$-AMP (hBiP-AMP). Scattering intensity data, $I(q)$, is plotted against the modulus of the scattering vector, q. SANS data is acquired over a range of sample buffer conditions with varying D_2O content (indicated). Overlaid dotted black lines are theoretical scattering curves based on the modelled heterotetramer shown in (**Figure 2.1.6**), dashed green lines are the theoretical scattering curves from flex-fitting of the input heterotetramer model with a constrained FICD dimer interface. Error bars represent SEM with respect to the number of pixels used in the radial data averaging.

Analysis of the low-q Guinier region provides information pertaining to the forward scattering, $I(0)$, and radius of gyration, R_g, in each solution (**Figure 2.2.2**); where q is the magnitude of the scattering vector.

$$q = \frac{4\pi \sin(\theta)}{\lambda} \tag{1}$$

where λ is the incident neutron beam wavelength (in nm) and the scattering angle (in degrees) is 2θ. The low-q region is described as the low scattering angle range where $qR_g < 1.5$ (ideally < 1.3) and the Guinier approximation is therefore valid (Guinier & Fournet, 1955).

$$I(q) = I(0)\exp\left(\frac{-q^2 {R_g}^2}{3}\right) \tag{2}$$

Plotting $\ln(I(q))$ against q^2 permits the fitting of a derivation of **Equation 2**:

$$\ln(I(q)) = \ln(I(0)) - \frac{{R_g}^2}{3}q^2 \tag{3}$$

This permits the extraction of $I(0)$ and R_g values for each scattering curve. The q limits for fitting are shown (vertical dashed lines in **Figure 2.2.2**) and result in $qR_g < 1.3$ (with the exception of the fitting of dFICD•hBiP-AMP in 80% D_2O buffer where $qR_g = 1.4$). On the whole, the Guinier scattering curves presented little evidence of polydispersity (in the form of interparticle repulsion or aggregation).

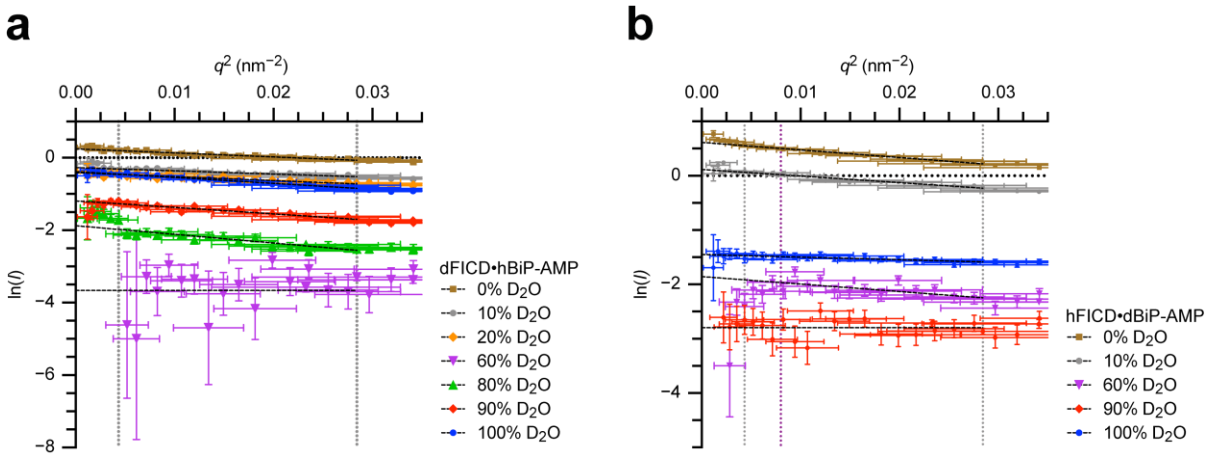

Figure 2.2.2: Guinier plots of the SANS data. a, Guinier plot of partially deuterated FICD and non-deuterated AMPylated BiP across a range of %D_2O buffer conditions. **b,** as in **a** but complexes of non-deuterated FICD and partially deuterated AMPylated BiP are analysed. Vertical dotted lines indicate the q-range over which the Guinier curve fitting was implemented. Due to apparent interparticle repulsion (which is evident as $q \rightarrow 0$) the lower q-fitting limit was increased for the dFICD•hBiP-AMP sample in 80% D_2O (purple dotted line) such that all fits (in both **a** and **b**) were made in a region where $qR_g \leq 1.4$.

The scattering amplitude, $I(0)$, is directly proportional to both the square of the contrast and the fractional term in **Equation 4**, also known as n the number density (Zaccai *et al*, 2016):

$$I(0) = \frac{cN_A}{M_w}\Delta\rho^2 V^2 \qquad (4)$$

where V is the volume of the complex (cm^3), c is the concentration of the protein complex (g/cm^{-3}), N_A is Avogadro's number (6.022×10^{23} mol^{-1}) and M_W is the molecular weight of the protein complex (g mol^{-1}, equivalent to Da). $\Delta\rho$ is the contrast of the sample (cm^{-2}), which is defined as the difference in scattering length density (SLD) between the protein complex and the buffer ($\rho_{protein} - \rho_{buffer}$). As the SLD of the buffer is dominated by the D_2O content (and therefore to a good approximation increases linearly with %D_2O) and the SLD of the protein also varies linearly with %D_2O, due to labile hydrogen/deuteron (H/D) exchange, it follows that $\sqrt{I(0)/c} \propto$ %D_2O.

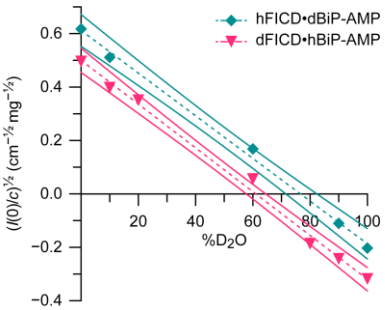

Figure 2.2.3: Scattering amplitude plot. Linear best-fit curves are displayed with dashed lines and 95% confidence interval bands in colour-matched solid lines. Error bars are derived from SE of Guinier fits (**Figure 2.2.2**).

The determination of $I(0)$ values, combined with measurement of the sample protein concentration, therefore facilitated the calculation of each complex's contrast match point (CMP; **Figure 2.2.3**) — the %D_2O value at which there is no contrast ($\Delta\rho = 0$). The resulting analysis produced CMP values of 77% D_2O (95% CI: 72 to 82% D_2O) for hFICD•dBiP-AMP and 61% D_2O (95% CI: 57 to 66% D_2O) for dFICD•hBiP-AMP.

Theoretical CMPs can also be calculated based on protein (complex) amino acid composition and buffer compositional effects. Assuming a 1:1 protein complex and 95% labile H/D-exchange, comparison of the experimentally observed CMPs with theoretical values calculated by MULCh (Whitten *et al*, 2008), suggest that dFICD was 63.8% deuterated at non-exchangeable hydrogens and dBiP-AMP was 66.5% deuterated. These values of protein partial-deuteration permit direct theoretical estimation of $I(0)/c$ values, using SASSIE (Curtis

	Input model	hFICD•dBiP-AMP	dFICD•hBiP-AMP	Best-fit (dimer constrained)	Best-fit (dimer unconstrained)
M_W (kDa)	220	220 ± 10	250 ± 30		
R_m [R_g of complex] (Å)	60.1	58 ± 19 (43 to 70)	63 ± 14 (58 to 68)	57.8	59.7
R_g of FICDs (Å)	34.5	41 (17 to 55)	38 (14 to 52)	36.9	37.2
R_g of BiPs (Å)	69.0	63 (52 to 73)	74 (69 to 79)	66.3	69.0
χ^2 (reduced data)	2.4 ± 2			2.4 ± 0.8	1.7 ± 0.4

Table 2: Low-*q* SANS parameters and flex-fitting results. Summary of biophysical parameters derived from forward scattering (M_W; molecular weight) and Stuhrmann analysis of the contrast variation SANS data over the low-q (Guinier) region. Copurified complexes of non-deuterated $FICD^{H363A}$ (hFICD) with partially deuterated $BiP^{T229A\text{-}V461F}$-AMP (dBiP-AMP) and partially deuterated $FICD^{H363A}$ (dFICD) with non-deuterated $BiP^{T229A\text{-}V461F}$-AMP (hBiP-AMP) were analysed. The mean M_W ± SD is calculated across all curves excluding the 60% D_2O datasets, which are close to the contrast match points for both partially deuterated complexes. Radii of gyration parameters are best fit or interpolated values ± SE (and/or 95% CI) from the Stuhrmann curve fittings (**Figure 2.2.4**). Parameters from the best flex-fit heterotetramer models are also shown with theoretical R_g values and overall χ^2 goodness of fit (mean ± SD) against the reduced scattering dataset (**Figure 2.2.5** and **Figure 2.2.6**).

et al, 2012). Comparison of the theoretical $I(0)/c$ values with those determined from the (above) experimental Guinier analysis facilitated experimental protein complex M_W estimation (**Table 2**) — which was in good agreement with a heterotetrameric 2:2 complex of FICD•BiP-AMP.

Based on the calculated protein deuteration values the contrast at each $\%D_2O$ can also be calculated. A Stuhrmann plot (derived from plotting the square of the R_g data against the reciprocal of the contrast) provides information on the internal arrangement and size of the complex and each component of the complex, according to the relationship (Ibel & Stuhrmann, 1975):

$$R_g{}^2 = R_m{}^2 + \frac{\alpha}{\Delta\rho} - \frac{\beta}{\Delta\rho^2} \qquad (5)$$

In which $R_m{}^2$ represent the R_g of the complex if it had a homogenous SLD; α reflects the radial distribution of SLD and β reflects the distance of the centre of the complex's SLD from the complex's centre of mass. Through this analysis (in concert with MULCh-derived individual component match points), a number of experimental R_g parameters were extracted (**Figure 2.2.4**). The R_g provides an indication of protein component/complex size and, in the context of SANS, is a measure of the average contrast weighted distance from the centre of mass to each scattering element. The Stuhrmann derived R_g parameters are in good agreement with the theoretical values calculated from the input heterotetramer model using CRYSON analysis software (Svergun *et al*, 1998) (**Table 2**).

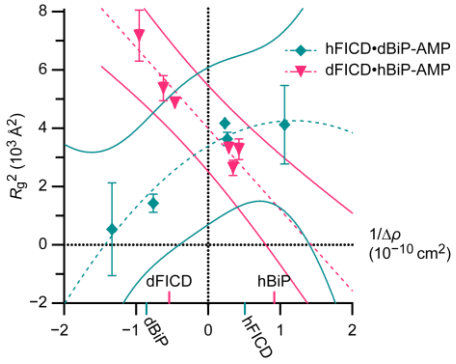

Figure 2.2.4: Stuhrmann plot. Best-fit curves are displayed with dashed lines and 95% confidence interval bands in colour-matched solid lines. The determined match points of the individual complex components are indicated on the *x*-axis. Error bars are derived from SE of Guinier fits (**Figure 2.2.2**).

In the case of the Stuhrmann plot of dFICD•hBiP-AMP a linear best-fit line (suggesting $\beta \approx 0$) was a considerably better fit to the data (shown in **Figure 2.1.6**; $R^2 = 0.93$) than the fitting of a quadratic curve ($R^2 = 0.66$). This suggests that the dFICD•hBiP-AMP complex has an SLD centre which is very close to the complex's centre of mass (COM). The converse is true for the Stuhrmann fit of the deuterated BiP-AMP complex, which is much more quadratic ($R^2 = 0.95$ for $\beta > 0$ versus 0.89 for $\beta = 0$) — revealing little overlap between the hFICD•dBiP-

AMP complex's SLD centre and COM. As semi-deuteration of a component increases its relative contribution to the overall SLD, these findings are consistent with a heterotetramer in which the centre of mass lies in the plane of the FICD dimer and above the plane of the majority of the BiP mass. This arrangement fits well with the structural model of the heterotetramer presented in **Figure 2.1.6.** Moreover, the value of α also provides valuable information about the structural organisation of the complex, with values of $\alpha > 0$ suggesting that the higher contrast component of the complex is located towards the outside of the complex. Thus, it can be inferred from the Stuhrmann analysis, of both hFICD•dBiP-AMP and dFICD•hBiP-AMP, that FICD is on the inside and BiP-AMP towards the outside of the complex; this is again entirely consistent with the modelled heterotetramer structure (**Figure 2.1.6**).

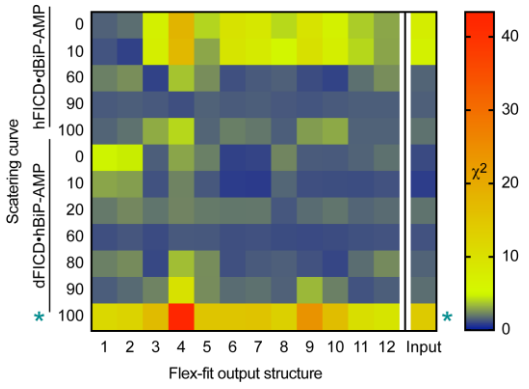

Figure 2.2.5: Goodness of fit from SANS structure modelling. Heat-map of the χ^2 goodness of fit of the theoretical scattering curve derived from each flex-fit model, against all observed experimental scattering datasets. The major NW to SE diagonal illustrates the optimised χ^2 of each flex-fit model from its progenitor dataset. For example, output structure 2 is derived from normal mode flex-fitting of the input structure (**Figure 2.1.6**) so as to minimise its χ^2 relative to the scattering data obtained from hFICD•dBiP-AMP in 10% D_2O. Note, the *flanked dataset resulted in anomalously poor model fits.

By analysing the data across the entire *q*-range it is possible to extract further information about the internal arrangement of the heterotetramer. Across all D_2O concentrations, the theoretical scattering profile of the heterotetramer (modelled in **Figure 2.1.6**) correlated well with the experimental scattering, with an overall average χ^2 of 3.4 ± 4 (mean ± SD) or 2.4 ± 2 following anomalous dataset removal (black dotted lines in **Figure 2.2.1**, quantified in **Figure 2.2.5**). This was true even at D_2O concentrations close to the CMP for each deAMPylation complex, where the scattering profile is very sensitive to both the shape and stoichiometry of the particles in solution. Furthermore, the best flex-fit structure (generated for each scattering dataset by allowing the input structure to undergo normal mode analysis (NMA) flexing of its domains in order to minimise the χ^2 of the output flex-fit structure from that scattering dataset) did not cause significant changes in the predicted scattering profile (green dashed lines in **Figure 2.2.1**). The SANS data thus indicate that the vast majority of particles in solution are engaged in a heterotetramer with neutron scattering properties closely aligned to those predicted by a heterotetramer model based on the heterodimer crystal structure (**Figure 2.1.6**).

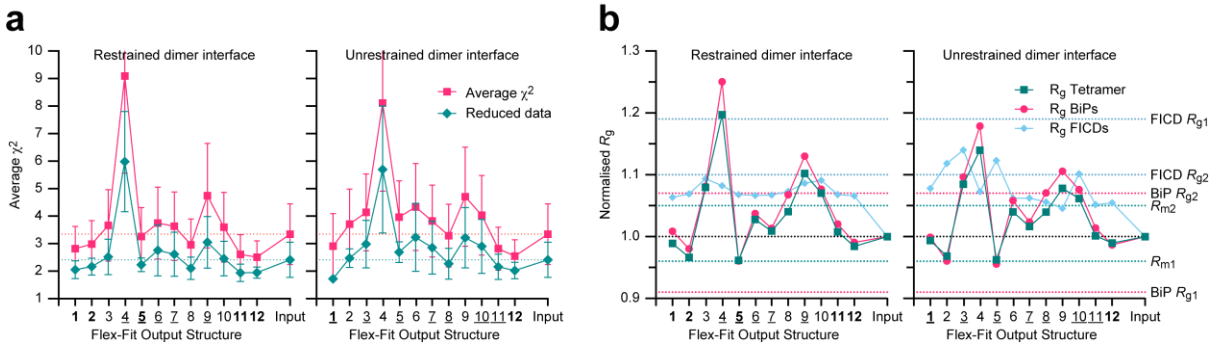

Figure 2.2.6: Evaluation of input and flex-fit heterotetramer models. **a**, Comparison of the average χ^2 for each model. The 'reduced data' average χ^2 (green) is derived from fitting to all data excluding the anomalous scattering observed for dFICD•hBiP-AMP in 100% D2O (*in **Figure 2.2.5**). Error bars represent SEM. **b**, Comparison of Stuhrmann analysis derived R_g (coloured, horizontal dotted lines) with the calculated R_gs of the input and output structures. In **c** and **d** symmetric output structures are underlined and flex-fit structures highlighted in bold have χ^2 SDs (derived from the analysis of the reduced SANS dataset; green in **a**) which are less than and significantly different to the input model's χ^2 SD ($P < 0.05$ by F-test).

As mentioned above, no individual flex-fit structure produced a significantly reduced average χ^2 across all datasets. The initial flex-fitting strategy (and that displayed in **Figure 2.2.1)** permitted non-linear rigid block NMA at all interdomain boundaries with the exception of the FICD dimer interface, which was constrained on account of its very low (nanomolar) in vitro K_D (Perera *et al*, 2019). However, the experimental FICD R_g values derived from the Stuhrmann analysis were slightly higher than that possessed by the input heterotetramer model and the dimer interface-restrained flex-fit output models (**Figure 2.2.6**). Therefore, a flex-fitting strategy with the dimer interface left unconstrained was also employed. This did not result in an overall improvement in output model quality (χ^2) relative to the dimer interface-constrained strategy (**Figure 2.2.6**). However, a number of flex-fit output structures (from both flex-fit strategies) did have significantly different and reduced χ^2 variances relative to that of the input model (**Figure 2.2.6a**, underlined). The majority of flex-fit structures possessed R_g parameters which were in good agreement with the Stuhrmann derived R_g values (**Figure 2.2.6b**). Moreover, when the dimer interface was constrained, the principal variation in the flex-fit structures was evident in BiP(NBD) and FICD(TPR) domain reorientation and in the BiP lid region (**Figure 2.2.7**).

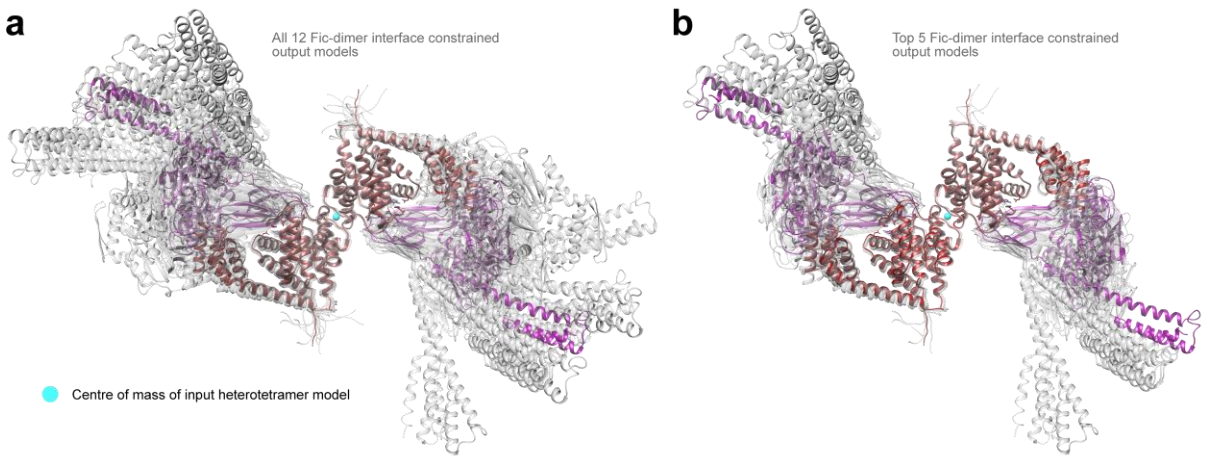

Figure 2.2.7: Comparison of flex-fit structures. Structures are derived from normal mode (inter-domain) flex-fitting with constraints only placed on the very tight dimer interface of FICD. All structures are aligned to FICD of the input heterotetramer structure (orthogonal view to that displayed in **Figure 2.1.6**), with FICDs in red and BiP-AMPs in magenta. Also, as in **Figure 2.1.6**, the centre of mass of the input model is indicated (cyan sphere). **a,** Superposition of all 12 flex-fit output structures. **b,** As in **a** but only displaying the top 5 flex-fit structures aligned to the input heterotetramer — those which produce statistically significant reductions in scattering χ^2 SDs relative to the input model.

Previous Michaelis-Menten analysis of FICD deAMPylation produced no evidence of (negative or positive) enzyme cooperativity (Preissler *et al*, 2017a), which suggests that the two BiP binding sites of an FICD dimer operate independently from one another. Consequently, symmetry is to be expected from an average solution structure of a heterotetrameric deAMPylation complex which has an FICD dimer (which itself possesses C2 rotational symmetry) at its core. Surprisingly, only around half of the flex-fit output structures maintained the C2 rotational of the input heterotetramer structure (**Figure 2.2.7**, highlighted in bold in **Figure 2.2.6**).

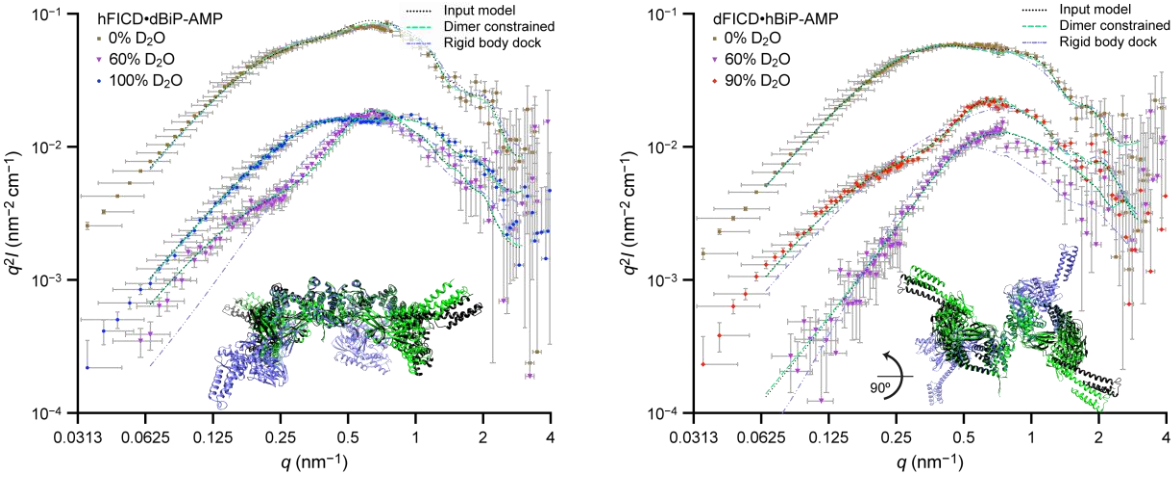

Figure 2.2.8: Kratky plots of a best-fit dimer-restrained solution structure. Kratky plots of selected scattering curves highlighting the relative fits of the input model, dimer constrained best-fit structure and a poorer fitting rigid-body docking model (dashed lines). Inset, colour-matched models aligned by the FICD dimer, shown in orthogonal views. As expected, the rigid body dock model produces a poorer fit to the scattering data, which is especially evident when the buffer D_2O content approaches the complex CMP (60% D_2O datasets). Note, the Kratky plot scattering intensity profiles (with internal scattering features and slowly descending right-hand-side tails) are consistent with FICD•BiP-AMP being a flexible protein complex.

Thus, each flex-fitting strategy yielded only one best-fit structure that possessed both symmetry and a significantly reduced χ^2 SD (**Figure 2.2.8**, **Figure 2.2.9** and **Figure 2.2.6**, bold and underlined). The best-fit structure derived from leaving the high affinity FICD dimer interface unconstrained (mean χ^2 goodness-of-fit across the reduced data set 1.7 ± 0.4) is closer in conformation to the input structure than that obtained with a restrained dimer interface (mean χ^2 2.4 ± 0.8) (**Table 2**), with an RMSD from the input heterotetramer structure of 5.4 and 7.1 Å (across all 1,892 Cα pairs), respectively (**Figure 2.2.9**). Both output structures demonstrate good R_g agreement with the Stuhrmann analysis. Importantly, the best-fit complexes' FICD R_gs are increased and in better agreement with the experimentally derived values, relative to the input structure (**Table 2** and **Figure 2.2.6b**, bold and underlined). Moreover, the observed model deviations (from input to best-fit models) are indicative of additional deAMPylation complex flexibility in solution, in particular in the composite FICD(TPR)-BiP(NBD) interface and in the disposition of the BiP lid (SBDα subdomain) (**Figure 2.2.9**). This flexibility is inaccessible to crystallographic analysis of BiP (complexes) but is consistent with previous observations of Hsp70 conformational dynamics (Zhuravleva *et al*, 2012; Wieteska *et al*, 2017).

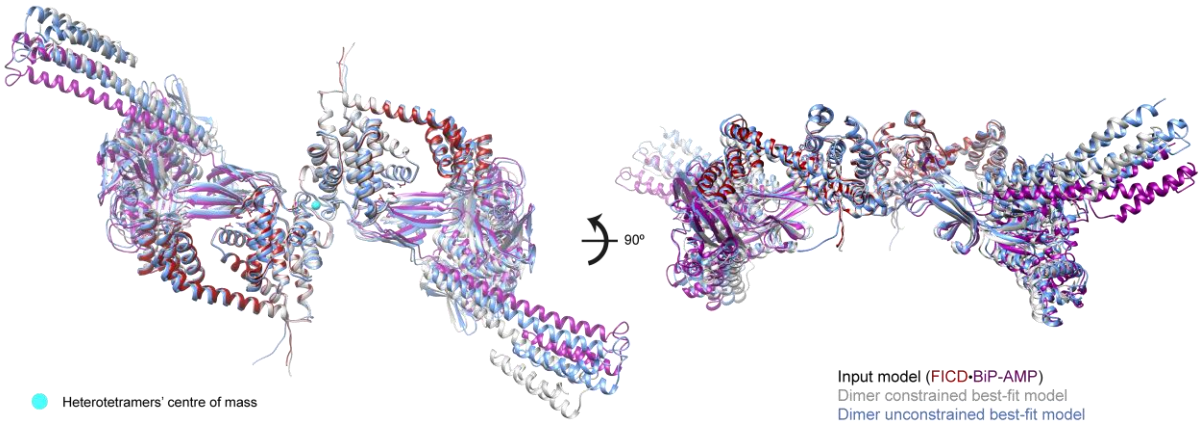

Figure 2.2.9: Optimal best-fit solution structures. Optimal flex-fit structures with respect to overall agreement (of their theoretical scattering profile) with all experimental contrast-variation SANS datasets. Output structures are aligned to FICD of the input heterotetramer model, itself derived by imposing the C2 symmetry of the FICD dimer (PDB 4U0U) onto the heterodimeric deAMPylation complex crystal structure (as shown in **Figure 2.1.6**). The structural deviation between the best-fit solution structures and the input model is indicative of inter-domain flexibility present in solution.

Chapter 2.3: The TPR domain is essential for deAMPylation

Having established the validity of the heterodimeric crystal structure, in the context of a heterotetrameric complex in solution, I was curious to understand the sensitivity of deAMPylation activity and complex assembly to perturbations in the observed contacts linking the FICD TPR domain to BiP (**Figure 2.1.3** and **Figure 2.1.4**). The ability of different FICDs to bind either modified or unmodified BiP can be assayed via the immobilisation of a protein ligand (BiP) onto a biosensor. Analyte (FICD) association and dissociation can then be monitored in real time utilising BioLayer Interferometry (BLI). By the introduction of a His363Ala mutation into all tested FICD variants that contain a catalytic domain, all analytes can be rendered catalytically dead and the effects of any given mutation on FICD•BiP±AMP complex assembly and disassembly can be monitored (without the possibility of any convoluting effects of covalent ligand modification).

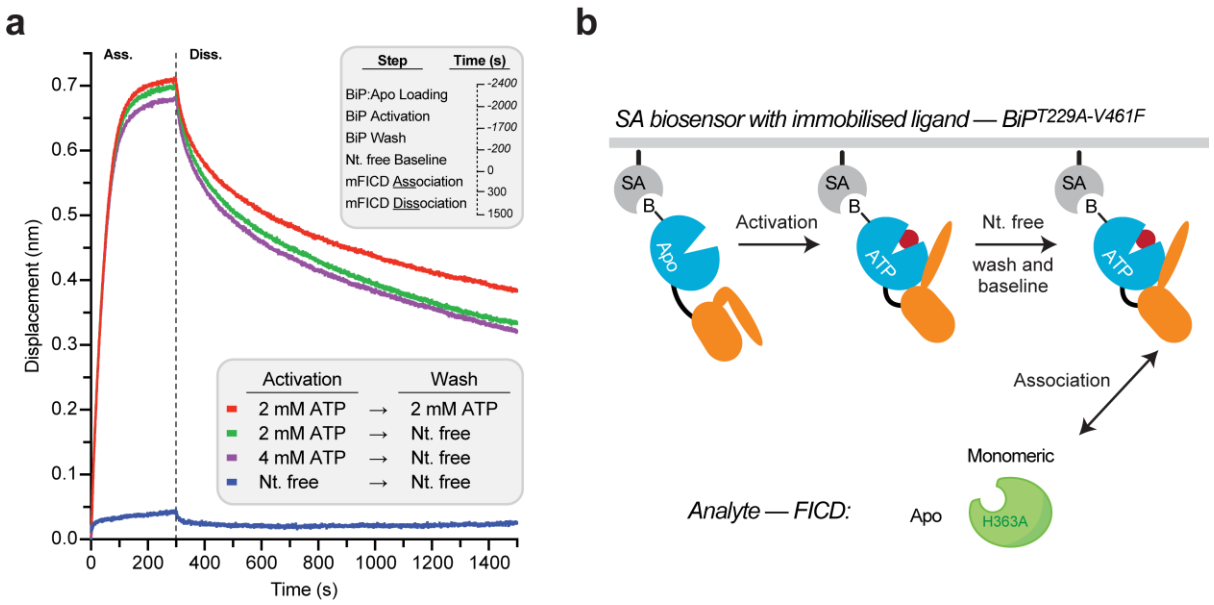

Figure 2.3.1: Immobilised BiP ligand can respond to and be saturated by ATP. **a**, BLI traces of the interaction between FICD$^{L258D-H363A}$ and immobilised biotinylated BiP$^{T229A-V461F}$ in different nucleotide states. Before exposure to FICD$^{L258D-H363A}$ immobilised BiP:Apo was subjected to two consecutive incubation steps (activation and wash) in the presence or absence of ATP as indicated. FICD association and dissociation steps (shown) were then conducted in a nucleotide (Nt.)-free solution. Note that BiP only interacts with FICD$^{L258D-H363A}$ when pre-saturated with ATP. Importantly, ATP pre-bound BiP retains its affinity for FICD$^{L258D-H363A}$ even if subsequently washed in a buffer lacking ATP (compare red and green traces). Thus, the majority of BiP remains in its ATP-state for the duration of the kinetic experiment, experimentally uncoupling the effect of nucleotide on the FICD analyte from its effect on the immobilised BiP ligand. **b,** Cartoon schematic of the BLI assays presented in **a**. The pre-AMPylation complex is formed between the immobilised BiP:ATP 'ligand' and the FICD 'analyte'.

As FICD has a preference for ATP-state BiP as an AMPylation substrate (Preissler *et al*, 2015b), it was important to establish that immobilised BiP could still respond allosterically to ATP. To this end, N-terminally avi-tagged, in vitro biotinylated, non-AMPylated, ATPase dead and substrate binding deficient apo BiP (BiP$^{T229A-V461F}$:Apo), was loaded onto the BLI streptavidin biosensor. Preincubation of the immobilised BiP with MgATP resulted in a significant increase in its ability to interact with monomeric and catalytically dead FICD (FICD$^{L258D-H363A}$) (**Figure 2.3.1**). This suggests that immobilised BiP is able to bind and respond allosterically to ATP and that FICD has both a preference for binding (as well as AMPylating as previously demonstrated) the ATP-state of BiP. Moreover, BiP's binding and response to ATP was saturable and the allosteric effect of ATP-binding was long lasting, even when incubated for a prolonged period of time in a buffer lacking ATP (**Figure 2.3.1**), a phenomenon presumably potentiated by BiP's ATPase activity–inhibiting Thr229Ala mutation.

As AMPylation of BiP both intrinsically biases the Hsp70 towards its ATP-state and decreases its intrinsic ATPase activity (Preissler *et al*, 2015b, 2017b; Wieteska *et al*, 2017); BiP$^{T229A-V461F}$-AMP once bound to ATP will release ATP at a much slower rate than its unmodified form. This is attested to by the observation that it becomes much more difficult to remove nucleotide from BiP, by dialysis, once the BiP is AMPylated (as measured by $A_{260/280}$ ratio, data not shown).

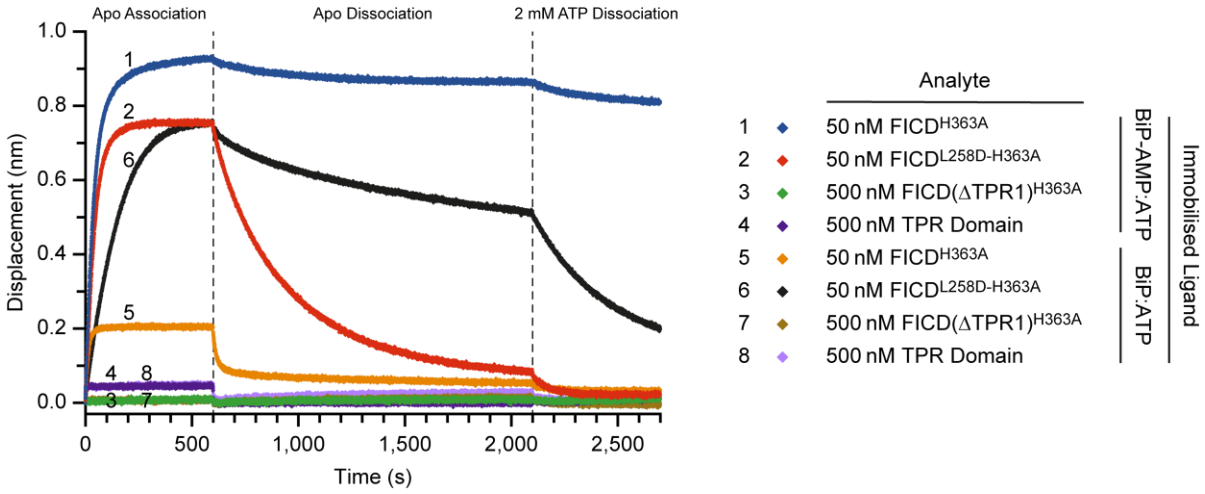

Figure 2.3.2: FICD's TPR domain is essential for binding BiP. Association and dissociation traces of FICD analytes (concentrations indicated in the legend) from immobilised BiP bound to ATP (either AMPylated or unmodified), are shown. Shown, is a single set of representative BLI curves from n = 3 independent experiments. Removal of the TPR1 motif (ΔTPR1) from FICD^{H363A} abrogates the ability of the FICD to bind either ATP-state BiP or BiP-AMP. The TPR domain alone (FICD residues 104–186) can interact with both BiP:ATP and BiP-AMP:ATP. The ability for full analyte dissociation suggests that there is little non-specific binding of analyte to the biosensor.

It was found that BiP bound more tightly to monomeric FICD$^{L258D-H363A}$ than to dimeric FICD (**Figure 2.3.2**). The converse was true for the binding to AMPylated BiP. Complex dissociation was further accelerated by the addition of ATP to the dissociation buffer; in the case of dissociation from immobilised BiP-AMP this is presumably via direct competition of ATP with the BiP's covalently linked AMP moiety for the active site of FICD, during a multi-step dissociation of the analyte. Crucially, upon removal of the TPR1 motif, dimeric FICD lost all ability to bind either BiP ligand (**Figure 2.3.2**). As predicted by the mode of TPR binding in the crystal structures, the isolated TPR domain measurably interacted with the ATP-bound BiP ligands in a manner that was not affected by BiP's covalent modification status.

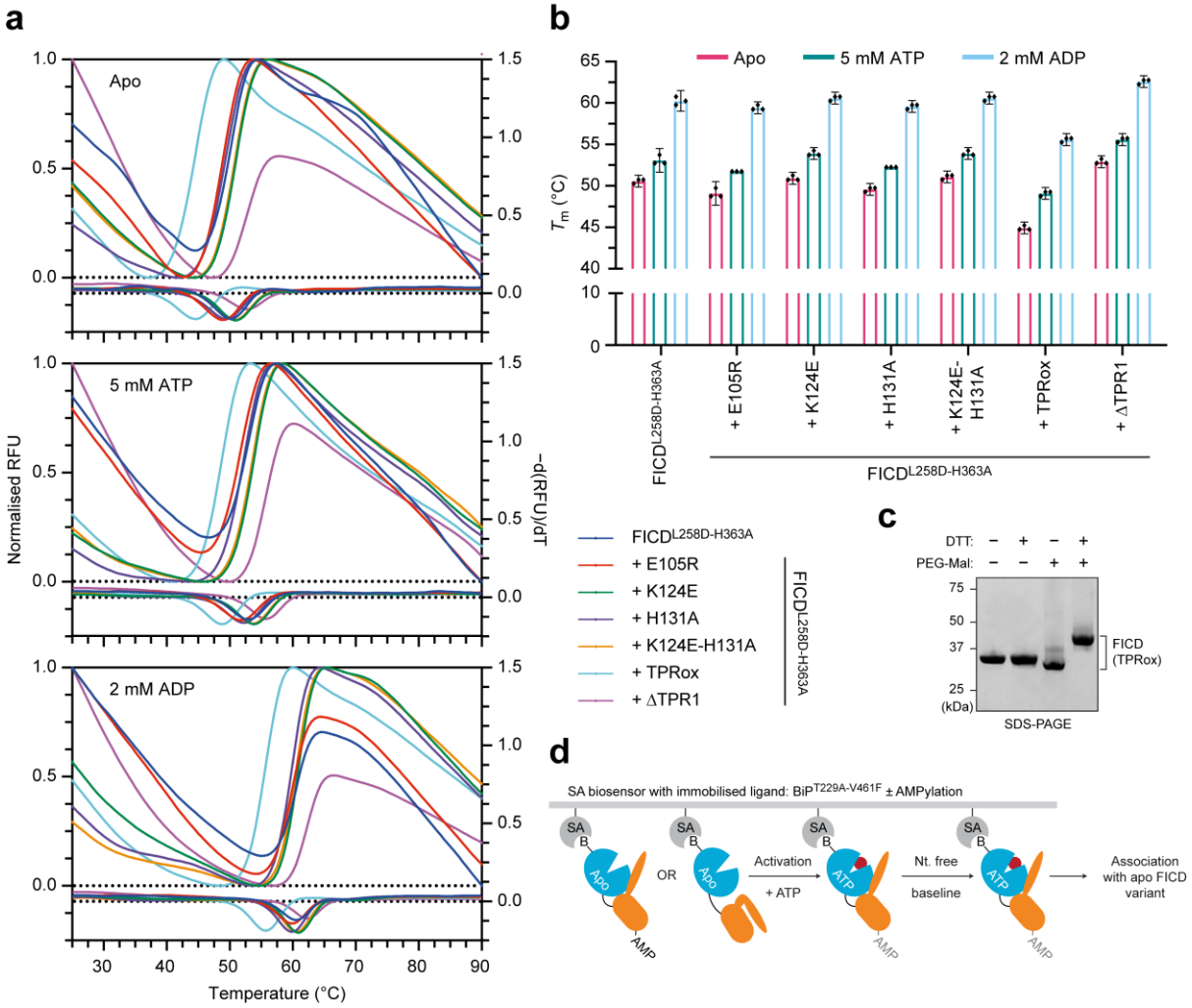

Figure 2.3.3: Biophysical characterisation of FICD mutants. **a**, Representative normalised differential scanning fluorimetry (DSF) melt curves (top curves and left *y*-axis) with corresponding negative first derivatives of the melt curves (bottom curves and right *y*-axis). Global minimums of the latter were used to calculate the melting temperature. Melt curves were collected in technical duplicate. RFU, relative fluorescent units. **b,** The derived protein melting temperatures (T_m, mean ± 95% CI) derived from n = 3 independent DSF experiments. Note, all FICD variants (like FICD$^{L258D-H363A}$) are stabilised by nucleotide binding. Most FICD mutations do not cause large changes in T_m. The most destabilised FICD variant is in fact FICD$^{L258D-H363A}$(TPRox) despite the presence of a disulphide bond fixing the TPR domain in place. **c,** PEG 2000 maleimide-based electrophoretic mobility assay analysis of the oxidation status of monomeric FICD$^{L258D-H363A}$(TPRox), demonstrating almost complete disulphide-stapling of the FICD's TPR domain to its α-helical linker/C-terminal capping helix (**Figure 2.1.3**). **d,** Schematised model of the BLI protocol (for immobilised BiP ± AMP) preceding the association and dissociation phases displayed in **Figure 2.3.2** and subsequent BLI figures.

The introduction of point-mutations into residues at the FICD(TPR1)-BiP interface (mutated residues highlighted in **Figure 2.1.3** and **Figure 2.1.4**), whilst not perturbing the structural integrity of the FICD variants (**Figure 2.3.3**), significantly affected the kinetics of FICD association and dissociation of both monomeric and dimeric FICD variants (**Figure 2.3.4**). This

agrees with the notion (suggested by the solution structure analysis) that monomeric and dimeric FICD similarly engage AMPylated BiP. Moreover, in keeping with the crystallographically observed multivalent nature of the deAMPylation complex, the kinetics of $FICD^{L258D\text{-}H363A}$•BiP-AMP interaction appears biphasic and becomes increasingly monophasic upon disruption of FICD(TPR1)-BiP contacts (**Figure 2.3.4a**).

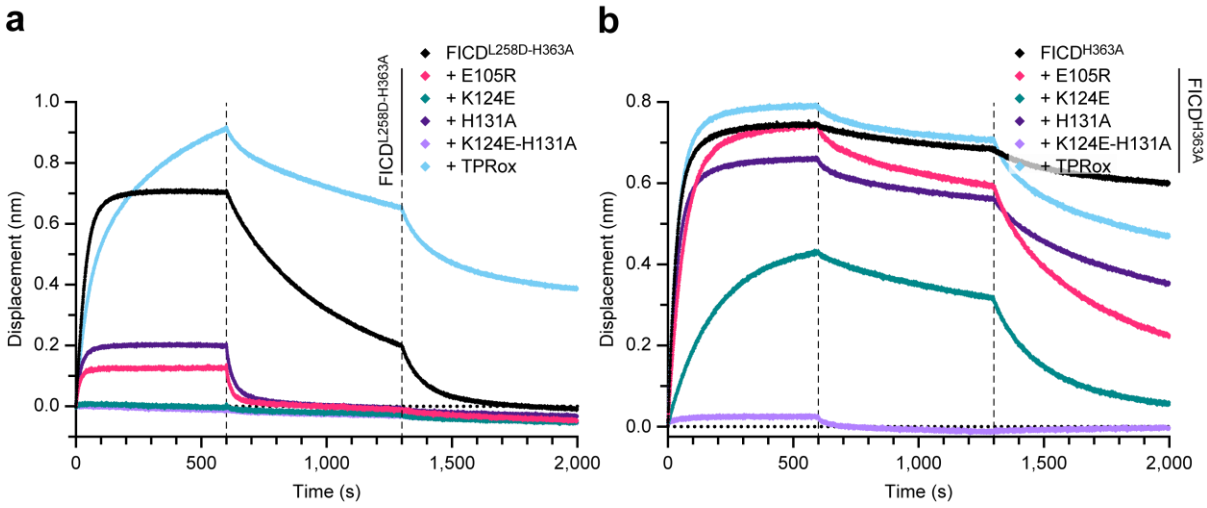

Figure 2.3.4: FICD(TPR1) mutations disrupt deAMPylation complex assembly. **a**, Representative BLI analysis of TPR domain mutants of monomeric $FICD^{L258D\text{-}H363A}$ binding to immobilised AMPylated BiP, from n = 3 independent experiments. Note, TPR domain oxidation (TPRox) appears to increase the affinity of $FICD^{L258D\text{-}H363A}$ for BiP-AMP. **b,** As in **a** but the tested analytes are all derivates of (dimeric) $FICD^{H363A}$. In **a** and **b**, as in **Figure 2.3.2**, the beginning of each dissociation phase is indicated with vertical dashed lines and the second dissociation buffer is supplemented with 2 mM ATP.

To address the role of interdomain contacts between FICD's TPR and catalytic Fic domain in deAMPylation complex stability, one of two contacting residues within FICD's TPR2 motif (Asp160) was mutated (highlighted in **Figure 2.1.3**). However, FICD's TPR domain has also been observed to fully disengage from the capping/linker helix, exhibiting a 'TPR-out' conformation (PDB 6I7K and 6I7L). To analyse the effect of perturbed interdomain contacts, whilst maintaining the BiP binding–competent 'TPR-in' conformation, Asp160 and Thr183 (the latter located within FICD's capping/linker helix; **Figure 2.1.3**) were both mutated to cysteines and oxidised to stoichiometrically form an intramolecular disulphide bond (TPRox, **Figure 2.3.3c**). TPR oxidation within monomeric $FICD^{L258D\text{-}H363A}$ resulted in more biphasic kinetics and a significant decrease in dissociation rate from BiP (**Figure 2.3.4a**), suggesting that the covalent fixation of the 'TPR-in' conformation outweighs the destabilising effects of perturbing an intramolecular Fic-TPR domain contact (also see the destabilising effect of TPR oxidation evident in terms T_m depreciation, **Figure 2.3.3a–b**). Notably, the effect on dimeric

FICD was less pronounced (**Figure 2.3.4b**). These measurements are consistent with the fact that the 'TPR-out' conformation has only been observed in monomeric FICD structures and suggests that dimeric FICD has an intrinsically less flexible TPR domain. Nevertheless, TPR oxidation does alter dimeric FICD binding kinetics. The increased FICD dissociation rate, which is further exaggerated by the addition of ATP in the second dissociation phase, implicates intramolecular Fic-TPR domain communication in the regulation of complex association-dissociation kinetics.

In order to assess the effects of the above TPR domain mutations on the ability of FICD to deAMPylate its substrate (BiP-AMP), a fluorescence polarisation (FP)-based assay was employed (based on the methodology originally published in Preissler *et al*, 2017a). In a previous study the effects of various FICD mutations (including the monomerisation inducing Leu258Asp mutation) were measured under substrate limiting conditions (Perera *et al*, 2019). That is to say, with micromolar concentrations of enzyme and only nanomolar concentrations of AMPylated BiP (labelled with a FAM fluorophore derivatised AMP molecule; BiP-AMP(FAM)). Such conditions are not consistent with quasi-steady state kinetics as the following relationship is not met: $[E]_0 << [S]_0 + K_M$; where $[E]_0$ and $[S]_0$ are the concentrations of enzyme and substrate at t = 0 and K_M is the Michaelis constant — $(k_{off} + k_{cat})/k_{on}$.

So as to facilitate approximate quasi-steady state kinetics at early reaction progress time points, $BiP^{T229A\text{-}V461F}$-AMP(FAM) was used as a (nanomolar) tracer for a much larger concentration of BiP-AMP (with $[E]_0$ = 0.5 µM FICD variant, $[S]_0$ = 5 µM $BiP^{T229A\text{-}V461F}$-AMP). Such a method was also previously employed in order to carry out a full Michaelis-Menten analysis of initial deAMPylation rate versus [BiP^{V461F}-AMP], catalysed by an N-terminally glutathione *S*-transferase tagged, dimeric, wild type FICD (GST-FICD) protein (Preissler *et al*, 2017a). In this work by Preissler *et al*, it was found that the K_M of GST-FICD for its substrate (BiP^{V461F}-AMP) was 16 ± 3 µM (best-fit ± SE). Therefore, assuming that the FICD variants tested here have $K_M \geq 16$ µM, $[S]_0$ may be considered small enough relative to the K_M such that, by derivation from the Michaelis-Menten equation (Michaelis *et al*, 2011), the following relationship holds true at early time points:

$$v \approx \frac{k_{cat}}{K_M}[E]_0[S]_0 \qquad (6)$$

where v is the measured initial deAMPylation rate or enzyme velocity. The value of k_{cat}/K_M, which can thus be derived from the measured initial reaction rate, reflects the catalytic efficiency or specificity of an enzyme.

With the aforementioned conditions of enzyme and substrate concentrations, the FICD deAMPylation reactions do not go to completion within the permissible time frame of the time course (which is limited by technical obstacles such as evaporative losses from the assay wells). Thus, in order to convert changes in mFP caused by liberation of AMP(FAM) from the BiP-AMP(FAM) tracer probe by FICD-mediated deAMPylation, the difference in FP (at t = 0) between the (0.5 µM) FICD^{L258D} FP time course and the same reaction preincubated for 5 h (and therefore fully deAMPylated) was considered to reflect the ΔFP equivalent of 5 µM deAMPylated BiP (**Figure 2.3.5a**). Initial (linear) FP deAMPylation rates (in units of mFP/s) were, in this way, converted to deAMPylation rates (in units of nanomolar BiP deAMPylated/s). Using this technique, by enzyme dilution, it could also be demonstrated that the FP-deAMPylation assay had a linear dynamic range down to 6.3% (1/16th) of the rate of 0.5 µM FICD^{L258D} (**Figure 2.3.5b–c**).

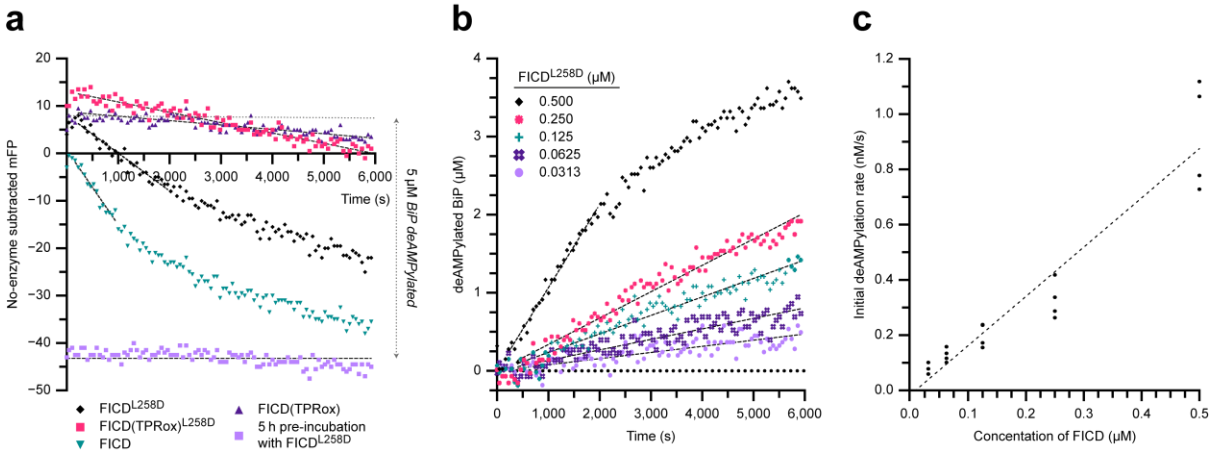

Figure 2.3.5: Establishing an in vitro FP deAMPylation assay. **a**, The FP curves from which **Figure 2.3.7** was derived illustrating the data processing carried out to facilitate deAMPylation rate calculation from FP time course data. The difference (in mFP units) at t = 0 between the FICD^{L258D} deAMPylation time course of BiP-AMP(FAM) and the pre-incubated and fully deAMPylated reaction was taken to represent the ΔFP corresponding to complete substrate deAMPylation (5 µM BiP-AMP). Fits of the linear enzyme velocities are overlaid. **b**, The FP-converted time course of BiP-AMP(FAM) deAMPylation with different concentrations of FICD^{L258D}. **c,** Quantification of the assay represented in **b**, from n = 4 independent experiments — demonstrating the minimum linear dynamic range of the assay. The dashed line illustrates the unconstrained best-fit linear relationship between the observed deAMPylation rate and enzyme concentration.

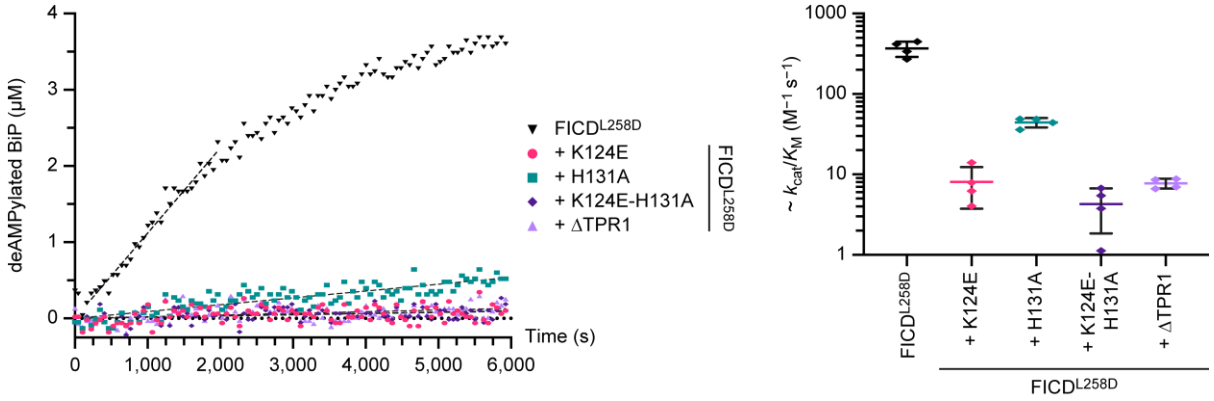

Figure 2.3.6: FICD(TPR1) mutation impairs deAMPylation activity. Left, representative deAMPylation time course (after conversion of mFP units into μM of enzyme product, deAMPylated BiP). Fits of the initial linear enzyme velocities are overlaid (dashed lines). From the calculated initial deAMPylation rates approximate values for catalytic efficiency can be derived (k_{cat}/K_M, right). Mean values are shown ± SD from n = 4 independent experiments. More accurately the presented ~ k_{cat}/K_M values represent the values of $k_{cat}/(K_M+[S]_0)$.

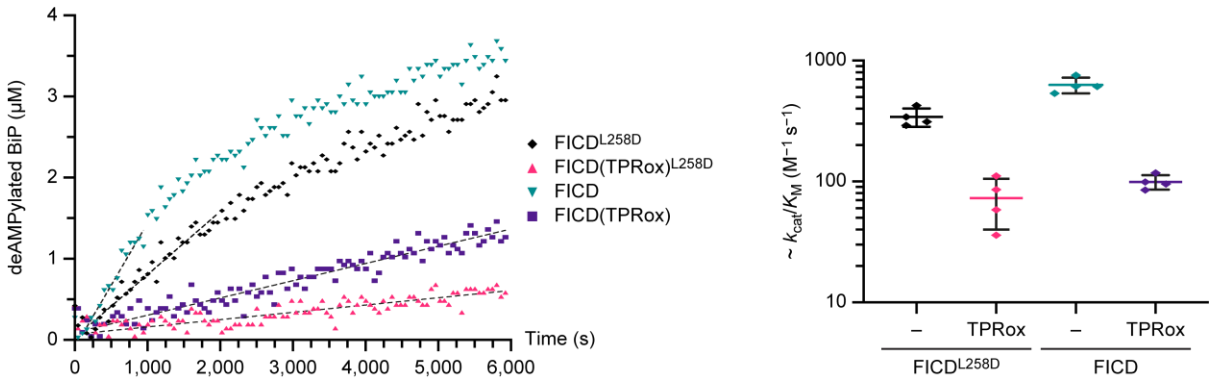

Figure 2.3.7: Disruption of FICD's TPR to catalytic domain communication impairs deAMPylation activity. As in **Figure 2.3.6** but the effect of FICD interdomain disruption (via TPR oxidation) is analysed. Note, the deAMPylation catalytic efficiency of monomeric FICD^{L258D} is also impaired with respect to wild type (dimeric) FICD.

Having established the basis of an in vitro deAMPylation assay, it was found that mutation or removal of the TPR1 motif (in the context of FICD^{L258D}) significantly reduced the catalytic efficiency (k_{cat}/K_M) of in vitro deAMPylation (**Figure 2.3.6**). This is consistent with the essential role played by the TPR domain in deAMPylation complex assembly. Moreover, of the set of TPR1 mutants only His131Ala still falls within the (tested) linear sensitivity range of the assay. Formally, the deAMPylation assay allows me to conclude that the other TPR1 mutants and deletion of the TPR1 motif (ΔTPR1) decrease the initial deAMPylation rate (and thus the approximate k_{cat}/K_M) to a value less than 6.3% of that exhibited by FICD^{L258D} (see **Figure 2.3.5c**).

Monomerisation of FICD was observed to diminish the rate of deAMPylation under a steady-state kinetic regime (**Figure 2.3.7**), with a 46% decrease in k_{cat}/K_M from dimeric to monomeric FICD (630 ± 50 to 340 ± 30 s^{-1} M^{-1}, mean ± SD, respectively). Coincidentally, this is a very similar to the depreciation in enzyme velocity that was previously attributed to the same monomerising Leu258Asp mutation, under a substrate-limited kinetic regime (Perera *et al*, 2019). Moreover, the k_{cat}/K_M value calculated here for wild type (dimeric) FICD is in good agreement with the value derived from a 'traditional' Michaelis-Menten analysis of GST-FICD: 600 ± 100 s^{-1} M^{-1} (best-fit ± SE) (Preissler *et al*, 2017a). This agreement between the calculated k_{cat}/K_M values, at least in the case of wild type FICD, validates the assumptions made in the use of **Equation 6** for FP-deAMPylation assay data processing (**Figure 2.3.6** and **Figure 2.3.7**).

Interestingly, disruption of FICD's TPR to Fic domain interaction (via TPR domain oxidation, TPRox) significantly compromised the deAMPylation activity of both monomeric and dimeric FICD (**Figure 2.3.7**), despite not appreciably decreasing the observed affinity for AMPylated BiP (**Figure 2.3.2**). The effect on catalytic efficiency presumably reflects a contribution of TPR flexibility or intra-FICD interdomain communication towards the deAMPylation turnover number (k_{cat}).

Chapter 2.4: The role of Glu234 in deAMPylation

The deAMPylation complex crystal structure contains well-resolved electron density for BiP's AMPylated Thr518 residue within FICD's (Fic domain) active site (**Figure 2.4.1**). Note, prior to deAMPylation complex assembly and copurification, the BiP protein is in vitro AMPylated by prolonged (16 h) incubation with millimolar concentrations of (excess) MgATP alongside the AMPylation hyperactive and deAMPylation defective GST-FICD^{E234G} (see **Materials and Methods**). Despite the extensive (preparative) in vitro BiP AMPylation, no extra density (corresponding to even partial AMPylation) was identified on a relatively buried (and very well-resolved) BiP NBD residue Thr366, which has been suggested as an alternative BiP AMPylation site (Ham *et al*, 2014; Sanyal *et al*, 2015; Casey *et al*, 2017; Moehlman *et al*, 2018) (**Figure 2.4.2**). Furthermore, this alternative modification is observed (to an unknown degree) upon in vitro modification of the isolated NBD (Casey *et al*, 2017) and appears completely incompatible with the mode of intact BiP engagement by FICD, as crystallographically observed in this study.

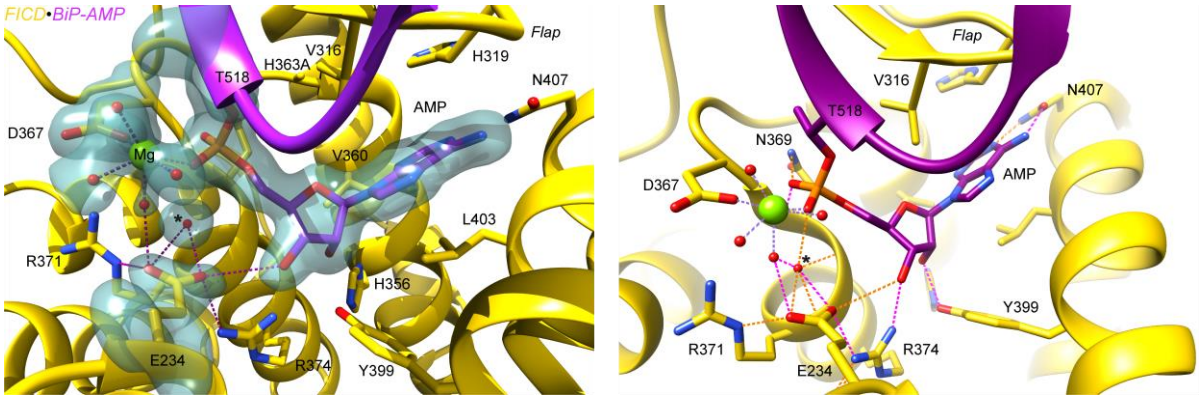

Figure 2.4.1: BiP's Thr518-AMP bound to FICD. Left, the arrangement of BiP's AMPylated Thr518 and Mg^{2+} cation within the Fic domain active site is shown. Thr518-AMP and important catalytic residues are overlaid with an unbiased polder OMIT electron density map (contoured at 4σ). All residues interacting with Mg^{2+} and the AMP moiety are shown as sticks and annotated (see **Figure 2.4.3**). Additionally, all potential hydrogen bonds formed by FICD's Glu234 side chain are depicted with pink dashed lines. The putative catalytic water, coordinated by Glu234 and located within the Fic domain oxyanion hole, is annotated with a *. The Mg^{2+} coordination complex is shown by blue dashed lines. **Right,** a slightly rotated and clipped view of the active site, shown on the left, with the electron density map omitted for clarity. In addition, all hydrogen bonds formed between FICD and the catalytic water* and BiP's Thr518-AMP are shown. Pink dashed lines represent strong hydrogen bonds, orange dashed lines are hydrogen bonds which only meet relaxed hydrogen bond criteria (in terms of angular range and/or distance).

The phosphate of Thr518-AMP is coordinated by a Mg^{2+} held in position by FICD's Asp367. A similarly-positioned Mg^{2+} coordinates the α and β phosphates of ADP in previous FICD structures and ATP in $FICD^{E234G}$ (Bunney *et al*, 2014). Moreover, the α-phosphate is also located within the Fic domain oxyanion hole, with coordination both from the main-chain amino group and side chain of FICD Asn369 (**Figure 2.4.1** [right] and **Figure 2.4.3**). The Fic domain oxyanion hole contributes towards the stabilisation of ATP's α and β phosphates in the AMPylating enzyme. In the context of deAMPylation it is likely that the location of the α-phosphate, being both coordinated by Mg^{2+} and localised within the oxyanion hole, stabilises the α-phosphate position and the extra negative charge development that occurs during the deAMPylation reaction. The resolved enzyme-substrate complex, therefore rationalises the observed dependence of FICD's deAMPylation reaction on divalent cations (with a preference for Mg^{2+}) (Veyron *et al*, 2019).

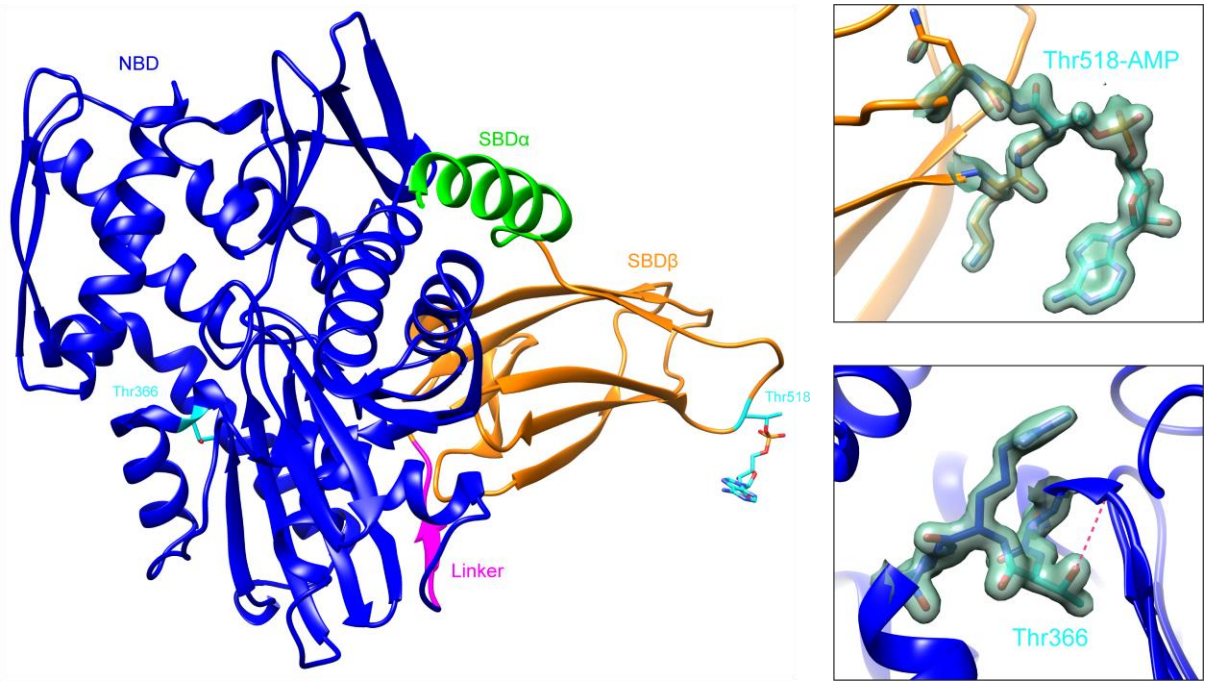

Figure 2.4.2: Electron density surrounding putative BiP AMPylation sites. **Left,** BiP-AMP from the deAMPylation complex, coloured and labelled by (sub)domain organisation. In addition, Thr518 within $\ell_{7,8}$ of the SBDβ and Thr366 within the BiP NBD are shown as sticks and coloured in cyan. Note, unlike Thr518, Thr366 is not a particularly solvent exposed residue within the isolated ATP-state BiP structure. **Right,** blow-ups of the highlighted residues with neighbouring amino acids also shown as sticks and overlaid with $2F_o$-F_c electron densities maps (contoured at 2σ). Note, there is no unaccounted-for electron density in the vicinity of the modelled Thr366 and Thr518-AMP residues. The hydroxyl group of Thr366 also forms a strong hydrogen-bond (pink dashed line) to the main-chain of its α-helix. The location of Thr366, a largely buried NBD residue within an α-helix, would appear to render this amino acid inaccessible for the intermolecular β-sheet engagement required for Fic domain-mediated AMPylation.

As in other crystal structures of isolated FICD bound to nucleotides (Bunney *et al*, 2014), the adenosine is bound in a hydrophobic pocket which is covered by the Fic flap domain. Indeed, residues Val316 and His319 of the latter form direct hydrophobic contacts to the adenine nucleobase (**Figure 2.4.1** and **Figure 2.4.3**). Moreover, a number of hydrogen bonds between the Fic domain and adenosine contribute to anchoring the AMP moiety (**Figure 2.4.1** [right] and **Figure 2.4.3**).

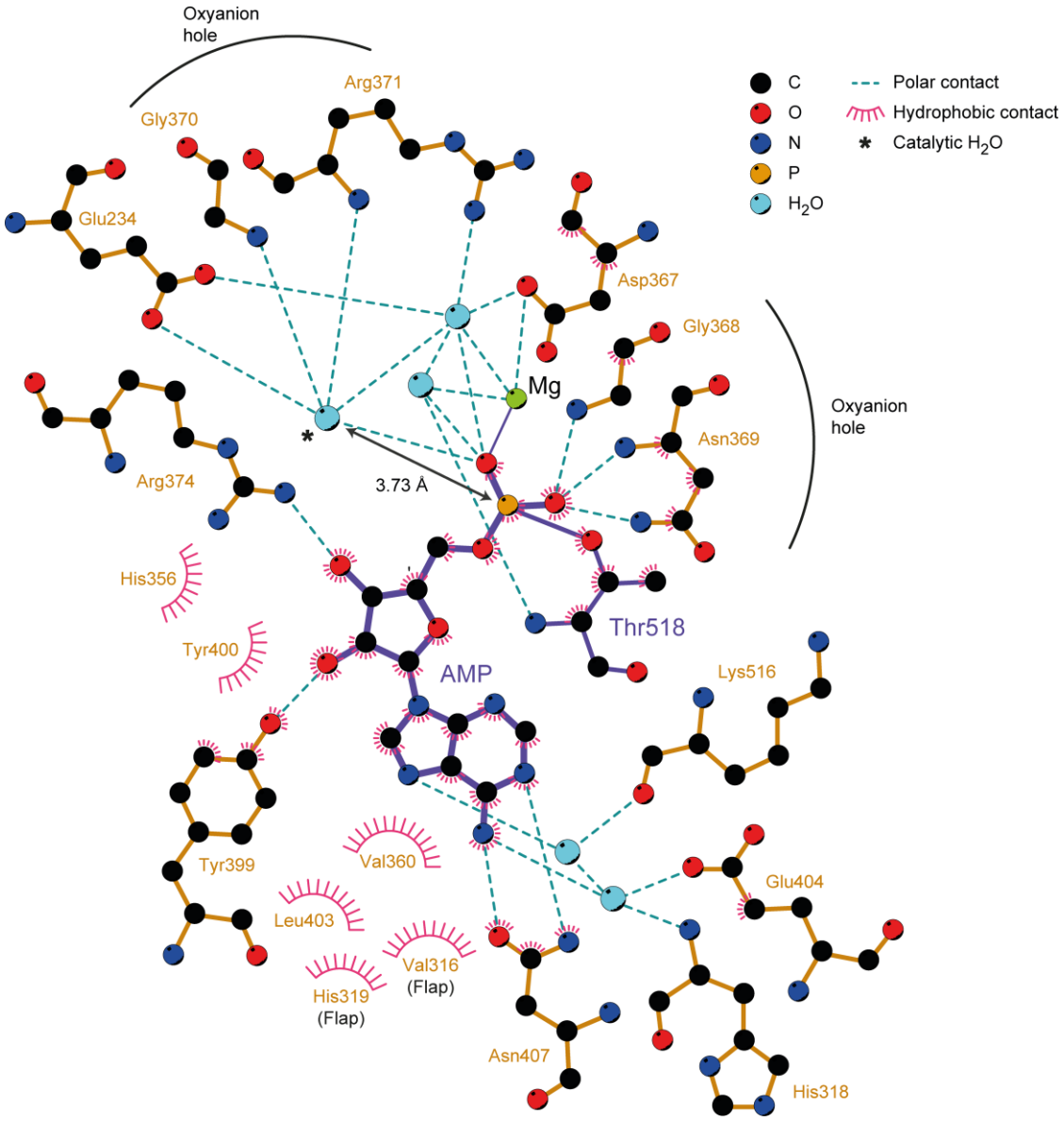

Figure 2.4.3: Intermolecular contacts between BiP's Thr518-AMP and FICD. All intermolecular contacts between BiP's Thr518-AMP, Mg^{2+} cation (green sphere) and FICD's catalytic Fic domain (from the state 1 deAMPylation crystal structure) are depicted (see **Figure 2.4.1**). Various Fic domain features and the distance between the putative catalytic water* and the AMP phosphorous atom (Pα) are also annotated. Note, the strong hydrogen bond schematised between FICD's Arg374 and the ribose 3'OH group (a Glu234 to ribose 3'OH hydrogen bond is not identified by LigPlot+, using default constraints). Also note, the lack of base in the vicinity of BiP's Thr518 Cα atom.

An anchimeric-assisted mode of deAMPylation (also known as neighbour group participation), could theoretically generate the observed products of deAMPylation — AMP and unmodified BiP (Preissler *et al*, 2017a). However, the aforementioned coordination of the α-phosphate and the binding mode of the adenosine region of the AMP moiety would make intramolecular cyclisation and nucleophilic attack (of the ribose 3'OH into the α-phosphate) improbable. This

unfavourable situation is further compounded by the fact that Thr518 is held in place by the intermolecular β-sheet formed between BiP's $\ell_{7,8}$ and the Fic domain flap. Moreover, aside from these steric considerations, an anchimeric-assisted deAMPylation reaction is also rendered infeasible on electrostatic grounds. Namely, the putative nucleophile (ribose 3'OH) only forms a very weak (3.44 Å and badly angled) hydrogen bond to FICD's Glu234 and forms a much stronger (2.94 Å) hydrogen bond to the side chain or Arg374 (**Figure 2.4.1** [right] and **Figure 2.4.3**). The latter will severely decrease the nucleophilicity of the 3'OH, which is also not within range of a potential base for 3'OH group deprotonation.

A similar argument can be made on structural and chemical grounds to dismiss an elimination reaction-based deAMPylation mode (which could also generate the observed deAMPylation products). That is to say, there is a lack of base within the vicinity of BiP's Thr518 Cα atom (**Figure 2.4.1** and **Figure 2.4.3**). Such a base would be required in order to carry out the proton abstraction necessary to catalyse an E1cB-type elimination reaction.

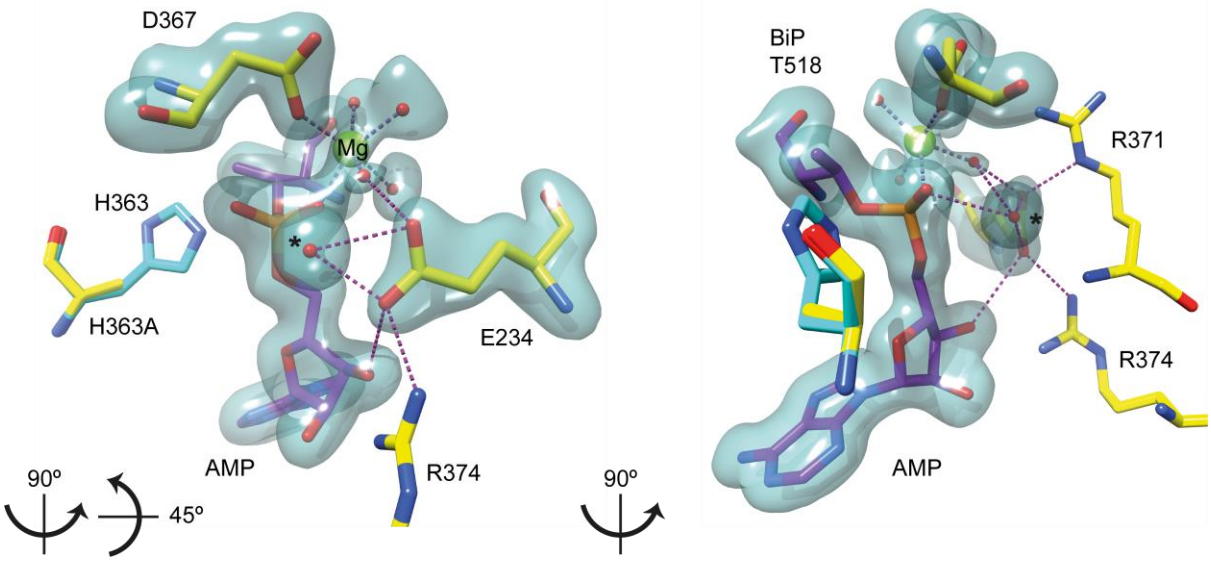

Figure 2.4.4: FICD's Glu234 coordinates a catalytic water molecule. A reduced active site view from the (state 1) deAMPylation complex, as in **Figure 2.4.1**. The same (4σ) polder OMIT map is displayed along with selected FICD residues (yellow) that contribute towards hydrolysis of BiP's AMPylated Thr518 (purple). The position of the catalytic water, which appears well-positioned for in line nucleophilic attack, is highlighted*. In addition, the putative general acid, FICD's His363, is modelled based on an alignment of the catalytically competent FICD structure PDB 6I7K (by residues 213–426 of the Fic domain). The view on the left is rotated relative to the left panel of **Figure 2.4.1**, approximately as indicated on the lower left-hand side, and displays the Pα-Oγ(Thr518) phosphodiester bond directly into and perpendicular to the plane of the page. The right panel displays an orthogonal view, with the phosphodiester bond parallel to the plane of the page. Pink dashed lines represent potential hydrogen bonds formed by Glu234 and also (in the right-hand side panel) the catalytic water.

Conversely, Glu234 (located atop the α_{inh}) tightly engages a water molecule within FICD's oxyanion hole (**Figure 2.4.1** and **Figure 2.4.3**). The aforementioned Glu234-coordinated water molecule sits almost directly in-line with the Pα-Oγ(Thr518) phosphodiester bond (**Figure 2.4.4**) and likely participates in catalysis. Moreover, the putative catalytic water-Pα distance observed in the deAMPylation complex crystal structure (3.73 Å; **Figure 2.4.3**) is consistent with this water's potentially nucleophilic role. For example, the attacking nucleophile (a serine oxygen atom) was found to be 3.86 Å from its target Pγ(ATP), in a quantum mechanically optimised model of reactants within the active site of protein kinase A (Valiev *et al*, 2003).

In **Figure 2.4.4** the active site is also modelled with a catalytic histidine from a catalytically competent FICD structure (PDB 6I7K), which was chosen on the basis of its very close similarity in Cα and Cβ position with the crystallographically observed His363Ala residue (also 0.45 Å RMSD over 214 Cα pairs of the Fic domain residues 213–426). The resulting deAMPylation complex active site structure is highly suggestive of an acido-basic hydrolytic mechanism of eukaryotic deAMPylation; with FICD's Nε2(His363) within comfortable hydrogen bonding distance (2.84 Å) of BiP's Oγ(Thr518) atom (**Figure 2.4.4**). In this hypothetical regime Glu234 aligns and activates a water molecule for an S_N2-type nucleophilic attack into the α-phosphate, with His363 positioned to facilitate a concerted protonation of the Thr518 alkoxide leaving group (generating unmodified BiP and AMP as observed experimentally (Preissler *et al*, 2017a)). As Glu234 is also forms salt bridges with FICD's Arg371 and Arg374 (**Figure 2.4.1** and **Figure 2.4.4**), it would seem unlikely that it would also be able to act as a general base in the above reaction scheme. Indeed, based on the crystal structure of monomeric $FICD^{L258D}$:Apo (PDB 6I7J), the pK_a of Glu234 is estimated to be depressed from an intrinsic value of 4.4 down to 3.0 [calculated using the Rosetta pK_a server (Kilambi & Gray, 2012; Lyskov *et al*, 2013)]. In the case of a number of protein kinases that contain a catalytic aspartate (which also has a low pK_a), quantum mechanical and molecular mechanical computational techniques have identified a role for the conserved aspartate as a catalytic (but not a general) base. The catalytic aspartate is thought to accept the attacking hydroxyl group proton at a late stage of the phosphorylation reaction, after the formation of the transition state (Valiev *et al*, 2003; Cheng *et al*, 2005). Such a role, as a late-stage proton trap, may also be played by FICD's Glu234.

Chapter 2.5: Conclusions

Through a structure-led approach I have demonstrated (by X-ray crystallography and SANS) that both monomeric and dimeric FICD proteins engage AMPylated BiP in a bivalent fashion: utilising both the catalytic Fic domain and the FICD(TPR) domain. The former engages the target residue region of BiP-AMP, principally via an intermolecular β-sheet formed between the Fic domain flap and BiP's SBDβ $\ell_{7,8}$. Such an interaction was anticipated based on the identified location of BiP AMPylation [Thr518 within $\ell_{7,8}$ (Preissler *et al*, 2015b)] and the previously observed sequence independent mechanism of Fic-target recognition, afforded by the flap region of other Fic proteins for their AMPylation substrates or pseudo-substrates (Xiao *et al*, 2010; Goepfert *et al*, 2013).

Conversely, the role of FICD's TPR domain is specific to the enzyme-substrate relationship of FICD and BiP. The crystal structure of a trapped heterodimeric deAMPylation complex, resolved in great detail the ability of FICD's TPR1 motif to bind a tripartite BiP surface composed of its NBD, interdomain linker and SBDβ. Solution structure analysis validated the overall conclusions derived from the heterodimeric crystal structure, in the context of a heterotetrameric deAMPylation complex with dimeric FICD at its core, and also hinted at the presence of increased intra-TPR domain flexibility and inter-domain flexibility existing in solution.

Furthermore, mutational analysis highlighted the sensitivity of deAMPylation complex assembly and BiP-AMP deAMPylation ability, to the disruption of specific FICD(TPR1)-BiP intermolecular contacts. Here, again, between monomeric and dimeric FICD the conserved mode of BiP-AMP engagement was highlighted. Moreover, catalysis of FICD-mediated deAMPylation (but not substrate binding) was also perturbed by the disruption of intramolecular contacts between FICD's TPR domain and catalytic domain.

Finally, the crystal structure presented in this work provides strong support for a mechanism of eukaryotic deAMPylation that is acido-basic in nature, rationalising the essential role of FICD's Glu234 in facilitating deAMPylation of BiP (Preissler *et al*, 2017a). It can be inferred that Glu234 serves to align a catalytic water molecule in-line for nucleophilic attack into α-phosphate of Thr518-AMP (**Figure 2.5.1**). Moreover, this acidic residue may act as a catalytic base, through a mechanism involving late proton transfer analogous to the role played by the catalytic aspartates of some protein kinases (Valiev *et al*, 2003; Cheng *et al*, 2005). The proposed deAMPylation mechanism (which also rationalises the essential role for a divalent

cations and FICD's His363) is far removed from the binuclear metal-catalysed reactions catalysed by the other two known (bacterial) deAMPylases (Xu *et al*, 2010; Chen *et al*, 2013).

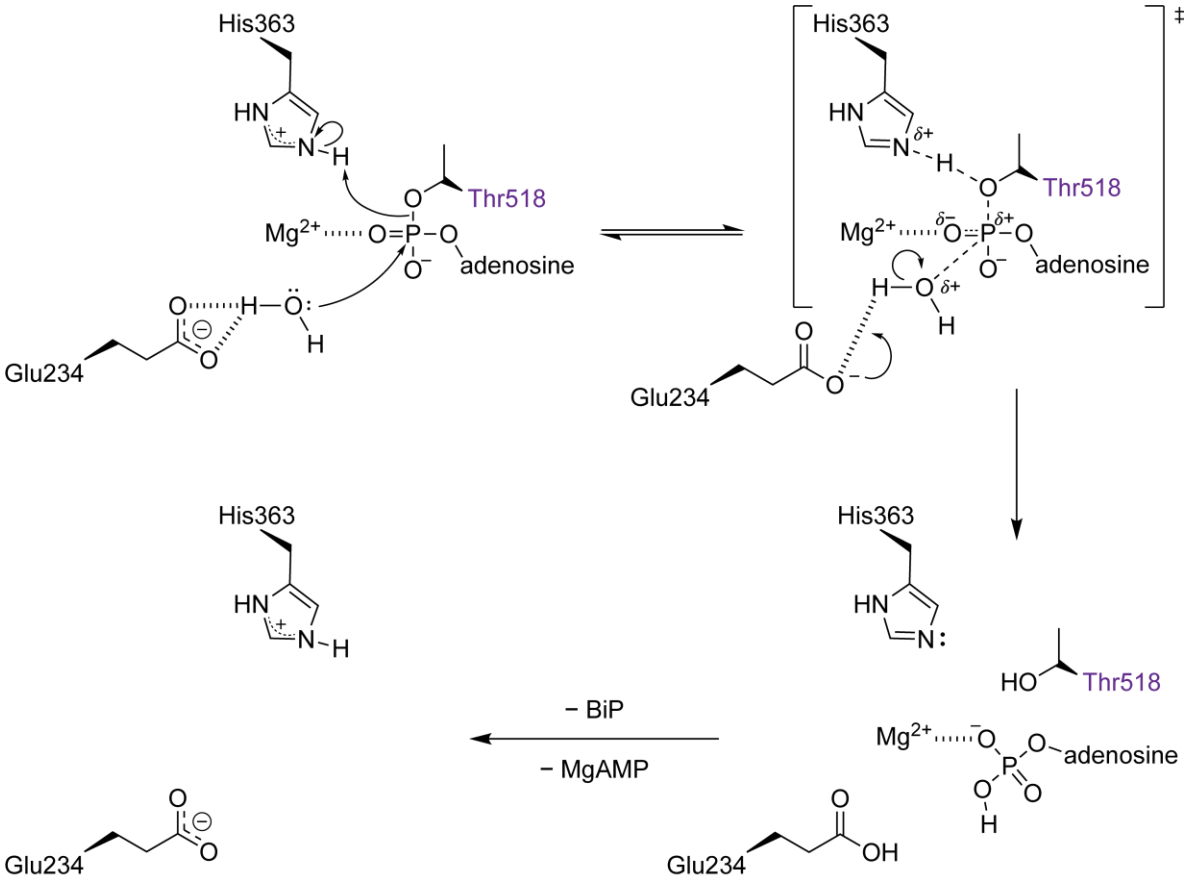

Figure 2.5.1: Proposed hydrolytic BiP deAMPylation mechanism. FICD's Glu234 activates and aligns a catalytic water molecule for in-line nucleophilic attack into the backside of AMPylated BiP's Pα-Oγ(Thr518) phosphodiester bond. The α-phosphate group coordination by Mg^{2+}, and localisation within FICD's electron withdrawing oxyanion hold (**Figure 2.4.1** and **Figure 2.4.3**), stabilises the position of Pα and increases its electrophilicity. His363 can exist in either a protonated or deprotonated state. The former is required for deAMPylation and is shown. The reaction likely proceeds via a nucleophilic S_N2-type pathway with concerted protonation of BiP's Thr518 alkoxide leaving group (catalysed by FICD's His363 acting as a general acid). A potential role for FICD's Glu234 acting as a catalytic (but not general) base, accepting a proton from the nucleophilic water at a late stage of the reaction after formation of the pentacoordinate transition state (‡), is shown. Glu234 acting as a proton trap is consistent with its interaction with Fic motif Arg371 and Arg374 (not shown), which will depress its pK_a. The schematised hydrolytic reaction generates BiP (with an unmodified Thr518) and AMP. Following product release Glu234 and His363 could facilely exchange protons with the solvent to regenerate the original FICD active site. Ionic or hydrogen bond interactions are denoted with hashed lines, dashed lines represent partial covalent bonds and partial charges are indicated by δ. BiP's Thr518 residue is annotated in purple.

As a bacterial Fic protein (EfFic) has also been observed to possess gatekeeper glutamate-dependent deAMPylation activity (Veyron *et al*, 2019), it is likely that the mechanism of deAMPylation outlined above is conserved across this class of proteins. Furthermore, other mechanisms of phosphodiester bond cleavage, including anchimeric assistance or an E1cB-type elimination reaction, which are capable of generating the products of FICD-mediated deAMPylation (AMP and unmodified BiP), are also rendered extremely unlikely by the resolved structure of the deAMPylation complex.

This body of work clarifies the mechanism of eukaryotic deAMPylation which, at the time of writing, is only exemplified by FICD. Notably, the disparate enzymatic mechanisms attributed to the two previously identified (bacterial) deAMPylators were both inferred based on the known products of their catalysed deAMPylation reactions and by similarity with enzymatic mechanisms defined in the context of evolutionarily related enzymes (Xu *et al*, 2010; Chen *et al*, 2013). Therefore, to the best of my knowledge the structures presented here represent the only deAMPylation (enzyme-substrate) complex structures yet solved. The unique FICD•BiP-AMP complex, elucidated here, also provides intriguing clues towards understanding the nature of FICD substrate engagement in the context of BiP AMPylation.

Chapter 3: FICD's TPR domain recognises the ATP-state of unmodified BiP

Chapter 3.1: The engagement of FICD and BiP-AMP is incompatible with the ADP-state of BiP

The importance of contacts between FICD's TPR domain and BiP to deAMPylation, demonstrated above, explains previous observations that the isolated AMPylated BiP SBD is refractory to FICD-mediated deAMPylation (Preissler *et al*, 2017a). It is noteworthy that FICD also specifically binds (**Figure 2.3.1**) and AMPylates ATP-state BiP with a preference for more domain-docked BiP mutants and fails to AMPylate the isolated BiP SBD (produced by SubA proteolysis of the interdomain linker of AMPylated intact BiP; Preissler *et al*, 2015b). Furthermore, the observation that FICD's interaction with unmodified BiP:ATP was abrogated by TPR1 deletion (**Figure 2.3.2**) hints at the possibility that FICD recognises the domain-docked ATP-state of unmodified BiP (for AMPylation) in a similar fashion to ATP-state biased BiP-AMP (for deAMPylation).

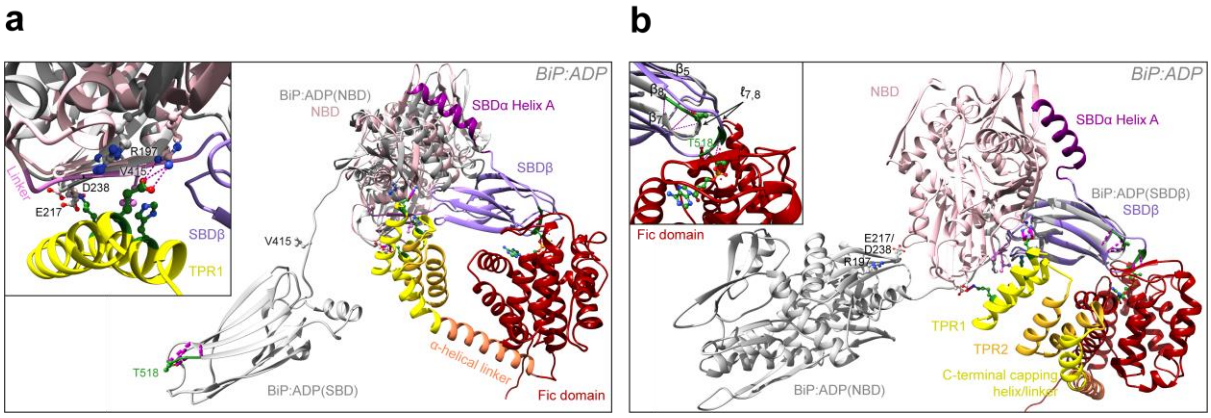

Figure 3.1.1: FICD binds the ATP-state of BiP. The deAMPylation complex (coloured as in **Figure 2.1.3** with subdomains labelled) is aligned via its NBD (**a**) or SBDβ (**b**) with an ADP-state BiP (PDB 7A4U; grey). As in **Figure 2.1.3** the TPR1 mutants mutated in this study are shown with ball and stick representation and coloured in green. The respective BiP interacting partners are also shown, labelled and coloured according to their subdomain localisation (in the deAMPylation complex structure) and grey in the BiP:ADP structure. **a,** Inset, a closeup view of FICD(TPR1)-BiP(NBD) contacts. Changes in NBD conformation (from ATP to ADP-state) would disrupt the intermolecular contacts present in the deAMPylation structure. **b**, The intermolecular β-sheet region of $\ell_{7,8}$ (highlighted in green) is shortened in ADP-state BiP. Inset, disposition of Thr518 is highlighted. In the BiP:ADP structure the shortened $\ell_{7,8}$ forms an intramolecular hydrogen bond network which includes the Thr518 hydroxyl group — making this region inaccessible for intermolecular interaction with the catalytic Fic domain (pink lines; hydrogen bonds).

Structures of unmodified BiP indicate that a domain-undocked ADP-state BiP loses the tripartite NBD-linker-SBDβ surface that is recognised by FICD's TPR1 motif in the context of deAMPylation (**Figure 3.1.1**). Furthermore, even if FICD were able to bind the NBD or the $\ell_{7,8}$ SBDβ region (which also becomes less accessible in BiP's ADP-state) of a nucleotide-free (apo) or ADP-bound BiP, the Hsp70's heavy bias towards the domain-undocked conformation (Marcinowski *et al*, 2011; Wieteska *et al*, 2017) would render engagement of the other FICD-BiP interaction surface unlikely (**Figure 3.1.1**).

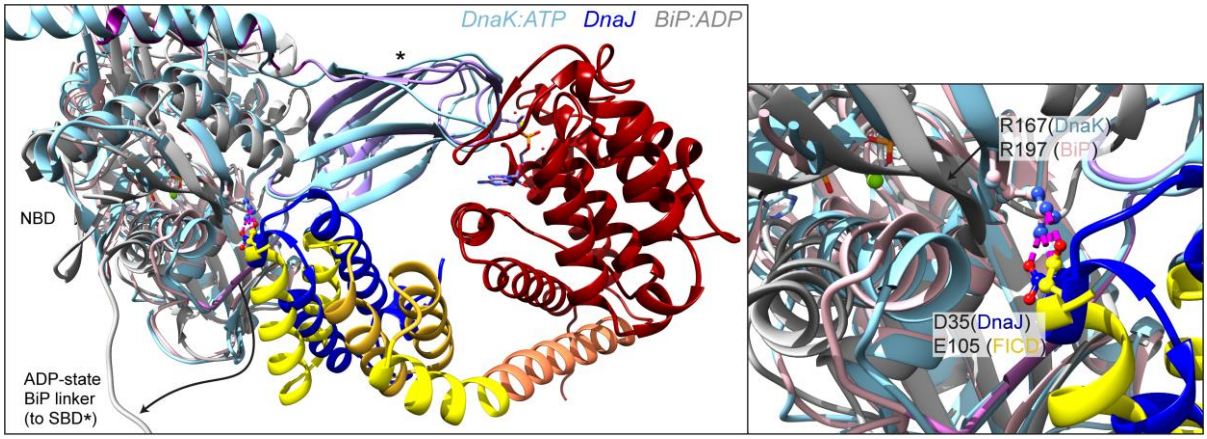

Figure 3.1.2: FICD's TPR domain and the J-domain recognise similar ATP state–specific Hsp70 surfaces. All structures are aligned via the Hsp70 NBD. The deAMPylation complex and BiP:ADP are coloured as in **Figure 3.1.1**. In addition, the DnaK:ATP•DnaJ cocrystal structure (PDB 5NRO) is also superposed (coloured in light and dark blue, respectively). The former displays excellent agreement with the ATP-state BiP from the deAMPylation complex. The JDP binds in a similar location to FICD's TPR1, with both molecules recognising an Hsp70 ATP state–specific, tripartite surface of NBD-linker-SBDβ. Blow-up, right-hand side, the aspartate of the characteristic and ubiquitously conserved J-domain 'HPD' motif is shown with its DnaK interaction partner (Arg167); this contact is conserved in all JDP-Hsp70 interactions. The same salt bridge is mimicked in the FICD(TPR1)-BiP(NBD) interaction, shown. Upon ATP hydrolysis, conformational changes in the NBD of an unmodified BiP (grey), including in the NBD β-sheet bearing BiP's Arg197 (arrow) will disrupt the FICD(TPR1)-BiP(NBD) contacts. Note, the curly arrow depicts the undocking of the BiP linker upon BiP ATP- to ADP-state transition.

These alignments suggest that the FICD's TPR1 motif recognises an ATP-state specific Hsp70 surface in order to catalyse deAMPylation. If this mode of binding was also common to a pre-AMPylation complex and was, therefore, also required for the engagement of FICD with unmodified BiP for AMPylation, this would rationalise the observed selectivity of FICD for the ATP-state of unmodified BiP. Indeed, the tripartite Hsp70 surface by which FICD's TPR1 motif is observed to engage BiP-AMP is in the same Hsp70 region known to be engaged by J-domain proteins (JDPs) (**Figure 3.1.2**). Like FICD (in the context of AMPylation) JDPs also

specifically engage ATP-state Hsp70s (Kityk *et al*, 2017; Preissler *et al*, 2017b) — suggesting a possible convergent evolution towards a similar mechanism of ATP state–specific Hsp70 recognition.

Chapter 3.2: FICD's TPR domain is essential for AMPylation complex assembly

In order to test the hypothesis that FICD's TPR domain may also be responsible for the engagement of unmodified BiP and thus in the formation of a (pre-)AMPylation complex, we returned to the BLI setup of **Figure 2.3.4**. In this instance, rather than BiP-AMP being immobilised on the biosensor, ATP-bound unmodified BiP was used as a ligand (see **Figure 2.3.3d** for a schematised methodological comparison). In this context the effect of TPR1 motif mutations on (catalytically dead) FICD binding were magnified relative to their effect on the deAMPylation complex (**Figure 3.2.1**, and for comparison **Figure 2.3.4**). This is consistent with the absence of a covalently BiP-linked AMP moiety engaging FICD's active site. This absence would increase the relative contribution of (wild type) TPR-BiP contacts to the net interaction across the entire complex.

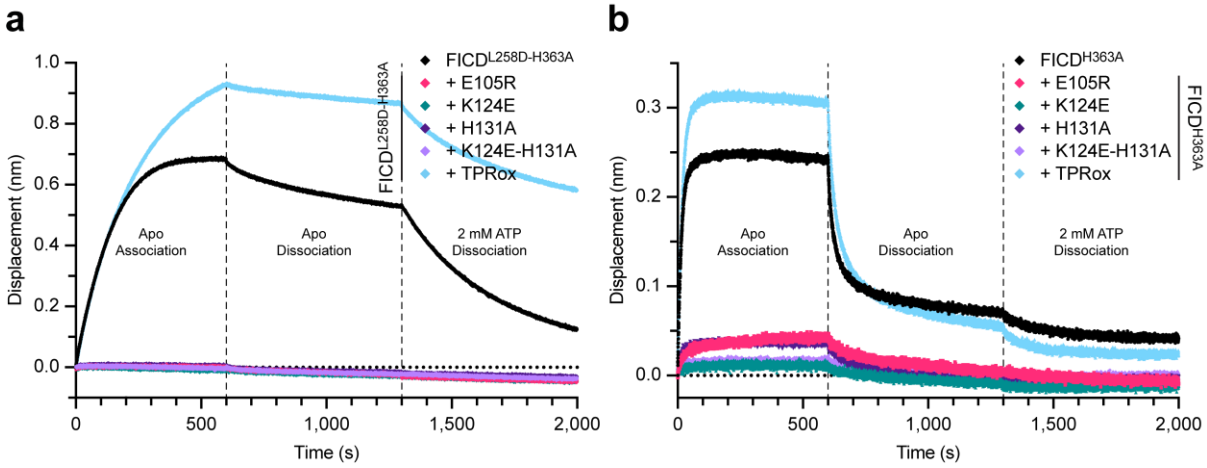

Figure 3.2.1: FICD's TPR domain is essential for recognition of unmodified BiP. Representative BLI analysis of TPR domain mutants of monomeric (**a**) and dimeric (**b**) FICD binding to immobilised ATP-bound BiP, from n = 3 independent experiments. This BLI experiment is a parallel to those conducted with BiP-AMP:ATP as an immobilised ligand in **Figure 2.3.4**. The ability of FICD to bind BiP:ATP is very sensitive to mutations in contacting FICD(TPR1) residues. Note, that disruption of the intramolecular FICD contact (TPRox) appears to increase the affinity for BiP:ATP, especially enhancing monomeric FICD$^{L258D-H363A}$ association and slowing its dissociation. Also, consistent with **Figure 2.3.2**, monomeric FICD$^{L258D-H363A}$ binds more tightly to the BiP:ATP ligand (resulting in a greater binding displacement) than dimeric FICD^{H363A}.

It should be noted that, in a parallel to the analysis of FICD variants binding to an AMPylated BiP ligand (**Figure 2.3.4**), disruption of an intramolecular (interdomain) contact between FICD's TPR and Fic domain (whilst locking the TPR domain in a TPR-in conformation compatible with the observed BiP-AMP binding mode; TPRox), appears to increase the affinity of both monomeric and dimeric FICD for unmodified BiP:ATP (**Figure 3.2.1**). As in the case of BiP-AMP:ATP binding, the ability of TPR domain oxidation to stimulate FICD binding is much more pronounced for monomeric FICD (**Figure 3.2.1a**). This (again) suggests that the effects of TPR domain stabilisation (by disulphide stapling) may, in the context of an otherwise more dynamic monomeric FICD(TPR) domain, outweigh the effects of disrupting FICD interdomain communication. Conversely, in the context of a potentially less dynamic TPR domain within dimeric FICD, upon TPR oxidation a more subtle effect on binding kinetics and increased FICD dissociation rates are observed (**Figure 3.2.1b**).

Chapter 3.3: In vitro and in vivo BiP AMPylation is dependent on FICD's TPR domain

In order to assess the role of FICD's TPR domain in catalysing in vitro AMPylation, in an analogous fashion to the FP-derived in vitro deAMPylation assay (**Figure 2.3.6** and **Figure 2.3.7**), the utility of fluorescent FAM-labelled nucleotide analogues was once again harnessed. Moreover, as previously characterised in the context of vitro AMPylation reactions using [α-^{32}P]-ATP (Perera *et al*, 2019), the assay presented here also benefited from the addition of an excess (7.5 µM) constitutively dimeric and catalytically dead (disulphide-linked) FICD ($_{S\text{-}S}$FICD$^{A252C\text{-}H363A\text{-}C421S}$; trap). This trap binds BiP-AMP for a prolonged period of time and thereby inhibits its deAMPylation by the catalytically (and deAMPylation) competent FICD under investigation. By providing 10 µM ATP(FAM) as the sole nucleotide, with 5 µM BiP and 0.5 µM (catalytically competent) monomeric FICD^{L258D} (the same concentration of substrate and enzyme that was used in the in vitro deAMPylation assay) it was found that the AMPylation reaction progress was linear over an extended time period (**Figure 3.3.1a–b**). Importantly, at the 1 h time point selected for endpoint measurement of the various FICD variants (**Figure 3.3.1c**), the amount of accumulated BiP-AMP is directly proportional to the initial rate of FICD^{L258D}-mediated AMPylation. It should also be noted that the difference in BiP AMPylation between overnight incubation of the AMPylation reaction at 4 and 20 °C, reflects the increased rate of BiP-AMP trap escape and deAMPylation (as evidenced by the

conspicuous increase in free AMP(FAM) nucleotide analogue resolved in **Figure 3.3.1b**). Moreover, BiP-AMP (presumably on account of being a specific FICD deAMPylation substrate) is much more sensitive to FICD-mediated deAMPylation than the (much less efficiently accrued) FICD autoAMPylation signal (**Figure 3.3.1a**).

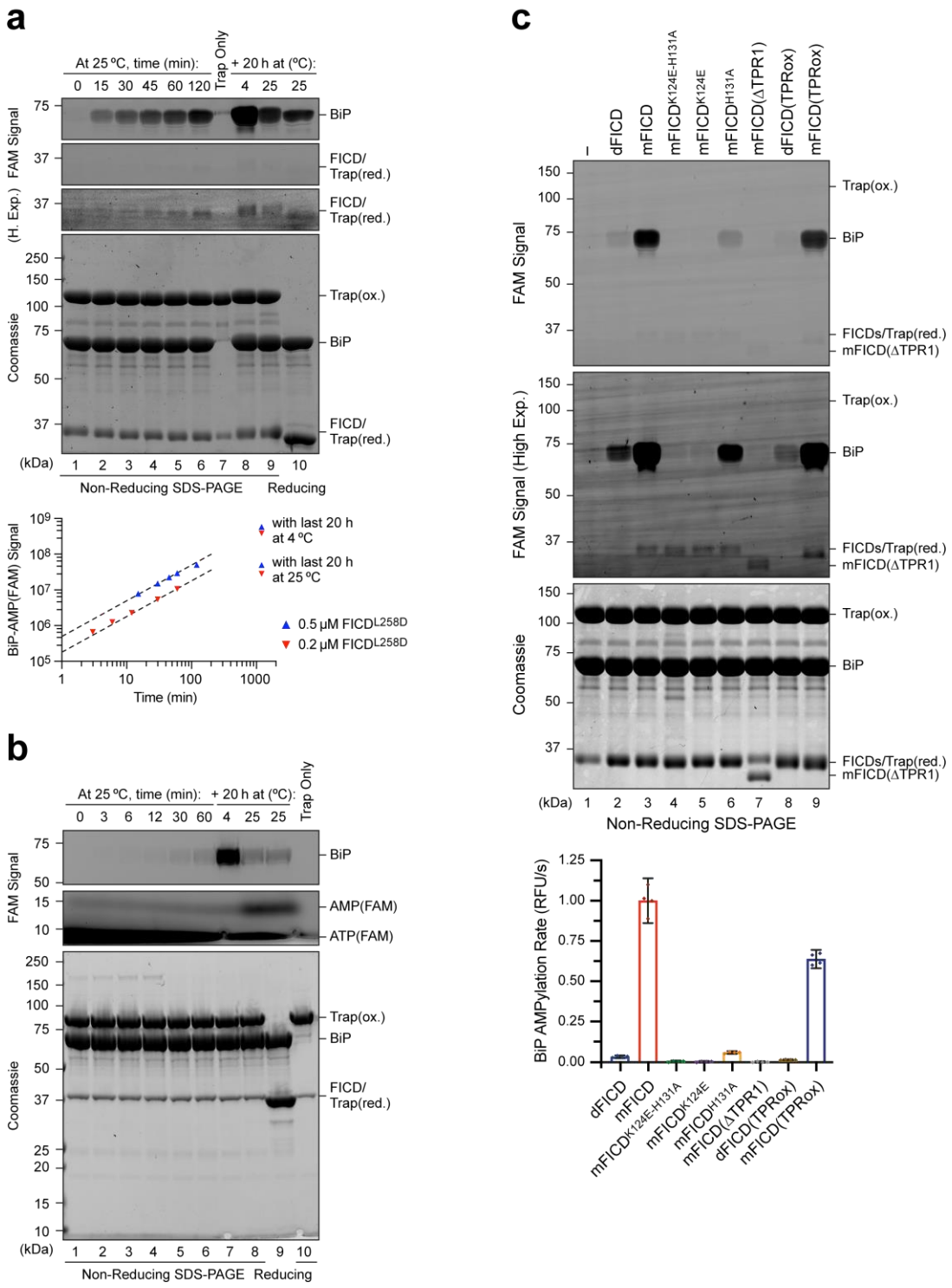

Figure 3.3.1: FICD(TPR1) mutation impairs in vitro AMPylation. Fluorescence and Coomassie gel images of in vitro AMPylation assays utilising ATP(FAM) as an AMPylation co-substrate, in the presence of excess

product trap (Trap(ox)) to discourage BiP-AMP(FAM) deAMPylation. **a,** Representative FICD^{L258D} (0.5 μM) BiP-AMPylation time course with quantification of two independent experiments (dashed lines; directly proportional fits). Proteins were resolved using a 10% SDS-PAGE gel. **b,** The FICD^{L258D} (0.2 μM) BiP-AMPylation time course that is also quantified in **a**. Using a 4–12% SDS-PAGE gel, free AMP(FAM) nucleotides can be resolved from the gel front (which contains a large amount of excess ATP(FAM)). Note, the increased AMP(FAM) production upon 25 °C overnight incubation of the AMPylation reaction, relative to the same reaction incubated at 4 °C (lane 8 [non-reducing SDS-PAGE] or lane 9 [reducing SDS-PAGE] versus lane 7). **c,** An in vitro AMPylation assay analysing the effects of deleting the TPR1 motif (ΔTPR1), mutating TPR1 motif residues or perturbing FICD intramolecular contacts (TPRox). All FICD perturbations cause significant depreciations in the rate of AMPylation catalysed by both dimeric FICD (dFICD) and monomeric FICD^{L258D} (mFICD). A gel from a representative experiment is shown with the initial rates (mean ± 95% CI) of BiP-AMPylation (in relative fluorescent units/s normalised to the rate of FICD^{L258D}-mediated BiP AMPylation), from n = 4 independent experiments. Note, the lack of correlation between FICD (*cis*)autoAMPylation and BiP substrate AMPylation visible in the high exposure (High Exp.) fluorescence gel image.

As previously observed, using trace amounts of [α-^{32}P]-ATP with ATP and by monitoring BiP-AMP production by autoradiograph (Perera *et al*, 2019), monomerisation of FICD resulted in a considerable BiP AMPylation rate enhancement — 32-fold in this instance (**Figure 3.3.1c**). Moreover, in agreement with the observed deleterious effects on pre-AMPylation complex affinity afforded by FICD(TPR1) mutations, loss of TPR-BiP contacts also impaired BiP AMPylation by monomeric FICD in vitro (**Figure 3.3.1c**). That is to say, surface mutations in TPR1 and deletion of the TPR1 motif paralleled the effects of these mutations on deAMPylation complex assembly and in vitro deAMPylation activity (**Figure 2.3.4–Figure 2.3.7**). Of note, impairment of interdomain (TPR-Fic) communication by TPR oxidation, although stabilising the pre-AMPylation complex of monomeric FICD and BiP:ATP (**Figure 3.2.1**), decreased the in vitro AMPylation rate of both monomeric and dimeric FICD (**Figure 3.3.1c**). This is consistent with a role for TPR to Fic domain communication in contributing both towards deAMPylation and AMPylation turnover number (k_{cat}).

It should also be noted that **Figure 3.3.1c** nicely illustrates that monomeric FICD^{L258D} (and derivates thereof) have a strong preference for (*cis*)autoAMPylation. It has previously been demonstrated that FICD^{E234G} can catalyse (*trans*)autoAMPylation (Bunney *et al*, 2014). However, the observation that the high concentration and very large molar excess of catalytically dead trap FICD (over catalytically active FICD) is almost imperceptibly modified, suggests (*trans*)autoAMPylation is a much less likely outcome relative to the *cis* reaction.

Furthermore, as previously observed (Perera *et al*, 2019), monomerisation does increase FICD autoAMPylation activity. Although, importantly, this experiment also demonstrates that amongst variants of monomeric FICD^{L258D} there is no correlation between (specific) AMPylation activity towards BiP and FICD (*cis*)autoAMPylation. In fact, in the case of TPR1 removal (ΔTPR1) and TPR domain oxidation (TPRox), (*cis*)autoAMPylation and BiP-AMPylation levels appear anti-correlative — with these FICD modifications resulting in increased autoAMPylation whilst simultaneously drastically reducing the rate of BiP AMPylation (**Figure 3.3.1c**).

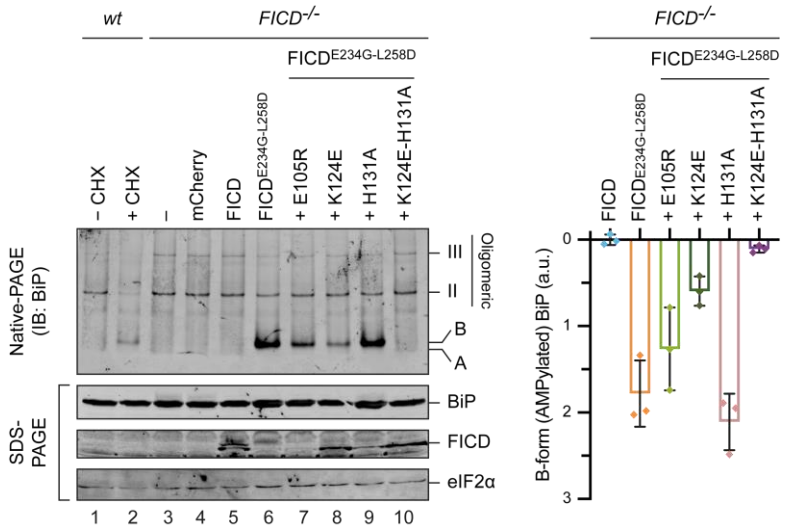

Figure 3.3.2: TPR1 mutated FICDs are deficient in their ability to promote a pool of AMPylated BiP in cells. Representative native-PAGE immunoblot analysis of the accumulation of AMPylated (B-form) BiP in *FICD*$^{-/-}$ CHO cells transfected with FICD variants, as indicated. Major non-AMPylated BiP species (monomeric A, dimeric II and trimeric III) are also annotated. Right, quantification of AMPylated B-form BiP from n = 3 independent experiments (mean ± SD). The eIF2α immunoblot acts as a loading control. Note the inverse relationship between the FICD expression levels and the ability of each respective FICD variant to catalyse BiP AMPylation.

To further corroborate the role of FICD's TPR domain in facilitating AMPylation we sought to test the effect of FICD(TPR1) mutations on in vivo BiP AMPylation. In agreement with previous studies (Preissler *et al*, 2017a) overexpression of wild type dimeric FICD into CHO cells lacking endogenous FICD (*FICD*$^{-/-}$) did not induce the accumulation of BiP-AMP (which migrates as the B-form of monomeric BiP on a native-PAGE gel) (**Figure 3.3.2**). Conversely, transient expression of an AMPylation unrestrained and deAMPylation defective, monomeric FICD$^{E234G-L258D}$ induced large amounts of BiP-AMP accumulation. Levels of AMPylated BiP, detected by its mobility on native-PAGE, were significantly lower in cells targeted with the

FICD$^{K124E-E234G-L258D}$ and FICD$^{K124E-H131A-E234G-L258D}$ TPR1 mutations (**Figure 3.3.2**). Moreover, the higher levels of expression of the TPR1 mutant FICDs (compared to FICD$^{E234G-L258D}$) is consistent with previous observations of FICD expression levels inversely correlating with the variant's AMPylation activity (within transiently transfected *FICD*$^{-/-}$ cells) (Perera *et al*, 2019). The lesser effect of His131Ala corresponds with the fact that this mutation exhibited the least effect of any tested TPR1 mutation with respect to in vitro complex assembly and AMPylation (**Figure 3.3.2**).

The nature of the above assay is quite crude, in that it relies on analysing the lysate from the entire cell population (which includes both transfected and untransfected cells). Overexpression of FICD$^{E234G-L258D}$ in *FICD*$^{-/-}$ cells is documented to cause a considerable amount of ER stress and possibly, as a result, cell death (Perera *et al*, 2019). Moreover, overexpression of FICD^{E234G} in *FICD*$^{-/-}$ cells, which causes a similar amount of ER stress and in vivo BiP-AMP accumulation to FICD$^{E234G-L258D}$ (Perera *et al*, 2019), has also been observed to reduce cell colony outgrowth (Preissler *et al*, 2017a). It is therefore likely that the above strategy for quantifying in vivo AMPylation of BiP underestimates the effect of FICD(TPR1) mutation (by underrepresenting the AMPylation induced by FICD$^{E234G-L258D}$).

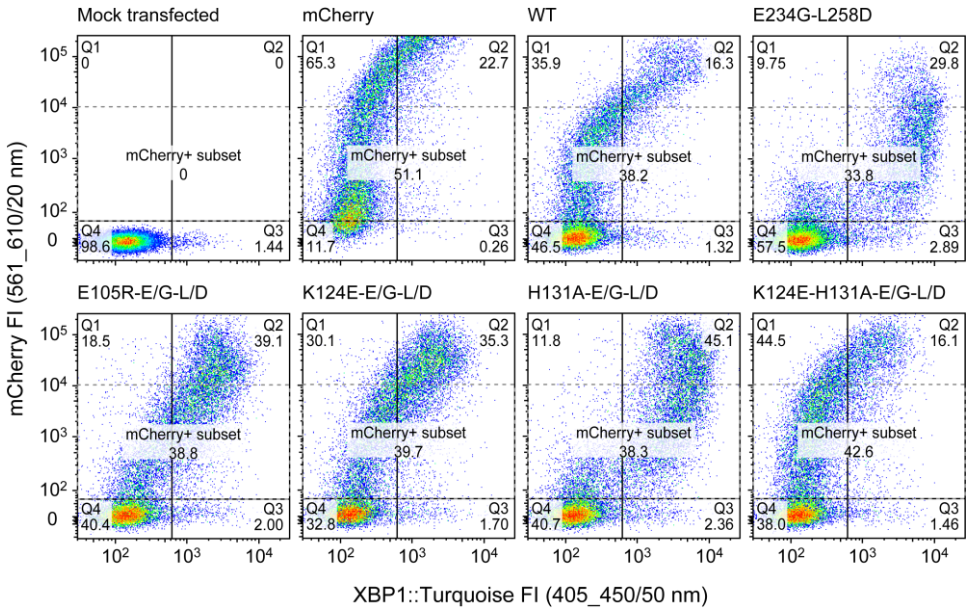

Figure 3.3.3: Dot-plot from FACS-based in vivo AMPylation assay. A representative dot-plot from n = 4 independent experiments. The mCherry signal acts as a transfection marker, being expressed in *trans* from the same plasmid as the transiently expressed FICD constructs (in *FICD*$^{-/-}$ CHO cells). Cells with mCherry+ signal $\leq 10^4$ were gated, thus eliminating the distorting effects of very high FICD and/or mCherry expression on the XBP1::Turquoise signal (an ER stress reporter). The gated mCherry+ subset is further analysed in **Figure 3.3.4**. Cell population quadrant percentages are also annotated. FI, fluorescence intensity.

In order to circumvent these technical issues, and to provide a more quantitative means of assessing the effects of TPR1 motif mutations on in vivo AMPylation, the ability for FICD-mediated BiP AMPylation to induce ER stress was exploited in an orthogonal flow cytometry-based assay (**Figure 3.3.3**).

As previously observed, overexpression of FICD$^{E234G-L258D}$, but not wild type FICD, induced considerable ER stress (as indicated by the XBP1::Turquoise ER stress reporter signal). From this more nuanced analysis of single, live and transfected cells, it is clear that the majority of FICD(TPR1) mutations reduce the percentage of cells undergoing ER stress (**Figure 3.3.4**). In instances where the decrease in the proportion of stressed cells is less obvious (Glu105Arg, His131Ala), it is obvious both from the representative histogram and from the quantification of the high stress median values that the severity of ER stress is reduced within the 'high stress' cell population (**Figure 3.3.4**). Moreover, the UPR reporter activity induced by various TPR1 mutant FICD derivatives correlated well with the hierarch of the mutations' effects on BiP binding (**Figure 2.3.4**).

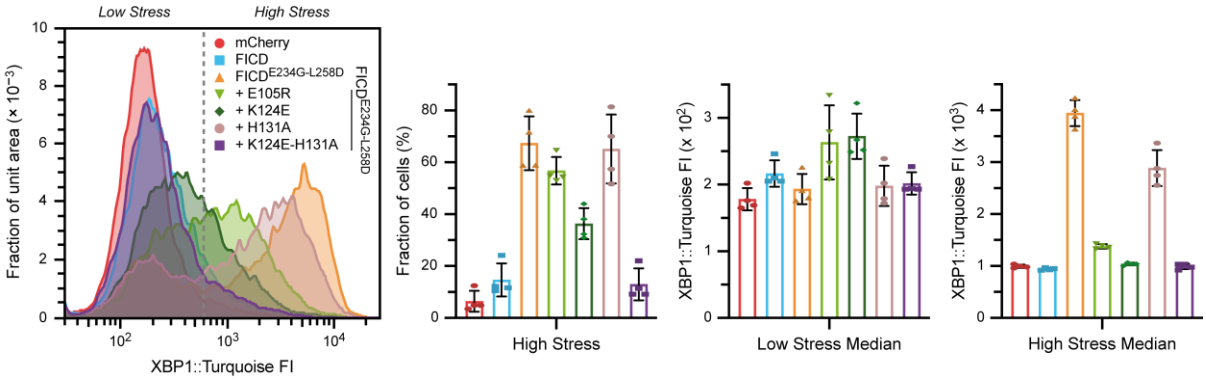

Figure 3.3.4: FICD(TPR1) mutations reduce BiP AMPylation-induced ER stress. Representative FACS histograms of the XBP1::Turquoise UPR reporter signal levels, in *FICD*$^{-/-}$ CHO cells expressing the indicated FICD derivatives. The overall histogram areas (derived from the respective mCherry+ subpopulations annotated in the representative **Figure 3.3.3** dot-plot) are each normalised to an arbitrary unit area. Note, the bimodal distribution of the fluorescent signal in FICD-transfected cells. Quantification of the fraction of cells that are stressed (XBP1::Turquoise fluorescent intensity > 600 fluorescent units; vertical dashed line), as well as the median FACS signal of the low and high stressed cell populations are shown from n = 4 independent experiments (mean values ± SD). Bars and datapoints are (colour) coded according to the histogram legend.

Chapter 3.4: Conclusions

Together, these observations parallel the effects of TPR1 mutations which were crystallographically predicted and experimentally demonstrated to affect deAMPylation complex assembly and deAMPylation activity. The same deAMPylation affecting FICD(TPR1) mutations robustly enfeebled pre-AMPylation complex assembly, in vitro AMPylation and in vivo AMPylation of BiP. This coherent ensemble of data leads me to conclude that TPR surface mutations in residues that contact BiP in the deAMPylation complex also contribute to enzyme-substrate interaction during FICD-mediated AMPylation.

This finding rationalises the observed selectivity possessed by FICD for AMPylating and binding to ATP-state BiP and provides a plausible and relatively intuitive mechanism for substrate-level regulation of BiP AMPylation in vivo. By this token, changes in unfolded protein load within the ER are transduced into changing levels of BiP AMPylation by the former binding to BiP's SBD and titrating these BiP species away from the ATP-state and into the ADP-state. The latter state is incompatible with the mode of FICD•BiP interaction (**Figure 3.1.1**) and thus not a substrate for FICD-mediated AMPylation. This mechanism of substrate-level regulation explains the residual response to cycloheximide treatment (in terms of a further increase in BiP-AMP level) observed in *FICD*$^{-/-}$ cells overexpressing constitutively monomeric FICD^{L258D} (Perera *et al*, 2019).

Chapter 4: The mechanistic basis of FICD state switching

Chapter 4.1: AMPylation competent binding of MgATP

The above results are entirely consistent with those previously published, that monomerisation is able to reciprocally regulate FICD's bifunctionality (Perera *et al*, 2019). Namely, under the same enzyme and substrate (steady state kinetic) conditions FICD monomerisation induced ~ 64-fold bias towards BiP AMPylation and away from its mutually antagonistic deAMPylation activity. Under the tested enzyme and substrate concentrations this change is predominantly due to a 32-fold increase in AMPylation activity of monomeric FICD^{L258D} over dimeric wild type FICD (**Figure 3.3.1c**); the rest of the difference being made up for by a 46% decrease in the rate of monomeric FICD^{L258D}-catalysed deAMPylation (**Figure 2.3.7**).

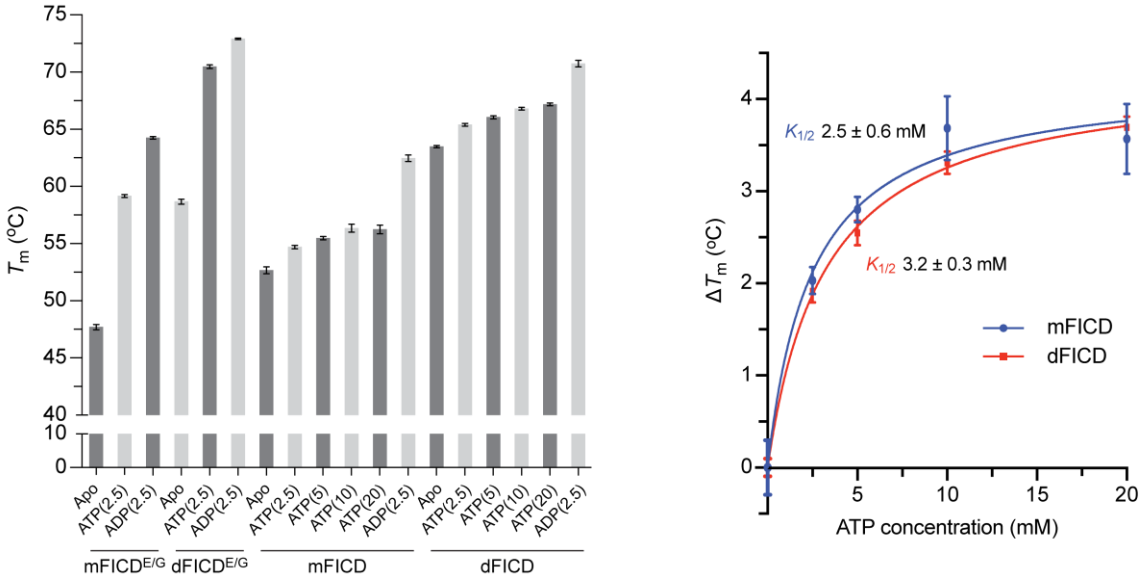

Figure 4.1.1: Monomeric and dimeric FICD bind ATP. Left, quantified protein melt temperatures of the indicated FICD proteins in absence (Apo) or presence of nucleotides (as indicated). Shown are the mean T_m values ± SD from n = 3 independent DSF experiments. Monomeric FICD^{L258D} (mFICD) and FICD$^{L258D-E234G}$ (mFICD$^{E/G}$) as well as dimeric wild type FICD (dFICD) and FICD^{E234G} (dFICD$^{E/G}$) were tested. ADP and ATP concentrations in mM are given in parentheses. The ATP titration was carried out in a buffer containing 25 mM $MgCl_2$. **Right,** plot of the derived increase in FICD melting temperature (ΔT_m) against ATP concentration, as measured by DSF. Note the similarity in the $K_{½}$s of ATP-induced T_m increase (annotated) between mFICD and dFICD. Although the $K_{½}$ of mFICD is slightly lower than that of dFICD, the difference is not statistically significant ($P > 0.05$ by a two-tailed Welch's t-test). Shown are mean ΔT_m values ± SD from n = 3 independent experiments with the best-fit lines from a one-site binding model.

As MgATP is known to be the co-substrate required for BiP AMPylation, it is possible that there may be a difference in either the mode of ATP binding between dimeric and monomeric

FICD or in the alibility of the two FICDs to bind ATP. The binding of small ligands can be monitored through their propensity to stabilise the native (folded) state of its binding partner protein. This increase in stability is often translated into a positive shift in the (melting) temperature required for protein unfolding. In order to measure changes in protein melt temperature differential scanning fluorimetry (DSF) was employed.

In agreement with earlier work (Bunney *et al*, 2014) it was found that both ADP and ATP were able to cause a significant change in protein melt temperature (ΔT_m) in the absence of the α_{inh} glutamate — in the context of a Fic domain Glu234Gly mutation (**Figure 4.1.1, left**). The ability for ATP to stabilise/bind FICD was drastically reduced by the presence of Glu234, although a seemingly saturable increase in T_m was still observed. Quantification of the thermal shift data indicated that both monomeric and dimeric FICD were both able to bind ATP in a buffer containing excess Mg^{2+} ions, displaying similar $K_{½}$s of ATP-induced T_m increase (**Figure 4.1.1, right**).

These results suggested that the variation in enzyme activity of different FICD mutants may arise not from variation in their affinity for nucleotide but rather from their particular manner of ATP binding. To explore this possibility, I set out to cocrystallise FICD variants (with varying BiP AMPylation abilities), with and without MgATP.

X-ray crystal structures of monomeric and dimeric FICD were obtained in assorted nucleotide-bound states (**Table 3** and **Table 4**). The tertiary structure of the Fic domain of both the apo, monomeric $FICD^{L258D}$ and the apo, dimer-relay mutant $FICD^{K256S}$ deviated little from that of the nucleotide-free wild type dimer structure (FICD:Apo; PDB: 4U04) (**Figure 4.1.2**). Moreover, cocrystallisation of $FICD^{L258D}$, $FICD^{K256A}$ or the wild type dimer with ATP or an ATP analogue (AMPPNP) also did not result in any significant conformational changes in the Fic domain (**Figure 4.1.2**). Accordingly, the greatest RMSD between the Fic domain of the FICD:ATP structure (over 195 Cα pairs across residues 213–407) and any other monomeric or dimer-relay FICD structure is 0.53 Å (observed between FICD:ATP and $FICD^{L258D}$:Apo). The only conspicuous change in global tertiary structure occurred in the TPR domain of $FICD^{L258D}$ cocrystallised with ATP or AMPPNP, which are isostructural outside of the active site region, in which the TPR domain is flipped almost 180° from its position in other FICD structures (**Figure 4.1.2**). Notably, in all FICD structures the α_{inh} remains firmly juxtaposed to the core Fic domain.

	FICD:ATP	FICD^{K256S}:Apo	FICD^{K256A}: MgATP	FICD^{L258D}:Apo	FICD^{L258D}: MgATP	FICD^{L258D}: MgAMP-PNP
Data collection						
Synchrotron stations	DLS I04	DLS I04	DLS I03	DLS I04	DLS I03	DLS I03
Space group	$P2_12_12$	$P22_12_1$	$P22_12_1$	$P3_121$	$P6_422$	$P6_422$
Molecules in a.u.[a]	2 (2)	1 (2)	1 (2)	1 (1)	1 (1)	1 (1)
a,b,c; Å	77.67, 107.65, 132.60	43.82, 76.51, 131.97	41.90, 73.98, 134.04	118.14, 118.14, 79.55	186.84, 186.84, 76.84	186.36, 186.36, 77.10
α, β, γ; °	90.00, 90.00, 90.00	90.00, 90.00, 90.00	90.00, 90.00, 90.00	90.00, 90.00, 120.00	90.00, 90.00, 120.00	90.00, 90.00, 120.00
Resolution, Å	83.58–2.70 (2.83–2.70)	65.99–2.25 (2.32–2.25)	134.04–2.32 (2.41–2.32)	62.80–2.65 (2.72–2.65)	93.42–2.54 (2.65–2.54)	93.18–2.31 (2.39–2.31)
R_{merge}	0.163 (0.717)	0.109 (0.385)	0.107 (0.636)	0.176 (0.856)	0.167 (1.009)	0.071 (0.611)
$\langle I/\sigma(I)\rangle$	19.2 (1.8)	6.8 (2.4)	5.6 (1.0)	8.6 (2.2)	13.0 (2.5)	10.3 (1.8)
$CC_{1/2}$	0.999 (0.720)	0.993 (0.547)	0.995 (0.567)	0.996 (0.549)	0.999 (0.503)	0.998 (0.523)
Unique reflections	31293 (4091)	21825 (1978)	18543 (1712)	18963 (1380)	26617 (3188)	34573 (3351)
Completeness, %	100.0 (100.0)	99.9 (99.5)	99.4 (97.3)	100.0 (100.0)	100.0 (100.0)	99.4 (99.1)
Redundancy	6.4 (6.5)	4.4 (4.4)	3.7 (3.7)	9.7 (10.0)	16.1 (16.5)	4.6 (4.6)
Refinement						
R_{work}/R_{free}	0.280 / 0.319	0.208 / 0.259	0.282 / 0.325	0.228 / 0.283	0.232 / 0.252	0.214 / 0.251
Atoms (non-H)	5650	2851	2731	2951	2828	2940
Average B-factors, Å^2	55.3	42.5	54.6	50.9	58.2	56.4
RMS Bond lengths, Å	0.002	0.003	0.003	0.003	0.002	0.003
RMS Bond angles, °	1.142	1.180	0.763	1.222	1.127	1.170
Ramachandran favoured region, %	96.5	98.5	98.2	97.9	98.5	99.4
Ramachandran outliers, %	0	0	0	0	0	0
MolProbity score[b]	1.33 (100th)	0.86 (100th)	0.74 (100th)	0.99 (100th)	0.97 (100th)	0.99 (100th)
PDB code	6I7G	6I7H	6I7I	6I7J	6I7K	6I7L

Table 3: Data collection and refinement statistics of FICD ± nucleotide complexes. Values in parentheses correspond to the highest-resolution shell, with the following exceptions: [a]The number of molecules in the asymmetric unit cell (a.u.), the number of molecules in the biological unit is shown in parentheses; [b]MolProbity percentile score is shown in parentheses (100th percentile is the best among structures of comparable resolutions, 0th percentile is the worst).

	PDB Code	Crystallisation Condition *(Protein:Seeds:Well Solution (nl))*	Seed Protein	Seed Crystal Conditions *(Seed Dilution)*
FICD:ATP	6I7G	0.1 M Tris pH 7.5; 20% PEG 300; 5% PEG8K; 10% Glycerol *(150:50:100)*	FICD	0.2 M $(NH_4)_2SO_4$, 0.1 M NaCacodylate, 30% PEG 8000 *(1/3)*
FICD^{K256S}:Apo	6I7H	0.1 M Tris pH 8.5; 0.05 M $MgCl_2$; 40% EtOH *(200:0:100)*	N/A	N/A
FICD^{K256A}:MgATP	6I7I	0.1 M Bis-Tris pH 6.5; 0.2 M $MgCl_2$; 25% PEG3350 *(100:25:100)*	FICD^{K256A}	0.1 M Na_3Citrate pH 5.5, 40% PEG 600 *(1/10)*
FICD^{L258D}:Apo	6I7J	0.1 M Tris pH 8.5; 2.0 M $(NH_4)_2SO_4$ *(150:50:100)*	FICD^{L258D}	0.1 M Tris pH 8.5, 0.2 M Li_2SO_4, 40% PEG 4000 *(1/2)*
FICD^{L258D}:MgATP	6I7K	1.0 M NaCl; 10% EtOH *(150:50:200)*	FICD$^{L258D-H363A}$	0.1 M HEPES pH 7.5, 1 M NaOAc *(1/100)*
FICD^{L258D}:MgAMP-PNP	6I7L	1.5 M NaCl; 10% EtOH *(150:50:200)*	FICD^{K256A}	0.1 M Na_3Citrate pH 5.5, 40% PEG 600 *(1/500)*

Table 4: Crystallisation conditions of FICD ± nucleotide complexes. Where applicable the crystallisation conditions (and seed dilution) of the crystals used for micro-seeding are also shown. Seeds stock suspensions were diluted, as indicate, in water. Note, PEG percentages are provided in terms of *w/v* and ethanol (EtOH) percentages in *v/v*.

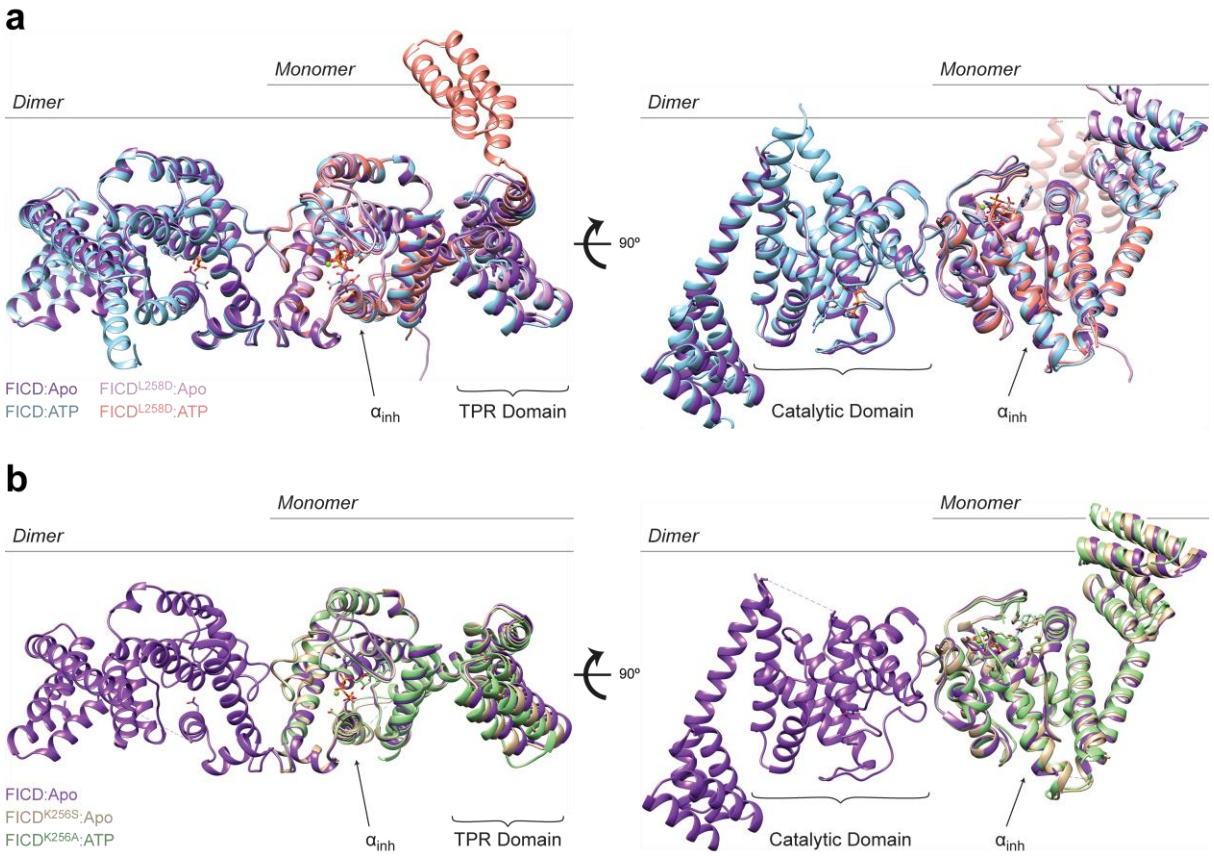

Figure 4.1.2: Monomerisation or dimer-relay disruption does not cause large-scale changes in the Fic domain. Superposition of FICD asymmetric unit molecules with FICD:Apo (PDB 4U04; purple) are presented, aligned by Fic domain residues 213–407. Glu234, His363 and ATP are shown as sticks with the Mg^{2+} cation as a green sphere (where applicable). The Fic domain inhibitory alpha helix (α_{inh}) and gross domain architecture are annotated. **a,** Wild type FICD and monomeric FICD^{L258D} ± ATP are superposed. Note, the only significant deviation in tertiary structure is the flipping of the TPR domain in the FICD^{L258D}:ATP structure. The FICD^{L258D}:AMPPNP structure is identical to FICD^{L258D}:ATP outside of the Fic domain active site and is not shown. **b,** FICDs mutated at the dimer-relay residue Lys256 ± ATP are superposed. Mutation of this residue also does not result in large conformational changes in FICD structure (relative to FICD:Apo).

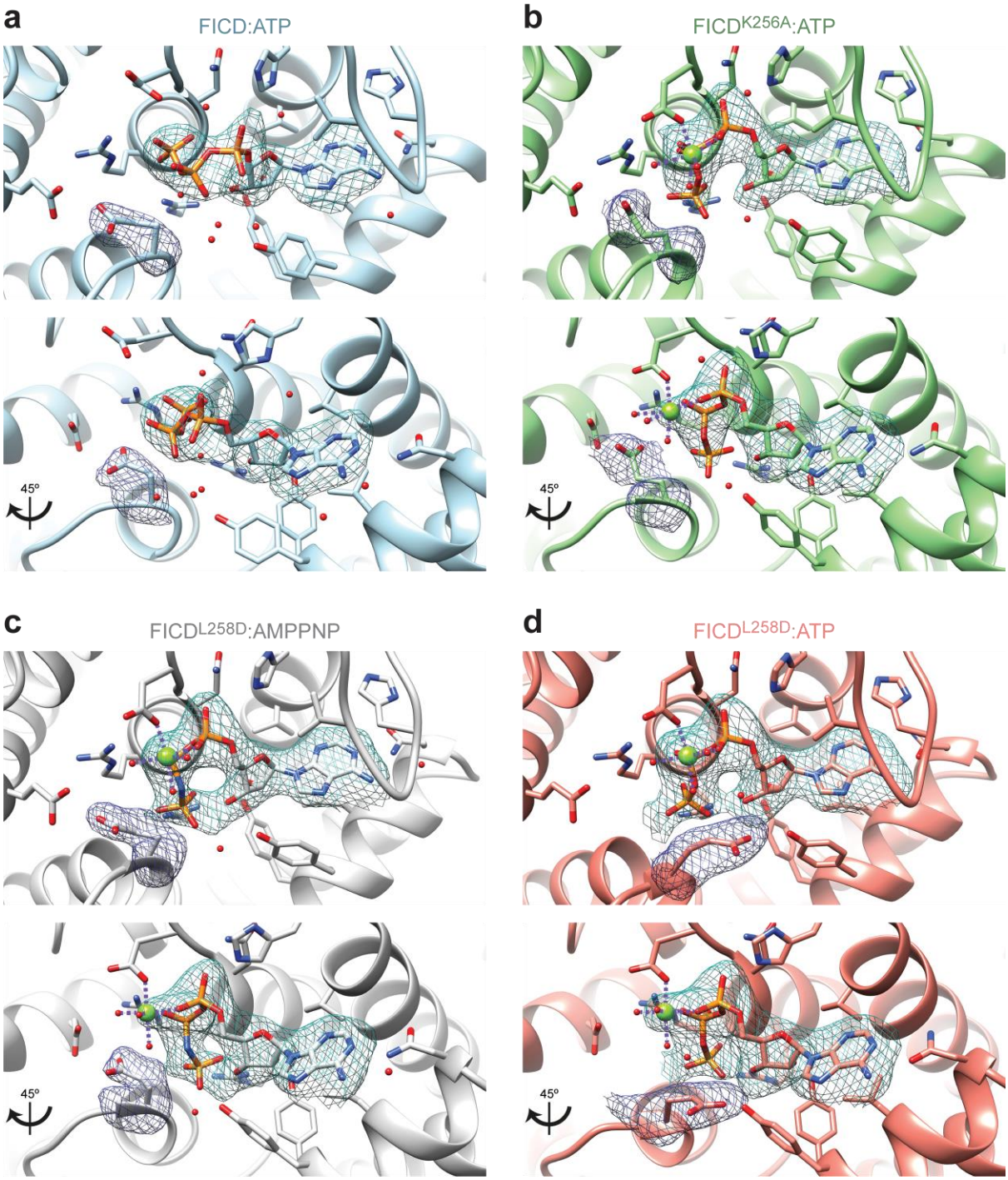

Figure 4.1.3: Electron density of FICD Glu234 and MgATP. FICD active sites are shown overlaid with unbiased polder OMIT maps (using mesh representation) in the region of MgATP and Glu234. **a,** The wild type dimer FICD structure displays a lack of density corresponding to a Mg^{2+} ion. The ATP density is contoured at 3.5σ and the Glu234 at 5.0σ. **b,** The dimeric dimer-relay mutant FICD^{K256A} displays a clear MgATP density up to and including the γ-phosphate phosphorous atom. The ATP density and Glu234 densities are both contoured at 3.0σ. **c,** The MgAMPPNP nucleotide analogue bound to monomeric FICD^{L258D} is clearly coordinated by a Mg^{2+} ion. The polder OMIT density does not cover the entirety of AMPPNP's γ-phosphate (in the region of O1γ and O2γ). The ATP density is contoured at 3.0σ and the Glu234 at 5.0σ. **d,** Monomeric FICD^{L258D} contains a clear

MgATP density although it is still not complete over the γ-phosphate's O3γ. The ATP density is contoured at 3.0σ and the Glu234 at 5.0σ.

However, upon closer inspection of the ATP-bound cocrystal structures differences between the FICD variants are apparent. Namely, although all structures that crystallised in the presence of millimolar concentrations of MgATP contained electron density attributable to the nucleotide, only the AMPylation-biased FICD mutants (Leu258Asp and Lys256Ala) also contained discernible, octahedrally coordinated Mg^{2+} ion density (**Figure 4.1.3**). As noted in other AMPylating Fic enzymes, this Mg^{2+} was coordinated by the α- and β-phosphates of ATP/AMPPNP and the conserved aspartate (FICD's Asp367) of the Fic motif (Khater & Mohanty, 2015b; Bunney *et al*, 2014). Conversely, the only possible candidate for Mg^{2+} in the dimeric, wild type FICD:ATP structure was a water density, located between all three phosphates, that fell in the Fic motif's oxyanion hole — a position incompatible with divalent cation coordination (Zheng *et al*, 2017).

The FICD:ATP structure (which lacks a coordinating Mg^{2+} ion) has a polder OMIT electron density which fully covers the region of the ATP molecule (**Figure 4.1.3a**). Conversely, none of the MgATP containing FICD structures contained polder OMIT density that completely covered the modelled ATP γ-phosphate (**Figure 4.1.3b–d**). Of these three structures $FICD^{L258D}$:ATP has the most well-defined density for both its ATP molecule and Glu234 (**Figure 4.1.3d**). The presumably lower occupancy regions, especially in the area of the ATP γ-phosphate, potentially speak towards the MgATP-bound active sites representing relatively high energy states and possibly sampling a number of different γ-phosphate (and Glu234) conformations.

Alignment of the nucleotide-bound structures revealed that ATP or AMPPNP were bound very differently by the wild type dimer and the AMPylation-biased monomeric or dimer-relay FICD mutants (**Figure 4.1.4a–b**). Concordantly, the RMSD of ATP between the wild type FICD and monomeric $FICD^{L258D}$ was 2.17 Å, and 2.23 Å between the ATPs bound to wild type FICD and $FICD^{K256A}$. As previously observed in other ATP-bound Fic proteins that possess an inhibitory glutamate, the nucleotide in FICD:ATP is not stably coordinated by a Mg^{2+} (Engel *et al*, 2012; Goepfert *et al*, 2013); a cation necessary for FICD-mediated AMPylation (Ham *et al*, 2014). Moreover, the closest interatomic distance between wild type FICD's ATP α-phosphate the Fic domain flap residue Val316 is markedly reduced relative to that observed in $FICD^{K256A}$ and $FICD^{L258D}$ (**Figure 4.1.4a–b**).

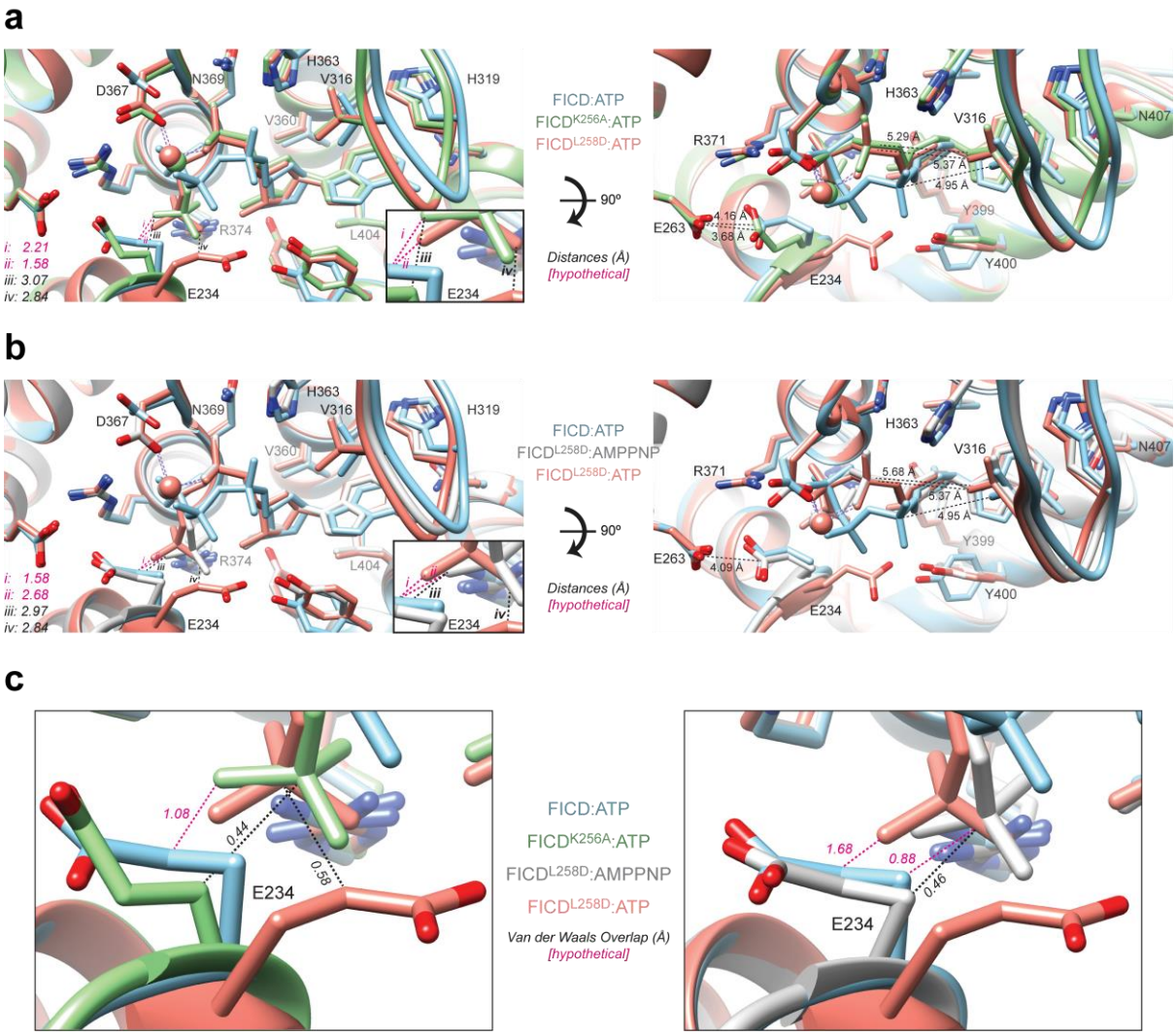

Figure 4.1.4: Monomeric FICD's Glu234 permits AMPylation competent MgATP binding. **a–b,** Superposition of the structures presented in **Figure 4.1.3** (upper panels). In **b** the FICD^{K256A}:ATP structure is replaced by the FICD^{L258D}:MgAMPPNP structure. ATP interacting residues are shown as sticks and annotated. Mg^{2+} and ATP are coloured to match the corresponding ribbons. Active site waters are omitted for clarity. Between active sites the only significant side chain deviation is in Glu234 position. Note, the FICD:ATP His363 side chain is also flipped. This assignment is based on the formation of a His363 hydrogen bond to a ribose interacting water, presumably enabled by the disposition of the α-phosphate which can no longer compete for the interaction with His363 (also see **Figure 4.1.3a**). **Inset,** blow-up displaying the smallest interatomic distances (*i–iv*) between γ-phosphates and Glu234 residues. Note, distances (*i*) and (*ii*) are hypothetical and are not experimentally observed. These represent the distances (pink) between catalytically competent γ-phosphates and FICD:ATP's Glu234. Distances between the closest point of the Fic domain flap [Val316(Cγ1)] and the corresponding Pα atom are shown in the right-hand side panel. Non-favourable Glu234-Glu263 interactions (present in all structures apart from FICD^{L258D}:ATP are also annotated. **c,** A focussed view of the γ-phosphate and Glu234 regions of the alignments in **a** and **b**, annotated with the greatest γ-phosphate to Glu234 Van der Waals radii overlap. A Van der Waals overlap < 0.6 Å is not generally considered to represent a steric clash. The much

greater hypothetical overlaps (pink) suggest that the Glu234 deviation observed within dimeric wild type FICD would be insufficient to accommodate the position of a catalytically competent γ-phosphate.

By overlaying 3 Å radius centroids centred on Pα and the nearest Val316 (non-hydrogen) atom Cγ1, it becomes clear that the space afforded by the ATP conformation in wild type FICD is insufficient to accommodate a putative attacking nucleophile (**Figure 4.1.5a**). Furthermore, an attacking nucleophile (BiP's Thr518 hydroxyl group) in-line with Pα-O3α would be at a considerable distance from the catalytic His363 (required to deprotonate Thr518's hydroxyl group) (**Figure 4.1.4a–b** and **Figure 4.1.5a**).

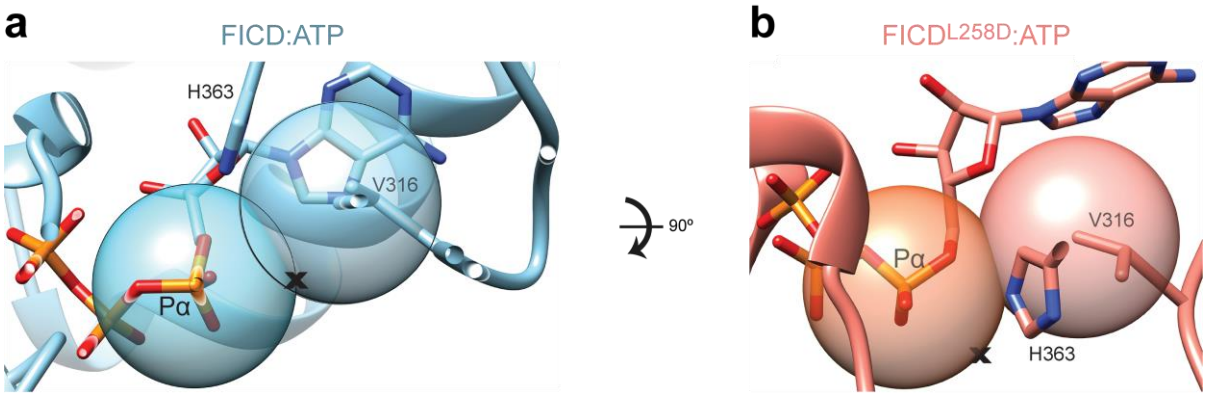

Figure 4.1.5: In-line nucleophilic attack is sterically occluded in the dimeric FICD:ATP structure. a, Semi-opaque 3 Å centroids centred on Pα and Val316(Cγ1) are shown. The putative BiP Thr518 nucleophile (depicted by the cross) is positioned in-line with the scissile phosphoanhydride (parallel to the plane of the paper) and 3 Å from Pα. This nucleophile position lies within the Val316 centroid (indicating a steric clash) and far away from His363, which would be required for nucleophile deprotonation. For clarity, the FICD:ATP structure is overlaid with a thin slice of the FICD:ATP structure in the plane of the Pα-O3α bond. **b,** As in **a** except without an overlaid slice within the plane Pα-O3α phosphoanhydride bond and rotated for clarity. In the monomeric AMPylation-competent FICD^{L258D}:ATP structure, the putative nucleophile (cross) lies outside the Val316 semi-opaque centroid (indicating a lack of steric clash with the Fic domain flap) and also in proximity to His363 (the general base).

In contrast, within FICD^{K256A} or FICD^{L258D} MgATP and MgAMPPNP are bound such that the interatomic Pα-Cγ1(Val316) distance is relatively large (**Figure 4.1.4a–b**). As a result, there is no steric overlap between Val316 and a potential nucleophile primed for in-line nucleophilic attack into the ATP α-phosphates bound to FICD^{K256A} or FICD^{L258D} (**Figure 4.1.5b**). Moreover, the α-phosphate position in these structures is the same as that assumed by AMPylation-active Fic proteins lacking inhibitory glutamates (Engel *et al*, 2012; Goepfert *et al*, 2013; Bunney *et al*, 2014) (**Figure 4.1.6**). In this position, as illustrated above, in-line nucleophilic attack into the α-β-phosphoanhydride bond of ATP is not sterically hindered and,

furthermore, the Nε2 of His363 is well positioned for general base catalysis (**Figure 4.1.6**). Together these data suggest that both monomeric and dimer-relay mutant FICDs bind MgATP in an AMPylation competent conformation, whereas dimeric FICD does not. The latter finding is consistent with previous observations of inhibitory glutamate containing, AMPylation-autoinhibited Fic proteins bound to ATP (Engel *et al*, 2012; Goepfert *et al*, 2013).

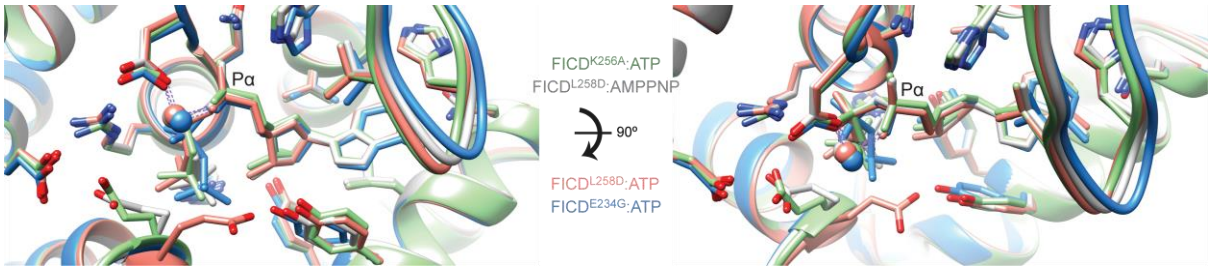

Figure 4.1.6: AMPylation competent MgATPs share a common Pα position. The ATP α-phosphates of monomeric or dimer-relay FICD mutants are in the same position as that of a MgATP molecule competently bound to the AMPylation unrestrained, dimeric FICD^{E234G} (dark blue, PDB: 4U07). All AMPylation competent MgATP structures are superposed as in **Figure 4.1.4**. All α-phosphates sit within the Fic domain oxyanion hole (formed by the Fic (sub)motif GN^{369}G) and are coordinated by a Mg^{2+} ion, which is also complexed by the respective β-phosphates and the Fic motif Asp367.

The presence of ATP in both dimeric, wild type FICD and monomeric FICD^{L258D} (although in different binding modes) is consonant with the DSF data (**Figure 4.1.1**). Apart from Glu234, the residues directly interacting with ATP are similarly positioned in all structures (maximum RMSD 0.83 Å). However, considerable variability is observed in Glu234, with an RMSD of 4.20 Å between monomeric and dimeric wild type ATP structures. The large disposition in Glu234 conformations may hint at the basis of monomerisation-induced AMPylation competency.

In all ATP-bound structures the inhibitory glutamate is displaced from the respective apo ground-state position, in which it forms an inhibitory salt bridge with Arg374 (R_2 of the Fic motif). However, the displacement of the Glu234 side chain observed in the FICD:ATP structure (from its position in FICD:Apo; PDB 4U0U) would be insufficient to accommodate the γ-phosphate of an ATP/AMPPNP bound in an AMPylation competent conformation (see distances *i* and *ii* in **Figure 4.1.4a–b** and **Figure 4.1.4c**). In the FICD^{L258D} and FICD^{K256A} structures the maximum Van der Waals radii overlap between the bound γ-phosphate and the respective Glu234 side chain is less than the default value considered to represent a steric clash (< 0.6 Å overlap). Conversely the Van der Waals overlap between any AMPylation competent

ATP γ-phosphate and the wild type FICD:ATP structure's Glu234 (despite being displaced relative to its apo state position) is > 0.88 Å (**Figure 4.1.4c**, pink dashed lines). The differences between AMPylation competent conformations of Glu234 and ATP γ-phosphate (within $FICD^{L258D}$ and $FICD^{K256A}$) may reflect the ability to trap diverse states of a dynamic system and/or may be indicative of variability in the protonation state of the γ-phosphate — pK_a 7.1 for the terminal phosphate proton of ATP and 7.7 for AMP-PNP (Yount *et al*, 1971). Moreover, changes in the charge borne by the ATP γ-phosphate may be facilitated by the different crystallisation conditions (pH 6.5 buffered condition for $FICD^{K256A}$:ATP crystal growth; in the $FICD^{L258D}$:nucleotide crystals the pH was likely dominated by the Tris-HCl present in the protein preparation [~ pH 8.0]; see **Table 3**). It is therefore possible that γ-phosphate within both the $FICD^{K256A}$:ATP and $FICD^{L258D}$:AMPPNP may be protonated (thereby reducing the electronic repulsion between the γ-phosphate and Glu234). Furthermore, there may also be differences in the flexibility or range in attainable bond angles between the β-γ-phosphate P-O-P and P-N-P linkages of ATP and AMPPNP, respectively, which may affect the propensity of the γ-phosphate to bind in a certain conformation. With these factors in mind the cocrystal structure of $FICD^{L258D}$:ATP should represent the most physiological AMPylation competent active site — with crystallisation conditions ~ pH 8.0 the bound ATP should have a net charge of –4 (the likely charge state of ATP at physiological pH).

Chapter 4.2: The role of Glu234 flexibility in AMPylation

The findings above suggest that the AMPylation-biased FICD mutants attain their ability to competently bind MgATP by increased flexibility at the top of the α_{inh} and by extension through increased Glu234 dynamism. This assertion is supported by analysis of average residue B-factors which provide a measure of the degree of molecular motion or static disorder. It was found that the temperature or B-factors in the vicinity of the dimer interface and Glu234 (of ATP-bound FICD structures) appears to correlate with AMPylation activity (**Figure 4.2.1**). This is despite similar crystal structure resolutions, overall B-factor averages (**Table 3**) and similar protein/crystal packing environments in the region of the dimer interface and Glu234 (**Figure 4.2.2** and **Figure 4.2.3**).

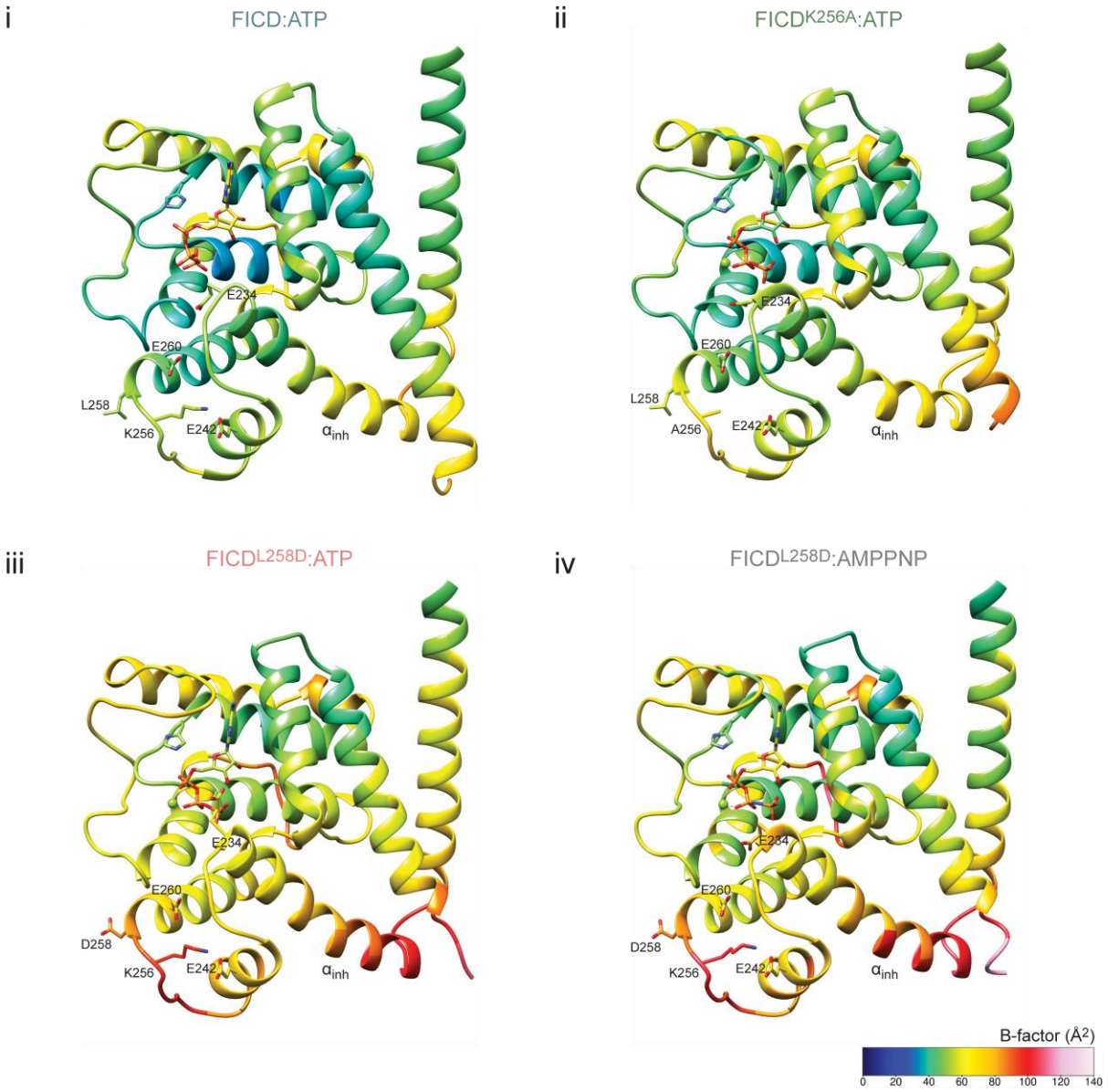

Figure 4.2.1: B-factors are suggestive of monomerisation increasing Glu234 flexibility. The residue average B-factors, for the four FICD complexes co-crystallised with ATP, are shown [in (**i–iv**)] with a cold to hot colour code. For clarity, the TPR domain (up to residue 182) is not shown. Selected residues involved in the putative hydrogen bond, dimer-relay network are shown and labelled.

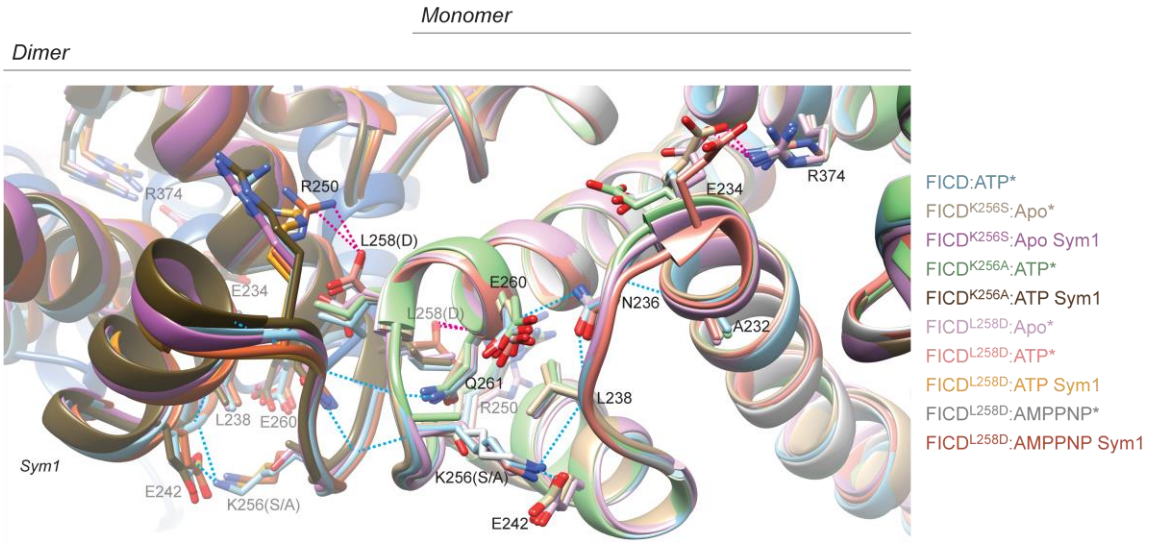

Figure 4.2.2: The dimer-relay hydrogen bond network is maintained in FICD crystal structures. An alignment of FICD structures in the region of the principal dimer interface. The hydrogen bond network linking the dimer interface to Glu234 is also shown (blue dashed lines). Where indicated, single molecules from the asymmetric unit (*) are displayed with their respective crystal symmetry mates (Sym1). Note, the side chains of Asp258 and (Sym1)Arg250 of the monomeric FICD^{L258D}:nucleotide structures, form a crystallographically induced intermolecular salt bridge (magenta dashed line). The salt bridges between Glu234 and the Fic motif Arg374 (magenta dashed lines) in the FICD^{L258D}:Apo and FICD^{K256S}:Apo structures, as observed in previous inhibitory glutamate-containing Fic crystal structures, are also shown.

Moreover, it is notable that the differences in nucleotide triphosphate binding, Glu234 disposition and average residue B-factors were observed despite all FICD:nucleotide structures crystallising with intact dimer interfaces (**Figure 4.2.2**). In the case of FICD^{L258D}, which appears completely monomeric even at concentrations in the order of hundreds of micromolar (Perera *et al*, 2019), a crystallographically induced salt bridge (which incorporates Asp258) in the structures of FICD^{L258D}:ATP and FICD^{L258D}:AMPPNP restores the canonical dimer interface. Moreover, with the exception of direct hydrogen bonds to the Lys256 side chains (which are lost upon mutation of this residue), in all FICD crystals the putative dimer-relay hydrogen-bond network (linking the dimer interface to the α_{inh} and FICD active site) was maintained (**Figure 4.2.2**). This is also the case even in the FICD^{L258D}:Apo crystal structure, which crystallised as a monomeric protein with a free dimer interface (**Figure 4.2.2** and **Figure 4.2.3iii**).

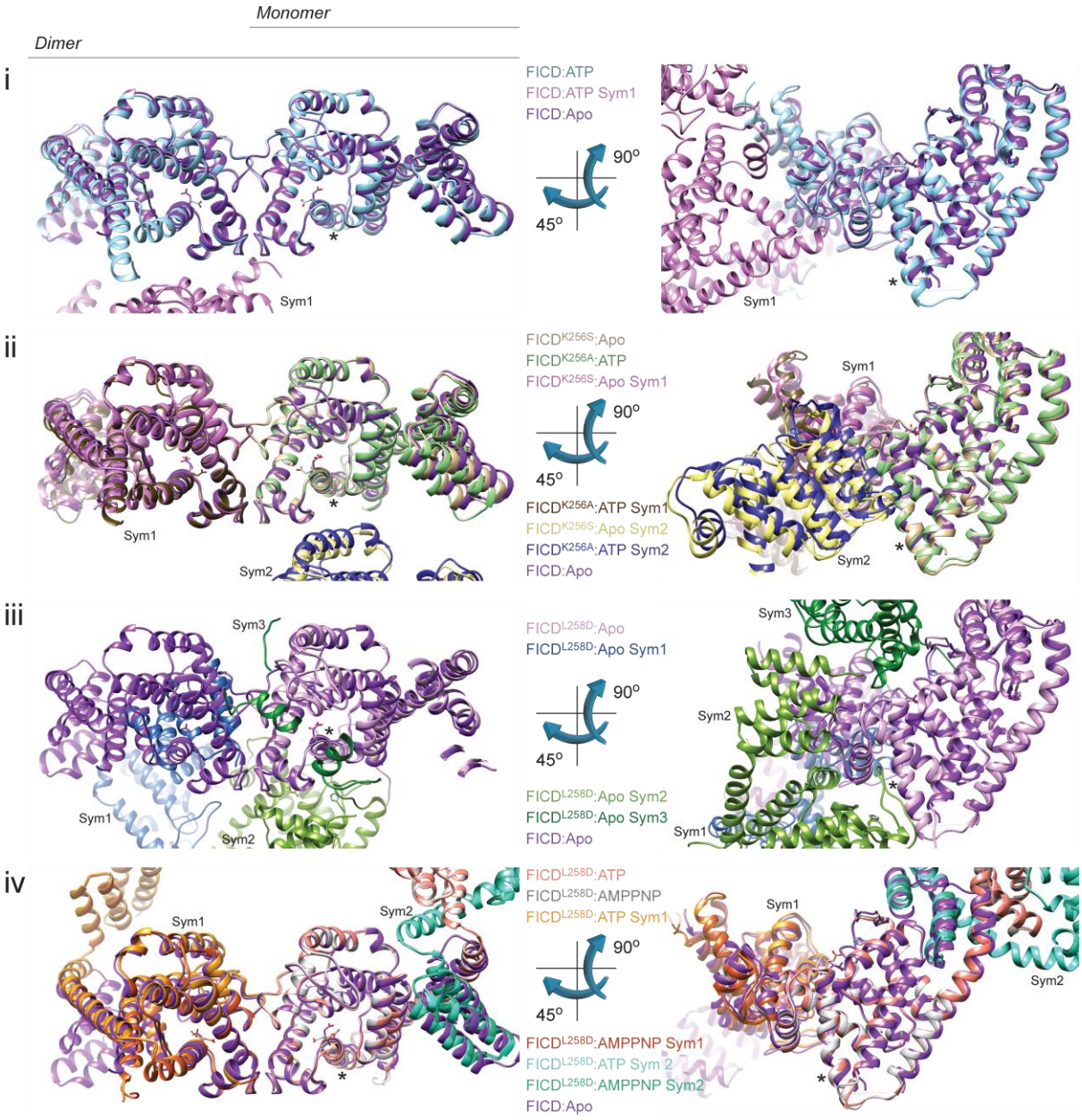

Figure 4.2.3: Crystal packing around α_{inh} is similar in all FICD structures. FICDs with similar crystal packings are grouped into panels (**i-iv**). The inhibitory alpha helix (α_{inh}) is denoted with an asterisk (*) and Glu234s are shown as sticks. The wild type, dimeric FICD:Apo structure (FICD:Apo; PDB: 4U0U) is provided in all panels for reference. Symmetry mates within 4 Å of the FICD dimer interface (Sym1) or the α_{inh} (Sym2/3) are also displayed. Note, the crystals structures of Lys256 mutant FICDs (**ii**) contain a single molecule in their asymmetric unit but are packed as dimers, crystallographically reconstituting the dimeric biological unit (see **3**). The asymmetric unit of FICD^{L258D} bound to ATP (or an ATP analogue) (**iv**) contain a single molecule and thus corresponds to the biological unit of this monomeric protein. However, packing against the symmetry mate (Sym1), crystallographically reconstitutes a dimer interface that is highly similar, but not identical, to that observed in the wild type protein (see **2**). In (**iv**) there are no crystal contacts in the vicinity of the α_{inh}. Instead, Sym2 in (**iv**) is included to highlight the intermolecular TPR domain swap, in which the intramolecular TPR

domain contacts (broken by the 'TPR out' conformation in the asymmetric unit) are compensated for by a symmetry related TPR domain.

Therefore, it seems likely that much of the monomerisation-linked conformational flexibility that facilitates binding of MgATP in solution cannot be trapped by the static snapshots which are obtainable crystallographically. Nonetheless, further circumstantial evidence for the increase in FICD AMPylation activity resulting from increased Glu234 flexibility arises from analysis of FICD protein melt temperatures, which provides an indication as to general protein stability and may be sensitive to increased flexibility in (the region of) the α_{inh}. At concentrations were the tested FICD variants (apart from FICD^{L258D} and FICD^{G299S}) were all principally dimeric (2 µM; K_Ds calculated by SEC in Perera *et al*, 2019) there is an inverse correlation between AMPylation ability (see **Figure 1.5.1**) and protein T_m (**Figure 4.2.4a**). This trend is present under various nucleotide conditions (**Figure 4.2.4b**).

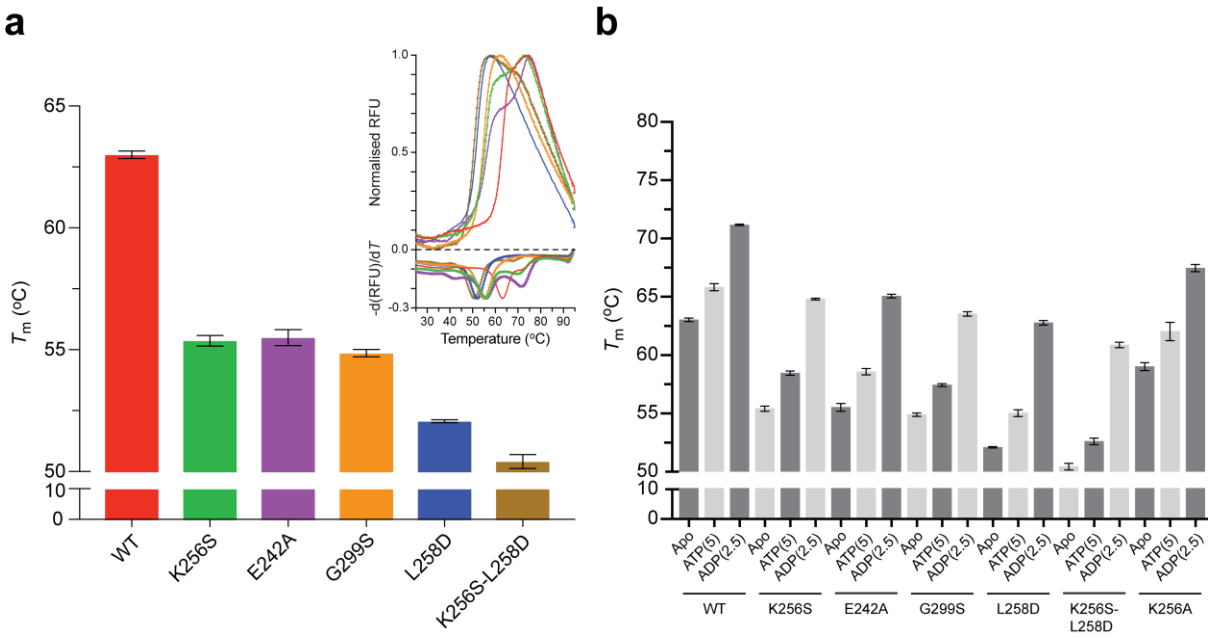

Figure 4.2.4: AMPylation biased FICD variants exhibit greater thermally lability. a, Melting temperatures (T_m) of the indicated FICD mutants (in the absence of nucleotide) were measured by differential scanning fluorimetry (DSF). Shown is the mean T_m ± SD from n = 3 independent experiments. The inset shows colour-matched melt curves with their negative first derivatives, from a representative DSF experiment conducted in technical triplicate. The T_m for each protein sample was calculated from global minimum analysis of the melt curve negative first derivative. RFU, relative fluorescence units. See **Figure 1.5.1** for quantification of respective FICD mutant AMPylation activities. **b,** Quantification of the indicated FICD variant T_ms in the presence of either no nucleotide (Apo), 5 mM ATP or 2.5 mM ADP. All FICD variants respond similarly to the binding of ATP and ADP. For reference, the data in **a** is also duplicated in **b**.

Chapter 4.3: Increased Glu234 flexibility decreases BiP deAMPylation activity

In **Chapter 2.4**, through analysis of the state 1 deAMPylation complex crystal structure, the mechanistic basis of the essential role played by the gatekeeper Glu234 residue in Fic domain-catalysed deAMPylation was elucidated. The above inferences regarding a monomerisation-induced increase in α_{inh} and Glu234 flexibility, suggests that such a change may also explain the ~ 50% reduced deAMPylation efficiency of monomeric relative to wild type, dimeric FICD (**Figure 2.3.7**). The second (state 2) sub-2 Å deAMPylation complex-crystal structure, which is almost identical to that previously presented (**Table 1** and **Figure 2.1.2**), appears to provide direct support for this assertion.

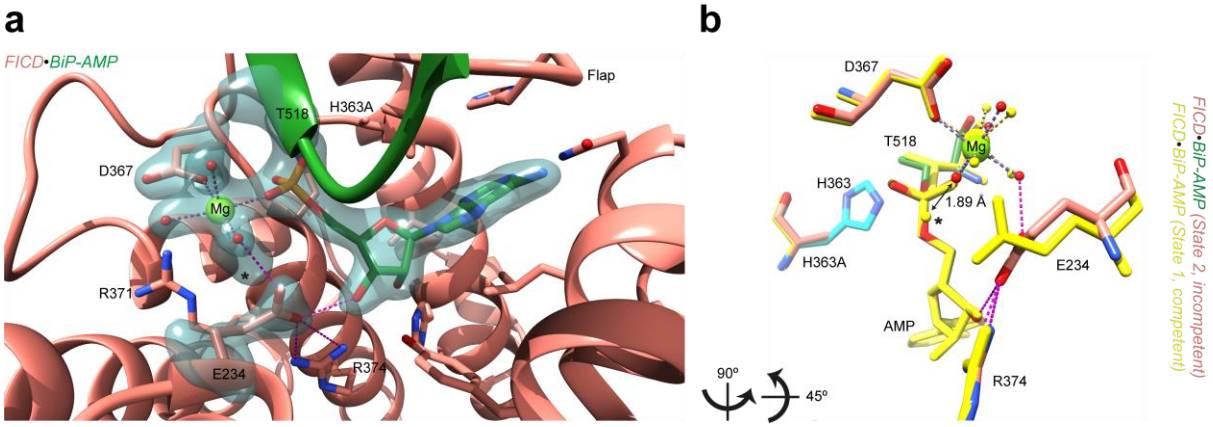

Figure 4.3.1: Monomerisation increases Glu234 flexibility in the deAMPylation complex. **a,** A second deAMPylation complex structure (state 2, orange) is overlaid with an unbiased polder OMIT electron density map, contoured at 6σ. The view is the same as that presented in **Figure 2.4.1**. The OMIT map was calculated over regions of Fic domain catalytic residues of particular interest (Asp367 and Glu234), the Mg^{2+} coordination complex, BiP's Thr518-AMP (green) and the approximate position of the state 1 catalytic water (marked with *). Hydrogen bonds formed by Glu234 are shown as pink dashed lines. Residues interacting with the AMP moiety are shown as sticks. **b,** A rotated and reduced view of the active site visible in **a**, aligned with the active site of the (deAMPylation competent) state 1 complex (yellow). His363 is modelled by superposition of a catalytically competent FICD (PDB 6I7K, as in **Figure 2.4.2**). The catalytic water (from state 1) is annotated with *. The distance between the closest Mg^{2+} first-coordination sphere water (red) from the state 2 complex and the (state 1) catalytic water* is annotated.

As in the state 1 structure (**Figure 2.4.1** and **Figure 2.4.2**), the FICD active site contains obvious electron density for BiP's Thr518-AMP, Fic domain catalytic residues and a coordinated Mg^{2+} cation (**Figure 4.3.1a**). However, alignment with the state 1 structure reveals a clear difference in the orientation of Glu234 (**Figure 4.3.1b**). In the second, state 2, structure

the Glu234 sidechain points further away from the position of the catalytic water molecule, that was so clearly visible in state 1, and more towards the Mg^{2+} cation.

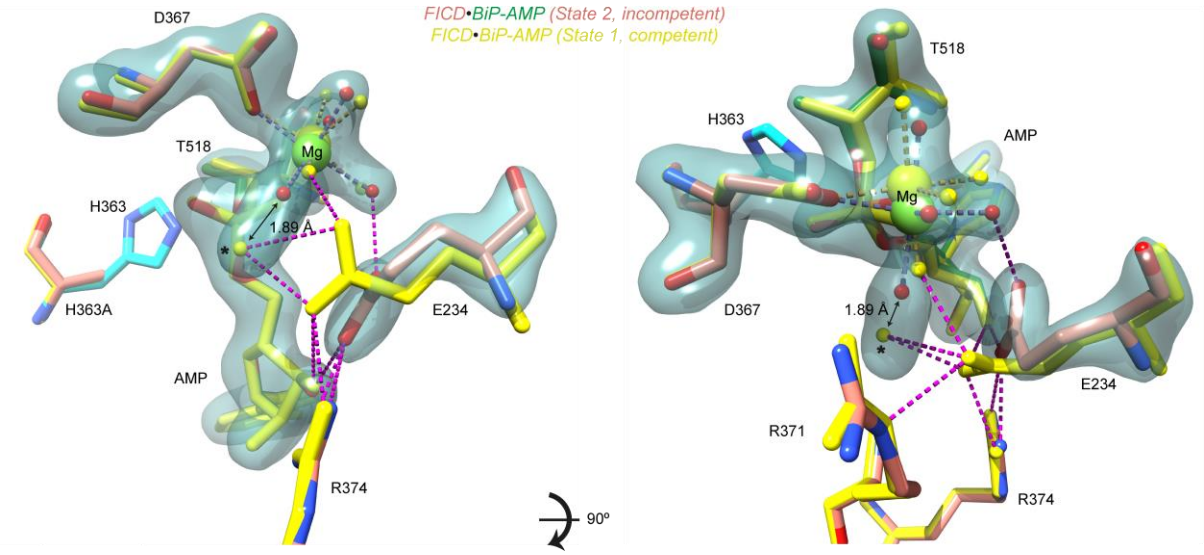

Figure 4.3.2: Increased Glu234 flexibility enfeebles positioning of the catalytic water. The same polder OMIT map is displayed over a reduced active site, as in **Figure 4.3.1**, highlighting the extended electron density covering the state 2 Mg^{2+} coordinating water and the position of the putative (state 1) catalytic water*. The orthogonal view, right, also helps to illustrate the shifted position of the Mg^{2+} coordination complex, which is presumably linked to the altered disposition and hydrogen bond contacts of the state 2 Glu234. Hydrogen bonds formed by both state 1 and 2 Glu234 residues are annotated with pink dashed lines.

As observed in the monomeric $FICD^{L258D}$:nucleotide structures it is possible that the state 1 and state 2 deAMPylation complexes capture different snapshots of a dynamic Glu234 and Fic domain active site. However, in the case of the deAMPylation complexes, these changes are much better resolved. The reorientation of Glu234 noted in the state 2 complex appears to directly affect the ability of the state 2 active site to carry out the proposed deAMPylation mechanism (**Figure 2.5.1**), through stabilising a slight shift in the position of the Mg^{2+} octahedral coordination complex (**Figure 4.3.2**). Glu234 in the state 2 conformation forms a hydrogen bond with a different Mg^{2+} coordinated water, which facilitates a movement in the entire metal ion coordination complex in the direction of the (state 1) catalytic water. Although there is some remaining electron density in the catalytic water molecule region, this density is merged with the electron density of a Mg^{2+} coordinating water molecule (**Figure 4.3.2**). Moreover, this elongated density is incompatible with the modelling of two water molecules (accommodating the Mg^{2+} coordination geometry requirements would necessitate an infeasible inter-water distance of 1.89 Å) and suggests that there may be a dynamic shuttling of a water to and from the primary Mg^{2+} coordination sphere into a position more conducive to catalysis.

Thus, it is clear that the Glu234 position observed in the state 2 crystal structure does not permit the stable positioning of a catalytic water molecule in-line for nucleophilic attack.

A corollary of the two tenets, that Glu234 is necessary for coordinating a catalytic water molecule for deAMPylation and that Glu234 flexibility increases upon monomerisation, is the prediction that FICD deAMPylation activity should decrease upon monomerisation. This has already been demonstrated in terms of a decrease in catalytic efficiency (**Figure 2.3.7**). However, an increase in Glu234 flexibility is expected to intrinsically affect the ability of the FICD active site to catalyse deAMPylation and should thus lower the k_{cat}.

In order to directly measure the turnover number (k_{cat}) for monomeric and dimeric FICDs both enzymes must be saturated with deAMPylation substrate, this necessitated adaptation of the previous FP-based in vitro deAMPylation assay. In order to compensate for the much-increased amount of substrate, the assay was modified to incorporate 10 µM rather than the previous 0.5 µM of FICD enzyme. This enabled near complete substrate deAMPylation in all samples, within the permissible time course of the assay, and therefore permitted an ability to convert (for each reaction) the observed changes in FP signal into units of µM BiP produced or (equivalently) µM BiP deAMPylated (**Figure 4.3.3**).

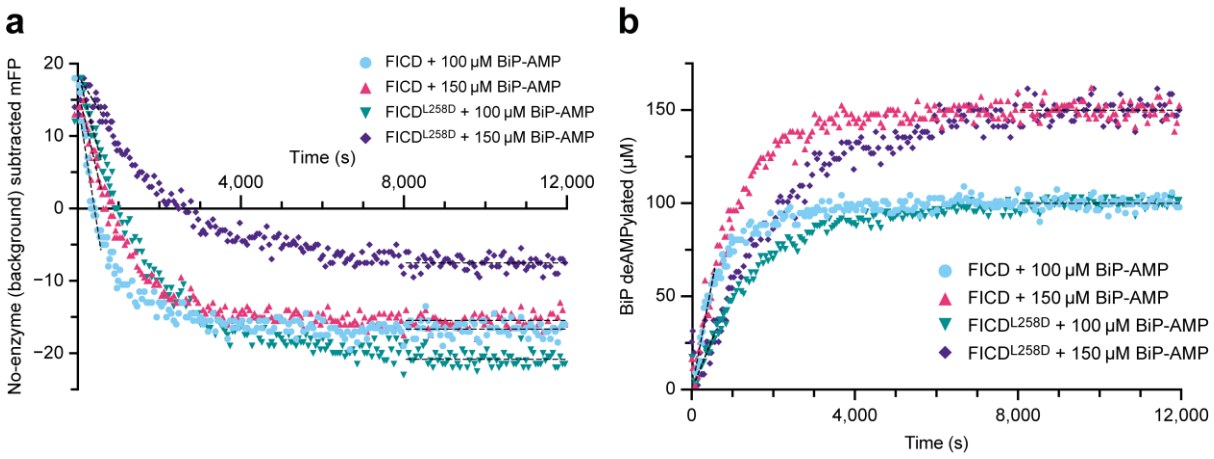

Figure 4.3.3: FP-based measurement of FICD deAMPylation k_{cat}. a, Representative background drift-subtracted FP deAMPylation time course. Linear best-fits are overlaid illustrating the initial reaction progress (from which y_0 values were obtained) and final plateau value (y_∞). The ΔFP between y_0 and y_∞ (for each sample) was taken to represent $[BiP\text{-}AMP]_0$. **b,** Using the calculated ΔFP to 'µM BiP deAMPylated' conversion factors, deAMPylation time courses are presented. This provides a visual indication that the initial rates for each enzyme (best fit dashed lines) are similar at both BiP-AMP substrate concentrations.

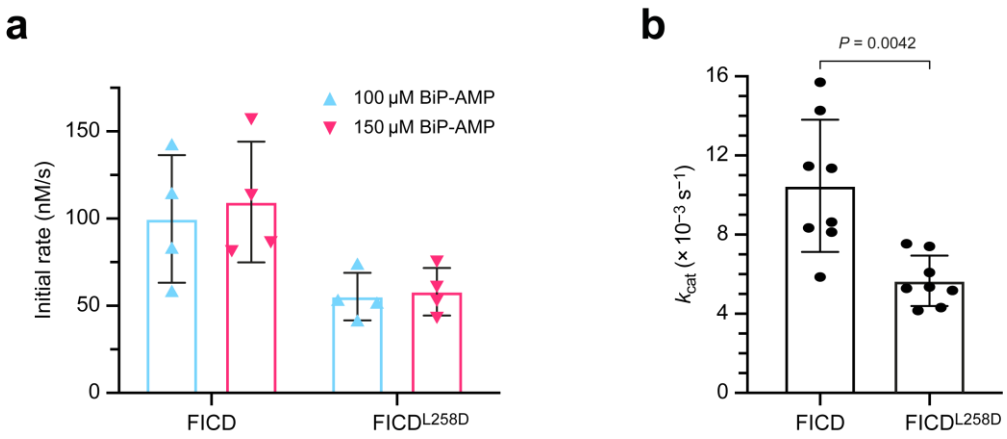

Figure 4.3.4: Monomerisation decreases FICD's deAMPylation k_{cat}. **a,** Quantification of the initial deAMPylation rates (mean ± SD) with either 100 or 150 µM BiP-AMP substrate at t = 0, derived from analysis as presented in **Figure 4.3.3**. Results are presented from n = 4 independent experiments. **b,** The resulting k_{cat} parameters were calculated using all initial enzyme velocities presented in **a**. The mean k_{cat} value ± SD is shown with the *P*-value from a two-tailed Welch's t-test annotated.

In this fashion, it was found that the initial rates of deAMPylation were indistinguishable at initial substrate concentrations of 100 and 150 µM BiP-AMP (**Figure 4.3.3** and **Figure 4.3.4a**), implying that FICD and FICD^{L258D} are saturated at both BiP-AMP concentrations. Therefore, the initial deAMPylation rates, observed at both substrate concentrations for each enzyme, represent maximal enzyme velocities from which a k_{cat} parameter can be extracted (**Figure 4.3.4b**). As expected for the less-flexible Glu234-bearing, dimeric, wild type FICD its deAMPylation k_{cat} ({10 ± 1} × 10^{-3} s^{-1}, mean ± SEM) was significantly greater (by a factor of 1.8 ± 0.2) than that of monomeric FICD^{L258D} ({5.7 ± 0.4} × 10^{-3} s^{-1}). The monomerisation-induced (proportional) decrease in k_{cat} is very similar to that observed for the respective decrease in k_{cat}/K_M (**Figure 2.3.7).**

A comparison of the turnover numbers calculated here and the previously derived deAMPylation catalytic efficiencies also facilitates calculation of monomeric and dimeric K_M values for BiP-AMP substrate — suggesting approximate Michaelis constants of 16 ± 2 µM for dimeric, wild type FICD and 17 ± 2 µM for monomeric FICD^{L258D} (mean ± SEM). One can also extrapolate that monomerisation of FICD must increase the effective K_D for BiP-AMP by a factor of 1.9 ± 0.4 (mean ± SEM of the estimated fold-change). This accords with the poorer binding of FICD$^{L258D\text{-}H363A}$, relative to FICD^{H363A}, to immobilised BiP-AMP measured by BLI (**Figure 2.3.2**). Furthermore, the k_{cat} and K_M values derived for dimeric FICD are in good agreement with those previously obtained from substrate titration and Michaelis-Menten

analysis of GST-FICD: k_{cat} {9.9 ± 0.9} × 10^{-3} s^{-1} and K_M 16 ± 3 µM (best-fit ± SE) (Preissler *et al*, 2017a). This adds credibility to the methods of k_{cat}/K_M and k_{cat} determination employed in the present study.

Chapter 4.4: Monomerisation regulates differential substrate binding kinetics

The monomeric FICD-containing AMPylation complex is particularly sensitive to ATP-mediated destabilisation

The enzymatic analysis conducted above suggests that FICD is able to modulate its deAMPylation k_{cat} in response to changes in its oligomeric state, whilst maintaining a relatively consistent K_M. It therefore appears that differential substrate affinities may help potentiate the changes enacted at the level of FICD's active site by monomerisation and dimerisation. For example, if a dimerisation-induced increase in deAMPylation k_{cat} were to occur without a compensatory decrease in the K_D for BiP-AMP, this would result in a proportional increase in deAMPylation K_M. If enzyme substrate concentrations were not much greater than the (new) K_M value this would also mean that a 1.8-fold increase in k_{cat} would translate into less than a 1.8-fold increase in deAMPylation activity. The differential substrate binding affinities possessed by monomeric and dimeric FICD may, therefore, contribute to the oligomerisation state-dependent reciprocal regulation of BiP AMPylation/deAMPylation.

The FP-based in vitro deAMPylation assays, discussed above, were conducted in conditions of no excess ATP or other nucleotide. As revealed in the BLI assays, addition of ATP to the buffer solution is able to stimulate dissociation of both monomeric and dimeric FICD from immobilised BiP-AMP (**Figure 2.3.2** and **Figure 2.3.4**). Destabilisation of the complex presumably occurs via competition of the exogenous nucleotide with the BiP-linked AMP moiety for the Fic domain active site, during a multi-step dissociation process.

However, it was also observed that the dissociation of both monomeric and dimeric FICD from unmodified BiP:ATP was stimulated by the presence of ATP (**Figure 2.3.2** and **Figure 3.2.1**). In this instance there is no possibility for a mechanism involving direct competition of nucleotide with a covalently attached AMP moiety, suggesting that there may be some form of allosteric mechanism at play. Moreover, it appeared from these BLI experiments that monomeric FICD was more sensitive to the addition of ATP in the (second) dissociation phase

than dimeric FICD. As ATP is the co-substrate for BiP-AMPylation, a reaction massively favoured by FICD monomerisation, this phenomenon warranted further investigation.

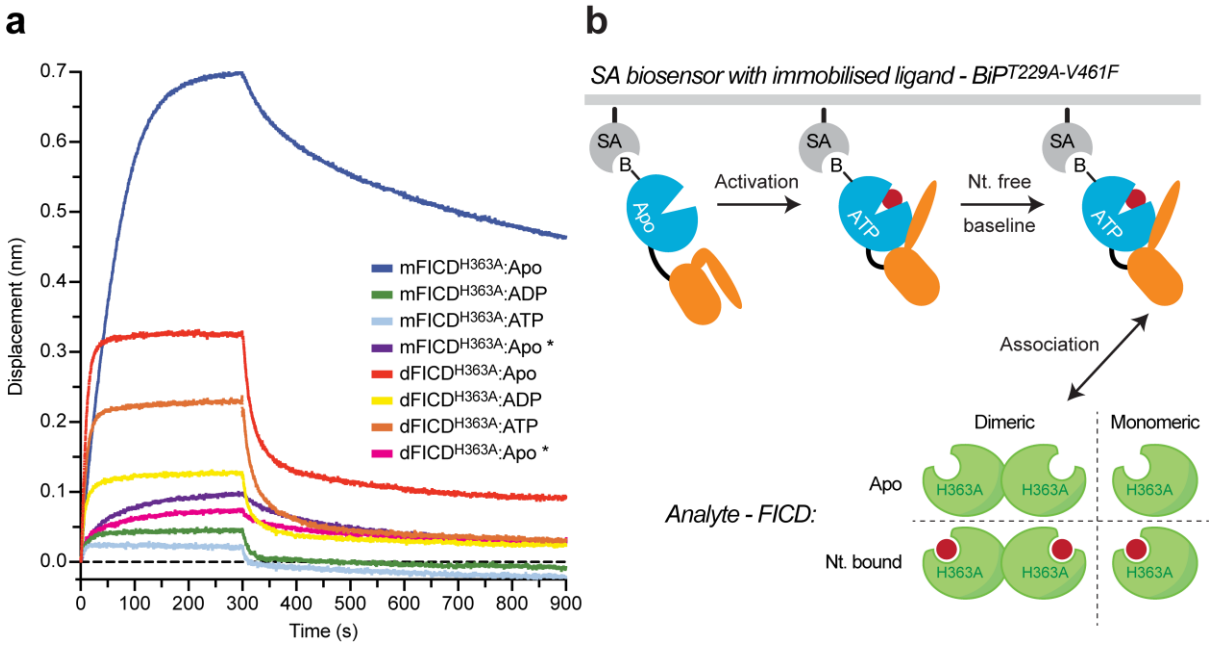

Figure 4.4.1: The binding of nucleotide to FICD enfeebles AMPylation complex formation. a, BioLayer interferometry (BLI) derived association and dissociation traces of monomeric FICD$^{L258D-H363A}$ (mFICD^{H363A}) or dimeric FICD^{H363A} (dFICD^{H363A}) from immobilised biotinylated BiP$^{T229A-V461F}$ in absence or presence of nucleotides. Unless indicated (*), BiP was saturated with ATP before exposure to FICD variants. A representative set of traces from n = 3 independent experiments is shown. Note, the binding of mFICD^{H363A} was more affected by presence of (saturating concentrations of) ATP (8 mM) and ADP (2 mM). **b,** Schematic of the BLI protocol used for testing the BiP:ATP binding response of FICD analytes to the presence of different nucleotides (as used to analyse the non-* samples in **a**).

I previously demonstrated that immobilised BiP can be bound to ATP and remain in its ATP-state for prolonged periods of time whilst immersed in nucleotide free buffer (**Figure 2.3.1**). This enables a deconvolution of the effect of nucleotide, on protein binding kinetics, mediated through BiP nucleotide binding and FICD nucleotide binding. Consistent with **Figure 2.3.1** and the revelation that FICD recognises the ATP-state of its AMPylation substrate, the binding of both apo monomeric or dimeric FICD to unmodified apo BiP was considerably accentuated by activation of the BiP ligand with ATP (**Figure 4.4.1**). As previously noted in the absence of extra nucleotide apo monomeric FICD$^{L258D-H363A}$ bound more tightly to immobilised BiP:ATP than apo dimeric FICD^{H363A}. Saturating concentrations of both ATP and ADP impaired the ability of both FICDs to bind the BiP ligand. However, this impairment was much more pronounced for FICD$^{L258D-H363A}$. Moreover, ATP actually had a reproducibly greater effect on

monomeric FICD binding than ADP (which contrasts with the corresponding nucleotide responses of dimeric FICD analyte binding).

It is clear that both ATP and ADP binding to FICD can elicit a diminution in its affinity for BiP:ATP, which is appreciable both in the association and dissociation phase of either FICD analyte. However, as noted previously, the kinetic profiles of FICD binding are multiphasic, which makes extraction of meaningful K_Ds (or other kinetic binding parameters) problematic. Therefore, in an effort to quantify the different sensitivities towards nucleotide, exhibited by monomeric and dimeric FICD, the effect of addition of nucleotide to a preformed pre-AMPylation complex (as in **Figure 2.3.2** and **Figure 3.2.1**) was revisited with modifications.

In this instance a single dissociation event was analysed in order to increase the analysable dissociation signal and to facilitate more reliable exponential decay curve fitting (**Figure 4.4.2)**. Where indicated 8 mM ATP was used to supplement the dissociation well buffer solution. This concentration was assumed to be saturating (being considerably above the low millimolar $K_{½}$s of ATP-induced T_m increase, **Figure 4.1.1**) and non-rate limiting for the dissociation reactions under investigation. That is to say, at a sufficiently high concentration such that the association rate of ATP into any exposed FICD active sites should be considerably faster than the rate of FICD dissociation from BiP:ATP. This later assumption is reasonable given the very high on rates generally associated with small molecule binding events and the sizeable concentration of ATP. The use of ATP during the dissociation phase also biases the analysis against any potential of confounding effects of the nucleotide on the status of the BiP ligand. As BiP:ATP has already been demonstrated to be a much better FICD binding partner, the addition of ATP to the dissociation well should actually strengthen the interaction from the point of view of the immobilised ligand (either by direct nucleotide exchange of any NBD-bound ADP, resulting from the small amount of residual $BiP^{V461F\text{-}T229A}$ ATPase activity, with the excess ATP in solution or replenishment of any ATP losses from the BiP NBD).

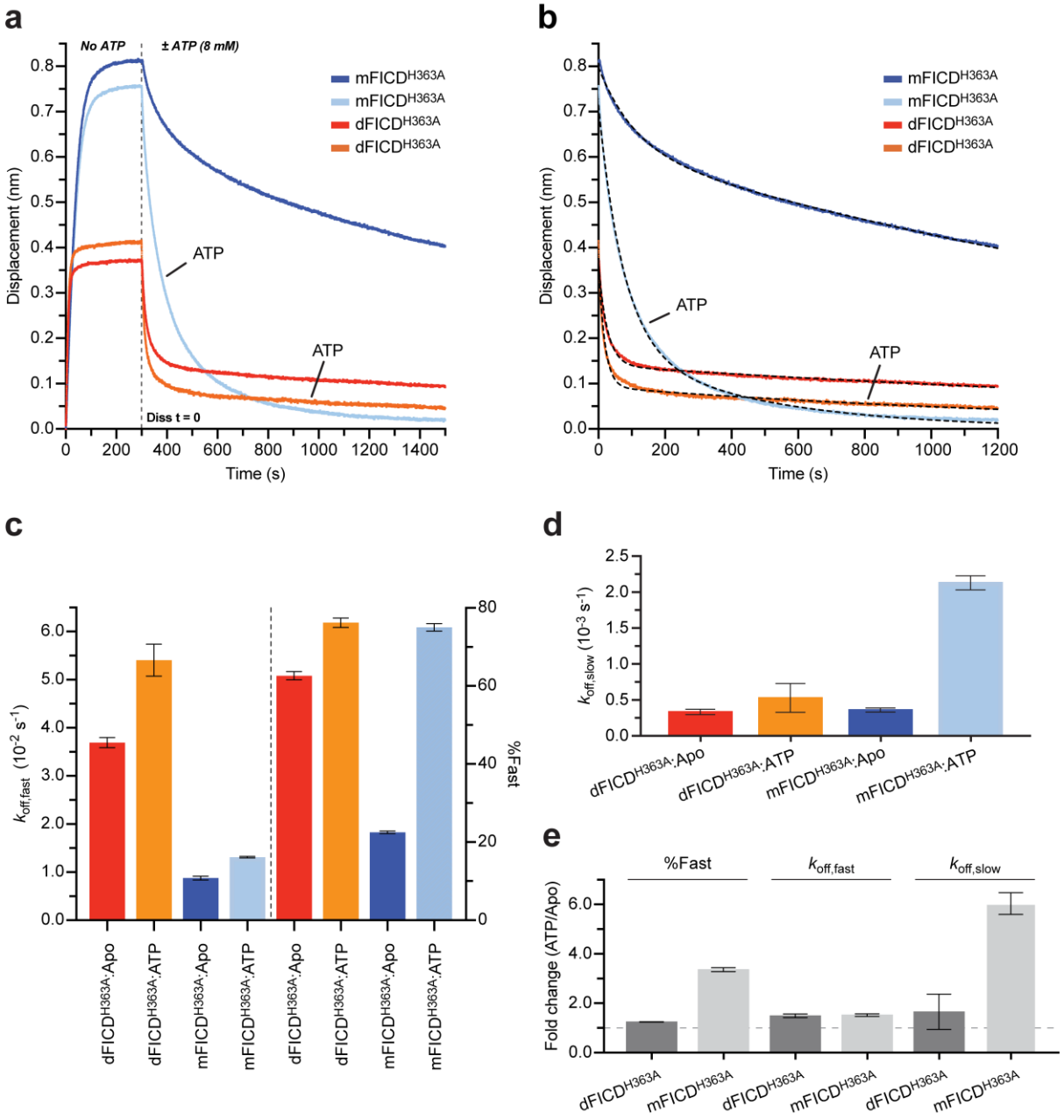

Figure 4.4.2: ATP destabilises the pre-AMPylation complex. a, A representative BLI experiment is shown. Similar to the setup employed in **Figure 4.4.1**, apo FICD analytes (all at 250 nM) were loaded onto BiP:ATP in the association phase (all in a no nucleotide buffer). At the start of the dissociation phase (indicated by the dashed vertical line), the pre-AMPylation complexes were transferred into wells containing only buffer (no analyte) ± ATP (as indicated). **b,** Quantification of the biphasic dissociation traces from **a**. The start of the dissociation phase in **a** was taken as t = 0. The best-fit biexponential decay curves are overlaid with dashed black lines. **c–e,** The parameters extracted from biphasic fitting of the FICD dissociation traces, all presented as mean values ± SD from n = 3 independent experiments. In **c** and **d,** bars are colour-matched to the BLI traces presented in **a** and **b**. Note, the $k_{off,fast}$, the percentage of the dissociation phase attributable to fast dissociation (%Fast) and the $k_{off,slow}$ parameters of both monomeric and dimeric FICD were all increased by ATP. However, the proportional effect of ATP (highlighted in **e**) was considerably greater for monomeric FICD with more pronounced sensitivity in terms of dissociation %Fast and $k_{off,slow}$.

The resulting analysis demonstrated a clear effect of ATP on the disassembly of dimeric and monomeric FICD-containing pre-AMPylation complexes (**Figure 4.4.2)**. The overall rate of dimeric FICD dissociation is faster (relative to monomeric FICD dissociation) both with and without ATP in the dissociation buffer. This is consistent with previous results that monomeric FICD binds its AMPylation substrate more avidly than dimeric FICD (**Figure 3.2.1**). In light of **Figure 4.4.1,** this suggests that ATP also has a very significant effect on the on rate(s) of monomeric FICD. Furthermore, although the overall dissociation rate in the presence of MgATP is greater for dimeric than monomeric FICD, the relative response of monomeric FICD dissociation to ATP is much greater than that exhibited by dimeric FICD (**Figure 4.4.2e**). The effect of MgATP was especially significant with respect to modulating monomeric FICD's rate of slow dissociation ($k_{off,slow}$) and the percentage of the dissociation attributed to the fast phase (%Fast).

Modelling the active site of the AMPylating Michaelis complex

As the overall manner of FICD•BiP-AMP engagement (captured crystallographically) is shared by the AMPylation complex, it stands to reason that AMPylation complex active sites can be approximated by alignment of the deAMPylation complex (after removal of the AMP moiety) and ATP-bound FICDs (**Figure 4.4.3**). BiP Thr518 can be accommodated by the active site of MgATP-bound, monomeric FICD and the resulting state appears conducive to AMPylation (**Figure 4.4.3a**). This supports two previous assertions — firstly, that FICD similarly engages BiP:ATP and BiP-AMP and, secondly, that monomeric FICD binds MgATP in an AMPylation competent conformation. Conversely, as anticipated, Thr518 does not bind in a position in line with the α-β-phosphoanhydride bond of ATP bound to dimeric, wild type FICD (**Figure 4.4.3b**). Moreover, Thr518 in the modelled dimeric FICD system would result in a significant steric clash with the ATP α-phosphate (**Figure 4.4.3b** inset). Therefore, it is feasible that there may be some degree of direct competition between the binding of BiP's unmodified Thr518 target residue and ATP within the active site of wild type FICD.

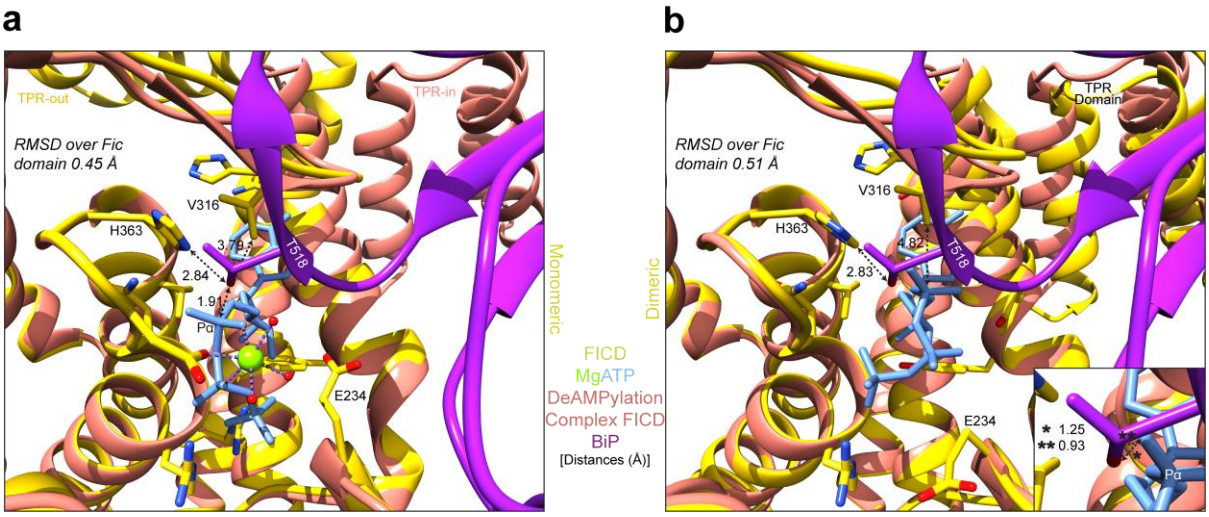

Figure 4.4.3: BiP's Thr518 can be accommodated in the active site of ATP-bound monomeric FICD. a, A pseudo AMPylation complex created by structural alignment, illustrating the ability of monomeric FICD bound to MgATP (yellow with purple nucleotide) to accommodate BiP's Thr518 in a catalytically competent conformation. The model is derived by alignment of $FICD^{L258D}$:ATP with the state 1 deAMPylation complex (FICD in orange; BiP in purple), over the Fic domain residues 213–426. Oγ of BiP's Thr518 (restored to its non-AMPylated state by in silico removal of the AMP moiety) is in-line with the Pα-O3α-phosphoanhydride bond and can be deprotonated by His363. Though not modelled here, flexibility in the Fic flap, FICD's Val316 and BiP($\ell_{7,8}$) likely permit Pα and Oγ(Thr518) to attain a distance consistent with an initial substrate engagement state. **b,** As in **a** but with alignment of dimeric FICD bound to ATP in a catalytically incompetent mode. Note the severe clash between Thr518 and the ATP α-phosphate. Inset, interatomic distances between BiP's Thr518 and the α-phosphate are annotated (* and **). Small rearrangements in the position of Thr518 will not be able to generate a sterically permissible and catalytically competent active site.

However, the observation that monomeric FICD-containing pre-AMPylation complexes are more sensitive to nucleotide (than dimeric FICD) speaks against direct substrate competition being the mechanism responsible for the nucleotide sensitivity observed in the above BLI experiment (**Figure 4.4.2**). Moreover, the fact that ADP can also elicit a similar response to ATP in both monomeric and dimeric FICD (**Figure 4.4.1**) is further evidence against an appreciable role for direct competition with BiP within the active site — as ADP binds dimeric, wild type FICD with high affinity (K_D 1.5 μM) and with its α-phosphate in the canonical position (see PDB 4U0U; Bunney *et al*, 2014), as exemplified by the ATP molecule in **Figure 4.4.3a**.

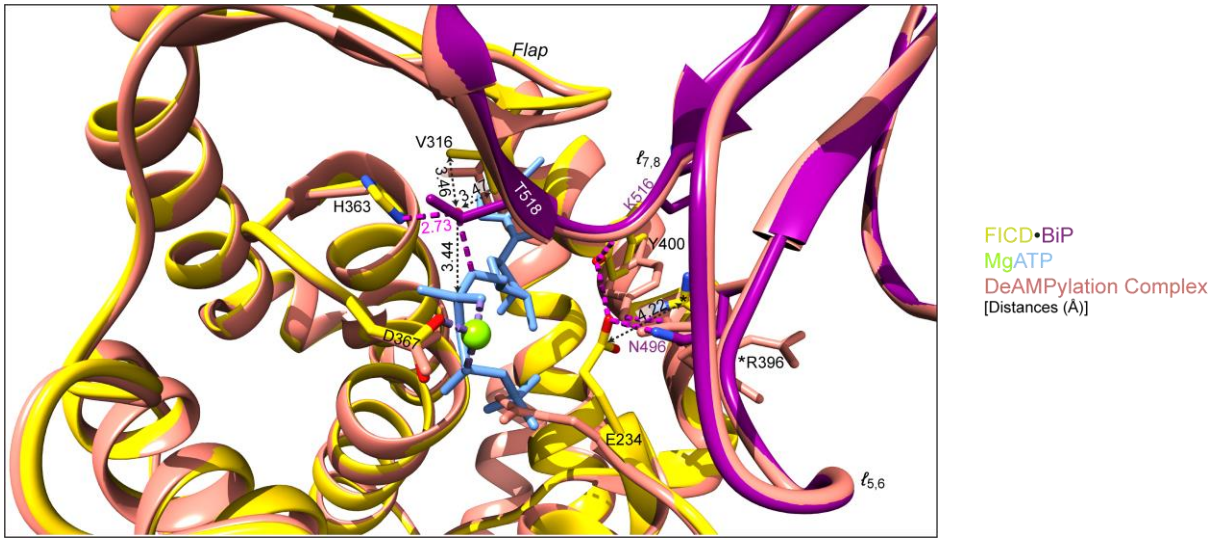

Figure 4.4.4: A putative AMPylation complex active site. The starting structure presented in **Figure 4.4.3a** (purple 'unmodified' BiP from the deAMPylation complex and yellow FICD^{L258D}:MgATP) was energy-minimised to produce the modelled AMPylation complex active site (FICD•BiP with MgATP). The derived local energy minimum is also superposed with the original state 1 deAMPylation complex (FICD•BiP-AMP with the AMP moiety removed, orange). Selected intermolecular hydrogen bonds (pink dashed lines) and interatomic distances (black dashed lines) are annotated. Note, unmodified BiP is able to form an intermolecular β-sheet with the flap of FICD^{L258D} whilst position its target reside Thr518 in line for nucleophilic attack into the ATP α-phosphate, within hydrogen bonding distance of the general base His363 and without any steric clashes. In the AMPylation complex Glu234 may form direct intermolecular contacts. Minimisation was carried out with the original position of ATP and FICD's Arg374 fixed. A portion of both FICDs' α-helical linkers and the complete TPR domains (in the background in **Figure 4.4.3**) are omitted for clarity.

Through minimisation of the hybrid AMPylation complex modelled in **Figure 4.4.3a**, speculative inferences about the nature of oligomerisation and FICD-nucleotide dependent changes in BiP substrate affinity can be made. In the deAMPylation complex, FICD's Tyr400 forms a hydrogen bond to BiP's SBDβ $\ell_{5,6}$ Asn496. The energy minimised FICD is based on the FICD^{L258D}:MgATP structure, in which Glu234 faces away from the active site and no longer forms the AMPylation inhibiting salt bridge to the Fic motif Arg374 (**Figure 4.4.4**). As such Glu234 in the minimised AMPylation complex forms a hydrogen bond to BiP's Asn496 and an intramolecular hydrogen bond to FICD's Tyr400 (**Figure 4.4.4**). This in turn permits Tyr400 to form a different intermolecular hydrogen bond to the main chain of BiP's Ly516 (within $\ell_{7,8}$ of the SBDβ). The position of the displaced monomeric FICD Glu234 is potentially stabilised by being within salt bridge forming distance of FICD's Arg396. The modelled end result is an intramolecular salt bridge-stabilised, intermolecular hydrogen bond network in which there is a net addition of one intermolecular hydrogen bond in the protein-protein

interface relative to the deAMPylation complex (**Figure 4.4.4**). This may be able to provide extra stabilisation of the target residue bearing BiP SBDβ $\ell_{7,8}$.

Speculation on the nature of FICD's oligomeric state–linked pre-AMPylation complex affinity and nucleotide sensitivity

If monomeric FICD possesses a more flexible α_{inh} and Glu234, as proposed in **Chapter 4.2**, it is plausible that the bolstered intermolecular hydrogen bond network (modelled in **Figure 4.4.4**) may also be favoured by monomerisation. This could explain the observed increase in BiP:ATP affinity induced by monomerisation of FICD (**Figure 2.3.2**). Conversely, in the context of binding BiP-AMP, Glu234 has a direct role in stabilisation of the Mg^{2+} coordination complex (**Figure 4.3.2**). This is not a role played by Glu234 during AMPylation as the divalent cation is tightly coordinated between the α and β-phosphates of ATP and likely enters the active site with the nucleotide. It is therefore plausible that the binding of BiP-AMP (and a Mg^{2+} ion) disfavours the hypothetical AMPylation complex-favouring Glu234 conformation. Correspondingly, increased Glu234 flexibility may also directly destabilise the deAMPylation complex by weakening the ionic interactions afforded by stable divalent cation positioning (as well as causing the aforementioned reduction in deAMPylation k_{cat} through less efficiently coordinating a catalytic water). This logic could indeed rationalise the observed monomerisation-induced decrease in FICD affinity for BiP-AMP (**Figure 2.3.2**).

Inspired by the modelled AMPylation complex active site, one could speculate further as to the nature of the allosteric pre-AMPylation complex destabilisation induced by nucleotide. The narrow ATP γ-phosphate to FICD Glu234 tolerances, and incomplete γ-phosphate electron density within the isolated $FICD^{L258D}$:ATP crystal structure (**Figure 4.1.3** and **Figure 4.1.4**) suggests that MgATP binding may itself induce greater displacement of FICD's α_{inh} and Glu234 (via steric and electronic repulsion) than that captured crystallographically. Addition of MgATP to the active site of monomeric FICD may, in this way, reduce the propensity for intermolecular Glu234 contacts. This hypothesis is also consistent with the similar, albeit reduced, response of monomeric FICD-containing pre-AMPylation complexes to ADP, as MgADP binding has previously been observed to have some electronically repulsive effect on the disposition of Glu234 (causing the population of two alternative Glu234 conformations in dimeric FICD soaked with MgADP; PDB 4U0U).

If dimeric wild type FICD is also able to sample the Glu234 flipped out state, as evidenced by PDB 4U0U (Bunney *et al*, 2014), it is possible that a small (potentially transient) population

of dimeric FICD-containing pre-AMPylation complexes is similarly affected by nucleotide binding in the active site. This would rationalise the (reduced) sensitivity of dimeric FICD-containing AMPylation complexes to nucleotide.

FICD's Tyr400 residue also forms direct hydrophobic contacts to the adenosine portion of nucleotides bound in FICD's active site in all nucleotide-bound FICD structures. Furthermore, the hydrophobic contacts to the adenosine are more pronounced in isolated FICD:nucleotide complexes than in the deAMPylation complex, where Tyr400 moves away from the adenosine to also form an intermolecular hydrogen bond with BiP (**Figure 4.4.4**). Thus, it is also a possibility that nucleotide may directly affect pre-AMPylation complex binding kinetics by directly affecting the conformation of nucleotide/BiP interacting residues in the active site. Furthermore, as contacts between the Fic domain and TPR domain have already been demonstrated to affect AMPylation and deAMPylation activity it would not be surprising if more long-range allosteric mechanisms also contribute to the particular sensitivity of the monomeric FICD-containing pre-AMPylation complex to ATP.

Chapter 4.5: ER energy status may modulate FICD's monomer-dimer equilibrium

The crystal structures of FICD:nucleotide complexes revealed that FICD's oligomeric state can impact significantly on the mode of ATP binding. **Figure 4.4.1** and **Figure 4.4.2** indicate that nucleotide binding within FICD can induce allosteric effects on FICD conformation (which are able to affect AMPylation complex stability). Together, these observations suggest that bidirectional intramolecular signalling from the FICD dimer interface to the nucleotide-binding active site may be possible and that ATP binding in FICD's active site may also influence the oligomeric state of the protein. Furthermore, I also speculated above that the relationship between α_{inh}/Glu234 flexibility and ATP binding may be bidirectional. That is to say, that monomerisation-induced Glu234 flexibility facilitates AMPylation competent MgATP binding and, reciprocally, that ATP binding may also stimulate greater deviation of the Glu234/α_{inh} position from the basal AMPylation inhibiting conformation of the side chain. If ATP binding does indeed contribute to destabilising the α_{inh}, this may then feedback through the same dimer-relay to weaken the dimer interface.

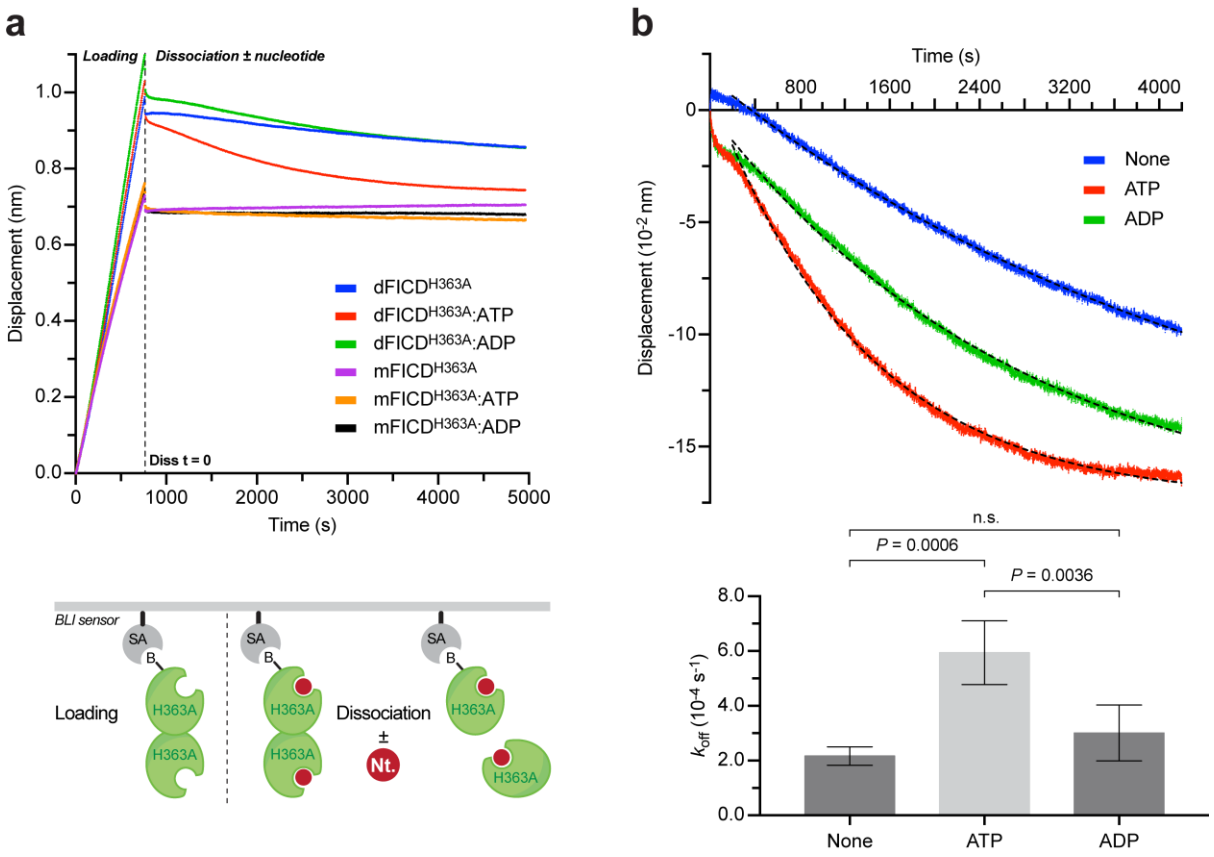

Figure 4.5.1: The FICD dimer off rate is increased by ATP. **a,** Above, representative BLI traces of an FICD dimer dissociation experiment. 3 nM of either N-terminally biotinylated dimeric FICD^{H363A} (dFICD) or biotinylated monomeric FICD$^{L258D\text{-}H363A}$ (mFICD) were incubated with a 100-fold molar excess of non-biotinylated FICD^{H363A} prior to biosensor loading. The legend indicates the ligand present in the dissociation buffer (at 5 mM), if applicable. Below, schematised version of dFICD loading and dissociation steps. **b,** Above, representative FICD dimer dissociation experiment derived from the traces in **a** following subtraction of the respective mFICD background drift traces. Best-fit single exponential decay curves are overlaid (black dashed lines). Below, quantification of the dimer dissociation rates in different nucleotide buffer conditions from n = 4 independent experiments. Statistical analysis was performed using a one-way ANOVA followed by a Tukey test for post hoc analysis. *P*-values are annotated (n.s.; not statistically significant, $P > 0.05$).

To investigate the hypothesis of nucleotide-modulated oligomerisation, N-terminally biotinylated FICD^{H363A} was incubated with a 100-fold molar excess of non-biotinylated FICD^{H363A}. This permitted all biotinylated FICD^{H363A} molecules to release and exchange their homodimeric binding partner for non-biotinylated FICD^{H363A} protomers. The resulting semi-biotinylated heterodimeric FICD^{H363A}s were loaded onto a BLI streptavidin biosensor. The dissociation of non-biotinylated FICD^{H363A} from its immobilised partner was then observed by quasi-infinite dilution into buffers varying in their nucleotide composition (as illustrated in **Figure 4.5.1a**). Biotinylated, monomeric FICD$^{L258D\text{-}H363A}$ was similarly incubated with the same excess of non-biotinylated FICD^{H363A} and also loaded onto the BLI tip (in order to provide

internal controls for baseline drift). It was found that ATP but not ADP induced a 3-fold increase in the dimer dissociation rate (k_{off}, **Figure 4.5.1b**). This is suggestive of a mechanism whereby changing ATP/ADP ratios in the ER may modulate the oligomeric state of FICD but does not preclude the possibility of a compensatory increase in dimer association rate (k_{on}).

In order to establish whether ATP is indeed able to modulate FICD's monomer-dimer equilibrium (and not simply cause proportional increases in dimer k_{off} and k_{on}), I developed a dimerisation-sensitive fluorescent FICD probe. Various residues were trialled for their ability to either permit a FRET or fluorophore self-quenching based readout of FICD oligomerisation state. Cysteines were introduced by site directed mutagenesis into the background of a dimerisation-competent, cysteine-free, catalytically inactive FICD$^{H363A\text{-}C421S}$. Mutated residues at surface-exposed positions predicted to lie within a FRET distance across the dimer interface were decorated with cysteine-reactive fluorophore derivatives. Residues on the N-terminal extension of the Fic domain (Ser241Cys, Lys256Cys) were either very poorly labelled or caused destabilisation of the protein upon being labelled, resulting in significant aggregation (see **Figure 1.3.2** for an illustration of the core Fic domain and its less conserved extensions). Stable and monodisperse fluorescent probes were engineered by the introduction of cysteine substitutions into the surface of the core Fic domain (Ser288Cys and Arg308Cys). FICD$^{S288C\text{-}H363A\text{-}C421S}$ was found to label efficiently with tetramethylrhodamine (TMR)-maleimide and to produce the greatest signal-to-noise optical readout of FICD's oligomeric state. Moreover, the original serine side chain was not observed to be engaged in inter-protomer contacts.

To validate the ability of FICD$^{S288C\text{-}H363A\text{-}C421S}$-TMR (FICD-TMR) to report on FICD's oligomerisation status, the probe was incubated with an escalating concentration of unlabelled dimerisation-competent FICD^{H363A}. It was found that dimeric (unlabelled) FICD^{H363A}, but not unlabelled monomeric FICD$^{L258D\text{-}H363A}$, led to a progressive increase in the fluorescence of FICD-TMR (**Figure 4.5.2a**). This observation is consistent with a reduction in fluorophore self-quenching as FICD-TMR homodimers are converted to heterodimers containing only one labelled protomer.

The dimerisation-sensitive probe was used to investigate the ability of ATP and ADP to modulate the FICD monomer-dimer equilibrium in solution. In agreement with the BLI experiment that reported on an ATP-stimulated FICD dimer dissociation rate from an immobilised FICD protomer (**Figure 4.5.1**), ATP was observed to increase the proportion of monomeric FICD-TMR in a concentration-dependent fashion (**Figure 4.5.2b**). Conversely,

supplementing the dissociation buffer with ADP appeared to push the FICD equilibrium towards the dimer and also effectively antagonised the monomerising effect of ATP (**Figure 4.5.2b**). Moreover, the apparent nucleotide-dependent modulation of FICD's oligomeric state occurs within a plausible physiological range of ER-luminal ATP and ADP concentrations. Together, these observations attest to an allosteric coupling of FICD's oligomeric state to the identity of the bound nucleotide and suggest a means of physiologically transducing changing levels of ER stress to alterations in overall BiP modification status.

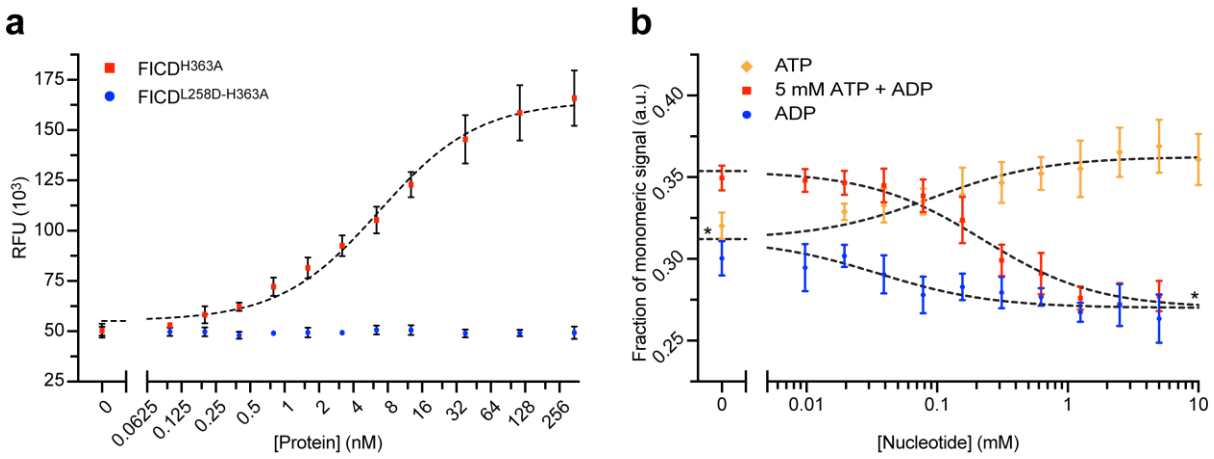

Figure 4.5.2: ATP stimulates FICD monomerisation. a, Validation of the fluorescent dimerisation probe. The dimerisation-sensitive TMR fluorescence of the labelled dimer (2.5 nM FICD-TMR) is dequenched specifically by equilibration with excess unlabelled dimerisation-competent FICD^{H363A} but not monomeric FICD$^{L258D-H363A}$. Mean values ± SD, from n = 3 independent experiments, are shown. RFU, relative fluorescence units. **b,** ATP increases, and ADP decreases, the proportion of monomeric FICD. Fluorescence measurement of nucleotide-dependent modulation of the FICD monomer-dimer equilibrium. The probe signal at each nucleotide condition is presented as a fraction of the completely monomeric FICD fluorescent signal (in other words, as a fraction of the fluorescent intensity of complete fluorophore dequenching). Regression lines from a one-site binding model are overlaid (black dashed lines in both **a** and **b**). *Plateaus were constrained to a shared best-fit value. Data shown are the mean ± SD from n = 4 independent experiments. a.u., arbitrary units.

Chapter 4.6: Conclusions

Here, I have dissected the mechanistic basis of the oligomerisation state-dependent switch in FICD enzymatic activity. In its dimeric state FICD can bind ATP (but not with a coordinating Mg^{2+} ion), although it will not do so in an AMPylation competent conformation. Monomerisation of FICD permits the binding of MgATP such that the ATP α-phosphate is conducive to the in-line nucleophilic attack required for BiP AMPylation. It appears that the change in AMPylation permissibility of the FICD active site stems from a monomerisation-

induced increase in gatekeeper Glu234 flexibility (and possibly also increased dynamism in the α_{inh}). These observed changes likely play a very significant role in the considerable AMPylation rate-enhancement of monomeric FICD over dimeric FICD (summarised in **Figure 4.6.1**).

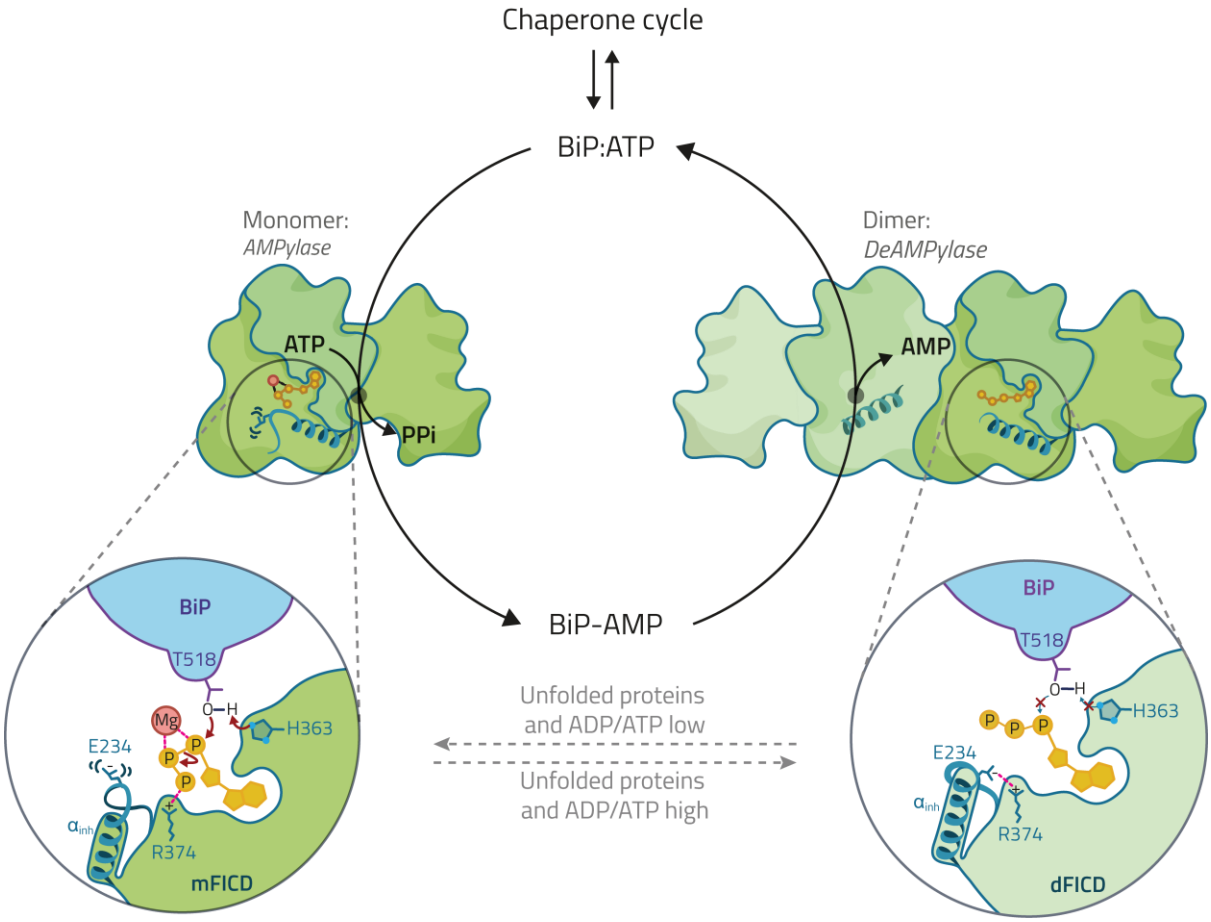

Figure 4.6.1: FICD monomerisation increases AMPylation activity. Monomerisation of FICD increases α_{inh} and gatekeeper Glu234 flexibility. This permits AMPylation competent binding of MgATP within the active site of monomeric FICD (mFICD; left-hand side). The dimeric FICD (dFICD) enzyme, with its more rigid Glu234, inhibits the positioning of the ATP γ-phosphate, which would otherwise engage the Fic motif Arg374. If ATP binds to the dimeric FICD active site it does so without the coordination of a Mg^{2+} cation and in an AMPylation incompetent conformation — incompatible with in-line nucleophilic attack into the scissile Pα-O3α phosphoanhydride bond (right-hand side). Monomeric FICD is therefore a much better BiP AMPylase than dimeric FICD. Changing levels of ER stress (possibly through indirect modulation of ER energy status) alters the monomer-dimer equilibrium so as to match the levels of inactive, AMPylated BiP to the burden of unfolded proteins.

Moreover, it seems likely that the process of crystallisation may mask the full effects of the monomerisation-induced increase in α_{inh} and Glu234 flexibility in solution — leading to crystallographically induced dimerisation within the monomeric $FICD^{L258D}$:nucleotide

structures and (presumably) also to the stabilisation of the dimer-relay hydrogen bond network. Such considerations could explain the comparatively small differences in the position of Glu234, but stark differences in nucleotide conformation, observed between the wild type and monomeric or dimer-relay mutated FICD structures. In solution, disruption of the dimer-relay network (either by mutation and/or monomerisation of FICD) may well induce partial unfolding of α_{inh} from the catalytic Fic domain. This then permits AMPylation competent binding of MgATP and results in the observed (considerable) relief of Glu234-mediated AMPylation autoinhibition. Conversely, the crystallisation process quite possibly favours rearrangements, including α_{inh} refolding and crystallographic reconstitution of the dimer interface, and convergence towards a low energy state (the one stabilised in solution by dimerisation). This then outweighs the energetic penalty of the resulting (crystallographically-induced) electronically or sterically strained carboxylate-carboxylate (Glu234-Glu263) or glutamate-phosphate contacts observed in the AMPylation competent structures (**Figure 4.1.4**).

Somewhat unsurprisingly, the increased Glu234 flexibility of monomeric FICD also reduces the catalytic efficiency and maximal velocity of BiP deAMPylation. As elucidated in **Chapter 2.4**, Glu234 plays an essential role in the catalysis of the deAMPylation reaction, aligning and activating an attacking catalytic water molecule for in-line nucleophilic attack into the phosphodiester bond linking BiP to its AMP moiety. In this chapter, I present a crystallographically captured corollary of decreased Glu234 stability in the context of FICD-mediated deAMPylation — an increased likelihood of Glu234 causing a shift in the Mg^{2+} coordination complex and being unable to effectively stabilise a catalytic water molecule (summarised in **Figure 4.6.2**). As in the case of the FICD:nucleotide crystal structures, the nature of the crystallisation process may underestimate the destabilising effect of monomerisation on the α_{inh} and gatekeeper Glu234.

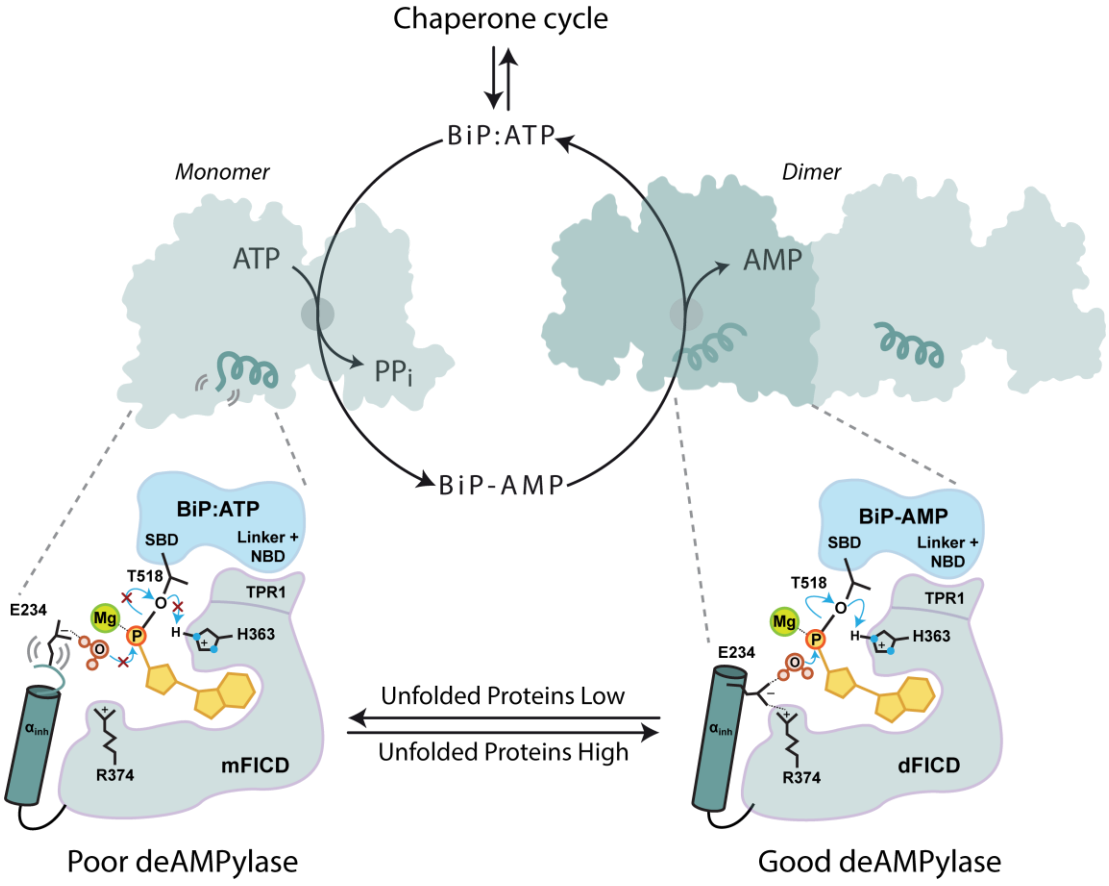

Figure 4.6.2: FICD dimerisation increases deAMPylation activity. BiP deAMPylation requires the positioning and activation of a catalytic water molecule in-line with the Pα-Oγ(Thr518) phosphodiester bond. These ends can only be met by Glu234 (see right-hand side). As monomerisation increases the flexibility of this gatekeeper residue, which sits atop the α_{inh}, it also decreases the ability for Glu234 to stably position a water molecule conducive to deAMPylation (left-hand side). Coordinated modulation of the FICD pool between more monomeric (mFICD) and more dimeric (dFICD) states therefore serves to reciprocally regulate the two functionally opposite enzymatic reactions catalysed by FICD, despite a similar mode of ATP-state BiP(±AMP) substrate binding.

It was also initially revealed in **Chapter 2.3** that monomeric FICD was able to bind unmodified BiP:ATP more avidly than dimeric FICD and, conversely, that dimeric FICD was able to bind BiP-AMP more tightly than monomeric FICD (**Figure 2.3.2**). These reciprocal substrate binding affinities align with the division of labour between monomeric and dimeric FICD; the former being a good AMPylase (binding unmodified BiP:ATP as its substrate) and the latter being a good deAMPylase (binding BiP-AMP as its substrate). Indeed, in the case of deAMPylation I have experimentally demonstrated that despite dimerisation increasing the deAMPylation k_{cat}, the concomitant increase in BiP-AMP affinity enables the K_M to remain unchanged. Moreover, the AMPylation complex affinity appears to be influenced by FICD-

bound nucleotide, with monomeric FICD particularly sensitive to the allosteric, destabilising effect of ATP.

Allosteric affinity-modulation induced by ATP, may stem from feedback between FICD's Glu234 or Tyr400 and the bound ATP molecule — depreciating potential intermolecular contacts with BiP's SBDβ that are made or stabilised by these Fic domain residues. There is also the additional possibility that long range allostery may also contribute to this observed nucleotide sensitivity phenomenon. For example, ATP binding within the Fic domain may affect other BiP contacting areas of FICD such as the dimer interface adjacent Glu260 region which forms hydrophobic contacts to parts of BiP's SBDβ $\ell_{5,6}$. Moreover, communication between the Fic domain and TPR domain has already been shown (in **Chapters 2** and **3**) to be important for FICD-mediated AMPylation and deAMPylation. It is therefore also plausible that the allosteric effect of FICD nucleotide binding may exploit this axis. Interestingly, based on molecular dynamics simulations, long range allostery extending from the ATP binding site to a distal target recognition module (affecting AMPylation substrate affinity) has also been implicated in the functioning of another Fic protein — IbpA (Khater & Mohanty, 2015b).

As ATP is the co-substrate for FICD-mediated AMPylation the utility of this ATP-induced destabilisation could be twofold. Firstly, by increasing the AMPylation complex K_D, the presence of ATP within the ER will increase the effective K_M for unmodified ATP-state BiP (the other AMPylation co-substrate). Having a high K_M (given that the total concentration of BiP in the ER may be in the order of hundreds of micromolar) may allow FICD-mediated AMPylation to be responsive to changing concentrations of ATP-state BiP in the ER. A K_M in the order of or greater than the range of luminal BiP:ATP concentration is necessary for the hypothesised existence of substrate-level regulation of BiP AMPylation, discussed earlier. Conversely, if the BiP:ATP concentration were considerably greater than the AMPylation K_M the rate of FICD-mediated AMPylation would cease to be sensitive to the amount of BiP:ATP (with the enzyme simply working at or close to its maximum velocity). Secondly, tight binding of an enzyme-substrate complex can be anti-catalytic (by increasing the Gibbs free energy of activation). It is therefore plausible that enzyme co-substrate (ground state) destabilisation, observed to be prevalent in the monomeric FICD-containing AMPylation complexes, may serve a catalytic function — reducing the Gibbs free energy of activation for the AMPylation reaction as observed in a number of other enzymes (Andrews *et al*, 2013; Ruben *et al*, 2013). As it is very likely that the co-substrates for BiP AMPylation will/must bind in a sequential

fashion, selective enzyme-substrate destabilisation in the context of both substrates may greatly increase both the efficiency and k_{cat} of monomeric FICD catalysed AMPylation.

In further support of the potential for long range and bidirectional allostery being prevalent across FICD, it was found that ATP and ADP were able to reciprocally modulate FICD's monomer-dimer equilibrium. Binding of ATP within the active site of dimeric FICD pushed the FICD equilibrium towards the monomeric state and also increased the dimer dissociation rate. Contrarily, a low (nanomolar) concentration of FICD binding ADP actually increased the proportion of homodimeric molecules in solution. In addition, the observed sensitivity of the FICD monomer-dimer equilibrium to nucleotide occurred within a plausible dynamic range of ER luminal ATP and ADP concentrations.

The major ER-resident ATPase proteins are all chaperone proteins (BiP, Hsp90 and Hsp110 family proteins). Moreover, the chaperoning capacity and, by extension, ATPase content of the ER is dominated by BiP (Bakunts *et al*, 2017). As the ER lumen is spatially and presumably temporally delineated (by the ER membrane) from the ATP buffering systems which are prevalent within the cytosol of eukaryotic cells, it is plausible that the ATP/ADP ratio may respond to changing levels of unfolded protein load in the ER. For example, an increase in co-translational protein translocation into the ER will raise the concentration of unfolded nascent chain protein able to be bound by BiP molecules and other protein chaperones. Binding of these unfolded proteins by BiP molecules will stimulating the intrinsic ATPase activity of these chaperone proteins and potentially induce a drop in the luminal ATP/ADP ratio. In this model the decreased ATP/ADP ratio is directly sensed by the FICD pool, as a proxy of ER stress, and translated into a more dimer biased FICD equilibrium. This, in turn, facilitates increased deAMPylation of any inactive reserves of BiP (BiP-AMP) and thus increases BiP chaperoning capacity (without the need for the induction of the transcriptional and translational machineries of the canonical UPR) (**Figure 4.6.1**).

Chapter 5: Discussion

Chapter 5.1: General Summary

In this study I have discovered that both monomeric and dimeric FICD recognise BiP through specific engagement of the FICD target recognition module (its TPR domain) with a tripartite Hsp70 ATP state–specific surface (composed NBD-linker-SBDβ). Both oligomeric states of FICD also form additional contacts between their catalytic Fic domains and BiP's SBDβ ($\ell_{5,6}$ and $\ell_{7,8}$). BiP's SBDβ $\ell_{7,8}$ contains the target residue (Thr518) which is both AMPylated and deAMPylated by FICD in its single, bifunctional active site.

FICD scaffolds a very similar mode of BiP engagement in order to catalyse both BiP AMPylation and deAMPylation. This facilitates the selective binding of ATP-state unmodified BiP (BiP:ATP) and the intrinsically ATP-state biased AMPylated BiP (BiP-AMP), respectively. The ability for FICD to discriminate between BiP:ATP and BiP in a domain undocked ADP-state potentially facilitates substrate-level regulation of BiP AMPylation. Such a regulatory mechanism would allow the rate of BiP AMPylation to inversely correlate with the protein folding demand in the ER — by binding to BiP's SBD unfolded peptides stimulate BiP's ATPase activity and will therefore titrate BiP out of the ATP-state and into the client-bound ADP-state.

These findings rationalise previous observations pertaining to the exquisite selectivity of FICD-mediated AMPylation for BiP. For example, it has been demonstrated that FICD is only able to AMPylate BiP proteins that are allosterically coupled or, in other words, respond to ATP binding in the BiP NBD by domain docking. Moreover, FICD has an AMPylation preference for BiP mutants that are more biased towards the ATP-state and, in addition, FICD is unable to AMPylate the isolated SBD of BiP (which cannot assume the ATP-like conformation of the SBDβ subdomain) (Preissler *et al*, 2015b). Likewise, although full-length BiP-AMP is intrinsically biased towards the ATP-state, FICD is also unable to deAMPylate the isolated BiP SBD (Preissler *et al*, 2017a).

FICD's gatekeeper glutamate is well characterised for its AMPylation autoinhibiting role as part of a inhibitory α-helix (α_{inh}) conserved throughout the Fic protein family (Engel *et al*, 2012; Goepfert *et al*, 2013). However, it is also necessary for the catalysis of Fic domain-mediated deAMPylation (Preissler *et al*, 2017a; Veyron *et al*, 2019). Here, I crystallographically demonstrate that Glu234 plays an essential role in coordinating a catalytic

water in-line for nucleophilic attack into the backside of the phosphodiester bond covalently linking BiP and the AMP moiety.

Monomerisation of FICD reciprocally regulates the mutually antagonistic activities of FICD, facilitating rapid and stable modulation of the inactivated BiP-AMP pool within the ER, in response to varying conditions of unfolded protein load. Monomerisation converts FICD from a strong homodimeric deAMPylase (and poor AMPylase) into a good AMPylating enzyme with diminished deAMPylation activity. Through a hydrogen bond network linking the FICD dimer interface to α_{inh} and Glu234, FICD monomerisation increases Glu234 (and potentially also α_{inh}) flexibility. Increased Glu234 flexibility serves two important functions which induce the described reciprocal regulation of FICD bifunctionality. The increased flexibility of this AMPylation-inhibiting residue permits the γ-phosphate of ATP to bind in a position coordinated by the Fic motif Arg374. In turn, this facilitates AMPylation competent binding of MgATP in the Fic domain active site. In a similar vein, increased Glu234 flexibility also reduces the likelihood of efficient catalytic water positioning, required for BiP-AMP deAMPylation. Conversely, wild type, dimeric FICD has a less flexible Glu234 which is more capable of positioning and activating the catalytic water molecule required for deAMPylation. Dimerisation therefore increases both the catalytic efficiency and turnover number of FICD-mediated deAMPylation. The more rigid nature of wild type, dimeric FICD's gatekeeper glutamate also does not permit the binding of MgATP in an AMPylation competent conformation within the Fic domain active site. Instead, the conformation of dimeric, wild type FICD-bound ATP sterically occludes the engagement of an attacking BiP Thr518 nucleophile in a position in-line for nucleophilic attack.

Further support for a monomerising switch existing in vivo comes from an appraisal of regulatory mechanisms employed by other evolutionarily related Fic proteins. For example, oligomerisation of the class III bacterial Fic protein from *Neisseria meningitides* (NmFic) antagonises both auto-AMPylation and NmFic catalysed AMPylation of its substrate, DNA gyrase (Stanger *et al*, 2016). In this instance, monomerisation of NmFic is proposed to facilitate unfolding and *cis*-autoAMPylation of the protein's C-terminal α_{inh}, which is thus prevented from folding back onto the Fic domain active site. Though the surface involved in oligomerisation of this class III Fic protein is different from that of FICD, the repressive mechanism still converges on the state of its α_{inh}.

Interestingly, the principal FICD dimerisation surface (which contains Leu258 and is situated at the boundary of the Fic domain core and the N-terminal Fic domain extension) also acts as a structurally conserved dimer interface in other class II bacterial Fic proteins. For example, this conserved dimer interface is present in the Fic proteins belonging to *Clostridium difficile* (CdFic; PDB 4X2C; Dedic *et al*, 2016) and *Bacteroides thetaiotaomicron* (BtFic; PDB 3CUC), but not in the *Shewanella oneidensis* Fic protein (SoFic; Das *et al*, 2009; Goepfert *et al*, 2013). Moreover, in a parallel to the effect of disrupting FICD's dimer-relay network a His57Ala mutation in CdFic (structurally homologous to $FICD^{K256A}$) results in increased solvent accessibility and auto-AMPylation activity towards CdFic's Thr38 (Dedic *et al*, 2016). This auto-AMPylation target residue is homologous to FICD's Thr237, a residue within the dimer-relay network and situated on the loop immediately following Glu234. The modulable solvent accessibility of the *Clostridium difficile* Fic homologue, upon His57Ala mutation, speaks to an evolutionary conserved Fic network, which terminates at the α_{inh}, whose dynamic nature is regulated by the stabilising effect of dimerisation.

To this end, it seems likely that α_{inh}, whose presence is largely ubiquitous throughout all Fic proteins, is in fact (in the absence of Fic domain engagement) intrinsically disordered. This was experimentally demonstrated to be the case for the inhibitory PhD antitoxin (homologous to α_{inh}) which only gains α-helicity upon engagement of its Fic-like binding partner, Doc (Garcia-Pino *et al*, 2008). Moreover, simultaneous mutation of both the inhibitory glutamate of NmFic (Glu186Ala) and a serine one turn N-terminal to the glutamate (Ser182Ala), causes a complete loss of electron density for α_{inh} (Engel *et al*, 2012). This disorder in the α_{inh} region appears to be caused by mutation of the serine, as the crystal structure of NmFic only mutated at the inhibitory glutamate (Glu186Gly) contains clearly defined electron density corresponding to the α_{inh} (Goepfert *et al*, 2013).

The –4 position, relative to the AMPylation inhibiting glutamate, is highly conserved throughout Fic proteins as a hydroxyl group containing amino acid (predominantly serine and sometimes threonine; Thr230 in FICD) (Engel *et al*, 2012). In available Fic protein structures bearing an α_{inh}, the serine/threonine residue forms a hydrogen bond to the conserved Fic domain arginine (R_2 of the Fic motif). It therefore seems likely that this contact to the Fic domain plays a role in stabilising and maintaining a folded state of the α_{inh}. This further supports the plausibility of evolutionarily conserved Fic protein regulation which focuses on the modulation of the intrinsic metastability of the α_{inh}. Potentially, this metastability enables

Fic proteins, via divergent mechanisms, to regulate their AMPylation activities selectively and dynamically and (possibly in the case of a number of Fic proteins) reciprocally their deAMPylation activities, in response to appropriate physiological cues.

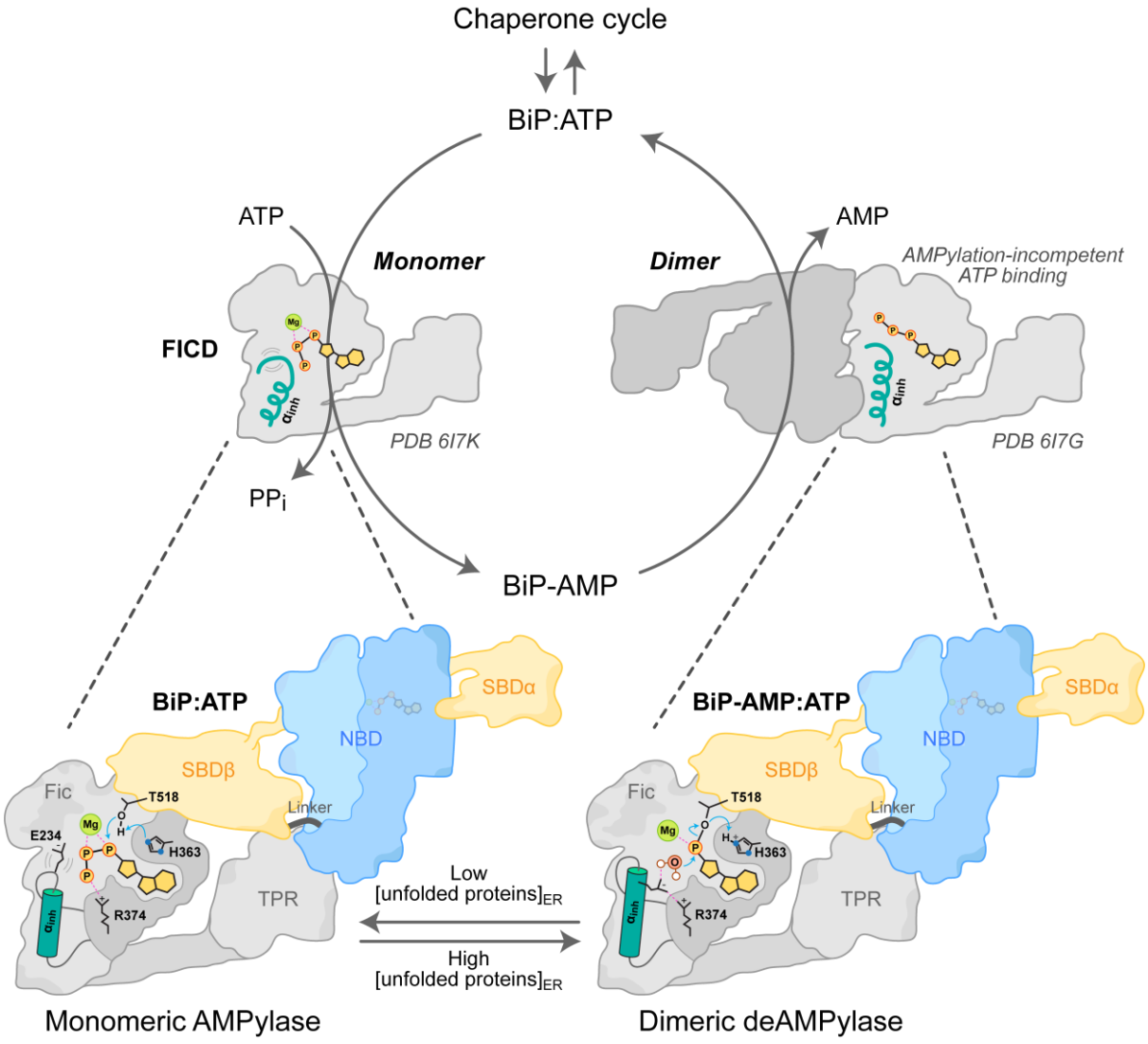

Figure 5.1.1: The post-translation UPR is mediated through regulation of FICD bifunctionality. FICD recognises (AMPylated or unmodified) BiP's linker-docked NBD and the $\ell_{7,8}$ region of the SBDβ, via its TPR and catalytic domain, respectively. This is only possible when BiP is in a domain-docked ATP-like state. Dimeric FICD has a relatively rigid gatekeeper Glu234 which facilitates efficient alignment of an attacking water for BiP deAMPylation whilst prohibiting AMPylation competent binding of ATP (right-hand side). Conversely, monomeric FICD has a more flexible Glu234 which decreases its deAMPylation efficiency whilst permitting AMPylation competent binding of MgATP (left-hand side). The FICD monomer-dimer equilibrium is adjusted in response to changing levels of unfolded proteins within the ER. This occurs, possibly in part, through direct (FICD) sensing of the ER luminal energy status — with low levels of unfolded protein causing an increase in the ATP/ADP ratio which biases FICD towards its monomeric state and vice versa.

In addition to the effects of monomerisation and dimerisation noted above, I also present experimental evidence of bidirectional and long range allostery transmitted from the nucleotide within the active site of FICD. This allostery manifests itself as destabilisation of the pre-AMPylation complex that is particularly prominent in monomeric FICD-containing complexes. I speculate that this may contribute to an additional level of monomerisation-induced stimulation of AMPylation activity, through catalytic co-substrate-mediated ground state destabilisation. Additionally, the oligomeric state of FICD can be directly manipulated by the identity of the adenine nucleotide bound within its Fic domain. The resulting picture of the dynamic and regulatable cycle of BiP AMPylation and deAMPylation, catalysed by FICD, is illustrated in **Figure 5.1.1**.

Chapter 5.2: Potential physiological regulators of FICD activity

The endogenous concentration of FICD

In vitro the predicted structured portion of human FICD, residues 104–445 with an additional N-terminal cysteine site-specifically labelled with a fluorescent dye, was measured by analytical ultracentrifugation to have a dimerisation K_D of 1.2 nM (95% CI: 1.1 to 1.4 nM) (Perera *et al*, 2019). This value was consistent with the dilution (into the low nanomolar range) required to observe accumulation of AMPylated BiP catalysed by wild type FICD (Perera *et al*, 2019). Likewise, in order to assess the capacity for nucleotide to modulate the monomer-dimer equilibrium of the fluorescent oligomeric-state probe a similarly sparse dilution of FICD was required (2.5 nM FICD-TMR).

It has been estimated that FICD is a relatively low abundance protein both in cell lines and across human tissue. For example, the inability to detect wild type FICD immunoblot signal from AR42j cell lysate derived from ~ 5 µl packed cell volume (without immunopurification of FICD), coupled with the detection sensitivity of the tested anti-FICD antibodies for recombinant *E. coli* FICD protein, produced an estimated upper bound of endogenous FICD concentration ~ 1 µM (Preissler *et al*, 2015b). In addition, proteomic analyses have in the past routinely failed to reliably detect FICD. For instance no FICD was identified in an analyses of HeLa cells conducted to relatively comprehensive (but not saturating) depths of ~ 9,000 and ~ 10,300 proteins (Hein *et al*, 2015; Nagaraj *et al*, 2011). FICD peptides were also non-detectable across a wide range of human tissues measured to a median depth of 6,400 proteins per tissue (Kim *et al*, 2014).

However, in a more recent proteomic and transcriptomic analysis conducted across a large number of human tissues with a median depth per tissue ~ 11,000 proteins, FICD peptides were identified (Wang *et al*, 2019). It was found that FICD was enriched in the bone marrow and secretory tissues, particularly in the pancreas, pituitary and salivary glands. On a per tissue basis FICD was most prevalent in the pancreas, with expression levels very close to the median protein expression level for this tissue. It should also be noted that protein expression levels across the measured pancreatic proteome ranged across 7 orders of magnitude and that the relative FICD protein expression level was considerably higher than the relative abundance of its RNA transcript. By applying the proteomic ruler approach (Wiśniewski *et al*, 2014) this study also provided label-free protein copy number estimates — including an estimate of ~ 29,000 FICD copies per pancreatic cell (Wang *et al*, 2019). Assuming the same volume (~ 1,000 μm^3) as a rat pancreatic β cell (Pipeleers & Pipeleers-Marichal, 1981) of which 10–30% of the total cell volume is ER (Stefan *et al*, 1987), gives an approximate FICD concentration (within the human pancreatic ER) of ~ 240 nM. This is consistent with the upper limit derived from immunoblot sensitivity, noted above.

In this same proteomic analysis, protein copy number estimates were also calculated for BiP (with an estimated 36 million BiP molecules per pancreatic cell). Using the same cell parameter assumptions, this suggests a total BiP concentration within the ER of 300 µM. This value of ER luminal BiP concentration is consistent with BiP copy number and ER volume estimates from budding yeast cells (Ghaemmaghami *et al*, 2003; West *et al*, 2011). Moreover, it has been observed on numerous occasions and by multiple methods (IEF, SILAC-based mass spectrometry and intact protein mass spectrometry) that a substantial proportion of the total BiP pool can be AMPylated, ranging from 40–60% (Chambers *et al*, 2012; Preissler *et al*, 2015b). Importantly, the changes in BiP modification status can occur over a relatively short time scale. For example, in the mouse pancreas the levels of AMPylated BiP increased from ~ 15 to 40% of the total pancreatic BiP content (as measured by IEF) in the space of 2 h following cycloheximide injection (Chambers *et al*, 2012). Note, the calculated 15% basal AMPylated BiP value is actually an upper limit as it is in fact derived from mouse pancreases which were fasted over-night and then analysed 1 h after refeeding; although, the basal estimate is similar in IEF gel appearance to the level of AMPylated BiP present in a number of untreated cell lines (Chambers *et al*, 2012; Preissler *et al*, 2015b).

Given the previous calculation of total pancreatic BiP concentration based on the above parameters one can estimate a lower bound for the average rate of physiological BiP

AMPylation of 10 nM/s. Assuming that the AMPylating FICD protein in this regime is working continuously at its V_{max} this necessitates an AMPylation k_{cat} of 4×10^{-2} s^{-1}. This k_{cat} value appears reasonable given that the AMPylating FICD species (monomeric FICD) is less active than $FICD^{E234G}$ (Perera *et al*, 2019) which has been measured to possess a $k_{cat} \sim 6 \times 10^{-1}$ s^{-1} (Sanyal *et al*, 2018), an order of magnitude greater than that estimated to be required for endogenous FICD. In the 2018 study by Sanyal *et al*, which measured BiP AMPylation through radioactive signal incorporation from an [α-^{32}P]-ATP source, the K_m of $FICD^{E234G}$ for (ATP-state) BiP was also derived and calculated to be in the low micromolar range (~ 5 µM), albeit in a non-physiological buffer (5 mM HEPES pH 7.5, 1 mM $MnCl_2$, 0.5 mM EDTA and 1 mM ATP). If the K_m of endogenous monomeric FICD (in a physiological ionic strength and nucleotide content environment) is also in the low micromolar range for ATP-state BiP, this is consistent with FICD being able to operate close to V_{max} except under conditions where a considerable pool of BiP is not free and in the ATP-state (either extensively occupied with unfolded client protein and/or depleted of ATP). However, given that the switch to an AMPylating state cannot occur instantaneously upon cycloheximide injection it stands to reason that the maximal rate of BiP AMPylation must be considerably higher than the average (10 nM/s) estimated across the entire 2 h time period post-injection. Therefore, for 240 nM endogenous FICD the k_{cat} must be markedly greater than 4×10^{-2} s^{-1} but also significantly less than the k_{cat} of $FICD^{E234G}$ (~ 6×10^{-1} s^{-1}). At concentrations ≤ 240 nM this does not provide a particularly wide window for the FICD AMPylation k_{cat} to fall within. With these consideration in mind, it seems plausible that the estimated ER luminal FICD concentration of 240 nM must, if anything, underestimate the endogenous pancreatic concentration.

Moreover, the rate of deAMPylation has been observed in the mouse pancreas to be faster still — with a return from 40% AMPylated BiP after over-night fasting to 15% AMPylated BiP within 1 h following refeeding (Chambers *et al*, 2012). With FICD's K_M for BiP-AMP measured, in this study and previously (Preissler *et al*, 2017a), to be ~ 16 µM it is again possible that FICD deAMPylation could proceed close to or near V_{max}; with the level of BiP-AMP at 1 h post-refeeding (~ 15% of the total BiP pool) representing around 45 µM residual deAMPylation substrate. Furthermore, there is less opportunity for sequestration of BiP-AMP as it is intrinsically ATP-state biased (Preissler *et al*, 2017b; Wieteska *et al*, 2017), and enfeebled with respect to ATPase activity and stable binding of unfolded proteins (Preissler *et al*, 2015b). This means that the total (final) concentration of BiP-AMP (~ 45 µM) will be very close to the concentration of free BiP-AMP accessible for deAMPylation. One can therefore

infer (at an effective deAMPylating FICD concentration of 240 nM) a lower limit for deAMPylation k_{cat} of 8×10^{-2} s^{-1}. This is in the order of, but still considerably greater than, the k_{cat} measured (here) for dimeric, wild type FICD (1×10^{-2} s^{-1}).

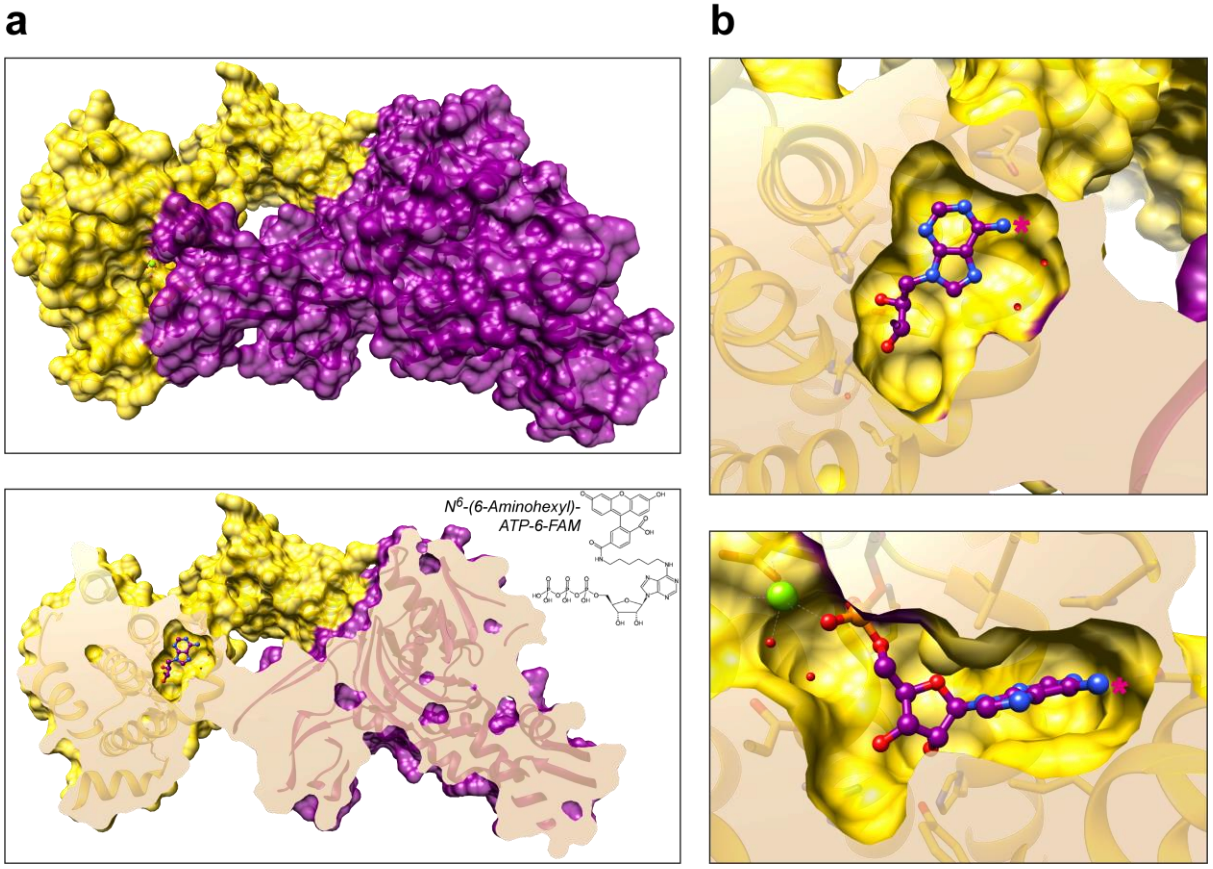

Figure 5.2.1: N^6-FAM conjugated nucleotides are likely poor FICD substrates. **a,** Above, surface view of the deAMPylation complex crystal structure with FICD (yellow) bound to BiP-AMP (purple). Below, the complex from the same perspective as above but displayed with surface capping just above the plane of the adenosine. Inset, the structure of ATP(FAM) [full name N^6-(6-Aminohexyl)-ATP-6-FAM]. **b,** The adenosine N^6 position, which is modified in FAM labelled nucleotides, is highlighted with a *. Above, close-up view of the sliced surface view shown in **a**. Note that the nucleotide moiety is completely enclosed with little extra space in the adenosine binding pocket. Below, an orthogonal view of the nucleotide binding cleft illustrating the lack of room above and below the adenosine able to accommodate a linker or fluorophore.

In this study, deAMPylation k_{cat} measurement was based on an assay utilising AMP(FAM)-labelled BiP as a tracer of the deAMPylation progress of an excess of unlabelled BiP-AMP. The resulting k_{cat}s will only be correct (in terms of absolute values) if BiP-AMP(FAM) is an equally good deAMPylation substrate as (unlabelled) BiP-AMP molecule. There is some evidence to suggest this is not the case. Namely, although it is generally a trivial matter to AMPylate BiP to completion (following incubation with $FICD^{E234G}$ in the presence of excess MgATP), a 50:50 mixture of ATP:ATP(FAM) generated a surprisingly low AMP(FAM)

labelling efficiency of only 1.8% (see **Materials and Methods**). Furthermore, it is clear from the crystal structure of BiP-AMP•FICD that there is no room for the bulky adenosine FAM fluorophore extension within the FICD active site without necessitating some disruption of either the deAMPylation or AMPylation complex (**Figure 5.2.1**). On this basis, it is easy to imagine that around 10–100 BiP-AMP molecules could be deAMPylated per molecule of BiP-AMP(FAM), this would result in an actual BiP-AMP deAMPylation k_{cat} in the order of 10–100-fold greater than that calculated in the FP-based deAMPylation assay (although the relative difference between the measured FICD variants should be accurate, as should the calculated K_M values). In the context of such a k_{cat} correction factor the estimated FICD ER concentration (in the order of hundreds of nanomolar) is compatible with the observed rate of murine pancreatic deAMPylation.

Extremely dynamic transitions in BiP AMPylation status have also been observed in cell culture systems. For example, GH3 cells upon exposure to cycloheximide AMPylated approximately 50% of their BiP pool in a period of 90 min (from an untreated state of no or very little AMPylated BiP). Likewise, upon subsequent exposure to pharmacological stressors (ionomycin and dithiothreitol) the complete reserve of AMPylated BiP was also deAMPylated within 90 min (Laitusis *et al*, 1999). GH3 cells have been measured to have an approximate volume of ~ 2,000 μm^3 (Nesin *et al*, 2011), as this cancer cell line is derived from a rat pituitary the relative expression levels of FICD and BiP in the human pituitary (Wang *et al*, 2019) give approximate total ER concentrations of 170 nM and 270 µM, respectively (assuming an ER volume that is 10% of the entire cell volume). Thus, in these GH3 cells both AMPylation and deAMPylation must be able to proceed at a rate > 25 nM/s, which implies that the k_{cat}s of AMPylation and deAMPylation must both be $> 1.5 \times 10^{-1}$ s^{-1}. This lower limit for an AMPylation k_{cat} (which assumes an FICD concentration of 170 nM, enzyme saturation and no counteracting substrate deAMPylation) is only 25% of the k_{cat} measured for the AMPylation hyperactive $FICD^{E234G}$ (Sanyal *et al*, 2018). As monomeric $FICD^{L258D}$ has been observed to catalyse AMPylation at a considerably slower rate than $FICD^{E234G}$, although not at saturating substrate concentrations (Perera *et al*, 2019), this again suggests that the calculated FICD concentration is an underestimate of the endogenous concentrations. This underestimation may be caused by an instability of the full-length (single-pass transmembrane) FICD protein. For example, if FICD is extremely labile following disruption of the cell/ER membrane, without specific precautions taken to maintain FICD in solution such as the use of optimised detergents,

a good proportion of the endogenous FICD protein may not be accessible to downstream analyses.

Plausibility of FICD undergoing oligomeric state-dependent switching in vivo

Having now established that endogenous FICD concentrations must be, at a minimum, in the order of hundreds of nanomolar this poses a fundamental issue for the proposed mechanism of reciprocal regulation through modulation of FICD's monomer-dimer equilibrium. Specifically, appreciable monomerisation of an FICD, that possesses an unperturbed dimer interface, can only be achieved in vitro by dilution of the protein into the low nanomolar range (on account of a dimerisation K_D ~ 1 nM). Moreover, at a very low concentration of 2.5 nM FICD, a saturating concentration of ATP (the only allosteric modulator yet identified to induce FICD monomerisation) was only able to induce an approximate 16% increase in fluorescent signal, to a value still less than 40% of the fluorescent signal of a completely (dequenched) monomerised FICD. If, FICD's ER concentration is indeed only 100-fold greater than its dimerisation K_D (which as noted above seems a conservative estimate) this would result in a 93% dimeric FICD population. Even if one allowed for a 10-fold increase in the in vivo dimerisation K_D, relative to the measured K_D in vitro, this would only facilitate the monomerisation of 20% of the total FICD protomers. Therefore, for monomer-dimer transitions to play a role in the regulation of FICD activity in vivo, it is necessary that the effective dimerisation K_D is increased by several orders of magnitude relative to that measured in vitro (at least under conditions of low ER protein folding load where appreciable BiP-AMP accumulation, and presumably FICD monomerisation, is induced).

How then can we reconcile a requirement of an effective dimerisation K_D in the order of hundreds of nanomolar with the measured K_D of 1.2 nM? The first and most trivial possibility is that FICD is not regulated by oligomeric state-dependent switching in vivo. In this scenario, the ability of *FICD*$^{-/-}$ cells to accumulate BiP-AMP only under regimes of low-level expression of recombinant FICD (Perera *et al*, 2019) must reflect the presence of an unidentified (allosteric) regulator of FICD activity. This regulator must be expressed at similarly low levels to endogenous FICD and is thus unable to regulate a large molar excess of FICD (such as that which occurs upon overexpression in conventional transient cell transfection experiment). Furthermore, the coherent and extensive set of observations pertaining to the in vitro and in vivo reciprocity of dimeric and monomeric FICD enzymatic activity would then represent an elaborate red herring. Indeed, efforts to directly observe potential endogenous fluctuations in

an FICD monomer-dimer equilibrium have been avoided on the basis of the perceived technical difficulties. This is in part a function of the lab's lack of technical expertise in the cell imaging techniques required to address such an issue, and also partly stems from concerns over the experimental tractability of being able to reliably assay the oligomeric state of an endogenous protein expressed at relatively low cellular concentrations.

Co-translational FICD glycosylation

In lieu of this somewhat troubling possibility, I believe that the balance of probabilities favours a situation where FICD's monomer-dimer equilibrium is key to regulation of BiP AMPylation and deAMPylation. As such, the effective K_D must be increased in vivo. Part of such an increase in effective dissociation constant (K_D^{eff}) may stem from post translational modification of FICD. For instance, FICD expressed in the ER has one major glycosylated residue, Asn275 (Sanyal *et al*, 2015). This glycosylation site is located within the Fic domain, on the opposite side to the active site and relatively close to the dimerisation interface. The asparagine in question is surface exposed in FICD crystal structures and does not form intramolecular hydrogen bonds via its side chain. It is therefore possible that the extended N-glycan floats relatively freely in solution, facing away from the surface of the protein (whilst covalently tethered to Asn275). In such a conformation it is difficult to imagine how Asn275 glycosylation would be able to effect FICD's dimerisation K_D^{eff}. However, upon inspection of the FICD surface in the vicinity of this residue, a conspicuous hole (followed by a groove) in the FICD structure became apparent (**Figure 5.2.2**).

Given that N-linked glycosylation of ER proteins occurs co-translationally it is possible that a proportion of FICD actually has the N-linked glycan locked within this cavity — enforced by the folding of the C-terminal FICD helix over the glycan and onto the rest of the Fic domain (**Figure 5.2.2e**). The putative locked glycan would protrude into a relatively hydrophobic (electro-neutral) extended groove which appears (sterically) to be able to accommodate a large amount of the covalently attached glycan structure. As glycans have electro-negative coulombic potentials, and in this hypothesised situation a very high effective concentration for binding within the hydrophobic Fic domain groove, it is possible that a glycan docked in this way would cause considerable allosteric and/or destabilising effects throughout the Fic domain. This destabilisation may, in turn, extend to include a weakening of the dimer interface able to raise the dimerisation K_D^{eff} closer to the luminal FICD concentration. Interestingly, the Asn275 glycosylation site appears completely conserved across all metazoan FICD homologues.

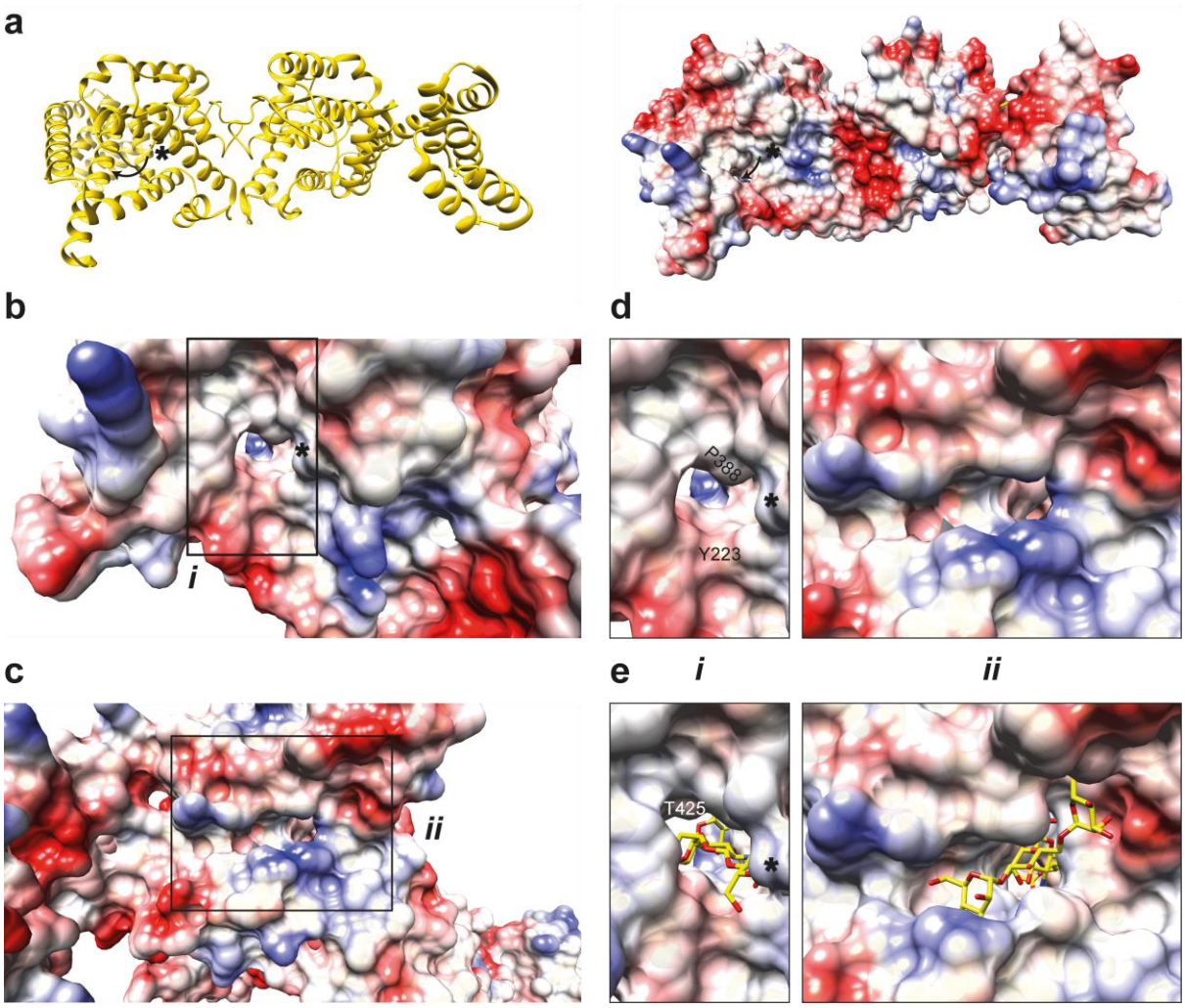

Figure 5.2.2: An FICD cavity for accommodating a glycan. **a,** View of an FICD dimer (using the FICD:ATP structure). On the right the ribbon representation is overlaid with a surface representation, coloured according to coulombic potential. *Indicates the position of the glycosylated reside Asn275 (in all applicable panels). The arrow represents the putative direction that the N-linked glycan may be locked in (co-translationally) by the C-terminal Fic domain helix. Note, in this view the carboxy terminus (of the left protomer) is pointing out of the page in the lower left quadrant of the structure. **b,** A more focussed view of the surface representation in **a**, highlighting the tunnel-like cavity which is adjacent to the Asn275 side chain. **c,** An orthogonal view (of the left-hand side) of **b** which illustrates the tunnel cavity exit. This cavity appears to open up into a relatively hydrophobic groove (the roof of which is formed by FICD's C-terminal helix). **d**, ***i*** and ***ii***, Zoomed in views of the boxed regions from **b** and **c**, respectively. ***i,*** Residue Pro388, from a Fic domain loop, forms part of the roof of the cavity and is annotated. Tyr223 which forms part of the helical floor is also labelled (see **a**). **e**, A basic glycan structure ($Man_3GlcNAc_2Asn$) was built into the protein, within covalent bonding distance of Asn275, and manually positioned through the cavity. The model was energy minimised, and the resulting local energy minimum is presented in ***i*** and ***ii*** (with identical perspectives as presented above in **d**). ***i,*** the rest of the roof of the tunnel cavity is now visible and Thr425 from FICD's C-terminal helix is annotated.

Moreover, the overall structure of the Fic domain appears conserved throughout FICDs (with almost identical crystal structures comparing human and *C. elegans* FICD homologues [*C. elegans* Fic-1; PDB 5JJ6]).

The hypothetical increase in dimerisation dissociation constant brought about by N-linked glycosylation of Asn275, would likely represent a constitutive increase in K_D^{eff}. Removal of the glycan from the aforementioned groove would require unfolding or disengagement of the C-terminal helix from the rest of the Fic domain. Moreover, enzymatic removal of the majority of the glycan cannot be catalysed within the secretory pathway. Likewise, a basal increase in K_D^{eff} may also be afforded by the transmembrane nature of FICD in vivo.

Membrane localisation

It is a widely accepted principal that restricting protein binding partners to a 2-dimensional plane can increase their effective concentrations by orders of magnitude. However, if the surface area to volume ratio of a membrane in which two binding partners are localised is sufficiently large, reduced protein complexation (or in other words an increase in K_D^{eff}) will occur. Based on empirical measurements of thermodynamic parameters which contribute to 2D protein-protein binding, it has been estimated that colocalization to a membrane with a surface area to volume ratio greater than 50 will induce an increase in K_D^{eff} (Yogurtcu & Johnson, 2018). Moreover, the rough endoplasmic reticulum (RER) has also been measured by high resolution electron microscopy-based cellular reconstructions to have a very large surface area to volume ratio. For example, the RER of a Syrian hamster (insulin secreting) pancreatic cell line was measured to have a surface area to volume ratio of 77 (Marsh *et al*, 2001), which is very similar to the ER surface area to volume ratio of 75 measured in budding yeast (Wei *et al*, 2012). As these represent average ratios across the entire measured volume of ER in each cell type, it is plausible that thinner, more tubular (and flat) sections of ER will have (locally) much greater ratios. Indeed, it has been demonstrated in yeast cells that there are multiple morphologically distinct ER domains, in which tubular ER was measured to have an elevated surface area to volume ratio relative to the bulk ER (West *et al*, 2011).

It is therefore conceivable that if FICD were to endogenously reside in flattened tubular ER its local membrane environment may possess a surface area to volume ratio > 100 but presumably < 1000. Using these as limits, one would expect a 2–20-fold increase in dimerisation K_D^{eff} (Yogurtcu & Johnson, 2018). However, like N-glycosylation, such a mechanism of increasing the in vivo dimerisation K_D^{eff}, relative to the in vitro measured K_D in solution, is more likely to

cause a constitutive increase in K_D^{eff}. That is to say, without their being extremely rapid morphological ER remodelling and/or active and dynamically regulatable mechanisms to redistribute FICD to different ER domains, FICD membrane localisation is unlikely to be able to contribute to the very dynamic enzymatic switching behaviour observed in vivo.

Post-translational Nε-lysine acetylation

Contrarily, a post-translational modification such as Nε-lysine acetylation may well be amenable to a regulatory switching mechanism that occurs on the time scales observed in vivo. Lysine acetylation of ER-resident and ER-transiting proteins has only been relatively recently discovered, and comparatively little is known about its prevalence or regulatability compared to, for example, N-glycosylation. However, a mechanism whereby Nε-lysine acetylation impairs the interaction of ER-resident binding partners has previously been proposed (Peng *et al*, 2018). In the case of FICD it is conceivable that the fairly surface exposed (Nε) amino group of Lys256 may be reversibly acetylated to regulate FICD activity. The backbone of Lys256 forms part of the principal FICD dimerisation surface and its side chain forms an intrinsic part of the proposed dimer-relay hydrogen bond network (making a hydrogen bond/salt bridge to Glu242) linking the dimer interface to FICD's active site (see **Figure 1.5.1**). It has also been shown that Lys256 mutation increases the dimerisation K_D (~ 7-fold), decreases deAMPylation activity and significantly increases BiP-AMPylation activity (even at concentrations where Lys256-mutated FICD is predominantly dimeric) (Perera *et al*, 2019). Moreover, even at concentrations where Lys256 mutated FICDs are dimeric the T_m data suggest that the resulting FICD is destabilised/more flexible. In addition, although crystallising as a dimer, $FICD^{K256A}$ is able to bind MgATP in an AMPylation competent conformation. Acetylation of FICD's Lys256 may therefore increase the K_D^{eff} by a factor of 10 or more. However, by abrogating the ability to interact with Glu242 (which can only act as a proton acceptor) and also by virtue of being a relatively bulky modification, acetylation may result in a considerable switch in enzymatic activity (by the same mechanism as achieved in vitro by monomerisation) without an explicit requirement for in vivo monomerisation. Evidence for Lys256 modification being able to induce considerable destabilisation of FICD is also provided anecdotally by the observation that although $FICD^{K256C}$ forms a stable protein in solution, labelling of this cysteine with maleimide or iodoacetamide conjugated fluorophores resulted in rapid aggregation of the protein.

In order to function as part of an FICD switching mechanism, given the time frames involved, the result of any such regulatory mechanism must be reversible. To this end, a number of ER acetyltransferase enzymes have been identified and deacetylation within the Golgi has also been observed (reviewed in Farrugia & Puglielli, 2018). Furthermore, a protein localised to the *cis*-Golgi and Golgi cisternae, has been characterised as possessing deacetylase enhancer activity (Lalioti *et al*, 2013). One could therefore speculate that under conditions of increased ER stress, where in the above model FICD deacetylation would be required, a decreased efficiency of the machinery required to retain FICD within the ER may allow transient escape of FICD into the *cis*-Golgi (where it could be rapidly deacetylated and become more dimeric and/or a better AMPylase) before retrieval back to the ER. The longer FICD spends (efficiently) retained within the ER (which may only occur for prolonged periods of time under low ER stress conditions) the more likely FICD is to be re-acetylated by ER-resident acetyltransferases and thus become more monomeric and/or a better AMPylase and poorer deAMPylase.

Intriguingly, the mechanism by which FICD is retained in the ER is also not well understood. It was demonstrated that the portion of FICD up to the end of its (single-pass) transmembrane domain (residues 1–45) is sufficient to cause localisation of a C-terminally fused GFP to the ER (Sanyal *et al*, 2015). However, the cytosolic N-terminus of FICD lacks any recognisable di-arginine motif associated with type II membrane protein retention within the ER (Schutze *et al*, 1994). It is an inviting possibility, therefore, that BiP may itself be essential in facilitating FICD's ER retention. It has been extensively demonstrated that BiP, by binding clients within its SBD, can perform such a role in retaining client proteins within the ER. Moreover, coordinated release of these clients from BiP can result in rapid and regulated trafficking out of the ER. For example, ER Ca^{2+} depletion, which results in a destabilisation of BiP-substrate complexes, is able to cause synchronised secretion of otherwise ER retained proteins (Preissler *et al*, 2020). This mechanism of BiP-coupled ER retention and reversible acetylation would also rationalise the observation that thapsigargin treatment (which depletes the ER Ca^{2+} stores) also rapidly induces BiP deAMPylation (Laitusis *et al*, 1999; Chambers *et al*, 2012; Preissler *et al*, 2015b) without necessarily inducing elevated levels of unfolded proteins (Preissler *et al*, 2020). This latter point is especially true of the experiment conducted in (Preissler *et al*, 2015b) in which significant deAMPylation of BiP was observed within 60 min of thapsigargin treatment in the (continued) presence of cycloheximide (which was initially applied to the cell culture medium 90 min before the addition of thapsigargin). Under these conditions not only

would the thapsigargin have limited time to induce potential protein unfolding, but the ER would already be depleted of labile clients and there would be no flux of newly synthesised proteins into the ER for the duration of the experiment.

Active monomerisation of FICD catalysed by BiP

As mentioned in **Chapter 1.1** the substrate binding ability and chaperoning functionality of all Hsp70 proteins are intrinsically linked to the action of co-chaperone proteins, in particular NEFs and JDPs. There is considerable diversification of the latter, allowing different JDPs to catalyse the binding of Hsp70s with specific classes or subsets of proteins. In support of a role for BiP substrate binding in the regulation of FICD activity, and by extension in the regulation of BiP's own activity, unpublished work from ex-lab members (Cláudia Rato da Silva and Martin J. Kamphuis) has shown that knockout of a particular ER-localised JDP abrogates the ability for CHO cells to induce BiP AMPylation. Moreover, this phenotype was dependent on the HPD motif, which is characteristic of all JDPs and is required for their interaction with Hsp70s and their ability to stimulate Hsp70 ATPase activity. In the case of the BiP AMPylation phenotype, mutation of the JDP's endogenous HPD motif (to QPD) resulted in a phenocopy of the JDP knockout. This is reminiscent of the mechanism of Ire1α regulation, another ER-localised transmembrane UPR transducer, which is responsible for the XBP1 branch of the canonical UPR.

It has been demonstrated that the ER-localised JDP (ERdj4) is required in order to load BiP onto Ire1α, causing monomerisation of the otherwise homodimeric UPR transducer (Amin-Wetzel *et al*, 2017, 2019). Ire1α monomerisation is presumably driven by entropic pulling stimulated via JDP-mediated ultra-affinity and ATP hydrolysis, which stabilise a non-equilibrium monomeric Ire1α steady-state (De Los Rios & Barducci, 2014; De Los Rios *et al*, 2006). In this so-called chaperone inhibition model, the inhibition of Ire1α dimerisation (and the resultant UPR signalling) is released upon an increase in ER protein folding load, this titrates ERdj4 away from Ire1α and causes ERdj4 to instead load BiP onto the extra burden of unfolded proteins. A similar mechanism, wherein an ER-localised JDP and BiP act as ER stress sensors could, therefore, also operate to regulate the oligomeric state of FICD effectively and rapidly, either with or without additional mechanisms of dimerisation K_D^{eff} enhancement. A further hint to this end is provided in the form of the particular crystal packing observed in the deAMPylation complex crystals. In both the state 1 and state 2 complexes, the crystal lattice is

strengthened by each AMPylated BiP binding the unfolded C-terminal tail of a symmetry related FICD molecule (as a canonical substrate within the BiP SBD) (**Figure 5.2.3**).

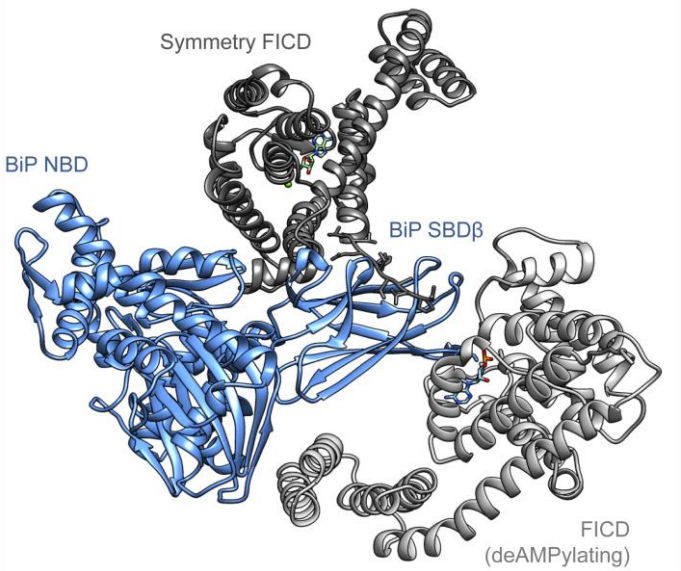

Figure 5.2.3: BiP can bind the unfolded C-terminus of FICD. The asymmetric unit protein molecules that comprise the heterodimeric deAMPylation complex are shown in blue and light grey. This structure has been discussed at length in **Chapter 2.1**. Additionally, as highlighted in this representation, an engagement of an unfolded C-terminal tail of a symmetry related FICD molecule (black) within the peptide binding groove of BiP-AMP's SBDβ is present in both the state 1 and state 2 deAMPylation complex crystal forms. This potentially represents a simple artefact of high protein concentrations and the particular crystal packing environment. However, it may also be suggestive of a role for BiP binding FICD, as a (partially unfolded) substrate, in enabling FICD monomerisation and thus in the reciprocal regulation of FICD activity.

Any combination of the above speculative mechanisms may or may not exist and/or operate simultaneously to increase, either constitutively or in a regulatory fashion, the effective dimer equilibrium dissociation constant. The prospect of BiP actively participating in the regulation of FICD monomerisation is a particularly attractive one as it directly reconciles experimental observations pertaining to rapid thapsigargin-stimulated BiP deAMPylation and, particularly, the ER-localised JDP knockout phenotype. Moreover, a central role of a JDP and BiP in the reciprocal-regulation of FICD bifunctionality would also provide a means of sensing changing levels of ER stress. In this model an elegant negative feedback system would exist, whereby an increased burden of unfolded ER protein titrates JDP and BiP away from FICD, permitting FICD dimerisation and increased BiP deAMPylation so as to create increased ER chaperoning capacity (and vice versa). This also parallels a seemingly ubiquitous feature of Hsp70 proteins — an ability to directly modulate the homo-oligomeric status, and thus activity, of their own

regulators within the eukaryotic ER, cytosol and nucleus (Amin-Wetzel *et al*, 2019; Kmiecik *et al*, 2020).

Chapter 6: Materials and Methods

Chapter 6.1: Plasmid construction

The plasmids used in this study have been described previously or were generated by standard molecular cloning procedures and are listed in **Table 5**.

Chapter 6.2:Protein purification

His_6-SUMO fused proteins

The majority of proteins used in this study (both FICD and BiP) were expressed as N-terminal His_6-Smt3 fusion constructs from either pET28-b vectors (expressed in T7 Express *lysY/I*^{q} (NEB) *E. coli* cells) or pQE30 vectors (expressed in M15 (Qiagen) *E. coli* cells). T7 Express cells were grown in LB medium containing 50 µg/ml kanamycin. M15 cells were grown in the same medium supplemented with an additional 100 µg/ml ampicillin. All cells were grown at 37 °C to an optical density (OD_{600nm}) of 0.6 and then shifted to 18 °C for 20 min, followed by induction of protein expression with 0.5 mM isopropylthio β-D-1-galactopyranoside (IPTG). Cells were eventually harvested by centrifugation after a further 16 h at 18 °C.

Following harvesting bacterial pellets were resuspended and lysed with a high-pressure homogenizer (EmulsiFlex-C3; Avestin) in buffer A (25 mM Tris-HCl pH 8.0, 500 mM NaCl, 40 mM imidazole, 1 mM $MgCl_2$, 0.1 mM tris(2-carboxyethyl)phosphine (TCEP)) containing protease inhibitors (2 mM PMSF, 4 µg/ml pepstatin, 4 µg/ml leupeptin, 8 µg/ml aprotinin), 0.1 mg/ml DNaseI, and 20 µg/ml RNaseA. The lysates were clarified by centrifugation at 45,000 × *g* for 35 min. The resulting supernatant was then incubated with 1 ml of Ni-NTA agarose (Thermo fisher) per 1 l expression culture, for 30 min at 4 °C with rotation. The Ni-NTA matrix was transferred to a gravity flow column and washed with 2 × 10 column volumes (CV) of buffer B (25 mM Tris-HCl pH 8.0, 150 mM NaCl, 10 mM imidazole, 0.1 mM TCEP) supplemented sequentially with (i) 1 M NaCl and then (ii) 10 mM $MgCl_2$ + 5 mM ATP, followed by 5 CV of buffer B. The matrix was then resuspended in 5 CV of TNT-Iz10 (25 mM Tris-HCl pH 8.0, 150 mM NaCl, 1 mM TCEP, 10 mM imidazole) containing 2 µg/ml Ulp1 protease C-terminally fused to a StrepII-tag [Ulp1-StrepII (UK1983)] and incubated with rotation for 16 h at 4 °C. The 16 h incubated material was eluted from the Ni-NTA matrix which was washed with a further 5 CV of TNT-Iz10. On-bead Ulp1-cleaved protein containing

eluate was collected and pooled and diluted 1:2 with 25 mM Tris-HCl pH 8.0 (AEX-A). The diluted protein was applied to an anion exchange column equilibrated in 95% AEX-A and 5% AEX-B (25 mM Tris-HCl, 1 M NaCl) and eluted using a linear gradient up to 50% AEX-A and 50% AEX-B (unless specified below). 1 mM TCEP was added to the pooled protein fractions (unless they had already been deliberately oxidised as detailed below) and the protein was concentrated using centrifugal filters (Amicon Ultra; Merck Millipore). The concentrated proteins were further purified by gel filtration using SEC columns equilibrated in 25 mM Tris-HCl pH 8.0, 150 mM NaCl. All purification was conducted at 4 ºC. Unless otherwise specified (**Table 5**) anion exchanges were conducted using a RESOURCE Q 6 ml column (GE Healthcare). Gel filtration was conducted, depending on protein size and amount, on either a HiLoad 16/60 Superdex 75 or 200 prep grade column, an S200 or S75 Increase 10/300 GL column, or an S200 10/300 GL column (see **Table 5**). All proteins were purified to homogeneity and > 95% purity, as assessed by Coomassie-stained SDS-PAGE. Unless the protein was deliberately oxidised, proteins were supplemented after gel filtration with 1 mM TCEP. Proteins were concentrated to > 150 µM using centrifugal filters, aliquoted and snap-frozen and stored at –80 ºC. All protein concentrations were measured with a NanoDrop Spectrophotometer (Thermo Fisher Scientific), using the A_{280} and the protein's predicted extinction coefficient at 280 nm (ε_{280}).

GST-TEV fused proteins

Proteins fused N-terminally to Glutathione *S*-transferase followed by a TEV cleavage sequence were purified as above, with minor alterations. Purification was performed without imidazole in the purification buffers. Cleared lysates were supplemented with 1 mM DTT and incubated with GSH-Sepharose 4B matrix (GE Healthcare) for 1 h at 4 ºC. 5 CV of TNT(0.1) (25 mM Tris-HCl pH 8.0, 150 mM NaCl, 0.1 mM TCEP) was used as a final wash step before elution. Proteins were eluted with 10 mM HEPES-KOH pH 7.4, 20 mM Tris-HCl pH 8.0, 30 mM KCl, 120 mM NaCl, 2 mM $MgCl_2$ and 40 mM reduced glutathione. Additionally, GST-TEV-BiP proteins were cleaved with TEV protease (1/100 *w/w*; UK759), whilst dialysing into TND (25 mM Tris-HCl pH 8.0, 150 mM NaCl plus 1 mM DTT) for 16 h at 4 ºC. Uncleaved BiP was depleted by incubation with GSH-Sepharose 4B matrix (1 ml matrix per 5 mg of protein) for 1 h at 4 ºC. The flow through was collected. Retained, cleaved material was washed from the matrix with 5 CV of TNT(0.1) and all cleaved protein fractions were pooled. BiP was AMPylated as detailed below. Proteins were concentrated to > 200 µM. Aliquots were snap-frozen in liquid nitrogen and stored at –80 °C.

ID	Plasmid name	Description	Encoded protein	Purification
759	pRK793 His6_ TEV(S219V)_Arg6	His6-TEV(S219V)-Arg6 from pRK793	TEV Protease	
1314	pCEFL_mCherry_ 3XFLAG_C	Mammalian expression of C-terminally 3xFLAG. Neomycin-resistance replaced by mCherry (under SV40 promoter control)	mCherry	
1397	hsHYPE_WT_pCEFL_ mCherry	FL CDS of WT HYPE in pCEFL marked with mCherry	FICD	
1479	hsHYPE_45-458_E234G _pGV67	Bacterial expression of hyperactive human GST-TEV-HYPE_45-458	GST-FICD^{E234G}	
1481	hsHYPE_104-445_E234G _pSmt3_pET28b	Bacterial expression of inactive human E234G mutant of His6-Smt3-HYPE_104-445	FICD^{E234G}	
1801	EcBirA_WT_pGEX_TEV	Bacterial expression of fastidious E. coli BirA biotin ligase (R118 intact)	GST-BirA	
1954	hsHYPE_104–445_H363A _pSmt3_ pET28b	Bacterial expression of inactive human H363A mutant of His6-Smt3-HYPE(104–445)	FICD^{H363A}	RQ, S200pg
1983	yUlp1(402-621)-StrepII _pET24a	Bacterial expression of yeast Ulp1 protease with a C-terminal StrepII tag	Ulp1-StrepII	
2051	hsFICD_104–186_ pSUMO(M3)	Bacterial expression of human FICD/HYPE TPR domain, residues 104–186	TPR Domain	RQ, S75Incr
2052	hsHYPE_104–445_pSmt3 _pET28b	Bacterial expression of wild type His6-Smt3-HYPE(104–445)	FICD	RQ, S200pg
2054	hsHYPE_138-445_H363A _pSmt3_pET28b	Bacterial expression of H363A ΔTPR1 mutant of human His6-Smt3-HYPE(138-445)	FICD(ΔTPR1)^{H363A}	MQ, S200Incr
2090	haBiP_27–549_T229A_ V461F_pQE30_ pSmt3	Bacterial expression of ATPase and substrate binding deficient, lid truncated BiP (N-terminal H6-Smt3 fusion)	Lid truncated BiP$^{T229A-V461F}$	RQ, S75pg
2091	hsHYPE_104–445_L258D _pSmt3_ pET28b	Bacterial expression of monomeric His6-Smt3-HYPE_104–445. Enzymatically active.	FICD^{L258D}	RQ, S75pg
2092	hsHYPE_104-445_E234G _L258D_pSmt3_pET28b	Bacterial expression of constitutively AMPylating and monomeric mutant of His6-Smt3-HYPE_104-445	FICD$^{E234G-L258D}$	RQ, S75pg
2093	hsHYPE_104–445_L258D _H363A_ pSmt3_pET28b	Bacterial expression of inactive and monomeric human H363A mutant of His6-Smt3-HYPE(104–445)	FICD$^{L258D-H363A}$	RQ, S75pg
2139	hsHYPE_E234G_L258D_ pCEFL_ mCherry	Mammalian expression of full-length human FICD with E234G and L258D mutations in pCEFL marked with mCherry	FICD$^{E234G-L258D}$	RQ, S200pg MQ, S200Incr
2217	hsHYPE_104-445_K256S _pSmt3_pET28b	Bacterial expression of K256S mutant FICD	FICD^{K256S}	RQ, S200pg
2218	hsHYPE_104-445_E242A _pSmt3_pET28b	Bacterial expression of E242A mutated FICD	FICD^{E242A}	RQ, S200pg
2269	hsHYPE_104–445_A252C _H363A_C421S_pSmt3_ pET28b	Catalytically dead and constitutively dimeric (disulphide stapleable dimer interface) FICD. Trap for BiP-AMP.	Trap [$_{s\text{-}s}$FICD$^{A252C-H363A-C421S}$]	RQ, S200pg
2270	hsHYPE_104-445_G299S _pSmt3_pET28b	Bacterial expression of partially monomerising G299S mutation into FICD(104–445)	FICD^{G299S}	RQ, S200pg
2274	hsHYPE_104-445_K256A _pSmt3_pET28b	Bacterial expression of K256A mutated FICD	FICD^{K256A}	RQ, S200pg
2296	hsHYPE_104_445_D160C _T183C_H363A_C421S_ pSmt3_pET28b	Dimeric FICD(H363A) made cysteine free apart from disulphide stapleable TPRs	FICD^{H363A}(TPRox) [$_{s\text{-}s}$FICD$^{D160C-T183C-H363A-C421S}$]	CQ, RQ, S200Incr
2306	hsHYPE_104-445_K256S _L258D_pSmt3_pET28b	Bacterial expression of monomeric K256S FICD	FICD$^{K256S-L258D}$	RQ, S200pg
2331	haBiP_28-635_T229A_ V461F_pGEX_TEV_ AviTag	Bacterial expression of N-terminal AviTag labelled Full-length hamster BiP T229A V461F	Biotinylated-BiP$^{T229A-V461F}$	MQ, S200
2359	haBiP_27–635_T229A_ V461F_pQE30_ Smt3_Avi	FL hamster BiP ATPase dead, substrate binding deficient with N-terminal H6-SUMO-AviTag and small GS linker	Biotinylated-BiP$^{T229A-V461F}$	MQ
2422	hsHYPE_104-445_H363A _pQE30_Smt3_Avi	Bacterial expression of human FICD/HYPE 104-445 H363A mutation with N-terminal H6-SUMO-AviTag	Biotinylated FICD^{H363A}	RQ, S200pg, S200

2473	hsHYPE_104-445_S288C _H363A_C421S_pSmt3_ pET28b	Bacterial expression of cysteine free FICD H363A dimer, potential dimer FRET probe S288C	FICD-TMR	RQ, S200
2521	haBiP_27–635_T229A_ V461F_pSmt3_ pET28b	Bacterial expression of FL ATPase and substrate binding deficient His6-Smt3-BiP(27–635)	$BiP^{T229A-V461F}$	RQ, S75pg
2579	hsHYPE_104–445_E105R _H363A_ pSmt3_pET28b	Bacterial expression of inactive human H363A mutant of His6-Smt3-HYPE_104–445 with TPR mutation	$FICD^{E105R-H363A}$	RQ, S200Incr
2582	hsHYPE_104–445_K124E _H363A_ pSmt3_pET28b	Bacterial expression of inactive human H363A mutant of His6-Smt3-HYPE_104–445 with TPR mutation	$FICD^{K124E-H363A}$	RQ, S200Incr
2583	hsHYPE_104–445_H131A _H363A_ pSmt3_pET28b	Bacterial expression of inactive human H363A mutant of His6-Smt3-HYPE_104–445 with TPR mutation	$FICD^{H131A-H363A}$	RQ, S200Incr
2607	hsHYPE_104–445_E105R _L258D_H363A_pSmt3_ pET28b	Bacterial expression of inactive human L258D H363A mutant of His6-Smt3-HYPE_104–445 with TPR mutation	$FICD^{E105R-L258D-H363A}$	RQ, S75Incr
2610	hsHYPE_104–445_H131A _L258D_H363A_pSmt3_ pET28b	Bacterial expression of inactive human L258D H363A mutant of His6-Smt3-HYPE_104–445 with TPR mutation	$FICD^{H131A-L258D-H363A}$	RQ, S75Incr
2612	hsHYPE_104_445_D160C _T183C_L258D_H363A_ C421S_pSmt3_pET28b	Bacterial expression of inactive human L258D H363A mutant of His6-Smt3-HYPE_104–445 with TPR stapleable cysteines	$FICD^{L258D-H363A}$(TPRox) [$_{s\text{-}s}FICD^{D160C-T183C-L258D-H363A-C421S}$]	CQ, RQ, S75Incr
2617	hsHYPE_104–445_K124E _H131A_L258D_H363A_ pSmt3_pET28b	Bacterial expression of inactive human L258D H363A mutant of His6-Smt3-HYPE_104–445 with 2x TPR mutation	$FICD^{K124E-L258D-H363A}$	RQ, S75Incr
2617	hsHYPE_104–445_K124E _H131A_L258D_H363A_ pSmt3_pET28b	Bacterial expression of inactive human L258D H363A mutant of His6-Smt3-HYPE_104–445 with 2x TPR mutation	$FICD^{K124E-H131A-L258D-H363A}$	RQ, S75Incr
2675	hsHYPE_104–445_K124E _H131A_H363A_pSmt3_ pET28b	Bacterial expression of inactive human H363A mutant of His6-Smt3-HYPE_104–445 with 2 TPR mutations	$FICD^{K124E-H131A-H363A}$	RQ, S200Incr
2676	hsHYPE_E105R_E234G_ L258D_ pCEFL_mCherry	Mammalian expression of FL CDS of L258D E234G HYPE plus TPR mutation in pCEFL marked with mCherry	$FICD^{E105R-E234G-L258D}$	
2677	hsHYPE_K124E_E234G_ L258D_ pCEFL_mCherry	Mammalian expression of FL CDS of L258D E234G HYPE plus TPR mutation in pCEFL marked with mCherry	$FICD^{K124E-E234G-L258D}$	
2678	hsHYPE_H131A_E234G_ L258D_ pCEFL_mCherry	Mammalian expression of FL CDS of L258D E234G HYPE plus TPR mutation in pCEFL marked with mCherry	$FICD^{H131A-E234G-L258D}$	
2679	hsHYPE_K124E_H131A_ E234G_L258D_pCEFL_ mCherry	Mammalian expression of FL CDS of L258D E234G HYPE plus 2 TPR mutations in pCEFL marked with mCherry	$FICD^{K124E-H131A-E234G-L258D}$	
2759	hsHYPE_104–445_K124E _H131A_L258D_pSmt3_p ET28b	Monomeric His6-Smt3-HYPE_104–445 TPR double mutant, bacterial expression. Enzymatically active.	$FICD^{K124E-H131A-L258D}$	RQ, S75Incr
2760	hsHYPE_104–445_K124E _L258D_ pSmt3_pET28b	Monomeric His6-Smt3-HYPE_104–445 TPR mutant, bacterial expression. Enzymatically active.	$FICD^{K124E-L258D}$	RQ, S75Incr
2761	hsHYPE_104–445_H131A _L258D_ pSmt3_pET28b	Monomeric His6-Smt3-HYPE_104–445 TPR mutant, bacterial expression. Enzymatically active.	$FICD^{H131A-L258D}$	RQ, S75Incr
2762	hsHYPE_138-445_L258D _pSmt3_ pET28b	Monomeric ΔTPR1 His6-Smt3-HYPE(138-445), bacterial expression. Enzymatically active.	$FICD(\Delta TPR1)^{L258D}$	RQ, S75Incr
2763	hsHYPE_104_445_D160C _T183C_C421S_pSmt3_ pET28b	FICD bacterial expression. TPR stapleable. Enzymatically active.	FICD(TPRox) [$_{s\text{-}s}FICD^{D160C-T183C-C421S}$]	CQ, RQ, S75Incr
2764	hsHYPE_104_445_D160C _T183C_ L258D_C421S_ pSmt3_pET28b:	Monomeric FICD bacterial expression. TPR stapleable. Enzymatically active.	$FICD^{L258D}$(TPRox) [$_{s\text{-}s}FICD^{D160C-T183C-L258D-C421S}$]	CQ, RQ, S75Incr

Table 5: List of plasmids used in this study. *ID* denotes the unique lab identification (UK) number of each plasmid. *Purification* contains information pertaining to any FPLC columns used in the purification of the protein (following strep-tactin, GSH-Sepharose, Ni-NTA affinity chromatography, and on bead cleavage and elution, as appropriate). CQ, HiTrap 5 ml capto Q; RQ, RESOURCE Q 6 ml; MQ, Mono Q 5/50 GL; S75pg, HiLoad 16/60

Superdex 75 prep grade; S200pg, HiLoad 16/60 Superdex 200 prep grade; S75Incr, S75 Increase 10/300 GL; S200Incr, S200 Increase 10/300 GL.

Preparative BiP AMPylation

Large-scale AMPylation of BiP was achieved post-on column Ulp1 cleavage or post-TEV protease treatment and GSH-Sepharose depletion of uncleaved material, by addition of 10 mM $MgCl_2$, 5 mM ATP and 1/50 (*w/w*) GST-TEV-FICD^{E234G} (UK1479). The AMPylation reaction was incubated for 16 h at 25 ºC. GST-TEV-FICD was then depleted by a 1 h incubation with GSH-Sepharose 4B matrix. AMPylation was confirmed as being stoichiometric by intact-protein mass spectrometry (LC-ESI-MS) as previously detailed (Preissler *et al*, 2017b).

Disulphide-linked FICD dimers

Disulphide-linked FICD dimers ($_{s\text{-}s}$FICD$^{A252C\text{-}H363A\text{-}C421S}$; UK2269), used as a 'trap' for BiP-AMP during in vitro AMPylation assays, were oxidised and purified as described above with modification. In brief, after the affinity chromatography step, on-column Upl1-StrepII cleavage the retained cleavage products were washed off the beads with TN-Iz10 (25 mM Tris-HCl pH 8.0, 150 mM NaCl, 10 mM imidazole) in the absence of reducing agent. The pooled eluate was concentrated and diluted 1:4 with TN-Iz10 (in order to further reduce the TCEP concentration). To allow for efficient disulphide bond formation the samples were supplemented with 20 mM oxidised glutathione and incubated overnight at 4 °C. Afterwards, the protein solutions were diluted 1:2 with 25 mM Tris-HCl pH 8.0 and further purified by anion exchange and size exclusion chromatography. The final preparations were analysed by non-reducing SDS-PAGE to confirm quantitative formation of covalently linked dimers (> 95%).

In vitro BiP biotinylation

In vitro biotinylation of N-terminally avi-tagged BiPs was conducted on the tag-cleaved forms of unmodified or AMPylated GST-TEV-AviTag-haBiP$^{T229A\text{-}V461F}$ (UK2331) or His_6-Smt3-AviTag-haBiP$^{T229A\text{-}V461F}$ (UK2359). Biotinylation was conducted in vitro with 100 µM target protein, 200 µM biotin (Sigma) and 2 µM GST-BirA (UK1801) in a buffer of 2 mM ATP, 5 mM $MgCl_2$, 25 mM Tris-HCl pH 8.0, 150 mM NaCl and 1 mM TCEP. The reaction mixture was incubated for 16 h at 4 ºC. The protein was made nucleotide-free by the addition of 2 U calf intestinal alkaline phosphatase (NEB) per mg of BiP, plus extensive dialysis into TN buffer supplemented with 1 mM DTT and 2 mM EDTA. The protein was then incubated with 0.5 ml GSH-Sepharose 4B matrix for 1 h at 4 ºC in order to deplete the GST-BirA. The biotinylated BiP-containing supernatant was diluted 1:1 with AEX-A and loaded onto a MonoQ 5/50 GL

column (GE Healthcare), equilibrated in 92.5% AEX-A and 7.5% AEX-B. BiP protein was eluted using a linear gradient of 7.5–50% AEX-B, over 20 CV at a flow rate of 1 ml/min. In the case of UK2359-derived BiP proteins the Mono Q eluted proteins were diluted with glycerol and stored at –20 ºC in a final buffer of TNTG (12.5 mM Tris-HCl pH 8.0, ~ 150 mM NaCl, 0.5 mM TCEP and 50% (*v/v*) glycerol) at a concentration > 1 µM. UK2331-derived BiPs were additionally gel filtered into HKM (25 mM HEPES-KOH pH 7.4, 150 mM NaCl and 10 mM $MgCl_2$) using S200 10/300 GL column with a distal 1 ml GSTrap 4B (GE Healthcare), connected in series. Proteinaceous fractions were pooled, supplemented with 1 mM TCEP, concentrated to > 20 µM, flash-frozen in small aliquots and stored at –80 °C. Protein samples were validated as being nucleotide-free (apo) by their $A_{260/280}$ ratio and reference to IP-RP-HPLC analysis as conducted previously (Preissler *et al*, 2017a). Proteins were confirmed as being > 95% biotinylated via a streptavidin gel-shift assay.

Biotinylated $FICD^{H363A}$ (UK2422) was purified like other FICD proteins, in vitro biotinylated as specified above and then excess biotin and residual BirA was removed by gel filtration as detailed for the polishing of UK2331-derived BiPs, but with the column equilibrated in TNT (25 mM Tris-HCl pH 8.0, 150 mM NaCl, 1 mM TCEP) rather than HKM. Pooled protein fractions were concentrated to > 20 µM, flash-frozen in small aliquots and stored at –80 °C.

Oxidation of FICD's TPR domain

Purification of TPR domain oxidised (TPRox) $FICD^{D160C\text{-}T183C\text{-}C421S}$ proteins was achieved as above (for other FICDs), with the addition of an oxidation and clean-up AEX step. Note, the cysteine free $FICD^{C421S}$ mutation was previously observed to have no effect on FICD-mediated deAMPylation or BiP-AMP binding and a slight stimulatory effect on FICD-mediated AMPylation (Perera *et al*, 2019).

In order to form the disulphide-bond, the FICD protein (post-Ulp1 cleavage and Ni-NTA column elution) was diluted down to a concentration of 5 µM in a final buffer of 25 mM Tris-HCl pH 8.0 and 100 mM NaCl, supplemented with 0.5 mM $CuSO_4$ and 1.75 mM 1,10-phenanthroline (Sigma), and incubated for 16 h at 4 ºC. The oxidation reaction was then quenched by the addition of 2 mM EDTA. The protein, diluted down to 50 mM NaCl with AEX-A, was then purified on a HiTrap 5 ml Capto Q column (equilibrated in 95% AEX-A and 5% AEX-B buffer) using a linear gradient of 5-50% AEX-B over 10 CV. Proteinaceous fractions were further purified as detailed above (beginning with RESOURCE Q column

purification), culminating in the purification of dimeric or monomeric FICD (as appropriate) by gel filtration.

Stoichiometric disulphide bond formation was confirmed by the use of an electrophoretic mobility assay (see **Figure 2.3.3c**), in which the putatively oxidised protein was heated for 10 min at 70 ºC in SDS-Laemmli buffer ± DTT; all available thiols were then reacted with a large excess of PEG 2000 maleimide (incubated for 30 min at 25 ºC). All unreacted maleimides were then quenched by the addition of a molar excess of DTT (incubated for 5 min at 25 ºC) before the samples were analysed by SDS-PAGE. Significant PEG modification of FICD(TPRox) proteins was only observed in samples that were initially denatured in reducing conditions (+ DTT), suggesting that the two TPR domain-cysteines were not accessible for alkylation in the absence of DTT (on account of being oxidised to form an intramolecular disulphide bond).

Chapter 6.3: Protein crystallisation and structure determination

FICD proteins (residues 104–445) and monomeric lid-truncated BiP$^{T229A-V461F}$-AMP (residues 27–549) [UK2090] were purified as above and gel filtered into a final buffer of T(10)NT (10 mM Tris-HCl pH 8.0, 150 mM NaCl and 1 mM TCEP). Heterodimer copurification was achieved by mixing FICD$^{L258D-H363A}$ (UK2093) and BiP$^{T229A-V461F}$-AMP in a 1.5:1 molar ratio, supplemented with an additional 250 µM ATP, 50 mM KCl and 2 mM $MgCl_2$. The mixture was incubated for 10 min at 4 ºC and purified by gel filtration on an S200 Increase 10/300 GL column equilibrated in TNKMT (10 mM Tris-HCl pH 8.0, 100 mM NaCl, 50 mM KCl, 2 mM $MgCl_2$ and 1 mM TCEP) with ≤ 5 mg of protein injected per SEC run. Heterodimeric protein fractions were pooled (as indicated in **Figure 2.1.1**) and concentrated to 10.3 mg/ml using a 50 kDa MWCO centrifugal filter.

Crystallisation solutions, consisting of 100 nl protein solution and 100 nl crystallisation reservoir solution, were dispensed using a mosquito crystal (SPT Labtech) and the complex was crystallised via sitting drop vapour diffusion at 25 ºC. State 1 crystals were obtained from reservoir conditions of 0.1 M MES pH 6.5, 10% PEG 4000 and 0.2 M NaCl; state 2 crystals were obtained from conditions of 0.1 M Tris pH 8.0 and 25% PEG 400 (see **Table 1**). Crystals were cryoprotected in a solution consisting of 25% glycerol and 75% of the respective reservoir solution (*v/v*) before being cryocooled in liquid nitrogen.

FICD:Apo and FICD:nucleotide crystals (**Table 3**) were grown by dilution of FICD proteins to 9 mg/ml in T(10)NT. For structures containing ATP/AMPPNP, diluted protein solutions were supplemented with MgATP/AMPPNP (from a pH 7.4, 100 mM stock solution) to a final concentration of 10 mM. A drop ratio of protein solution to crystallisation well solution of 200:100 nl was used. Where applicable crystals were obtained by microseeding (D'Arcy *et al*, 2007), from conditions provided in **Table 4**. In these instances, a drop ratio of protein solution to water-diluted seeds to crystallisation well solution of 150:50:100 nl was used. The best diffracting crystals were obtained from the crystallisation conditions detailed in **Table 4**, cryoprotected by briefly soaking in cryoprotectant solution (also noted in **Table 4**) and then cryocooled in liquid nitrogen.

Diffraction data were collected from the Diamond Light Source at 100 K and the data processed using DIALS (Beilsten-Edmands *et al*, 2020) [state 1 deAMPylation complex crystal], xia2 (Winter, 2010) [state 2 deAMPylation complex crystal] or XDS (Kabsch, 2010) [isolated FICD ± nucleotide crystals] and the CCP4 module Aimless (Winn *et al*, 2011; Evans & Murshudov, 2013). Structures were solved by molecular replacement using the CCP4 module Phaser (McCoy *et al*, 2007; Winn *et al*, 2011). For the $FICD^{L258D}$:Apo and FICD:ATP structures the human FICD protein (FICD:MgADP) structure (PDB 4U0U) from the Protein Data Bank (PDB) was used as a search model. For subsequent FICD ± nucleotides structures the solved $FICD^{L258D}$:Apo structure was used as a search model. AMPylated BiP (PDB 5O4P) and monomeric $FICD^{L258D}$:MgAMPPNP (PDB 6I7L) structures from the Protein Data Bank were used as initial search models for the deAMPylation complexes. Manual model building was carried out in COOT (Emsley *et al*, 2010) and refined using refmac5 (Winn *et al*, 2003) (in the case of the deAMPylation complexes with TLS added). Metal binding sites were validated using the CheckMyMetal server (Zheng *et al*, 2017). Polder OMIT maps were generated using the Polder Map module of Phenix (Liebschner *et al*, 2017; Adams *et al*, 2010). Structural figures were prepared using UCSF Chimera (Pettersen *et al*, 2004) and PyMol (Schrödinger, LLC, 2015), estimates of interaction surface areas were derived from PISA analysis (Krissinel & Henrick, 2007), interaction maps were based on an initial output from LigPlot+ (Laskowski & Swindells, 2011) and the chemical reaction pathway was created in ChemDraw (PerkinElmer Informatics).

Chapter 6.4: Contrast variation small angle neutron scattering (SANS)

Non-deuterated BiP$^{T229A-V461F}$-AMP (residues 27–635; UK2521) and FICD^{H363A} (residues 104–445; UK1954) [hBiP-AMP and hFICD] were purified as detailed above but were gel filtered into a final buffer of TNKMT(0.2) [TNKMT buffer with TCEP reduced to 0.2 mM]. The matchout deuterium labelled protein equivalents were produced in the ILL's deuteration laboratory (Grenoble, France). Deuterated proteins were expressed from *E. coli* BL21 Star (DE3) cells (Invitrogen) that were adapted to 85% deuterated Enfors minimal media containing unlabelled glycerol as carbon source, as described previously (Haertlein *et al*, 2016; Dunne *et al*, 2017), in the presence of kanamycin at a final concentration of 35 µg/ml. The temperatures at which the cells produced the highest amount of soluble matchout-deuterated BiP or FICD were chosen for cell growth using a high cell density fermentation process in a bioreactor (Labfors, Infors HT). For BiP expression, cells were grown using a fed-batch fermentation strategy at 30 °C to an OD_{600} of 20. The temperature was then decreased to 18 °C and protein expression was induced by addition of 1 mM IPTG. After a further 22 h of protein expression at 18 °C, bacteria were harvested by centrifugation. FICD expression was conducted likewise, but with induction at OD_{600} 19 and at a temperature of 22 ºC. FICD expressing cells were incubated for a further 21.5 h at 22 ºC before harvesting. Matchout-deuterated proteins (dBiP$^{T229A-V461F}$-AMP and dFICD^{H363A}) were isolated and purified from deuterated cell pastes using H_2O-based buffer systems, as mentioned above, and gel filtered into TNKMT(0.2).

Heterotetrameric complexes were copurified by gel filtration of a mixture of either dBiP-AMP and hFICD or hBiP-AMP and dFICD (in a 1.25:1 molar ratio of BiP-AMP:FICD), with ≤ 5 mg of protein injected per SEC run, supplemented with 250 µM ATP. The gel filtration was conducted on an S200 Increase 10/300 GL column equilibrated with TNKMT(0.2). Heterotetrameric complex fractions were collected and concentrated to > 7 mg/ml. Some of this purified complex was further exchanged by the same SEC process into TNKMT(0.2) in which the solvent used was D_2O. That is to say, the complex was exchanged into 100% D_2O buffer. Protein fractions in 100% D_2O buffer were subsequently concentrated to > 6 mg/ml. The elution profile appeared largely identical in both deuterated and non-deuterated buffers. Complexes at different %D_2O were obtained by either dilution with the appropriate matched buffer (± D_2O) or by the mixing of one complex purified in 0% D_2O buffer with the same complex in 100% D_2O buffer.

SANS data were collected from a total of 17 samples with various D_2O buffer compositions at 12 ºC, at the ILL beamline D11. Protein complexes (ranging from 4.3 to 5.5 mg/ml) were analysed in a 2 mm path-length quartz cell with a 5.5 Å wavelength neutron beam at distances of 1.4, 8 and 20.5 m. Data from relevant buffer-only controls were also collected with similar data collection times and subtracted from the radially averaged sample scattering intensities to produce the $I(q)$ against q scattering curves. Scattering data were initially processed with the GRASP (Graphical Reduction and Analysis SANS Program for Matlab; developed by Charles Dewhurst, ILL) and with the Igor Pro software (WaveMetrics) using SANS macros (Kline, 2006). Data analysis was conducted using Prism 8.4 (GraphPad) and PEPSI-SANS (for fitting of theoretical scattering curves and flex-fit model generation; software based on PEPSI-SAXS (Grudinin *et al*, 2017)).

Comparison of the ln(Transmission) of the 0% and 100% D_2O buffer only controls with the ln(Transmission) of each sample (not shown) confirmed that the $\%D_2O$ of each sample was within the margin of error of the theoretical D_2O content (Zaccai, 2012). Theoretical R_g values, derived from structural models, were calculated using CRYSON (Svergun *et al*, 1998). The symmetry of structural models was assessed through the use of AnAnaS software (Pagès & Grudinin, 2020).

Chapter 6.5: Differential scanning fluorimetry (DSF)

DSF experiments presented in **Chapter 3** were performed on a CFX96 Touch Real-Time PCR Detection System (Bio-Rad) in 96-well plates (Hard-Shell, Bio-Rad) sealed with optically clear Microseal 'B' Adhesive Sealer (Bio-Rad). Each sample was measured in technical duplicate and in a final volume of 20 µl. Protein was used at a final concentration of 2 µM, ATP or ADP (if applicable) at 5 and 2 mM, respectively, and SYPRO Orange dye (Thermo Fisher) at a 10 × concentration in a buffer of HKM. Solutions were briefly mixed, and the plate spun at 200 × *g* for 10 s before DSF measurement. Fluorescence of the SYPRO Orange dye was monitored on the FRET channel over a temperature range of 25–90 ºC with 0.5 ºC intervals. Background fluorescence changes were subtracted from the protein sample fluorescence data using no-protein control (NPC) wells. NPC fluorescence was unchanged by the addition of ATP or ADP. Data was then analysed in Prism 8.4 (GraphPad), with melting temperatures calculated as the global minimums of the negative first derivatives of the relative fluorescent unit (RFU) melt curves (with respect to temperature).

The DSF experiments shown in **Chapter 4** were conducted as above with modifications. These DSF experiments were performed on an ABi 7500 qPCR machine (Applied Biosciences). Experiments were carried out in 96-well qPCR plates (Thermofisher), with each sample in technical triplicate and in a final volume of 20 µl in a buffer of HKM plus 1 mM TCEP. Ligands were used at the indicated concentrations (2.5–20 mM). In the ATP titration experiment, the DSF buffer was supplemented with an additional 15 mM $MgCl_2$ (25 mM final $MgCl_2$ concentration). Fluorescence of the SYPRO Orange dye was monitored over a temperature range of 20–95 ºC using the VIC filter set. Data was then analysed in Prism 7.0 (GraphPad) as above.

Chapter 6.6: Bio-layer interferometry (BLI)

All BLI experiments were conducted on the FortéBio Octet RED96 System (Pall FortéBio) in a buffer basis of HKM supplemented with 0.05% (*v/v*) Triton X-100 (HKMTx). Streptavidin (SA)-coated biosensors (Pall FortéBio) were hydrated in HKMTx for at least 30 min at 25 °C prior to use. Experiments were conducted at 30 ºC. BLI reactions were prepared in 200 µl volumes in 96-well microplates (greiner bio-one). Ligand loading was conducted at low nanomolar biotinylated BiP concentrations such that the rate of all ligand loading reactions was roughly equivalent and all tips reached a loading threshold of 1 nm binding signal (displacement) within 300–600 s. All ligands loaded with a range of 1.0–1.2 nm. After loading of the immobilised ligand, BiP was activated in 2 mM ATP for 200 s, followed by a 50 s baseline in HKMTx alone, before association with apo FICD variants (all bearing a catalytically inactivating His363Ala mutation and at 50 nM unless otherwise specified) in HKMTx. The first dissociation step was initiated by the dipping of all tips into wells lacking FICD analyte (only HKMTx). The second dissociation step was induced by the dipping of the biosensor tips into HKMTx supplemented with 2 mM ATP. Experiments were conducted at a 1000 rpm shake speed and with a 5 Hz acquisition rate. Data were processed in Prism 8.4 (GraphPad).

For the kinetic experiments presented in **Figure 3.1.1** and **Chapter 4** GST-TEV cleaved biotinylated BiPs (UK2331-derived) were used as ligands. BLI experiments were performed as above with some modifications. Biotinylated-AviTag-haBiP$^{T229A\text{-}V461F}$:Apo (UK2331) was loaded onto the tip. The immobilised ligand sensor was then baselined in assay solution for at least 200 s. A 10 Hz acquisition rate was used and the baseline, association and dissociation

steps were conducted at a 400 rpm shake speed. Preceding the baseline step biotinylated BiP$^{T229A-V461F}$:Apo was also activated with or without 2 mM ATP (unless otherwise stated), for 300 s at a 1000 rpm shake speed. In these experiments 250 nM FICD analyte association or dissociation steps were conducted in the presence or absence of nucleotide, as indicated, with ATP at 8 mM and ADP at 2 mM.

In the dimer dissociation BLI experiments biotinylated AviTag-FICD^{H363A} (UK2422) was diluted to 3 nM and incubated for 10 min at 25 ºC with either dimeric FICD^{H363A} or monomeric FICD$^{L258D-H363A}$ (at 300 nM) in HKMTx. After this incubation period the streptavidin biosensors were loaded until the hetero-labelled dimers (biotinylated AviTag-FICD^{H363A} with FICD^{H363A}) were loaded to a 1 nm displacement. Dissociation was initiated by dipping in HKTx buffer (50 mM HEPES-KOH pH 7.4, 150 mM KCl and 0.05% Triton X-100) ± nucleotide at 5 mM, as indicated. Data was processed by subtracting the respective monomer incubated biotinylated FICD tip from the dimeric hetero-labelled dimer dissociation, followed by fitting of the corrected dissociation to a mono-exponential decay function using Prism 7.0 (GraphPad).

Chapter 6.7: Fluorescence polarisation deAMPylation assay

Measurement of deAMPylation kinetics was performed as described previously (Preissler *et al*, 2017a) with modifications. The probe BiP$^{T229A-V461F}$ (UK2521) modified with FAM-labelled AMP, BiP$^{T229A-V461F}$-AMP(FAM), was generated by pre-incubating 100 µM apo BiP$^{T229A-V461F}$ with 5 µM GST-FICD^{E234G} (UK1479) and 110 µM ATP in HKM for 5 min at 20 ºC, followed by addition of 100 µM ATP-FAM [N^6-(6-Amino)hexyl-ATP-6-FAM; Jena Bioscience] and further incubation for 19 h at 25 ºC. To ensure complete BiP AMPylation 2 mM ATP was then added to the reaction which was incubated for an additional 1.25 h at 25 ºC. The reaction mixture was then incubated with GSH-Sepharose 4B matrix for 45 min at 4 ºC in order to deplete the GST-FICD^{E234G}. The BiP containing supernatant was buffer exchanged into HKM using a Zeba Spin desalting column (7K MWCO, 0.5 ml; Thermo Fisher) in order to remove the majority of free (FAM labelled) nucleotide. 2 mM ATP was added to the eluted protein and incubated for 15 min at 4 ºC (to facilitate displacement of any residual FAM-labelled nucleotide derivates bound by the NBD of BiP). Pure BiP-AMP(FAM) with BiP-AMP was then obtained by gel filtration using an S75 Increase 10/300 GL column equilibrated in HKM at 4 ºC. 1 mM TCEP was added to the protein fractions, which were

concentrated using a 50K MWCO centrifugal filter and snap frozen. A labelling efficiency of 1.8% was estimated based on the extinction coefficient for BiP-AMP:ATP (ε_{280} 33.5 mM^{-1} cm^{-1}), FAM (ε_{492} 83.0 mM^{-1} cm^{-1}) and a 280/492 nm correction factor of 0.3 (Jenna Biosciences).

DeAMPylation reactions were performed in HKMTx(0.1) [HKM supplemented with 0.1% (*v/v*) Triton X-100] in 384-well polystyrene microplates (black, flat bottom, µCLEAR; greiner bio-one) at 30 °C in a final volume of 30 µl containing trace amounts of fluorescent $BiP^{T229A-V461F}$-AMP(FAM) probe (10 nM), supplemented with $BiP^{T229A-V461F}$-AMP (5 µM) and FICD proteins (0.5 µM). A well lacking FICD protein was used for baseline FP background subtraction. 10 nM ATP-FAM alone was also included as a low FP control (not shown).

Fluorescence polarisation of FAM (λ_{ex} = 485 nm, λ_{em} = 535 nm) was measured with an Infinite F500 plate reader (Tecan). The mFP y_0 difference between the $FICD^{L258D}$ time course and the same reaction composition pre-incubated for 5 h at 25 ºC before the beginning of data collection, was interpreted as the ΔmFP equivalent to complete (5 µM) BiP-AMP deAMPylation. Data analysis was achieved using Prism 8.4 (GraphPad).

For direct calculation of k_{cat} values deAMPylation assays were conducted as above but with 10 µM FICD or $FICD^{L258D}$ and 100 or 150 µM BiP-AMP substrate. Following subtraction of a no enzyme background from all datasets, the mFP difference for each sample (between t = 0 and the mFP plateau) was interpreted as the ΔmFP equivalent to complete BiP-AMP deAMPylation ($[S]_0$).

Chapter 6.8: In vitro AMPylation

In vitro AMPylation reactions were performed in HKM buffer in a 7 µl volume. Reactions contained 10 µM ATP-FAM, 5 µM ATP-hydrolysis and substrate-binding deficient $BiP^{T229A-V461F}$ (UK2521), 7.5 µM oxidised $_{S\text{-}S}FICD^{A252C-H363A-C421S}$ (UK2269, trap) to sequester any modified BiP [BiP-AMP(FAM)] and, unless otherwise stated, 0.5 µM FICD. Reactions were started by addition of nucleotide. Apart from in the presented time courses, after a 60 min incubation at 25 °C the reactions were stopped by addition of 3 µl 3.3 × LDS sample buffer (Sigma) containing NEM (40 mM final concentration) for non-reducing SDS-PAGE or DTT (50 mM final concentration) for reducing SDS-PAGE and heated for 10 min at 70 °C. Samples were applied to a 10% SDS-PAGE gel (unless otherwise stated), the FAM-label was imaged

with a Chemidoc MP (Bio-Rad) using the Alexa Flour 488 dye setting. Gels were subsequently stained with Quick Coomassie (Neo Biotech).

Chapter 6.9: Mammalian cell culture and lysis

All cells were grown on tissue culture dishes or multi-well plates (Corning) at 37 °C and 5% CO_2. All CHO-K1 derived cells (ATCC CCL-61) were phenotypically validated as proline auxotrophs and their *Cricetulus griseus* origin was confirmed by genomic sequencing. The CHO-K1 *FICD*$^{-/-}$ cell line used in this study was described previously (Preissler *et al*, 2015b). The CHO-K1 S21 *FICD*$^{-/-}$ cell line (genetically engineered by Cláudia Rato da Silva) was generated by CRISPR-Cas9 knockout of both FICD alleles (as previously (Preissler *et al*, 2015b)) into the earlier described CHO-K1 S21 cell line bearing UPR reporters *CHOP::GFP* and *XBP1s::Turquoise* (Sekine *et al*, 2016). Cells were cultured in Nutrient mixture F-12 Ham (Sigma) supplemented with 10% (*v/v*) serum (FetalClone II; HyClone), 1 × Penicillin-Streptomycin (Sigma), and 2 mM L-glutamine (Sigma). Experiments were performed at cell densities of 60–90% confluence. Where indicated, cells were treated for 3 h with cycloheximide (Sigma) by exchanging the culture medium with pre-warmed (37 °C) medium supplemented with cycloheximide at 100 µg/ml. Cell lines were subjected to random testing for mycoplasma contamination using the MycoAlert Mycoplasma Detection Kit (Lonza).

Cell lysates were obtained and analysed as in (Preissler *et al*, 2015a) but with some modifications. Mammalian cells were cultured on 10 cm dishes and treated as indicated and transfected using Lipofectamine LTX with 5 µg plasmid DNA, and allowed to grow for a further 40 h. Before lysis, the dishes were placed on ice, washed with ice-cold PBS, and cells were detached in PBS containing 1 mM ethylenediaminetetraacetic acid (EDTA) using a cell scraper. The cells were sedimented for 5 min at 370 × *g* at 4 °C and lysed for 10 min on ice in HG lysis buffer consisting of 20 mM HEPES-KOH pH 7.4, 150 mM NaCl, 2 mM $MgCl_2$, 33 mM D-glucose, 10% (*v/v*) glycerol, 1% (*v/v*) Triton X-100 and protease inhibitors (2 mM phenylmethylsulphonyl fluoride (PMSF), 4 µg/ml pepstatin, 4 µg/ml leupeptin, 8 µg/ml aprotinin) with 100 U/ml hexokinase (from *Saccharomyces cerevisiae* Type F-300; Sigma). The lysates were cleared for 10 min at 21,000 × *g* at 4 °C. Bio-Rad protein assay reagent (BioRad) was used to determine the protein concentrations of lysates and all samples were normalised to 6 mg/ml using HG lysis buffer. For analysis by SDS-PAGE, LDS sample buffer was added to the lysates and proteins were denatured by heating for 10 min at 70 °C before

separation on 12.5% SDS polyacrylamide gels. For immunoblot detection 30 µg of lysate was loaded per lane, except in the case of FICD immunoblot detection where 60 µg of lysate was loaded.

Chapter 6.10: Native polyacrylamide gel electrophoresis (native-PAGE)

Non-denaturing native-PAGE was performed as described previously (Preissler *et al*, 2015a). Briefly, Tris-glycine polyacrylamide gels (4.5% stacking gel and a 7.5% separation gel) were used to separate proteins from mammalian cell lysates to detect BiP monomers and oligomers. The separation was performed in running buffer (25 mM Tris, 192 mM glycine, pH ~8.8) at 120 V for 2 h. Afterwards, the proteins were transferred to a polyvinylidene difluoride (PVDF) membrane in blotting buffer (48 mM Tris, 39 mM glycine; pH ~9.2) supplemented with 0.04% (*w/v*) SDS for 16 h at 30 V for immunodetection. The membrane was washed for 20 minutes in blotting buffer (without SDS) supplemented with 20% (*v/v*) methanol before blocking. Equal volumes of lysates, corresponding to 30 µg of total protein, were loaded per lane to detect endogenous BiP from cell lysates by immunoblotting.

Chapter 6.11: Immunoblot (IB) analysis

After separation by SDS-PAGE or native-PAGE proteins were transferred onto PVDF membranes. The membranes were blocked with 5% (*w/v*) dried skimmed milk in TBS (25 mM Tris-HCl pH 7.5, 150 mM NaCl) and incubated with primary antibodies followed by IRDye fluorescently labelled secondary antibodies (LI-COR). The membranes were scanned with an Odyssey near-infrared imager (LI-COR). Primary antibodies and antisera against hamster BiP [chicken anti-BiP (Avezov *et al*, 2013)], eIF2α [mouse anti-eIF2α (Scorsone *et al*, 1987)] and FICD [chicken anti-FICD (Preissler *et al*, 2015b)] were used.

Chapter 6.12: Flow cytometry

FICD over-expression-dependent induction of unfolded protein response signalling was analysed by transient transfection of CHO-K1 S21 *FICD*$^{-/-}$ UPR reporter cell lines with plasmid DNA encoding the complete FICD coding sequence (with mutations as indicated) and mCherry as a transfection marker, using Lipofectamine LTX (Thermo Fisher) as described

previously (Preissler *et al*, 2015b). 0.5 µg DNA was used to transfect cells growing in 12-well plates. 40 h after transfection the cells were washed with PBS and collected in PBS containing 4 mM EDTA, and single live-cell fluorescent signals (20,000 collected per sample) were analysed by dual-channel flow cytometry with an LSRFortessa cell analyser (BD Biosciences). Turquoise and mCherry fluorescence was detected using a 405 nm excitation laser with a 450/50 nm emission filter and a 561 nm excitation laser with a 610/20 nm emission filter, respectively. Data were processed using FlowJo and the extracted population parameters were plotted in Prism 8.4 (GraphPad).

Chapter 6.13: Fluorescence monomer-dimer assay

To generate an oligomeric state-sensitive fluorescent FICD probe Ser288Cys was introduced into the dimerisation-competent, cysteine-free, catalytically inactive $FICD^{H363A-C421S}$. The resulting construct (UK2473; $FICD^{S288C-H363A-C421S}$) was expressed and Ulp1-cleaved, as detailed above, in reducing conditions. The protein was then subject to site-specific labelling of the cysteine, using tetramethylrhodamine-maleimide [TMR-maleimide, a fluorophore chosen based on its narrow Stokes shift and therefore well-suited for homoFRET (Pietraszewska-Bogiel & Gadella, 2011; Yang *et al*, 2017)]. In brief, 100 µM protein was mixed with 1 mM TMR-5-maleimide (Sigma) in a final buffer composed of 50 mM HEPES pH 7.2, 150 mM KCl, 0.5 mM TCEP, 1 mM EDTA and 4% DMF. The 250 µl reaction mixture was incubated for 16 h at 4 °C in the dark. The resulting labelled protein was first buffer exchanged into HKT(0.2) (50 mM HEPES-KOH pH 7.4, 150 mM KCl, 0.2 mM TCEP) using a Centri Pure P2 desalting column (emp Biotech). Any unlabelled cysteines in the eluted protein were then alkylated by incubation with 1 mM NEM for 1 h at 4 °C, followed by incubation with 5 mM DTT for a further 1 h at 4 °C to quench the excess NEM. The resulting protein was diluted 1:2 with 25 mM Tris pH 8.0 and loaded onto a Mono Q 5/50 GL column. The labelled protein was eluted with a linear gradient of AEX-A (plus 0.2 mM TCEP) to AEX-B (plus 0.2 mM TCEP) of 5–35% over 30 CV. Labelled protein fractions were pooled and concentrated using a 30 kDa MWCO centrifugal filters (Amicon Ultra; Merck Millipore). The concentrated labelled protein was then buffer exchanged into HNKM (25 mM HEPES-KOH pH 7.4, 100 mM NaCl, 50 mM KCl and 2 mM $MgCl_2$), and confirmed as being dimerisation competent, using an S200 Increase 10/300 GL column. Protein fractions were pooled and concentrated. The resulting protein concentration and TMR labelling efficiency were estimated

by measurement of the A_{280nm} and A_{555nm} using a NanoDrop Spectrophotometer (Thermo Fisher Scientific). The protein concentration was calculated using the following equation:

Protein concentration (M) = $[A_{280nm} - (A_{555nm} \times 0.30)]/\varepsilon$

Where 0.30 is the correction factor for the fluorophore's absorbance at 280 nm, and ε is the calculated molar extinction coefficient of FICD (29,340 $cm^{-1}M^{-1}$). The labelling efficiency of the preparation was 41% as calculated based on the A_{555nm} value and assuming an extinction coefficient for TMR of 65,000 $cm^{-1}M^{-1}$.

For the fluorescence assay, $FICD^{S288C\text{-}H363A\text{-}C421S}$-TMR (FICD-TMR) was diluted to 2.5 nM and mixed with the titrant, as indicated, in a buffer of HKTx dispensed into 384-well non-binding, low volume, HiBase, black microplates (greiner bio-one). Note, all FICD variants were dispensed directly into the microplate well solutions using a D300e digital dispenser (Tecan). The plate was then sealed and the final 20 µl (**Figure 4.5.2a**) or 15 µl reactions (**Figure 4.5.2b**) were incubated for 45 minutes at 10 °C, whilst shaking at 300 rpm on a ThermoMixer C (Eppendorf). The plate seal was then removed, and fluorescent measurements were conducted using a CLARIOstar Plus plate reader (BMG Labtech), exciting at 535/20 nm and top reading emission at 585/30 nm. For each condition, a reference well lacking FICD-TMR was included. This background fluorescence was subtracted from the respective condition with $FICD^{S288C\text{-}H363A\text{-}C421S}$-TMR. In order to correct for any non-specific effects of the nucleotide titrants on TMR fluorescence, each fluorescence value in **Figure 4.5.2b** is presented as a fraction of the de-quenched monomeric signal from a parallel sample containing an additional 250 nM $FICD^{H363A}$ (UK1954). Independent repeat data were collected in technical duplicate. The displayed best fit lines were derived by non-linear regression fitting of a one site binding saturation model using Prism 7.0 (Graphpad).

Chapter 7: References

Adams PD, Afonine P V, Bunkóczi G, Chen VB, Davis IW, Echols N, Headd JJ, Hung L-W, Kapral GJ, Grosse-Kunstleve RW, McCoy AJ, Moriarty NW, Oeffner R, Read RJ, Richardson DC, Richardson JS, Terwilliger TC & Zwart PH (2010) PHENIX: a comprehensive Python-based system for macromolecular structure solution. *Acta Crystallogr. D. Biol. Crystallogr.* **66:** 213–21

Amin-Wetzel N, Neidhardt L, Yan Y, Mayer MP & Ron D (2019) Unstructured regions in IRE1α specify BiP-mediated destabilisation of the luminal domain dimer and repression of the UPR. *Elife* **8:** 1–35

Amin-Wetzel N, Saunders RA, Kamphuis MJ, Rato C, Preissler S, Harding HP & Ron D (2017) A J-Protein Co-chaperone Recruits BiP to Monomerize IRE1 and Repress the Unfolded Protein Response. *Cell* **171:** 1625-1637.e13

Anderson WB & Stadtman ER (1970) Glutamine synthetase deadenylylation: A phosphorolytic reaction yielding ADP as nucleotide product. *Biochem. Biophys. Res. Commun.* **41:** 704–709

Andrews LD, Fenn TD & Herschlag D (2013) Ground State Destabilization by Anionic Nucleophiles Contributes to the Activity of Phosphoryl Transfer Enzymes. *PLoS Biol.* **11:** e1001599

Avezov E, Cross BCS, Kaminski Schierle GS, Winters M, Harding HP, Melo EP, Kaminski CF & Ron D (2013) Lifetime imaging of a fluorescent protein sensor reveals surprising stability of ER thiol redox. *J. Cell Biol.* **201:** 337–49

Bakunts A, Orsi A, Vitale M, Cattaneo A, Lari F, Tadè L, Sitia R, Raimondi A, Bachi A & van Anken E (2017) Ratiometric sensing of BiP-client versus BiP levels by the unfolded protein response determines its signaling amplitude. *Elife* **6:**

Balch WE, Morimoto RI, Dillin A & Kelly JW (2008) Adapting proteostasis for disease intervention. *Science* **319:** 916–9

Beilsten-Edmands J, Winter G, Gildea R, Parkhurst J, Waterman D & Evans G (2020) Scaling diffraction data in the DIALS software package: Algorithms and new approaches for multi-crystal scaling. *Acta Crystallogr. Sect. D Struct. Biol.* **76:** 385–399

Broncel M, Serwa RA, Bunney TD, Katan M & Tate EW (2016) Global Profiling of Huntingtin-associated protein E (HYPE)-Mediated AMPylation through a Chemical Proteomic Approach. *Mol. Cell. Proteomics* **15:** 715–725

Brown MS, Segal A & Stadtman ER (1971) Modulation of glutamine synthetase adenylylation and deadenylylation is mediated by metabolic transformation of the P II -regulatory protein. *Proc. Natl. Acad. Sci. U. S. A.* **68:** 2949–53

Bunney TD, Cole AR, Broncel M, Esposito D, Tate EW & Katan M (2014) Crystal structure of the human, FIC-domain containing protein HYPE and implications for its functions. *Structure* **22:** 1831–43

Campanacci V, Mukherjee S, Roy CR & Cherfils J (2013) Structure of the Legionella effector AnkX reveals the mechanism of phosphocholine transfer by the FIC domain. *EMBO J.* **32:** 1469–1477

Carlsson L & Lazarides E (1983) ADP-ribosylation of the Mr 83,000 stress-inducible and glucose-regulated protein in avian and mammalian cells: modulation by heat shock and glucose starvation. *Proc. Natl. Acad. Sci.* **80:** 4664–4668

Casey AK, Moehlman AT, Zhang J, Servage KA, Krämer H & Orth K (2017) Fic-mediated deAMPylation is not dependent on homo-dimerization and rescues toxic AMPylation in flies. *J. Biol. Chem.***:** jbc.M117.799296

Castro-Roa D, Garcia-Pino A, De Gieter S, Van Nuland NAJ, Loris R & Zenkin N (2013) The Fic protein Doc uses an inverted substrate to phosphorylate and inactivate EF-Tu. *Nat. Chem. Biol.* **9:** 811–817

Chambers JE, Petrova K, Tomba G, Vendruscolo M & Ron D (2012) ADP ribosylation adapts an ER chaperone response to short-term fluctuations in unfolded protein load. *J. Cell Biol.* **198:** 371–85

Chan C-P, Siu K-L, Chin K-T, Yuen K-Y, Zheng B & Jin D-Y (2006) Modulation of the Unfolded Protein Response by the Severe Acute Respiratory Syndrome Coronavirus Spike Protein. *J. Virol.* **80:** 9279–9287

Chang SC, Erwin AE & Lee AS (1989) Glucose-regulated protein (GRP94 and GRP78) genes share common regulatory domains and are coordinately regulated by common trans-acting factors. *Mol. Cell. Biol.* **9:** 2153–2162

Chen Y, Tascón I, Neunuebel MR, Pallara C, Brady J, Kinch LN, Fernández-Recio J, Rojas AL, Machner MP & Hierro A (2013) Structural basis for Rab1 de-AMPylation by the Legionella pneumophila effector SidD. *PLoS Pathog.* **9:** e1003382

Cheng Y, Zhang Y & McCammon JA (2005) How does the cAMP-dependent protein kinase catalyze the phosphorylation reaction: An ab Initio QM/MM study. *J. Am. Chem. Soc.* **127:** 1553–1562

Curtis JE, Raghunandan S, Nanda H & Krueger S (2012) SASSIE: A program to study intrinsically disordered biological molecules and macromolecular ensembles using experimental scattering restraints. *Comput. Phys. Commun.* **183:** 382–389

D'Arcy A, Villard F & Marsh M (2007) An automated microseed matrix-screening method for protein crystallization. *Acta Crystallogr. Sect. D Biol. Crystallogr.* **63:** 550–554

Das D, Krishna SS, McMullan D, Miller MD, Xu Q, Abdubek P, Acosta C, Astakhova T, Axelrod HL, Burra P, Carlton D, Chiu H-J, Clayton T, Deller MC, Duan L, Elias Y, Elsliger M-A, Ernst D, Feuerhelm J, Grzechnik A, et al (2009) Crystal structure of the Fic (Filamentation induced by cAMP) family protein SO4266 (gi|24375750) from Shewanella oneidensis MR-1 at 1.6 A resolution. *Proteins* **75:** 264–71

Dedic E, Alsarraf H, Welner DH, Østergaard O, Klychnikov OI, Hensbergen PJ, Corver J, van Leeuwen HC & Jørgensen R (2016) A Novel Fic (Filamentation Induced by cAMP) Protein from Clostridium difficile Reveals an Inhibitory Motif-independent Adenylylation/AMPylation Mechanism. *J. Biol. Chem.* **291:** 13286–300

Dunne O, Weidenhaupt M, Callow P, Martel A, Moulin M, Perkins SJ, Haertlein M & Forsyth VT (2017) Matchout deuterium labelling of proteins for small-angle neutron scattering studies using prokaryotic and eukaryotic expression systems and high cell-density cultures. *Eur. Biophys. J.* **46:** 425–432

Emsley P, Lohkamp B, Scott WG & Cowtan K (2010) Features and development of *Coot*. *Acta Crystallogr. Sect. D Biol. Crystallogr.* **66:** 486–501

Engel P, Goepfert A, Stanger F V., Harms A, Schmidt A, Schirmer T & Dehio C (2012) Adenylylation control by intra- or intermolecular active-site obstruction in Fic proteins. *Nature* **482:** 107–10

Evans PR & Murshudov GN (2013) How good are my data and what is the resolution? *Acta Crystallogr. D. Biol. Crystallogr.* **69:** 1204–14

Farrugia MA & Puglielli L (2018) Nε-lysine acetylation in the endoplasmic reticulum – a novel cellular mechanism that regulates proteostasis and autophagy. *J. Cell Sci.* **131:** jcs221747

Feng F, Yang F, Rong W, Wu X, Zhang J, Chen S, He C & Zhou JM (2012) A Xanthomonas uridine 5′-monophosphate transferase inhibits plant immune kinases. *Nature* **485:** 114–118

Garcia-Pino A, Christensen-Dalsgaard M, Wyns L, Yarmolinsky M, Magnuson RD, Gerdes K & Loris R (2008) Doc of prophage P1 is inhibited by its antitoxin partner Phd through fold complementation. *J. Biol. Chem.* **283:** 30821–30827

Gaut JR (1997) In vivo threonine phosphorylation of immunoglobulin binding protein (BiP) maps to its protein binding domain. *Cell Stress Chaperones* **2:** 252–62

Gaut JR & Hendershot LM (1993) Mutations within the nucleotide binding site of immunoglobulin-binding protein inhibit ATPase activity and interfere with release of immunoglobulin heavy chain. *J. Biol. Chem.* **268:** 7248–55

Ghaemmaghami S, Huh W-K, Bower K, Howson RW, Belle A, Dephoure N, O'Shea EK & Weissman JS (2003) Global analysis of protein expression in yeast. *Nature* **425:** 737–41

Goepfert A, Stanger F V., Dehio C & Schirmer T (2013) Conserved Inhibitory Mechanism and Competent ATP Binding Mode for Adenylyltransferases with Fic Fold. *PLoS One* **8:** e64901

Grudinin S, Garkavenko M & Kazennov A (2017) *Pepsi-SAXS* : an adaptive method for rapid and accurate computation of small-angle X-ray scattering profiles. *Acta Crystallogr. Sect. D Struct. Biol.* **73:** 449–464

Guinier A & Fournet G (1955) Small-angle scattering of X-rays (Translation by C. B. Walker) New York: Wiley; London: Chapman and Hall

Gulow K, Bienert D & Haas IG (2002) BiP is feed-back regulated by control of protein translation efficiency. *J. Cell Sci.* **115:** 2443–2452

Haertlein M, Moulin M, Devos JM, Laux V, Dunne O & Trevor Forsyth V (2016) Biomolecular Deuteration for Neutron Structural Biology and Dynamics. In *Methods in Enzymology* pp 113–157. Academic Press Inc.

Ham H, Woolery AR, Tracy C, Stenesen D, Krämer H & Orth K (2014) Unfolded protein response-regulated Drosophila Fic (dFic) protein reversibly AMPylates BiP chaperone

during endoplasmic reticulum homeostasis. *J. Biol. Chem.* **289:** 36059–69

Harms A, Stanger F V. & Dehio C (2016) Biological Diversity and Molecular Plasticity of FIC Domain Proteins. *Annu. Rev. Microbiol.* **70:** annurev-micro-102215-095245

Hein MY, Hubner NC, Poser I, Cox J, Nagaraj N, Toyoda Y, Gak IA, Weisswange I, Mansfeld J, Buchholz F, Hyman AA & Mann M (2015) A Human Interactome in Three Quantitative Dimensions Organized by Stoichiometries and Abundances. *Cell* **163:** 712–723

Hendershot LM, Ting J & Lee AS (1988) Identity of the immunoglobulin heavy-chain-binding protein with the 78,000-dalton glucose-regulated protein and the role of posttranslational modifications in its binding function. *Mol. Cell. Biol.* **8:** 4250–4256

Hennig SB, Anderson WB & Ginsburg A (1970) Adenosine triphosphate: glutamine synthetase adenylyltransferase of Escherichia coli: two active molecular forms. *Proc. Natl. Acad. Sci. U. S. A.* **67:** 1761–8

Ibel K & Stuhrmann HB (1975) Comparison of neutron and X-ray scattering of dilute myoglobin solutions. *J. Mol. Biol.* **93:** 255–265

Kabsch W (2010) XDS. *Acta Crystallogr. D. Biol. Crystallogr.* **66:** 125–32

Khater S & Mohanty D (2015a) In silico identification of AMPylating enzymes and study of their divergent evolution. *Sci. Rep.* **5:** 10804

Khater S & Mohanty D (2015b) Deciphering the Molecular Basis of Functional Divergence in AMPylating Enzymes by Molecular Dynamics Simulations and Structure Guided Phylogeny. *Biochemistry* **54:** 5209–24

Kilambi KP & Gray JJ (2012) Rapid calculation of protein pKa values using rosetta. *Biophys. J.* **103:** 587–595

Kim MS, Pinto SM, Getnet D, Nirujogi RS, Manda SS, Chaerkady R, Madugundu AK, Kelkar DS, Isserlin R, Jain S, Thomas JK, Muthusamy B, Leal-Rojas P, Kumar P, Sahasrabuddhe NA, Balakrishnan L, Advani J, George B, Renuse S, Selvan LDN, et al (2014) A draft map of the human proteome. *Nature* **509:** 575–581

Kinch LN, Yarbrough ML, Orth K & Grishin N V. (2009) Fido, a Novel AMPylation Domain Common to Fic, Doc, and AvrB. *PLoS One* **4:** e5818

Kingdon HS, Shapiro BM & Stadtman ER (1967) Regulation of glutamine synthetase VIII. ATP:glutamine synthetase adenylyltransferase, an enzyme that catalyses alterations in the

regulatory properties of glutamine synthetase. *Proc.Natl.Acad.Sci.USA.* **58:** 1703–1710

Kityk R, Kopp J & Mayer MP (2017) Molecular Mechanism of J-Domain-Triggered ATP Hydrolysis by Hsp70 Chaperones. *Mol. Cell*

Kityk R, Vogel M, Schlecht R, Bukau B & Mayer MP (2015) Pathways of allosteric regulation in Hsp70 chaperones. *Nat. Commun.* **6:** 8308

Kline SR (2006) Reduction and analysis of SANS and USANS data using IGOR Pro. *J. Appl. Crystallogr.* **39:** 895–900

Kmiecik SW, Le Breton L & Mayer MP (2020) Feedback regulation of heat shock factor 1 (Hsf1) activity by Hsp70-mediated trimer unzipping and dissociation from DNA. *EMBO J.* **39:**

Kozutsumi Y, Segal M, Normington K, Gething MJ & Sambrook J (1988) The presence of malfolded proteins in the endoplasmic reticulum signals the induction of glucose-regulated proteins. *Nature* **332:** 462–4

Krissinel E & Henrick K (2007) Inference of Macromolecular Assemblies from Crystalline State. *J. Mol. Biol.* **372:** 774–797

Laitusis AL, Brostrom MA & Brostrom CO (1999) The dynamic role of GRP78/BiP in the coordination of mRNA translation with protein processing. *J. Biol. Chem.* **274:** 486–493

Lalioti VS, Vergarajauregui S, Villasante A, Pulido D & Sandoval I V. (2013) C6orf89 encodes three distinct HDAC enhancers that function in the nucleolus, the golgi and the midbody. *J. Cell. Physiol.* **228:** 1907–1921

Laskowski RA & Swindells MB (2011) LigPlot+: Multiple ligand-protein interaction diagrams for drug discovery. *J. Chem. Inf. Model.* **51:** 2778–2786

Lau E, Cao Q, Ng DCM, Bleakley BJ, Dincer TU, Bot BM, Wang D, Liem DA, Lam MPY, Ge J & Ping P (2016) A large dataset of protein dynamics in the mammalian heart proteome. *Sci. Data* **3:**

Liebschner D, Afonine P V., Moriarty NW, Poon BK, Sobolev O V., Terwilliger TC & Adams PD (2017) Polder maps: improving OMIT maps by excluding bulk solvent. *Acta Crystallogr. Sect. D Struct. Biol.* **73:** 148–157

De Los Rios P & Barducci A (2014) Hsp70 chaperones are non-equilibrium machines that achieve ultra-affinity by energy consumption. *Elife* **2014:**

De Los Rios P, Ben-Zvi A, Slutsky O, Azem A & Goloubinoff P (2006) Hsp70 chaperones accelerate protein translocation and the unfolding of stable protein aggregates by entropic pulling. *Proc. Natl. Acad. Sci. U. S. A.* **103:** 6166–6171

Luong P, Kinch LN, Brautigam CA, Grishin N V, Tomchick DR & Orth K (2010) Kinetic and structural insights into the mechanism of AMPylation by VopS Fic domain. *J. Biol. Chem.* **285:** 20155–63

Lyskov S, Chou F-C, Conchúir SÓ, Der BS, Drew K, Kuroda D, Xu J, Weitzner BD, Renfrew PD, Sripakdeevong P, Borgo B, Havranek JJ, Kuhlman B, Kortemme T, Bonneau R, Gray JJ & Das R (2013) Serverification of molecular modeling applications: the Rosetta Online Server that Includes Everyone (ROSIE). *PLoS One* **8:** e63906

Marcinowski M, Höller M, Feige MJ, Baerend D, Lamb DC & Buchner J (2011) Substrate discrimination of the chaperone BiP by autonomous and cochaperone-regulated conformational transitions. *Nat. Struct. Mol. Biol.* **18:** 150–158

Marsh BJ, Mastronarde DN, Buttle KF, Howell KE & McIntosh JR (2001) Organellar relationships in the Golgi region of the pancreatic beta cell line, HIT-T15, visualized by high resolution electron tomography. *Proc. Natl. Acad. Sci. U. S. A.* **98:** 2399–2406

Mayer MP & Gierasch LM (2019) Recent advances in the structural and mechanistic aspects of Hsp70 molecular chaperones. *J. Biol. Chem.* **294:** 2085–2097

McCoy AJ, Grosse-Kunstleve RW, Adams PD, Winn MD, Storoni LC & Read RJ (2007) Phaser crystallographic software. *J. Appl. Crystallogr.* **40:** 658–674

Michaelis L, Menten ML, Johnson KA & Goody RS (2011) The original Michaelis constant: translation of the 1913 Michaelis-Menten paper. *Biochemistry* **50:** 8264–9

Moehlman AT, Casey AK, Servage K, Orth K & Krämer H (2018) Adaptation to constant light requires Fic-mediated AMPylation of BiP to protect against reversible photoreceptor degeneration. *Elife* **7:**

Muller MP, Peters H, Blumer J, Blankenfeldt W, Goody RS & Itzen A (2010) The Legionella Effector Protein DrrA AMPylates the Membrane Traffic Regulator Rab1b. *Science (80-.).* **329:** 946–949

Nagaraj N, Wisniewski JR, Geiger T, Cox J, Kircher M, Kelso J, Pääbo S & Mann M (2011) Deep proteome and transcriptome mapping of a human cancer cell line. *Mol. Syst. Biol.*

7: 548

Nesin OM, Pakhomova ON, Xiao S & Pakhomov AG (2011) Manipulation of cell volume and membrane pore comparison following single cell permeabilization with 60- and 600-ns electric pulses. *Biochim. Biophys. Acta - Biomembr.* **1808:** 792–801

Otero JH, Lizák B & Hendershot LM (2010) Life and death of a BiP substrate. *Semin. Cell Dev. Biol.* **21:** 472–8

Pagès G & Grudinin S (2020) AnAnaS: Software for Analytical Analysis of Symmetries in Protein Structures. In *Methods in Molecular Biology* pp 245–257. Humana Press Inc.

Peng Y, Shapiro SL, Banduseela VC, Dieterich IA, Hewitt KJ, Bresnick EH, Kong G, Zhang J, Schueler KL, Keller MP, Attie AD, Hacker TA, Sullivan R, Kielar-Grevstad E, Arriola Apelo SI, Lamming DW, Anderson RM & Puglielli L (2018) Increased transport of acetyl-CoA into the endoplasmic reticulum causes a progeria-like phenotype. *Aging Cell* **17:** e12820

Perera LA, Rato C, Yan Y, Neidhardt L, McLaughlin SH, Read RJ, Preissler S & Ron D (2019) An oligomeric state-dependent switch in the ER enzyme FICD regulates AMPylation and deAMPylation of BiP. *EMBO J.* **38:** e102177

Petrova K, Oyadomari S, Hendershot LM & Ron D (2008) Regulated association of misfolded endoplasmic reticulum lumenal proteins with P58/DNAJc3. *EMBO J.* **27:** 2862–72

Pettersen EF, Goddard TD, Huang CC, Couch GS, Greenblatt DM, Meng EC & Ferrin TE (2004) UCSF Chimera - A visualization system for exploratory research and analysis. *J. Comput. Chem.* **25:** 1605–1612

Pietraszewska-Bogiel A & Gadella TWJ (2011) FRET microscopy: From principle to routine technology in cell biology. *J. Microsc.* **241:** 111–118

Pipeleers DG & Pipeleers-Marichal MA (1981) A method for the purification of single A, B and D cells and for the isolation of coupled cells from isolated rat islets. *Diabetologia* **20:** 654–663

Preissler S, Chambers JE, Crespillo-Casado A, Avezov E, Miranda E, Perez J, Hendershot LM, Harding HP & Ron D (2015a) Physiological modulation of BiP activity by trans-protomer engagement of the interdomain linker. *Elife* **4:** e08961

Preissler S, Rato C, Chen R, Antrobus R, Ding S, Fearnley IM & Ron D (2015b) AMPylation

matches BiP activity to client protein load in the endoplasmic reticulum. *Elife* **4:** e12621

Preissler S, Rato C, Perera L, Saudek V & Ron D (2017a) FICD acts bifunctionally to AMPylate and de-AMPylate the endoplasmic reticulum chaperone BiP. *Nat. Struct. Mol. Biol.* **24:** 23–29

Preissler S, Rato C, Yan Y, Perera LA, Czako A & Ron D (2020) Calcium depletion challenges endoplasmic reticulum proteostasis by destabilising BiP-substrate complexes. *Elife* **9:** 2020.11.03.366484

Preissler S, Rohland L, Yan Y, Chen R, Read RJ & Ron D (2017b) AMPylation targets the rate-limiting step of BiP's ATPase cycle for its functional inactivation. *Elife* **6:** e29428

Preissler S & Ron D (2019) Early Events in the Endoplasmic Reticulum Unfolded Protein Response. *Cold Spring Harb. Perspect. Biol.* **11:** a033894

Rahman M, Ham H, Liu X, Sugiura Y, Orth K & Krämer H (2012) Visual neurotransmission in Drosophila requires expression of Fic in glial capitate projections. *Nat. Neurosci.* **15:** 871–875

Rist W, Graf C, Bukau B & Mayer MP (2006) Amide hydrogen exchange reveals conformational changes in Hsp70 chaperones important for allosteric regulation. *J. Biol. Chem.* **281:** 16493–16501

Ruben EA, Schwans JP, Sonnett M, Natarajan A, Gonzalez A, Tsai Y & Herschlag D (2013) Ground state destabilization from a positioned general base in the Ketosteroid isomerase active site. *Biochemistry* **52:** 1074–1081

Sanyal A, Chen AJ, Nakayasu ES, Lazar CS, Zbornik EA, Worby CA, Koller A & Mattoo S (2015) A Novel Link between Fic (Filamentation Induced by cAMP)-mediated Adenylylation/AMPylation and the Unfolded Protein Response. *J. Biol. Chem.* **290:** 8482–8499

Sanyal A, Zbornik EA, Watson BG, Christoffer C, Ma J, Kihara D & Mattoo S (2018) Kinetic And Structural Parameters Governing Fic-Mediated Adenylylation/AMPylation of the Hsp70 chaperone, BiP/GRP78. *bioRxiv***:** 494930

Schrödinger, LLC (2015) The {PyMOL} Molecular Graphics System, Version~1.8

Schutze MP, Peterson PA & Jackson MR (1994) An N-terminal double-arginine motif maintains type II membrane proteins in the endoplasmic reticulum. *EMBO J.* **13:** 1696–

1705

Scorsone KA, Panniers R, Rowlands AG & Henshaw EC (1987) Phosphorylation of eukaryotic initiation factor 2 during physiological stresses which affect protein synthesis. *J. Biol. Chem.* **262:** 14538–43

Sekhar A, Rosenzweig R, Bouvignies G & Kay LE (2015) Mapping the conformation of a client protein through the Hsp70 functional cycle. *Proc. Natl. Acad. Sci. U. S. A.* **112:** 10395–10400

Sekine Y, Zyryanova A, Crespillo-Casado A, Amin-Wetzel N, Harding HP & Ron D (2016) Paradoxical Sensitivity to an Integrated Stress Response Blocking Mutation in Vanishing White Matter Cells. *PLoS One* **11:** e0166278

Sreelatha A, Yee SS, Lopez VA, Park BC, Kinch LN, Pilch S, Servage KA, Zhang J, Jiou J, Karasiewicz-Urbańska M, Łobocka M, Grishin N V., Orth K, Kucharczyk R, Pawłowski K, Tomchick DR & Tagliabracci VS (2018) Protein AMPylation by an Evolutionarily Conserved Pseudokinase. *Cell* **175:** 809-821.e19

Stanger F V, Burmann BM, Harms A, Aragão H, Mazur A, Sharpe T, Dehio C, Hiller S & Schirmer T (2016) Intrinsic regulation of FIC-domain AMP-transferases by oligomerization and automodification. *Proc. Natl. Acad. Sci. U. S. A.* **113:** E529-37

Stefan Y, Meda P, Neufeld M & Orci L (1987) Stimulation of insulin secretion reveals heterogeneity of pancreatic B cells in vivo. *J. Clin. Invest.* **80:** 175–83

Svergun DI, Richard S, Koch MHJ, Sayers Z, Kuprin S & Zaccai G (1998) Protein hydration in solution: Experimental observation by x-ray and neutron scattering. *Proc. Natl. Acad. Sci. U. S. A.* **95:** 2267–2272

Sydow JF & Cramer P (2009) RNA polymerase fidelity and transcriptional proofreading. *Curr. Opin. Struct. Biol.* **19:** 732–9

Taguwa S, Maringer K, Li X, Bernal-Rubio D, Rauch JN, Gestwicki JE, Andino R, Fernandez-Sesma A & Frydman J (2015) Defining Hsp70 Subnetworks in Dengue Virus Replication Reveals Key Vulnerability in Flavivirus Infection. *Cell* **163:** 1108–1123

Taguwa S, Yeh M Te, Rainbolt TK, Nayak A, Shao H, Gestwicki JE, Andino R & Frydman J (2019) Zika Virus Dependence on Host Hsp70 Provides a Protective Strategy against Infection and Disease. *Cell Rep.* **26:** 906-920.e3

Truttmann MC, Cruz VE, Guo X, Engert C, Schwartz TU & Ploegh HL (2016) The Caenorhabditis elegans Protein FIC-1 Is an AMPylase That Covalently Modifies Heat-Shock 70 Family Proteins, Translation Elongation Factors and Histones. *PLoS Genet.* **12:** e1006023

Utsumi R, Nakamoto Y, Kawamukai M, Himeno M & Komano T (1982) Involvement of cyclic AMP and its receptor protein in filamentation of an Escherichia coli fic mutant. *J. Bacteriol.* **151:** 807–12

Valiev M, Kawai R, Adams JA & Weare JH (2003) The role of the putative catalytic base in the phosphoryl transfer reaction in a protein kinase: First-principles calculations. *J. Am. Chem. Soc.* **125:** 9926–9927

Veyron S, Oliva G, Rolando M, Buchrieser C, Peyroche G & Cherfils J (2019) A Ca 2+ -regulated deAMPylation switch in human and bacterial FIC proteins. *Nat. Commun.* **10:** 1142

Vitale M, Bakunts A, Orsi A, Lari F, Tadé L, Danieli A, Rato C, Valetti C, Sitia R, Raimondi A, Christianson JC & Van Anken E (2019) Inadequate BiP availability defines endoplasmic reticulum stress. *Elife* **8:**

Walter P & Ron D (2011) The unfolded protein response: from stress pathway to homeostatic regulation. *Science* **334:** 1081–6

Wang D, Eraslan B, Wieland T, Hallström B, Hopf T, Zolg DP, Zecha J, Asplund A, Li L, Meng C, Frejno M, Schmidt T, Schnatbaum K, Wilhelm M, Ponten F, Uhlen M, Gagneur J, Hahne H & Kuster B (2019) A deep proteome and transcriptome abundance atlas of 29 healthy human tissues. *Mol. Syst. Biol.* **15:**

Wang J, Lee J, Liem D & Ping P (2017) HSPA5 Gene encoding Hsp70 chaperone BiP in the endoplasmic reticulum. *Gene* **618:** 14–23

Wei D, Jacobs S, Modla S, Zhang S, Young CL, Cirino R, Caplan J & Czymmek K (2012) High-resolution three-dimensional reconstruction of a whole yeast cell using focused-ion beam scanning electron microscopy. *Biotechniques* **53:** 41–48

West M, Zurek N, Hoenger A & Voeltz GK (2011) A 3D analysis of yeast ER structure reveals how ER domains are organized by membrane curvature. *J. Cell Biol.* **193:** 333–46

Whitten AE, Cai S & Trewhella J (2008) MULCh: Modules for the analysis of small-angle

neutron contrast variation data from biomolecular assemblies. *J. Appl. Crystallogr.* **41:** 222–226

Wieteska L, Shahidi S & Zhuravleva A (2017) Allosteric fine-tuning of the conformational equilibrium poises the chaperone BiP for post-translational regulation. *Elife* **6:** e29430

Winn MD, Ballard CC, Cowtan KD, Dodson EJ, Emsley P, Evans PR, Keegan RM, Krissinel EB, Leslie AGW, McCoy A, McNicholas SJ, Murshudov GN, Pannu NS, Potterton EA, Powell HR, Read RJ, Vagin A & Wilson KS (2011) Overview of the CCP4 suite and current developments. *Acta Crystallogr. D. Biol. Crystallogr.* **67:** 235–42

Winn MD, Murshudov GN & Papiz MZ (2003) Macromolecular TLS Refinement in REFMAC at Moderate Resolutions. *Methods Enzymol.* **374:** 300–321

Winter G (2010) Xia2: An expert system for macromolecular crystallography data reduction. *J. Appl. Crystallogr.* **43:** 186–190

Wiśniewski JR, Hein MY, Cox J & Mann M (2014) A 'proteomic ruler' for protein copy number and concentration estimation without spike-in standards. *Mol. Cell. Proteomics* **13:** 3497–506

Xiao J, Worby CA, Mattoo S, Sankaran B & Dixon JE (2010) Structural basis of Fic-mediated adenylylation. *Nat. Struct. Mol. Biol.* **17:** 1004–10

Xu Y, Carr PD, Vasudevan SG & Ollis DL (2010) Structure of the adenylylation domain of E. coli glutamine synthetase adenylyl transferase: evidence for gene duplication and evolution of a new active site. *J. Mol. Biol.* **396:** 773–84

Xu Y, Zhang R, Joachimiak A, Carr PD, Huber T, Vasudevan SG & Ollis DL (2004) Structure of the N-terminal domain of Escherichia coli glutamine synthetase adenylyltransferase. *Structure* **12:** 861–9

Yang J, Nune M, Zong Y, Zhou L & Liu Q (2015) Close and Allosteric Opening of the Polypeptide-Binding Site in a Human Hsp70 Chaperone BiP. *Structure* **23:** 2191–2203

Yang J, Zong Y, Su J, Li H, Zhu H, Columbus L, Zhou L & Liu Q (2017) Conformation transitions of the polypeptide-binding pocket support an active substrate release from Hsp70s. *Nat. Commun.* **8:** 1201

Yang Y, Yue Y, Song N, Li C, Yuan Z, Wang Y, Ma Y, Li H, Zhang F, Wang W, Jia H, Li P, Li X, Wang Q, Ding Z, Dong H, Gu L & Li B (2020) The YdiU Domain Modulates

Bacterial Stress Signaling through Mn2+-dependent UMPylation. *bioRxiv***:** 692707

Yarbrough ML, Li Y, Kinch LN, Grishin N V., Ball HL & Orth K (2009) AMPylation of Rho GTPases by Vibrio VopS Disrupts Effector Binding and Downstream Signaling. *Science (80-.).* **323:** 269–272

Yogurtcu ON & Johnson ME (2018) Cytosolic proteins can exploit membrane localization to trigger functional assembly. *PLoS Comput. Biol.* **14:** e1006031

Yount RG, Babcock D, Ballantyne W & Ojala D (1971) Adenylyl imidodiphosphate, an adenosine triphosphate analog containing a P--N--P linkage. *Biochemistry* **10:** 2484–9

Zaccai G (2012) Straight lines of neutron scattering in biology: A review of basic controls in SANS and EINS. *Eur. Biophys. J.* **41:** 781–787

Zaccai NR, Sandlin CW, Hoopes JT, Curtis JE, Fleming PJ, Fleming KG & Krueger S (2016) Deuterium Labeling Together with Contrast Variation Small-Angle Neutron Scattering Suggests How Skp Captures and Releases Unfolded Outer Membrane Proteins. In *Methods in Enzymology* pp 159–210. Academic Press

Zheng H, Cooper DR, Porebski PJ, Shabalin IG, Handing KB & Minor W (2017) *CheckMyMetal* : a macromolecular metal-binding validation tool. *Acta Crystallogr. Sect. D Struct. Biol.* **73:** 223–233

Zhuravleva A, Clerico EM & Gierasch LM (2012) An Interdomain Energetic Tug-of-War Creates the Allosterically Active State in Hsp70 Molecular Chaperones. *Cell* **151:** 1296–1307

Zhuravleva A & Gierasch LM (2015) Substrate-binding domain conformational dynamics mediate Hsp70 allostery. *Proc. Natl. Acad. Sci. U. S. A.* **112:** E2865-73